

Mechanistic Studies of Improved Foam EOR Processes

Final Report
Sept. 1, 2001 - Dec. 31, 2004

Principal Author:

William R. Rossen

Date Report Issued: March 16, 2005

Work Performed under Contract DE-FC26-01BC15318

The University of Texas at Austin
Center for Petroleum and Geosystems Engineering
1 University Station, C0300
Austin, TX 78712-1061

DISCLAIMER

This report was prepared as an account of work sponsored by an agency of the United States Government. Neither the United States Government nor any agency thereof, nor any of their employees, makes any warranty, express or implied, or assumes any legal liability or responsibility for the accuracy, completeness, or usefulness of any information, apparatus, product, or process disclosed, or represents that its use would not infringe privately owned rights. Reference herein to any specific commercial product, process, or service by trade name, trademark, manufacturer, or otherwise does not necessarily constitute or imply its endorsement, recommendation, or favoring by the United States Government or any agency thereof. The views and opinions of authors expressed herein do not necessarily state or reflect those of the United States Government or any agency thereof.

Mechanistic Studies of Improved Foam EOR Processes

Contract No. DE-FC26-01BC15318

The University of Texas at Austin
1 University Station, C0300
Austin, TX 78712-1061

Contract Date: Sept. 1, 2001
Completion: Dec. 31, 2004

ABSTRACT

The objective of this research is to widen the application of foam to enhanced oil recovery (EOR) by investigating fundamental mechanisms of foams in porous media. This research is to lay the groundwork for more-applied research on foams for improved sweep efficiency in miscible gas, steam and surfactant-based EOR. Task 1 investigates the pore-scale interactions between foam bubbles and polymer molecules. Task 2 examines the mechanisms of gas trapping, and interaction between gas trapping and foam effectiveness. Task 3 investigates mechanisms of foam generation in porous media.

For Task 1, we investigated the interactions of polymers and foam in search of means to stabilize and strengthen foam using polymers, especially in the presence of oil. For the polymers (xanthan and partially hydrolyzed polyacrylamide), oils (decane and 37.5° API crude oil), and surfactant (alpha-olefin sulfonate) tested here, it appears from coreflood pressure gradient $|\nabla p|$ that polymer destabilizes foam modestly, raising water saturation S_w and water relative permeability k_{rw} . The increased viscosity of the aqueous phase with polymer partially compensates for the destabilization of foam. For the same polymers and surfactant, polymer does not stabilize foam in the presence of decane or 37.5° API crude oil.

Complex behavior, in contradiction to the expected two steady-state strong-foam regimes, was sometimes observed. At the limit of, or in the place of, the high-quality regime, there was sometimes an abrupt jump upwards in $|\nabla p|$ as though from hysteresis and a change of state. In the low-quality regime, $|\nabla p|$ was not independent of liquid superficial velocity, but decreased with increasing liquid superficial velocity. This curious behavior in the low-quality regime was also found in studies of CO₂ foam; an explanation was discovered in research on Task 2. Pressure gradient can decrease upon increasing liquid superficial velocity in the low-quality regime because the drag on bubbles decreases as the liquid film between the bubble and the pore wall thickens.

A new theory developed for the drag on bubbles moving through tubes suggests that polymer should make foam more shear-thinning than foam without polymer, both in the high-quality and low-quality flow regimes.

Regarding Task 2, a new model for gas trapping was incorporated into a foam simulator. In this model, trapped-gas saturation is a function of pressure gradient, fit to

data for liquid relative permeability following foam injection and the gas relative-permeability curve. This model can fit steady-state data for the two strong-foam flow regimes and in limited trials it also fitted the transition period between foam injection and injection of liquid following foam in coreflood experiments. The simulator would be most helpful in modeling liquid injectivity in SAG foam processes.

Coreflood experiments during liquid injection following foam concluded that liquid saturation rose more upon liquid injection; i.e., less gas was trapped during liquid injection, than had been previously thought. In this study the liquid relative-permeability function that applied to foam flow was also reasonably accurate during post-foam liquid injection, as assumed in the simulator described above. However, data implied that liquid does not uniformly sweep the foam, but only contacts a portion of trapped gas. CT studies confirm that liquid fingers through gas rather than displacing it. This casts doubt on the ability of simulators to scale-up laboratory data unless applied in 2D or 3D on a scale fine enough to resolve the fingering patterns.

Direct imaging of gas-phase tracer concentration *in situ* during corefloods shows that the conventional 1D mass-transport model used to interpret tracer effluent data makes several serious false assumptions. Moreover, in several cases examined, flowing-gas fractions inferred from the 1D model can vary by as much as a factor of 2 among reasonable fits to the data.

In spite of the uncertainty in individual estimates of trapped-gas fraction, trends are evident in our results. The trapped-gas fraction S_t obtained from the 1D model fit to the five experiments shown here decreases with increasing gas injection rate; it may increase weakly with increasing liquid injection rate. It is hard to distinguish effects of pressure gradient $|\nabla P|$ in our experiments, in part because $|\nabla P|$ is similar in most of the cases, in spite of significant changes in injection rates. The cases with increasing liquid injection rate appear to reflect the low-quality foam regime. If so, and if the fitted values of S_t are correct, then they contradict the conjecture of Rossen and Wang (1999) that trapped-gas fraction should decrease slightly with increasing liquid injection rate. One pair of cases with increasing gas injection rate may reflect the high-quality regime, but it is hard to be sure because foam quality changes substantially along the core due to gas expansion.

Data from several other gas-tracer experiments, without the benefit of CT imaging, were less conclusive. The 1D mass-transport model can fit the data satisfactorily with a wide variety of values of trapped-gas saturation. The reason appears to be that mass transfer between flowing and trapped gas is rapid in these experiments on the time scale of the coreflood. Strategies for minimizing this problem in future studies include use of other tracer gases or shorter cores, though use of shorter cores increases the influence of the entrance region where foam is not fully developed.

Regarding Task 3, Experiments with N_2 and CO_2 foam in a variety of porous media show that there is a minimum pressure gradient ∇p^{\min} required to trigger foam generation in steady flow through homogeneous porous media. In beadpacks and sandpacks, ∇p^{\min} was seen to vary with permeability k as $(1/k)$ over $2\frac{1}{2}$ orders of magnitude in k . The relation between ∇p^{\min} and k is more complex in consolidated media, in part because the relations between permeability, pore-throat size and pore length are more complex. ∇p^{\min} was a factor of 20 lower with CO_2 than with N_2 foams under similar conditions. Part, but not all, of this difference can be explained by the lower surface tension with dense CO_2 .

Meanwhile, the evidence for the competing view that foam is steadily created by Roof snap-off in narrow pore throats upstream of wide pore bodies was reviewed in detail. Our conclusion is that there is no substantial evidence for Roof snap-off as a foam-generation mechanism at steady state in homogeneous porous media.

If pressure gradient is fixed rather than injection rates in coreflood experiments, one observes an unstable state between coarse foam (or weak foam) and strong foam. This regime manifests its instability in fluctuating flow rates at fixed $|\nabla p|$, and, at least sometimes, in $|\nabla p|$ that is not uniform. This regime may have practical importance in field applications with limits on injection pressure.

A population-balance foam simulator incorporating a lamella-creation function that depends on $|\nabla p|$, in agreement with the above results, fits numerous features observed in foam-generation experiments: in particular, the three foam states referred to above (coarse foam, strong foam and the unstable intermediate state), the high-quality and low-quality strong-foam regimes, and trends of foam generation with injection rates. Applied to dynamic displacements, the simulator confirms the stability of the coarse- and strong-foam states and the instability of the intermediate state. The model predicts a transition from coarse foam to strong foam ("foam generation") as injection rates increase, in agreement with experiments. Most of the model can be fit to steady-state data; the remaining kinetic parameters can be fit to the length of the region near the core inlet in which foam is created.

A pore-network model for foam generation resolves two paradoxes troubling our model of foam generation by mobilization and division. First, the model shows how new lamellae are created near the inlet of the porous medium to replace those mobilized and transported downstream. Second, the model reconciles the two halves of the theory of Rossen and Gauglitz (1990) at the percolation threshold.

A series of sandpack experiments found several effective ways of enhancing foam generation, and some that were not effective. In homogeneous sandpacks, foam generation occurs at lower pressure gradient and lower gas velocity at higher liquid injection rates, lower permeability, and higher surfactant concentration. Foam generation occurred more easily in flow across sharp increases in permeability than in homogeneous packs. Temporarily increasing pressure gradient did not facilitate foam generation in homogeneous sandpacks, but did trigger lasting foam generation in layered packs. When gas was injected following a slug of liquid, or into a pack pre-saturated with liquid, foam generation occurred at a lower pressure gradient than with steady co-injection of liquid and gas.

LIST OF PUBLICATIONS FROM PROJECT

in press:

- Chen, M., Rossen, W. R., and Yortsos, Y. C.: "The Flow and Displacement in Porous Media of Fluids with Yield Stress," accepted for publication by *Chemical Engineering Science*.
- Kim, J. S., Dong, Y., and Rossen, W. R., "Steady-State Flow Behavior of CO₂ Foam," SPE 89351 presented at the 2004 SPE/DOE Symposium on Improved Oil Recovery, Tulsa, OK, 17-21 April; accepted for publication by *SPE J*.

2005:

- Chen, M., Yortsos, Y. C., and Rossen, W. R.: "Insights on Foam Generation in Porous Media from Pore-Network Studies," *Colloids Surfaces A: Physicochem Eng. Aspects*, **256** (2-3), 181-189 (2005).
- Nguyen, Q. P., Rossen, W. R., Zitha, P. L. J., and Currie, P. K.: "Determination of Gas Trapping With Foam Using X-Ray CT and Effluent Analysis," SPE 94764 prepared for presentation at the SPE European Formation Damage Conference, Scheveningen, The Netherlands, 25-27 May 2005.
- Nguyen, Q. P., Zitha, P. L. J., Currie, P. K., and Rossen, W. R.: "CT Study of Liquid Diversion with Foam," SPE 94764 prepared for presentation at the 2005 SPE Production and Operations Symposium, Oklahoma City, OK, 17 – 19 April 2005.

2004:

- Xu, Q., and Rossen, W. R., "Experimental Study of Gas Injection in Surfactant-Alternating-Gas Foam Process," *SPEREE* **7** (Dec. 2004), 438-448.
- Cox, S.J., Neethling, S., Rossen, W.R., Schleifenbaum, W., Schmidt-Wellenburg, P., and Cilliers, J.J., "A Theory of the Effective Yield Stress of Foam in Porous Media: The Motion of a Soap Film Traversing a Three-Dimensional Pore," *Colloids Surfaces A: Physicochem Eng. Aspects* **245**, 143–151 (2004).
- Rossen, W.R., and van Duijn, C.J., "Gravity Segregation in Steady-State Horizontal Flow in Homogeneous Reservoirs," *J. Petr. Sci. Eng.* **43**, 99-111 (2004).
- Shan, D. and Rossen, W.R., "Optimal Injection Strategies for Foam IOR," *SPE Journal* **9** (June 2004), 132-150.
- Kam, S. I., Nguyen, Q. P., Li, Q., and Rossen, W. R.: "Dynamic Simulations With an Improved Model for Foam Generation," SPE 90938 presented at the 2004 SPE Annual Technical Conference and Exhibition held in Houston, Texas, U.S.A., 26–29 September.
- Chen, M., Yortsos, Y. C., and Rossen, W. R.: "A Pore-Network Study of the Mechanisms of Foam Generation," SPE 90939 presented at the 2004 SPE Annual Technical Conference and Exhibition held in Houston, Texas, U.S.A., 26–29 September.
- Rossen, W. R., and Bruining, J., "Foam Displacements With Multiple Steady States," SPE 89397 presented at the 2004 SPE/DOE Symposium on Improved Oil Recovery, Tulsa, OK, 17-21 April.

2003:

- Kam, S. I., and Rossen, W. R., "A Model for Foam Generation in Homogeneous Porous Media," *SPE Journal* **8** (Dec. 2003), 417-425.
- Rossen, W. R., "A Critical Review of Roof Snap-Off as a Mechanism of Steady-State

- Foam Generation in Homogeneous Porous Media," *Colloids Surfaces A: Physicochem Eng. Aspects*, **225** (1-3) 1-24 (2003).
- Xu, Q., and Rossen, W. R., "Effective Viscosity of Foam in Periodically Constricted Tubes," *Colloids Surfaces A: Physicochem Eng. Aspects* **216** (1-3), 175-194 (2003).
- Xu, Q., and Rossen, W. R., "Laboratory Study of Gas Trapping in Foam-Acid Diversion," SPE 84133 presented at the 2003 SPE Annual Technical Conference and Exhibition, Denver, CO, 5-8 Oct.
- Kam, S. I., Frenier, W. W., Davies, S. N., and Rossen, W. R., "Experimental Study of High-Temperature Foam for Acid Diversion" paper SPE 82266 prepared for presentation at the 2003 SPE European Formation Damage Conference, The Hague, The Netherlands, 13-14 May.

2002:

- Gauglitz, P.A., Friedmann, F., Kam, S. I., and Rossen, W.R., "Foam Generation in Homogeneous Porous Media," *Chem. Eng. Sci.* **57**, 4037-4052 (2002).
- Cheng, L., Kam, S. I., Delshad, M. and Rossen, W.R., "Simulation of Dynamic Foam-Acid Diversion Processes," *SPE Journal* **7** (Sept. 2002), 316-324.
- Mamun, C. K., Rong, J. G., Kam, S. I., Liljestrand, H. M., and Rossen, W. R., "Extending Foam Technology from Improved Oil Recovery to Environmental Remediation," paper SPE 77557, presented at the SPE 2002 Annual Technical Conference and Exhibition, San Antonio, 29 Sept. - 2 Oct.
- Mamun, C.K., Rong, J.G., Kam, S.I., Liljestrand, H.M. and Rossen, W.R., "Simulating Use of Foam in Aquifer Remediation," Proceedings of the XIVth International Conference on Computational Methods in Water Resources (CMWR XIV), June 23-28 2002, Delft, The Netherlands, S.M. Hassanizadeh, R.J. Schotting, W.G. Gray, G.F. Pinder, eds., Volume 1, 867-874.

2001:

- Alvarez, J. M., Rivas, H., and Rossen, W.R., "A Unified Model for Steady-State Foam Behavior at High and Low Foam Qualities," *SPE Journal* **6** (Sept. 2001), 325-333.

TABLE OF CONTENTS

	<u>Page</u>
ABSTRACT	3
LIST OF PUBLICATIONS FROM PROJECT	6
OBJECTIVES	10
EXPERIMENTAL	10
RESULTS AND DISCUSSION	10
Task 1 - Interactions Between Polymer and Foam	10
Previous Research on Polymers and Foams	11
Effect of Polymer on Surface Properties	13
Corefloods	14
Initial Experiments	14
Further Experiments on the Effect of Oil in Sandpacks	15
Experiments in Boise Sandstone	16
Modeling the Viscosity of Foam with Polymer	17
Conclusions From Task 1	24
Task 2	24
Overview	24
Modeling Gas Trapping in Foam Simulation	25
Initial Experiments: Water Saturation and Gas Trapping with Foam	26
Gas Trapping and the Low-Quality Foam Regime	27
Previous Experimental Studies with Gas-Phase Tracers	29
Tracer Experiments at UT	31
Foam Yield Stress	35
Direct Observation of Tracer Distribution Through CT Imaging	35
Experimental	36
Original Analysis of Data	36
Reconstruction of Effluent Tracer Profile	37
Mass Transfer Between Flowing and Trapped Gas	38
Standard 1D Model for Interpreting Tracer Effluent Data	38
Results and Discussion	41
Effect of Gas Injection Rate	42
Effect of Liquid Injection Rate	44
Discussion of CT Experiments	46
Conclusions From CT Study	48
CT Images of Liquid Injection After Foam	48
Network Modeling of Gas Trapping	50
Conclusions from Task 2	50
Task 3 - Foam Generation	52

Initial Experiments: Foam Generation as a Jump Between Steady States	52
Incorporation of Mechanisms into Population-Balance Simulator: Steady State Behavior	53
Critique of Foam Generation by Roof Snap-Off	56
Foam Displacements With Abrupt Changes in State	57
Pore-Level Mechanisms of Foam Generation	59
Population-Balance Simulator: Modeling Dynamic Displacements	60
Further Experiments in Sandpacks	61
Two Foam States	62
Foam Generation in Flow Across Layer Boundaries	63
Enhanced Foam Generation: Pulsed-Pressure and Alternate-Slug Injection	65
Conclusions from Task 3	67
CONCLUSIONS	69
ACKNOWLEDGMENTS	73
REFERENCES	74
TABLES	80
Task 1	80
Task 2	81
FIGURES	82
Task 1	82
Task 2	95
Task 3	121

OBJECTIVES

The objective of this research is to widen the application of foam to enhanced oil recovery (EOR) by investigating fundamental mechanisms of foam in porous media. This research will lay the groundwork for more applied research on foams for improved sweep efficiency in miscible gas, steam and surfactant-based EOR. Task 1 investigates the pore-scale interactions between foam bubbles and polymer molecules. Task 2 examines the mechanisms of gas trapping, and interaction between gas trapping and foam effectiveness. Task 3 investigates mechanisms of foam generation in porous media.

EXPERIMENTAL

The experimental techniques employed vary with the specific task addressed. Therefore the experimental techniques are discussed together with the Results and Discussion section on each task, below.

RESULTS AND DISCUSSION

TASK 1: INTERACTIONS BETWEEN POLYMER AND FOAM

This work is motivated by a hypothesis about how polymer interacts with foam in porous media. The hypothesis derives in turn from the observation that steady-state strong-foam behavior appears to comprise two very different flow regimes, at high and low foam qualities (injected gas volume fraction) (Fig. 1.1) (Alvarez *et al.*, 2001). The high-quality regime is controlled by lamella stability, while in the low-quality regime foam lamellae are relatively stable, bubble size is fixed, and behavior is controlled by gas trapping and mobilization. In the high-quality regime, water saturation S_w is held nearly constant at the water saturation S_w^* corresponding to the "limiting capillary pressure" P_c^* (Khatib *et al.*, 1988; Rossen and Zhou, 1995). In the high-quality regime, applying Darcy's law to the aqueous phase at fixed water saturation S_w^* gives

$$|\nabla p| = U_w \mu_w / (k k_{rw}(S_w^*)) \quad (1.1)$$

where U_w is water superficial velocity, μ_w is aqueous-phase viscosity, k is permeability and $k_{rw}(S_w^*)$ is the relative permeability to the aqueous phase at S_w^* . These two regimes are observed in experiments with N_2 and CO_2 foam, in a variety of porous media including sandstones and sandpacks over a wide range of permeabilities, with many surfactant formulations (Alvarez *et al.*, 2001; Mamun *et al.*, 2002; Kim *et al.*, 2004).

Our hypothesis is that polymer affects foam in the high-quality regime by (a) viscosifying the aqueous phase (increasing μ_w) and (b) stabilizing or destabilizing foam lamellae (reducing or increasing S_w^* , respectively, thereby changing k_{rw}). One can distinguish between these effects by measuring the viscosity of the aqueous phase separately from the foam (accounting if possible for the effects of shear rate on polymer viscosity). If, upon addition of polymer, $|\nabla p|$ in porous media in the high-quality regime increases more than does μ_w , then polymer stabilizes foam lamellae (reduces S_w^* and k_{rw}); if $|\nabla p|$ increases less than does μ_w , then polymer destabilizes the lamellae (raises

S_w^* and k_{rw}). If measured $|\nabla p|$ data are in the low-quality regime, then the relation between $k_{rw}(S_w)$ and foam stability is less direct, but one would still expect $|\nabla p|$ to reflect water saturation and water viscosity, and one can separate the effects of polymer on each.

Before describing our research on polymer and foams, we begin with a survey of previous research:

Previous Research on Polymers and Foams

Some of the earliest studies on surfactant/polymer interaction in the petroleum literature were in relation to surfactant flooding (Pope *et al.*, 1982). These studies show that surfactant and polymer coexist in solution up to a certain salinity, beyond which a surfactant-rich and a polymer-rich phases are formed, suggesting that surfactant and polymer strongly repel each other. Sabbadin *et al.* (1984) studied interaction between sodium dodecyl sulfate and partially hydrolyzed polyacrylamide (HPAM) in order to address the questions of (i) what is the influence of polymer on the micellar properties of surfactant (CMC, aggregation number, etc.); (ii) how does surfactant modify the polymer molecular conformation (viscosity, radius of gyration); and (iii) whether there is association between surfactant and polymer.

These results suggest that, at least for polymer-enhanced foams (PEF's) made of anionic surfactants and HPAM polymer, it is unlikely that polymer molecules would be adsorbed at gas-liquid interface in association with surfactant molecules. We confirm this below for one pair of anionic surfactant and HPAM polymer. With molecular repulsion between surfactant and polymer, it is also unlikely that polymer molecules would be inside the thin lamella films. Most of the polymer is expected to stay in the relatively thick liquid film on tube wall or in Plateau borders. The implication is that the addition of anionic polymer to a foam made of an anionic surfactant does not help improve the foam's stability. On the other hand, the increase in water viscosity may significantly increase the apparent viscosity of foam.

In the literature, a wide range of polymer structures has been employed to study the effects of polymer addition on foam behavior in porous media. Anionic polymers such as polyacrylamide and xanthan gum that are commonly used for enhanced oil recovery, and nonionic polymers such as polyvinyl pyrrolidone, have been used.

An important early work on polymer-enhanced foam (PEF) is by Sydansk (1993a, b), who studied properties and effectiveness of PEF formed from C₁₄-C₁₆ alpha-olefin sulfonate (AOS) surfactant and HPAM polymer. Use of PEF was intended to improve gas mobility during its injection into a naturally fractured reservoir. Due to the large permeability contrast between fracture and matrix, even the use of foam sometimes is not sufficient to reduce gas mobility in fractures.

High concentrations (0.35 – 0.7 wt%) of polymer were employed for control of gas mobility in fractures. Bulk PEF viscosity, PEF mobility in Hele-Shaw cell as an idealized fracture model, and mobility in sandpack, were compared with those for surfactant-free polymer solutions and polymer-free foams. PEF were pre-formed before injection into the fracture model or the sandpack. Results suggested greatly reduced gas mobility, and also improved stability of foam due to the polymer addition.

Aarra *et al.*(1997) studied the enhancement of the gas blocking ability of foam formed from AOS, by addition of different polymers. The foam mobility in Berea sandstone and reservoir cores has been measured for PEF with xanthan, polyvinyl alcohol, or HPAM. The best gas blocking performance was observed with xanthan biopolymer. For gas-control in Prudhoe Bay field, Thach *et al.*(1996) tested PEF that

consists of AOS or Chevron Chaser surfactant, and HPAM polymer. After laboratory evaluations with bulk-foam stability tests and sandpack mobility tests, the PEF's were tested at three hydraulically fractured wells to determine their effectiveness in reducing GOR.

Dalland and Hanssen (1997) carried out laboratory investigations on the use of PEF to control gas influx into production wells. As foam-forming surfactants, AOS and a highly fluorinated C9-alkyl ethoxylated alcohol with about 3 EO's were employed, together with HPAM polymer. PEF's were shown to improve gas-blocking performance significantly. In some repeated experiments, however, PEF was not as effective and, in particular, adding too much polymer could result in sharply decreased foam effectiveness. One desired benefit of adding polymer to foam is the tolerance of foam stability to resident oil. Hanssen and Dalland (2000) investigated the reasons for the improved oil tolerance by carrying out foam corefloods with crude oil in the core. Based on their study comparing results with and without polymer, and with and without oil, they concluded that the only effect of polymer addition is to lower oil saturations before and during foam generation and propagation, with increased pressure gradient. The more efficient removal of oil by the low-mobility PEF bank reduced the exposure of PEF to oil, thus prolonging its integrity. ***In other words, they suggest that there is no intrinsic stabilizing effect of polymer on foam in the presence of crude oil.***

In order to remedy the severe gas coning problem in reservoirs with thin oil rim below a gas cap, Chukwueke *et al.*(1998) investigated the use of PEF for gas-blocking, by carrying out reservoir-condition corefloods. The surfactants tested were AOS, a fluoro ammonium hydrocarbon, and an ethoxylated nonionic fluoro surfactant, and HPAM was used as polymer. Eight wells were treated using two foamer systems. The field results vary between a significant reduction in GOR for more than 12 months and a minor GOR reduction for only a few weeks. Judging from laboratory core tests and field tests, the AOS/HPAM combination appeared to perform better than others.

An extreme form of PEF is foam-gel or gelled foam, which is created by injection of an aqueous solution of surfactant, polymer and cross-linker, together with a gas. Friedmann *et al.*(1997) and Hughes *et al.*(1998) carried out laboratory development and evaluation, and the field testing, of a foam-gel to improve in-depth conformance during a CO₂ flood in a fractured reservoir. Laboratory testing involved foam flow mobility measurements in sandpicks. Two important findings are: (1) generation of foam-gel required a critical gelation pH (> 4.0 to 4.25); and (2) to achieve the in-depth conformance improvement without unmanageable injectivity losses, gelation must be delayed up to 250 hours.

In order to attain pore-level understanding of PEF transport in porous media, Romero *et al.*(2002) carried out micromodel studies to observe movements of PEF in constricted capillaries. PEF's studied were made of AOS surfactant and five different polymers: two HPAM's with different degrees of hydrolyzation; a non-hydrolyzed polyacrylamide; a sulfonated polyacrylamide copolymer; and a hydrophobically modified polyacrylamide. Their study on effects of polymer addition focused on determining whether the two distinct foam flow regimes generally observed (Alvarez *et al.*, 2001) can still be observed: a high quality regime where pressure gradient was independent of gas flow rate, and a low quality regime in which pressure gradient was independent of liquid flow rate. PEF's in micromodels showed quite different behavior, where the high quality regime seemed to be absent. This type of behavior was seen in our own experiments under this Task with and without polymer, discussed below. It is partially explained by Kim *et al.* (2004) and as discussed in connection with Task 2 below.

The effects of HPAM polymer addition on foam made of a variety of surfactants have also been studied by Zhu *et al.*(1998). They measured PEF mobility in sandpacks of varying permeability (130, 50, 13 and 3 darcy) and in sandstone cores of 1.0 and 0.2 darcy. The surfactants investigated were AOS, ethoxylated sulfate, ethoxylated nonylphenol, ethoxylated alcohol, and linear alkyl sulfonate. Their study is notable in that the effects of oil on foam stability with and without polymer addition were investigated for a number of different liquid hydrocarbons and crude oils. Their results show that contact with lighter oils resulted in less stable foam.

Kutay and Schramm (2004) studied the effects of HPAM polymer addition on the foams that were generated employing a 1:1 mixture of surfactants (C₁₀ diphenylether disulfonate and AOS), and another surfactant (alkylamido sulfobetaine). For the foam mobility measurements, a variety of sandstone cores with permeabilities ranging from 61 md to 904 md were employed. One important finding they made is that PEF made of sulfobetaine was much more effective than PEF made of the disulfonate/AOS mixture. Their mobility data and the SEM images, while very qualitative, suggest that the sulfobetaine-based PEF forms a very stable lamella film, possibly by surfactant/polymer association at the film. It appears that, with the sulfobetaine-based PEF, the polymer molecules manage to stay inside the lamella even when it is very thin.

Effect of Polymer on Surface Properties

Polymer can stabilize foam only if polymer resides in the lamellae to stabilize them against drainage. As noted above, it is hard to rationalize how polymer coils could exist in the narrow confines of a lamella (~30-100 nm wide) unless polymer complexes with surfactant at the interface. If polymer does so, it should affect the surface tension of surfactant solution against air. We examined this issue with Alcoflood 935 polyacrylamide polymer (Ciba Specialty Chemicals, Suffolk, VA), with average molecular weight between 8,000,000 and 10,000,000 and 10% hydrolysis. This same polymer is one of those used in our coreflood studies described below.

Fig. 1.2 shows the effect of polymer and surfactant concentrations on surface tension at room temperature of aqueous solutions of surfactant Bio-Terge AS-40, an alpha-olefin sulfonate, with no added salt in this case. Surface tensions were measured by du Nuoy ring. There is little effect of polymer on surface tension, and the small effect that is present (higher surface tension with polymer than without) does not suggest positive association between polymer and surfactant at the surface.

Fig. 1.3 illustrates the effect of polymer and surfactant concentrations and shear rate on viscosity. At 1 wt% NaCl, surfactant has virtually no effect on polymer-solution viscosity, and shear-thinning effects begin above about 50 s⁻¹ for polymer concentrations of 0.2 wt% and below. According to Lake (1989), the characteristic shear rate for single-phase flow in a 1 darcy porous medium at a superficial velocity of 1 ft/d would be about 10 s⁻¹. However, this shear rate-estimate is based on the assumption that polymer fully occupies all pores and flows at a moderate velocity. Polymer in thin films between bubbles and pore walls, moving at the velocity of flowing gas in foam, may experience a higher shear rate. The variety of shear regimes for polymer in water-filled pores, in the films surrounding bubbles, and in the Plateau borders between bubbles makes it difficult to relate rheology measured at fixed shear rate in the laboratory to that experienced in foam in porous media.

Corefloods

Initial Experiments

As noted above, our plan was to characterize the effect of polymer on foam by its effect on the two widely observed steady-state strong-foam regimes illustrated in Fig. 1.1. Characterizing foam behavior in a plot like Fig. 1.1 is time-consuming, because it takes many data to make a plot, and each datum may take one or more days to reach steady-state. Our coreflood apparatus is similar to that in other published foam studies (Alvarez *et al.*, 2001) and is shown schematically in Fig. 1.4. An aqueous solution of surfactant and possibly polymer is injected at fixed rates, while gas is injected simultaneously at fixed mass flow rates. The porous medium could be a sandpack or consolidated core. Pressure drop is measured across four sections of the core or pack. In contrast to the schematic in Fig. 1.4, the core or pack is held vertically, with injection from the top. We did not use a foam separator in these experiments.

Our first experiments were conducted in sandpacks of permeability 6.6 and 16.6 darcy. The surfactant was a 0.39-wt% active (1 wt% as received) solution of Bio-Terge AS-40 (an alpha olefin sulfonate), manufactured by Stepan Chemical Co., in brine with 0.25 wt% NaCl and 0.01 wt% CaCl₂. Back-pressure was about 600 psi and nitrogen was the gas. Polymer solutions were 0.1 wt% of, respectively, a low-molecular-weight polyacrylamide (MW~500,000), a high-molecular-weight polyacrylamide (MW~10-12,000,000), or a 0.05 wt% solution of xanthan polymer (Xanvis, from Kelco Oil Field Group) (MW~5-7,000,000). The viscosities of the three aqueous foam formulations with polymer were 1.2 cp, 2.4 cp, and 3.9 cp, respectively. In all cases viscosity was independent of shear rate over the range measured, which was from 0.9 to from 8 to 19 s⁻¹, depending on the formulation. All experiments were carried out at room temperature.

Fig. 1.5 shows the behavior of foam without polymer in a 6.6-darcy sandpack. There appears to be a high-quality regime (vertical $|\nabla p|$ contours) at lower liquid superficial velocity U_w . At higher U_w (right-hand side of the plot) the $|\nabla p|$ contours are not horizontal as expected in the low-quality regime (*cf.* Fig. 1.1), but show decreasing $|\nabla p|$ as U_w increases at fixed gas superficial velocity U_g . Similar behavior was seen with polymer in the study of Romero *et al.* (2002). We discuss this aspect of the results further under Task 2. There is one other aspect of these results that is unexpected. Rather than a smooth transition from the high-quality to low-quality regimes (Fig. 1.1), one finds a drastic increase in $|\nabla p|$ between them. Fig. 1.6 plots a transect through the $|\nabla p|$ data of Fig. 1.5 at $U_g \sim 9$ ft/d. $|\nabla p|$ increases gradually with U_w in the two low- U_w data points, as expected in the high-quality regime (*cf.* Fig. 1.1), and decreases gradually in the two data at high U_w . Between these pairs of data there is a drastic increase in $|\nabla p|$, which implies an extremely shear-thickening response to increasing U_w . Normally, we would associate this sort of behavior with hysteresis resulting from a foam-generation event (Gauglitz *et al.*, 2002). But we found the $|\nabla p|$ data on both sides of the jump in $|\nabla p|$ to be reproducible. We have no explanation for this behavior. Figs. 1.5, 1.7 and 1.8 show the same abrupt jump in $|\nabla p|$ with polymer in a 6.6-darcy pack and without polymer in a 11.8-darcy sandpack. Both plots also show decreasing $|\nabla p|$ as water superficial velocity increases in the low-quality regime.

Comparison of Figs. 1.5 and 1.7 shows that the polyacrylamide polymer destabilizes foam in the 6.6-darcy sandpack in the absence of oil. One would expect pressure gradient to increase slightly given the slightly higher viscosity of the low-MW polyacrylamide polymer over water, but pressure gradient is lower at all injection rates.

Figs. 1.9 to 1.11 show data for this surfactant formulation in a 16.6-darcy sandpack with, respectively, 0.1 wt% high-MW polyacrylamide (MW~10-12,000,000); 0.05 wt% xanthan (MW~5-7,000,000); and foam without polymer in the same sandpack

after the polymer-foam experiments in that pack. The solution of surfactant and high-MW polymer has a viscosity of 2.4 cp, while the solution of surfactant plus xanthan has viscosity 3.9 cp.

With higher-MW polymer (Fig. 1.9), values of $|\nabla p|$ are comparable to those in Fig. 1.11, i.e. without polymer. The values of $|\nabla p|$ in Fig. 1.10, with xanthan polymer (3.9 cp viscosity for the aqueous phase) are likewise comparable to those on Fig. 1.11. Again, one concludes that polymer destabilizes foam (increases water saturation and k_{rw}), while the increase in the viscosity of the aqueous phase partially compensates for this effect.

Comparison of these figures suggests that without oil, polymer increases the foam pressure gradient by a factor less than it increases the viscosity of the aqueous formulation alone (or does increase pressure gradient at all). This suggests that ***polymer destabilizes foam modestly***, raising water saturation S_w and water relative permeability k_{rw} (Eq. 1.1), ***but the increase in the viscosity of the aqueous phase partially compensates for this effect in the measured pressure gradient.***

Experiments on the Effect of Oil in Sandpacks

One goal of this work is to examine the effect of oil on foam both with and without polymer. We used decane as the oil in the initial tests, because in separate tests decane appeared to destabilize bulk foam made with our surfactant formulation more effectively than crude oils we then had on hand. We follow here the procedure of Mamun *et al.* (2002). Oil is easily displaced from sandpacks by high pressure gradients. Therefore, to produce reproducible, fairly constant conditions with oil present, we inject oil along with the foam at a fixed volume fraction of injected liquids. This approach also avoids the artifact criticized by Hanssen and Dalland (2000), i.e. that the apparent effect of polymer stabilizing foam may in fact reflect lower residual oil saturation with polymer before foam is introduced. In this case the injected oil volume fraction is 22% of injected liquid.

These experiments on the effect of oil on foam with and without polymer were conducted in a 3.67-darcy sandpack. We used first decane as the oil. The surfactant formulation was the same as before (0.39 wt% active Bio-Terge AS-40 in 0.25 wt% NaCl and 0.01 wt% CaCl_2 brine). Polymer-foam solutions in this portion of the study contained 0.05 wt% xanthan polymer in the surfactant formulation, one of the formulations used before. However, the viscosity of the aqueous surfactant formulation with polymer (without gas) was 4.6 cp, rather than 3.9 cp as cited above. The viscosity varies slightly from one batch of mixed polymer solution to another.

Fig. 1.12 shows behavior with no polymer and no oil in the 3.67 darcy sandpack. Fig. 1.13 shows behavior with decane but no polymer. Decane reduces the pressure gradient with foam moderately here, i.e. by about 30-40%. Thus decane does destabilize this foam in the sandpack. $|\nabla p|$ is lower in Fig. 1.13 than in any of the plots presented so far at any permeability.

Fig. 1.14 shows the same system with decane and with xanthan polymer in the foam formulation. Pressure gradient is actually a little lower than without polymer. ***Polymer did not stabilize foam in the presence of decane.*** In fact, given that the aqueous phase is 4.6 times as viscous in Fig. 1.13 than in Fig. 1.12, polymer must have destabilized foam, reflected in a rise in water saturation and water relative permeability (Eq. 1.1).

Fig. 1.15 shows the behavior of foam without polymer or oil injected along with the foam in the same sandpack as the preceding figures, after that sandpack had contacted both polymer and oil. Evidently some oil remains in the pack; the pressure gradient is less than in Fig. 1.12. Thus foam is sensitive to even the relatively small residual oil saturation in this sandpack left behind at high pressure gradient.

Experiments in Boise Sandstone

Our final experiments were conducted using a 0.94-Darcy Boise sandstone core (Gerhard Borbonus Landscaping, Boise, ID) with two oils, decane and a sample of 37.5°API crude oil. Initial tests of shaking 100 ml of surfactant solution in a 500 ml plastic bottle, with and without polymer, with and without decane or crude oil, suggested that this crude oil is more detrimental to foam than is decane, and that polymer does help stability of the foam. In these experiments we used the Alcoflood 935 polyacrylamide polymer, with average molecular weight between 8,000,000 and 10,000,000 and 10% hydrolysis, used to prepare Figs. 1.2 and 1.3.

With lower permeability than sandpacks (about 1 darcy v. several or tens of darcy) there is a greater chance of polymer adsorption altering the permeability of the medium. We found that injection of many pore volumes of 0.1 wt% polymer solution (in 1 wt% NaCl), followed by many pore volumes of polymer-free brine, reduced the permeability of our first Boise core from 1.59 darcy to 0.94 darcy, a decline of about 40%. Subsequent injection of 0.2-wt% polymer solution had no further effect on permeability. The second Boise core had an initial permeability of 1.67 darcy. We did not measure its permeability after polymer injection, but it probably decreased by about the same amount as the first core.

Fig. 1.16 shows the behavior of foam made with 0.39 wt% active surfactant Bio-Terge AS-40 (an alpha olefin sulfonate) in 1 wt% NaCl brine in the first Boise sandstone core. The two regimes look much as they do in Fig. 1.1, with no abrupt jump in $|\nabla p|$ in the high-quality regime, and virtually horizontal contours in the low-quality regime. Fig. 1.17 shows the behavior of the same formulation in the same core with 0.2 wt% Alcoflood 935 polymer added to the surfactant formulation. The low-quality regime is nearly unchanged by the addition of polymer. There is an increase of about a factor of 2 in $|\nabla p|$ in the high-quality regime (vertical contours at low U_w). The viscosity of the liquid phase is about 6 cp with this polymer, however (Fig. 1.3). If polymer left the stability of foam unchanged, as reflected in P_c^* and S_w^* , ∇p then would be expected to increase by roughly a factor of 6 (Eq. 1.1). The fact that ∇p increases by much less than this means that ***the presence of polymer destabilizes foam by an amount sufficient to raise S_w^* and $k_{rw}(S_w^*)$ by about a factor of 3.***

Fig. 1.18 shows the behavior of foam with both polymer and added decane. Pressure gradient is substantially reduced in what used to be the low-quality regime, but increases somewhat at the lowest liquid injection rates (upper-right portion of figure). The data have lost the characteristic trends of the low- and high-quality regimes. Similar trends to Fig. 1.18 were observed in experiments with dense CO₂ foam described under task 2 below, as well as (in the low-quality regimes) in Figs. 1.5, 1.7 and 1.8 above. Emulsions between oil and surfactant solution can substantially change the rheology of foam and in some cases increase the pressure gradient over that in the absence of foam (Yang and Reed, 1989). Over most of the range of injection rates, however, ***the addition of decane reduces the pressure gradient with foam.***

Fig. 1.19 shows the behavior of foam with polymer and added decane. The presence of polymer had virtually no effect on pressure gradient with foam and oil. ***This polymer does not stabilize the foam to the presence of decane in this Boise core.***

Fig. 1.20 shows the behavior of the same foam formulation with no polymer or oil in the second Boise sandstone core. The pattern is substantially similar to that in the first Boise core. The high-quality regime appears to extend to higher liquid superficial velocity in Fig. 1.20 than in Fig. 1.16, but this may be an artifact of interpolation: data were taken at higher liquid and gas superficial velocities ($U_w = 1.5$, $U_g = 1$ ft/d) in this case than in Fig. 1.16, and contours constructed around this datum extend the high-quality regime. In this case, unlike Fig. 1.16, the core had not yet contacted polymer when this foam was injected. Fig. 1.21 shows the same foam formulation with 0.2 wt% polymer but not oil in the second Boise core. The pattern of the data in this figure is consistent with Fig. 1.17 and is reminiscent of Figs. 1.5, 1.7, 1.8, 1.10, 1.11, 1.18 and 1.19. As with Fig. 1.17, polymer does not increase the pressure gradient with foam as much as expected from the viscosity of the polymer solution alone. Over most of the range of superficial velocities it has little or no effect on pressure gradient. At high gas superficial velocity and low liquid superficial velocity, addition of polymer produces a small increase in pressure gradient, but less than the increase in the viscosity of the aqueous solution. Therefore, as with Fig. 1.17, we conclude that ***the presence of polymer destabilizes foam, but the increase in aqueous-solution viscosity partially of fully compensates for this.***

Fig. 1.22 shows the effect of the injection of the 37.5° API crude oil on the foam. As with decane, ***the addition of crude oil destabilizes the foam*** (cf. Figs. 1.20 and 1.22). Fig. 1.23 shows the effect of addition of polymer to the aqueous solution in the presence of crude oil. As with Figs. 1.18 and 1.19, ***this polymer does not stabilize the foam in the presence of crude oil in this Boise core.***

Modeling the Viscosity of Foam with Polymer

Falls *et al.* (1989) split the effective viscosity with foam into a yield stress and the drag on bubbles moving in tubes. For foams of bubbles at least as large as pore size, Hirasaki and Lawson (1985) split the drag portion into three terms: drag on liquid slugs between bubbles; hydrodynamic drag along the bubbles; and effect of surface-tension gradient on the bubble interface. The first term is irrelevant to most foams in porous media. The second and third terms both scale with bubble velocity to the $2/3$ power for Newtonian fluids. As a result the pressure drop along a chain of bubbles moving through a smooth cylindrical tube scales like velocity $U^{2/3}$, and the effective viscosity of foam scales like $U^{-1/3}$. All published mechanistic foam models incorporate this approach (Falls *et al.*, 1988; Friedmann *et al.*, 1991; Kovysek *et al.*, 1997; Bertin *et al.*, 1998; Myers and Radke, 2000; Kam and Rossen, 2003; Kam *et al.*, 2004), though most leave out the yield stress.

Results like Fig. 1.2 make it unlikely that polymer plays a strong role in surface-tension gradients. Therefore the third term in Hirasaki and Lawson's (1985) analysis is probably unchanged by polymer. The hydrodynamic drag on bubbles would be affected, however, by the shear-thinning rheology of polymer solutions. Here we present a model for the effect of polymer on the effective viscosity of foam in porous media, or, more precisely, in straight capillaries.

Rossen and Wang (1999) and Kim *et al.* (2004) successfully employed a capillary-tube model to match the pressure-gradient data for strong foams in the low-quality regime. Their model will be extended to delineate the relative importance of

various process parameters, with the aim of helping to develop polymer-enhanced foams effective in porous media. The model derivation is lengthy; those interested primarily in results can skip to the section headed "Summary of Model Results" below. This work was carried forward by Dr. Chun Huh, formerly of ExxonMobil Upstream Research, now a Research Professor at UT and participant in our research group.

Before the capillary-tube model is described, the non-Newtonian rheology of polymer solution will be first described, as the addition of polymer is the key feature of the present modeling work. The simplest non-Newtonian, shear-thinning rheology model is the power-law model:

$$\mu = K\gamma^{\frac{1-\alpha}{\alpha}} \dots\dots\dots(1.2)$$

where γ is shear rate; and $\alpha = 1$ for Newtonian viscosity, but generally $\alpha > 1$ (for shear-thinning fluids). One serious difficulty with the above power-law model is that, near the bubble head, a zone of very low shear rate arises and the power-law model predicts an unrealistically high viscosity. A more realistic rheological model to use is the Carreau model that is widely employed for various oil industry applications (Cannella *et al.* 1988). Use of the Carreau model to calculate the pressure drop and wetting film thickness, however, turns out to be quite difficult; and another rheological model known as Ellis model is employed here:

$$\gamma = \left[\frac{1}{\mu_n} + \frac{\tau^{\alpha-1}}{K^\alpha} \right] \tau \dots\dots\dots(1.3)$$

where μ_n is the limiting Newtonian viscosity at the low-shear limit; τ is the shear stress; and the viscosity is defined as

$$\mu \equiv \tau / \gamma \dots\dots\dots(1.4)$$

We note that, at the low-shear limit, the Newtonian viscosity μ_n is obtained; and at high shear rates, the power-law relation (Eq. 1.2) is again recovered.

Pressure Drop Due To Steady Movement of a Bubble in a Circular Tube.

The dynamic pressure drop for foam bubbles flowing through circular capillary tubes has been calculated by Hirasaki and Lawson (1985) and Ratulowski and Chang (1989), as briefly described above. A key feature in their theoretical development is the use of the asymptotic matching, first adopted by Bretherton (1961), to calculate the pressure drop and wetting film thickness for isolated bubbles and bubble trains. This allows estimation of the effective gas viscosity as a function of bubble density in a porous medium, assuming it could be approximately modeled as a collection of straight, capillary tubes of circular cross-section.

In addition to the pressure drop due to viscous dissipation in and near the Plateau border, an additional pressure drop occurs due to the surface-tension gradient generated by gradients of surfactant adsorption along the gas/water interface. Hirasaki and Lawson (1985) account for this contribution in an *ad-hoc* manner. A consistent treatment of both the viscous dissipation term and the surface-tension gradient term has been given by Ginley and Radke (1989), Ratulowski and Chang (1990), and Park (1992). In the model derivation below, we assume that the effect of polymer addition to viscous dissipation is dominant over that due to the surfactant transport and the resultant surface-tension gradient.

To assess the effects of polymer addition to the viscous dissipation, Bretherton's derivation is first extended for a liquid which follows the Ellis model of shear-thinning rheology. The resultant pressure drop expression is then utilized to calculate the apparent viscosity of polymeric foam, in the manner of Hirasaki and Lawson (1985). The Bretherton's theory (1961) for a long gas bubble moving in a circular tube has been extended by Kamisli and Ryan (1999) for a shear-thinning power-law fluid being displaced by a bubble, which however causes problem as discussed above.

Consider a long gas bubble intruding into a circular tube filled with an Ellis liquid, leaving a thin liquid film on the tube wall around the bubble. As Bretherton did, we consider the flow behavior at the zone between circular bubble head and the flat film. Because the film is very thin, the radial ($y = R - r$) and axial (x) components of the momentum equation simplify to, respectively,

$$p = p(x) \dots\dots\dots(1.5)$$

$$\frac{\partial \tau}{\partial y} = -\frac{dp}{dx} \dots\dots\dots(1.6)$$

where R is tube radius; p is liquid pressure; and τ is the shear stress. The normal- and tangential-stress boundary conditions at the film surface are, respectively,

$$p = -\sigma \frac{d^2 h}{dx^2} - \frac{\sigma}{R} \quad \text{at } y = h(x) \dots\dots\dots(1.7)$$

$$\tau = 0 \quad \text{at } y = h(x) \dots\dots\dots(1.8)$$

where σ is surface tension; and $h(x)$ is the thickness of liquid layer. The right-hand side of Eq.1.7 represents the interfacial curvatures for the longitudinal and azimuthal directions, respectively. Eq.1.8 implies that the surface-tension gradient on the film surface is negligible. The no-slip condition at tube wall is

$$u = 0 \quad \text{at } y = 0 \dots\dots\dots(1.9)$$

With the boundary condition 1.8, Eq.1.6 can be integrated as

$$\tau = \frac{\partial p}{\partial x} (h - y) \dots\dots\dots(1.10)$$

which can be inserted into Eq.1.3 and rewritten in the following form:

$$\frac{\partial u}{\partial y} = \left[\frac{1}{\mu_n} + \frac{\tau^{\alpha-1}}{K^\alpha} \right] \tau \dots\dots\dots(1.11)$$

The integration of the above equation provides the horizontal velocity distribution in the liquid film:

$$u = \int_0^y \left[\frac{\tau}{\mu_n} + \frac{\tau^\alpha}{K^\alpha} \right] dy = \frac{1}{2\mu_n} \left(\frac{\partial p}{\partial x} \right) y(2h - y) + \frac{K^{-\alpha}}{\alpha + 1} \left(\frac{\partial p}{\partial x} \right)^\alpha \left[h^{\alpha+1} - (h - y)^{\alpha+1} \right] \dots\dots(1.12)$$

Because the bubble movement is in steady state, the total flux can be also expressed in terms of the steady bubble velocity, U_g , and the flat film thickness far away from the bubble head, h_0 :

$$q = U_g(h - h_o) = \int_0^y u \, dy = \frac{1}{3\mu_n} \left(\frac{\partial p}{\partial x} \right) h^3 + \frac{K^{-\alpha}}{\alpha + 2} \left(\frac{\partial p}{\partial x} \right)^\alpha h^{\alpha+2} \quad (1.13)$$

Inserting the following derivative form of the boundary condition (Eq. 1.7) into the above equation,

$$\frac{\partial p}{\partial x} = -\sigma \frac{d^3 h}{dx^3} \quad (1.14)$$

we can obtain a non-linear ordinary differential equation for $h(x)$:

$$\frac{\sigma}{3\mu_n} h^3 \frac{d^3 h}{dx^3} + \frac{(\sigma/K)^\alpha}{\alpha + 2} h^{\alpha+2} \left(\frac{d^3 h}{dx^3} \right)^\alpha = U_g(h - h_o) \quad (1.15)$$

Inserting the following dimensionless variables as Bretherton did

$$\eta \equiv h/h_o ; \quad \xi \equiv \frac{x}{h_o} C_a^{1/3} \quad (1.16 \text{ a,b})$$

we obtain

$$\eta^3 \frac{d^3 \eta}{d\xi^3} + \beta \eta^{\alpha+2} \left(\frac{d^3 \eta}{d\xi^3} \right)^\alpha = \eta - 1 \quad (1.17)$$

where

$$\beta \equiv \frac{3^\alpha}{\alpha + 2} \left(\frac{\mu_n}{K^\alpha} \right) \left(\frac{\mu_n U_g}{h_o} \right)^{\alpha-1} \quad \text{and} \quad C_a \equiv \frac{3\mu_n U_g}{\sigma} \quad (1.18 \text{ a,b})$$

We see that, if $1/K^\alpha \rightarrow 0$, the Newtonian viscosity is recovered (see Eq.1.3) and, with $\beta \rightarrow 0$, the above equation 1.17 reduces to the Bretherton equation. Therefore, the non-Newtonian shear-thinning behavior can be represented with a single parameter, β (Eq. 1.18).

Ratulowski and Chang (1989) and Teletzke (1998) further describe how to integrate the (modified) Bretherton equation for short bubbles within a bubble train. We make the simplifying approximation that the front-end and rear-end solutions for the long bubbles can be applied for short bubbles.

The key quantity that is obtained from the integration of Eq. 1.17 is the curvature of the liquid film at $\xi \rightarrow \infty$ (for “front end” of the bubble) and at $\xi \rightarrow -\infty$ (for “rear end” of the bubble). These dynamic curvatures are asymptotically matched with the static curvatures of the front and rear spherical caps of the bubble, from which the limiting film thickness, h_o , and the overall pressure drop can be obtained. As described by Bretherton (1961) and others, for $\xi \rightarrow \infty$, the film thickness will take the form

$$\eta \approx \frac{1}{2} P \xi^2 + Q \xi + R \quad (1.19)$$

where P , Q and R are constants. For the Newtonian case ($\beta = 0$), Bretherton obtained $P_o = 0.643$, $Q_o = 0$, and $R_o = 2.79$ (Q_o simply represents the transition of η in ξ -direction, and thus has no physical significance). For our non-Newtonian case, the values of P and

R have been obtained as functions of β and α . Fig. 1.24 shows P in terms of β and α . Fig. 1.25 shows PR in terms of β and α .

At the limit of small Ca , the limiting film thickness is given by

$$h_o = PC_a^{2/3} r_o \dots\dots\dots (1.20)$$

and the pressure drop across the front interface is given by Hirasaki and Lawson (1985)

$$\Delta p_f = PR \left(\frac{\sigma}{r_c} \right) C_a^{2/3} \left[\left(\frac{r_c}{r_o} \right)^2 + 1 \right] \dots\dots\dots (1.21)$$

where r_o is the tube radius and r_c is radius of curvature for film Plateau border.

A similar integration of Eq. 1.17 for the rear end of the bubble can be carried out, and the dynamic curvature terms, P and R , for the rear end can be obtained. As with the Newtonian case ($\beta = 0$), sample calculations show that the contribution from the rear end is much smaller than that from the front end. It is therefore assumed that, for the total pressure drop from the front and rear ends, (Δp_t), the (β, α) dependence obtained for the front end, given as shown in Fig. 1.25, can be approximately employed, with $(P_o R_o)_t$ from the case of $\beta = 0$, which is calculated to be $= 1.79 + 0.47 = 2.26$ by Bretherton (1961).

Because h_o in β of Eq. 1.18a is initially unknown, $[PR]$ in Eq.1.21 cannot be explicitly given in terms of known quantities; and the following manipulation is needed. If we express $\beta = \theta (h_o/r_o)^{1-\alpha}$ where

$$\theta \equiv \frac{3^\alpha}{\alpha + 2} \left(\frac{\mu_n}{K} \right)^\alpha \left(\frac{U_g}{r_o} \right)^{\alpha-1} \dots\dots\dots (1.22)$$

we can calculate (h_o/r_o) from Eq. 1.20 and Fig. 1.24, by successive approximation, for given θ and Ca . We could then express PR in terms of θ (which consists of all known quantities), instead of β , as in Figure 1.25.

Power-Law Approximation

Sample calculations reveal that for typical values of gas velocity and polymer rheological parameters, $\beta \gg 1$. For a large β , Eq. 1.17 can be re-written with a newly scaled coordinate, $\gamma \equiv \xi \beta^{-1/3\alpha}$:

$$\beta^{-1/\alpha} \eta^3 \frac{d^3 \eta}{d\gamma^3} + \eta^{\alpha+2} \left(\frac{d^3 \eta}{d\gamma^3} \right)^\alpha = \eta - 1 \dots\dots\dots (1.23)$$

which can be approximated as

$$\eta_p^{\alpha+2} \left(\frac{d^3 \eta_p}{d\gamma^3} \right)^\alpha = \eta_p - 1 \dots\dots\dots (1.24)$$

For $\gamma \rightarrow \infty$, the asymptotic expression for the film thickness can be given, similar to Eq. 1.19, as

$$\eta_p \approx \frac{1}{2} S \gamma^2 + T \dots\dots\dots (1.25)$$

where S and T are constants depending on α only. Table 1.1 lists S and T as functions of α . Kamisli and Ryan (1999) solved the power-law limit, Eq. 1.24, and their values for S match ours in Table 1.1. As they did not express their solutions in the form of Eq. 1.25, it is difficult to compare their results with ours for T . We note that, due to numerical instability, accurate value of T is difficult to obtain, e.g., $T = 2.68$ for $\alpha = 1$ is lower than the value of 2.79 from Bretherton (1961), even though reasonably acceptable in view of the approximate nature of derivation.

For the power-law limit ($\beta \gg 1$), therefore, P and R can be approximated as

$$P = S\beta^{-2/3\alpha} \quad R = T \dots\dots\dots (1.26a,b)$$

The limiting film thickness, Eq. 1.20, can be written with the above Eq. 1.26a for approximate P and $\beta = \theta(h_o/r_o)^{1-\alpha}$ as

$$\frac{h_o}{r_o} = S\theta^{-\frac{2}{3\alpha}} \left(\frac{h_o}{r_o}\right)^{2(\alpha-1)/3\alpha} Ca^{2/3} \dots\dots\dots (1.27a)$$

and it can now be expressed in terms of known quantities

$$\frac{h_o}{r_o} = \left(SCa^{2/3} \theta^{-\frac{2}{3\alpha}} \right)^{3\alpha/(2+\alpha)} \dots\dots\dots (1.27b)$$

Using Eq. 1.27b, PR in Eq. 1.21 can then be approximated as

$$PR = \frac{T}{(3\mu_n)^{2/3}} \left[(2+\alpha)^2 S^{3\alpha} K^{2\alpha} \left(\frac{r_o}{\sigma^{2/3}}\right)^{\alpha-1} \right]^{1/(2+\alpha)} U_g^{\frac{2(\alpha-1)}{3(\alpha+2)}} \dots\dots\dots (1.28)$$

which is now in terms of known quantities, and also shows its dependency on gas velocity clearly. We see that, if $\alpha = 1$ and $K = \mu_n$, the above expression reduces to the Newtonian value given above ($= TS = P_oR_o$).

Dependence of PEF Apparent Viscosity on Gas Velocity

With the above calculation of pressure drops due to liquid films on tube wall accompanying gas bubble movement, we can now calculate the apparent foam viscosity. To account for the polymer addition, the viscosity expression of Hirasaki and Lawson (1985) is re-visited. As discussed above, for simplicity, we assume the contribution from liquid slugs is negligible, and also neglect the pressure drop arising from the surfactant migration on film surfaces. In the modified viscosity expression given below, the reference viscosity is now the polymer-solution viscosity at the low-shear limit, μ_n , instead of the water viscosity, μ :

$$\frac{\mu_f}{\mu_n} = \frac{(PR)_t (n_L r_o) [(r_c/r_o)^2 + 1]}{\left(\frac{8}{3}\right) \left(\frac{r_c}{r_o}\right) \left(\frac{3\mu_n U_g}{\sigma}\right)^{1/3}} \dots\dots\dots (1.29)$$

Note that the factor 0.85 in Hirasaki and Lawson's equation is from $= (3/8)(P_oR_o)_t = (3/8) 2.26$; while $(PR)_t$ in Eq. 1.29 is a function of θ and α .

In order to investigate qualitatively the effect of polymer addition and non-Newtonian rheology on the apparent foam viscosity, Eq. 1.29 is re-written as follows in order to examine the dependence on gas velocity explicitly:

$$\psi \equiv \left(\frac{\mu_f}{\mu_n} \right) \frac{\left(\frac{8}{3} \right) \left(\frac{r_c}{r_o} \right) \left(\frac{3\mu_n}{\sigma} \right)^{1/3}}{(P_o R_o)_t (n_L r_o) [(r_c / r_o)^2 + 1]} = \frac{(PR)_t}{(P_o R_o)_t} U_g^{-1/3} \quad \dots \dots \dots (1.30)$$

Employing the power-law approximation of PR given above as Eq. 1.28, the dependence of the apparent foam viscosity on gas velocity can be more clearly seen:

$$\psi = \frac{T}{(P_o R_o)_t (3\mu_n)^{2/3}} \left[(2 + \alpha)^2 S_t^{3\alpha} K^{2\alpha} \left(\frac{r_o}{\sigma^{2/3}} \right)^{\alpha-1} \right]^{1/(2+\alpha)} U_g^{-\frac{\alpha}{\alpha+2}} \quad \dots \dots \dots (1.31)$$

We see that, if $\alpha = 1$ and $K = \mu_n$, the above expression reduces to $\psi = U_g^{-1/3}$. (As with $(PR)_t$, S_t approximately represents sum of S for the front and rear ends of bubble.) Fig. 1.26 shows ψ above in terms of U_g , which reveals that, while the apparent foam viscosity with Newtonian liquid depends on gas velocity to the power of -1/3, **the apparent foam viscosity with a shear-thinning liquid shows more highly shear-thinning behavior than with Newtonian liquid in the foam.** For the most extreme case in Fig. 1.26, foam viscosity scales like gas velocity to the (-1/2) to (-2/3) power instead of the (-1/3) power for a Newtonian liquid phase (Hirasaki and Lawson, 1985). Table 1.2 lists the Ellis model parameters employed for Fig. 1.26, which are from Cannella *et al.* (1988) for a xanthan polymer of different concentrations (C_p). Values of $\sigma = 72$ dyne/cm and $r_o = 20 \mu m$ are used in the calculations.

In the approximate pore-level model presented, it was assumed that no surfactant-polymer association occurs at the lamella surface; polymer molecules do not go into the lamella; and the surface-tension gradient on the film surface is negligible. Lamella stability is assumed not to be affected by polymer addition, which merely helps to increase the pressure drop due to movement of Plateau border zone on solid surface. While a cursory comparison with the available coreflood data suggests that the above simplifying assumptions are reasonable, those effects need to be investigated further, as was carried out for polymer-free systems (Ginley and Radke 1989; Ratulowski and Chang 1990; Park 1992).

Summary of Model Results

The behavior of polymer solution in the water-filled capillaries of a porous medium matches that of the straight polymer solution (Bird *et al.*, 1960) - i.e., it is shear-thinning as predicted for a power-law or Ellis fluid. Foam rheology in the high-quality regime is effectively set by the rheology of the aqueous phase (Rossen and Zhou, 1995; Alvarez *et al.*, 2001; *cf.* Eq. 1.1 with S_w fixed at S_w^*). Therefore, foam with polymer in the aqueous phase would be expected to be shear-thinning in the high-quality regime as the polymer solution itself is shear-thinning.

In the low-quality regime, foam rheology is controlled by the mobility of gas bubbles (Rossen and Wang, 1999; Kim *et al.*, 2004). The model derived above shows that foam in the low-quality regime is more shear-thinning than predicted by the model of Hirasaki and Lawson (1985), because of the shear-thinning rheology of the aqueous film

of water coating the pores filled with gas bubbles. This is in addition to any effects of gas trapping and relative permeability on foam rheology.

Conclusions From Task 1 - Interactions Between Polymer and Foam

1. For the polymers (xanthan and partially hydrolyzed polyacrylamide), oils (decane and 37.5° API crude oil), and surfactant (Bio-Terge AS-40, an alpha-olefin sulfonate) tested here, it appears from coreflood pressure gradient $|\nabla p|$ that polymer *destabilizes* foam somewhat, raising water saturation S_w and water relative permeability k_{rw} (Eq. 1.1). Any increase in pressure gradient $|\nabla p|$ observed results from the increased viscosity of the aqueous phase. In all cases examined, this increase is less than predicted from the increase in the viscosity of the aqueous phase alone.
2. For the same polymers and surfactant, polymer does not stabilize foam in the presence of decane or 37.5° API crude oil.
3. Complex behavior, in contradiction to the expected two steady-state strong-foam regimes, was sometimes observed. At the limit of, or in the place of, the high-quality regime, there was sometimes an abrupt jump upwards in $|\nabla p|$ as though from hysteresis and a change of state. In the low-quality regime, $|\nabla p|$ was not independent of liquid superficial velocity, but *decreased* with increasing liquid superficial velocity. This curious behavior in the low-quality regime was also found in studies of CO₂ foam; an explanation is offered in the section on Task 2, below.
4. Theory predicts that polymer should make the flow of foam more shear-thinning than without polymer. In the high-quality regime, where pressure gradient is controlled by water transport at fixed water saturation (Eq. 1.1), the shear-thinning nature of the aqueous polymer solution would make flow shear-thinning. In the low-quality regime, where rheology depends on the resistance to movement of gas bubbles, flow is predicted to be more shear-thinning because of the presence of polymer (Figs. 1.24 and 1.25). This is in addition to the shear-thinning effective viscosity of foam without polymer (Hirasaki and Lawson, 1985) and any relative-permeability effects of gas trapping and mobilization.

TASK 2: GAS TRAPPING

Overview

Gas trapping has a substantial effect on the mobility of foam and also on the injectivity of liquids injected following foam, whether acid for well stimulation or surfactant solution in a Surfactant-Alternating-Gas (SAG) process. Low liquid mobility following foam injection in SAG, caused by gas trapping in the liquid slug, caused fracturing of the well and failure of the foam process in a foam field test at the Snorre field (Blaker *et al.*, 1999). Attempts to represent gas mobility in foam flow mechanistically (Falls *et al.*, 1988; Friedmann *et al.*, 1991; Kovscek *et al.*, 1997; Bertin *et al.*, 1998; Myers and Radke, 2000) estimate that effective gas relative permeability varies with the flowing-gas fraction in foam raised to a power of between 1 and 3, depending on the model. A flowing gas fraction of 0.1 then reduces gas mobility by a power of between 10 and 1000. Thus characterization of the gas-trapping process is crucial to fully mechanistic representation of foam rheology. This has been a challenging task.

Our research effort on the effect of gas trapping on foam mobility and the factors that control gas trapping comprised experimental study, a careful review of experimental

methods, and parallel research on the theory and modeling of gas trapping to guide the experimental work. We made substantial progress in the modeling of gas trapping in foam, but found serious limitations in the ability to measure gas trapping in the laboratory using conventional gas-phase tracers.

Our efforts on this task were boosted by the arrival of Dr. Quoc Nguyen in fall of 2004, upon completion of his PhD in Petroleum Engineering at the Technical University of Delft (TUD) in The Netherlands. A significant part of Dr. Nguyen's PhD dissertation work at TUD concerned gas trapping and gas-phase tracer experiments with foam. He continued the analysis of his experiments while at UT; that analysis is summarized below.

Modeling Gas Trapping in Foam Simulation

Gas trapping during liquid injection is crucial both to injectivity during liquid injection in surfactant-alternating-gas foam (SAG) projects and to acid diversion in well stimulation. In the recent foam field trial at the Snorre field, low injectivity during liquid-slug injection caused fracturing and the loss of all subsequently injected surfactant (Blaker, *et al.*, 1999). This low injectivity is a result of gas trapping by the liquid slug. Injectivity of liquid after foam is also a window into trapping mechanisms that apply during foam flow.

We updated our foam simulator (Rossen *et al.*, 1999; Cheng *et al.*, 2000) to account explicitly for the first time for the effects of gas trapping on gas mobility in foam and in liquid injected after foam, and for the effects of pressure gradient on gas trapping (Cheng *et al.*, 2002). The procedure is as follows: Rossen and Wang (1999) provide data for liquid mobility at steady-state during post-foam liquid injection, when all gas remaining is trapped (Fig. 2.1). Assuming a plausible liquid relative-permeability function, this implies the trapped-gas saturation with foam S_{gr}^f as a function of pressure gradient ∇p , shown in Fig. 2.2. The crucial assumption of this work is that this function applies to gas trapping in steady-state foam flow as well. The relative-permeability function for gas then incorporates this function $S_{gr}^f(\nabla p)$ rather than a fixed, constant value of S_{gr} as in the previous model (Cheng *et al.*, 2000). The other parameters in the model must be recalculated given the new functional form for S_{gr}^f . A detailed procedure for fitting the parameters is given in Cheng *et al.* (2002) and Cheng's dissertation (2002).

The foam model fits steady-state foam behavior in both high- and low-quality flow regimes (Alvarez *et al.*, 2001) and steady-state liquid mobility after foam - see Figs. 2.1, 2.3 and 2.4. The simulator fits the transition period between foam injection and quasi-steady-state liquid injection in laboratory corefloods qualitatively with no additional adjustable parameters (Figs. 2.5, 2.6).

The dynamics in the transition period are complex. For instance, simulations indicate that in the laboratory most of the core experiences a period of drier flow at the start of liquid injection, due to expansion of gas already in the core. Simulations and experiments agree that the transition is faster at higher pressure (with lower gas compressibility) and that response to a shut-in period depends on how much gas escapes during the shut-in - i.e., on how long the shut-in lasts.

Extended to radial flow, the simulator suggests that the transition period may not be so crucial in field application as at first appeared from laboratory corefloods. In the cases examined, injection-well pressure approaches its steady-state value within about 15 minutes or less of the start of liquid after foam (Fig. 2.7).

We also found experimental artifacts that have affected previous studies of liquid injectivity after foam. Specifically, a foam generator and associated tubing and fittings upstream of the core in most previous coreflood studies acts as a "dead volume" during liquid injection that can significantly affect the results and especially the transition period between foam and liquid-only injection. Simulations suggest that this dead volume is the cause of the simultaneous decline in pressure gradient in all sections of the core observed in previous studies. New laboratory experiments without the dead volume qualitatively confirm several of the trends predicted by simulation. Further details are in Cheng *et al.* (2002).

Initial Experiments: Water Saturation and Gas Trapping with Foam

Our initial experiments focused on gas trapping during liquid injection following foam. A novel apparatus, similar to that in Kibodeaux and Rossen (1997), monitors average water saturation in a core, moment-by-moment, by weighing the core. Our experiments find that water saturation increases more during liquid injection than previously conjectured - in other words, less gas is trapped by liquid injection than previously thought (*cf.* Zeilinger *et al.*, 1995). The trapped-gas saturation during liquid injection decreased with increasing quality (gas fraction) of the previously injected foam. In these experiments relatively high-quality (high gas-fraction) foams were used, so the increase in liquid velocity after foam injection is greater. As a result, pressure gradient increased in these experiments during liquid injection (Fig. 2.8); all our previous experiments (Kibodeaux *et al.*, 1994; Zeilinger *et al.*, 1995; Rossen and Wang, 1999) had seen a decrease in pressure gradient during liquid injection.

This finding may be significant for liquid injectivity in SAG process and attempts to divert liquid injection with foam: injectivity would be lower, and liquid diversion greater, if pressure gradient increases initially upon liquid injection. The early modeling work of Kibodeaux *et al.* (1994) concluded that the decline in pressure gradient seen shortly after liquid injection begins reduces the ability of foam to overcome the effects of permeability and divert the flow of liquid in acid-diversion processes.

Other surprising trends in behavior were observed. As liquid injection follows foam, there is a rapid rise in liquid saturation in the core, as expected (Fig. 2.8). For a period after this, there is a gentle rise in liquid saturation, while pressure gradient rises in some sections of the core. Later on, as pressure gradient in the downstream sections falls over time, average liquid saturation also falls in the core - in spite of the fact that no gas is being injected. Finally, liquid saturation rises slowly again.

These apparent contradictions can be reconciled using the model for gas trapping and gas dissolution with foam, discussed above. An increase in pressure gradient would have been predicted by the model of Cheng *et al.* (2002) for a case where initial foam quality was high and liquid was later injected at the same volumetric rate as foam. The possibility was not explicitly foreseen because all previous experiments had involved relatively low-quality foams.

In these experiments, a water relative-permeability function fit to steady-state foam flow also roughly fits post-foam liquid injection before gas dissolution starts to alter the process. In other respects, however, the results suggest nonuniform sweep of liquid injected after foam. Later, after gas dissolution into injected liquid becomes significant, the relative-permeability function derived from foam-flow data is no longer accurate.

The apparently contradictory behavior of average water saturation and pressure gradient can be understood by considering the effects of gas dissolution and expansion of

trapped gas. In previous work, pressure gradient decreased during liquid injection and gas expanded during this period. Thus gas saturation everywhere was at its maximum trapped-gas saturation for the given pressure gradient (Cheng *et al.*, 2002). In these experiments, pressure gradient increased during liquid injection, and gas was compressed. As a result, gas saturation was below its residual saturation, especially in upstream sections of the core. Then, as unsaturated liquid entered the core and dissolved a fraction of this trapped gas, it raised liquid mobility locally. As the dissolution wave moved toward the outlet of the core, pressure in the upstream sections decreased, and gas there expanded, reducing liquid saturation. Most of the pressure drop was in the downstream sections, where gas saturation was being reduced by dissolution. Therefore average gas saturation rises even as overall pressure drop across the core falls.

One implication of this work is that liquid fingers through foam rather than displacing it: the wave of increased liquid saturation moving through the core during liquid injection, and the magnitude of the change in liquid saturation, are both consistent with only partial contact between the injected liquid and the resident gas. This conjecture was later proved in direct CT imaging experiments, described below.

Details of this work are in Xu (2003) and Xu and Rossen (2003b).

Gas Trapping and the Low-Quality Foam Regime

Gas trapping is thought to play its most important role in the low-quality foam-flow regime (Fig. 1.1); Rossen and Wang conjecture that gas trapping and mobilization is the key to the insensitivity of pressure gradient to liquid injection rate in this regime. Recent research has caused us to reconsider the nature of this regime. Figs. 1.5, 1.7 to 1.11, 1.17 to 1.19, and 1.21 to 1.23 above show altered behavior in the low-quality regime observed in connection with our study of foam with polymer: rather than pressure gradient $|\nabla p|$ independent of liquid superficial velocity U_w at fixed gas superficial velocity U_g , $|\nabla p|$ decreases upon increasing U_w at fixed U_g . Similar behavior was observed in our laboratory in some cases with CO₂ foam above the critical pressure of CO₂. Our surfactant formulation in this work was 1 wt% Neodol® 25-9 in a brine of 3 wt% NaCl and 0.01 wt% CaCl₂. Neodol 25-9 is a nonionic C₁₂₋₁₅ alcohol ethoxylate with average 9 moles of ethylene oxide per mole of alcohol, manufactured by Shell Chemical Company. The experimental apparatus for these experiments is described in Kim *et al.* (2004).

Figs. 2.9 and 2.10 show, respectively, liquid-CO₂ foam (i.e., below the critical temperature of CO₂) in a Boise sandstone core and a sandpack. Figs 2.11 and 2.12 show supercritical CO₂ foam (i.e., above the critical temperature of CO₂) in a Boise sandstone core and a sandpack. The conventional two foam-flow regimes are observed in the Boise core above the critical temperature of CO₂ (Fig. 2.11), but not in a sandpack above the critical temperature (Fig. 2.12) or in Boise sandstone below the critical temperature (Fig. 2.9). In the other cases, the unconventional behavior is observed. There is no one factor in our studies that determines whether one observes the unconventional behavior or not. A series of experiments at the New Mexico Petroleum Recovery Research Center were conducted above and below the critical temperature of CO₂ with different surfactant formulations in a variety of porous media. Kim *et al.* (2004) show that all these experiments reflect either the conventional high- or low-quality foam regimes.

This behavior we report here, where $|\nabla p|$ decreases at increasing U_w , may be unique to foam. It is remarkable that in two-phase flow, upon increasing the injection rate of the more viscous phase, pressure gradient should decrease. Also, to the extent that

water injection rate affects bubble size, one would expect bubble size to decrease as water injection rate increases (Alvarez *et al.*, 2001). A decrease in bubble size would give an increase in $|\nabla p|$, not a decrease as shown here.

Since the low-quality regime is thought to be controlled by gas mobilization and trapping, we investigated this further to determine whether gas trapping is the root of the unconventional behavior.

Theoretical work summarized below suggests that the answer is "yes and no." The root of the trend where $|\nabla p|$ decreases as U_w increases is in the foam viscosity function, not gas trapping. However, if gas trapping is sufficiently sensitive to pressure gradient, then $|\nabla p|$ becomes independent of U_w as in the conventional low-quality regime.

Gas Effective Viscosity With Foam

Rossen and Wang (1999) proposed their explanation for the low-quality regime based on a simple bundle-of-tubes model for foam in porous media. Water is a Newtonian, wetting fluid that occupies the narrower tubes. Gas occupies the wider tubes, but a yield stress prevents flow in these tubes unless the pressure gradient is sufficient to mobilize gas in the given tube. As a result, the widest tubes are occupied by gas that flows, the intermediate tubes by gas that is trapped, and the narrowest tubes by water. Gas is represented in this model as a Bingham plastic (Bird *et al.*, 1960). If one assumes that the parameters of the Bingham plastic are fixed and constant in the low-quality regime, then an increase in U_w causes water to displace some trapped gas from intermediate-size tubes, with no change in the flow of gas in the widest tubes. Thus $|\nabla p|$ stays constant as U_w increases at fixed U_g . As U_g increases, $|\nabla p|$ increases, but less than proportionately to U_g , because as a plastic fluid gas is shear-thinning in the tubes in which it flows, and because gas flows in more tubes as $|\nabla p|$ increases.

The Bingham parameters for the gas in this model reflect the bubble size in the foam. The behavior of the low-quality regime ($|\nabla p|$ independent of U_w) is observed only if these parameters are independent of liquid injection rate. Therefore Rossen and Wang reasoned that bubble size is independent of liquid and gas injection rates in the low-quality regime. Qualitative observations of bubble size by Alvarez *et al.* (2001) partially confirm this conjecture. A fixed bubble size is reasonable if bubble size is at about pore size. Foam generation by lamella division and snap-off both stop for bubbles much smaller than pore size, and gas diffusion would rapidly eliminate bubbles smaller than pores if they were formed (Rossen, 1996). Thus the low-quality regime is thought to reflect a fixed bubble size at roughly the volume of a pore.

Model of de Vries and Wit

However, even if bubble size is fixed, there is no reason why the rheological (e.g., Bingham) parameters of foam should be fixed. This can be seen in terms of two previously published models for foam. The first is the model of de Vries and Wit (1990) for two flow regimes similar to the high- and low-quality regimes. Fig. 2.13 shows that the model of de Vries and Wit in the low-quality regime fits the trend seen in much of our recent data: $|\nabla p|$ decreasing with increasing U_w at fixed U_g . The model of de Vries and Wit is not entirely satisfactory, however. It makes unphysical assumptions about the nature of foam flow in capillary tubes.

Model of Hirasaki and Lawson

The standard model for the effective viscosity of foam in capillaries is that of Hirasaki and Lawson (1985). Although usually cited for its shear-thinning rheology with respect to gas velocity, the model also predicts that foam viscosity at fixed bubble size depends on capillary pressure. Specifically, the drag on the Plateau borders between bubbles depends on how swollen or constricted the Plateau borders are; the lower the capillary pressure, the more swollen the Plateau borders, and the lower the effective viscosity of bubbles flowing through capillaries. If one assumes that bubbles flow through all pores in the medium, which are represented as cylindrical capillaries of identical diameter, and that all water flows in the Plateau borders between bubbles, one obtains behavior shown in Fig. 2.14: $|\nabla p|$ decreases as U_w increases at fixed U_g .

A somewhat more sophisticated approach builds on the bundle-of-tube model of Rossen and Wang (1999), where gas remains trapped in some tubes and water flows through its own set of narrow tubes. Here (Kim *et al.*, 2004), instead of representing the gas as a Bingham plastic, we use an effective viscosity based on the model of Hirasaki and Lawson (1985), as adapted by Falls *et al.* (1989), with a yield stress, shear-thinning rheology with respect to gas velocity, and decreasing gas viscosity with decreasing capillary pressure. The results are shown in Fig. 2.15, for a bundle of tubes, with a log-normal distribution of tube diameters with 95% of the diameters within a factor of 3.4 of the median. The behavior of the unconventional regime is reproduced: $|\nabla p|$ decreases with increasing U_w at fixed U_g .

However, if gas trapping is a very sensitive function of $|\nabla p|$, then one recovers the behavior of the conventional low-quality regime. In the context of this bundle-of-tubes model, gas trapping is a function of tube radius and yield stress of the foam (Bird *et al.*, 1960). Thus in a bundle of tubes of nearly identical radius, gas trapping would be extremely sensitive to $|\nabla p|$: one would pass from nearly all gas trapped to nearly all gas flowing with a small increase in $|\nabla p|$. An example is shown in Fig. 2.16, in which 95% off all tubes have a diameter within 2% of the median value. $|\nabla p|$ contours are horizontal, but behavior is also extremely shear-thinning with respect to gas velocity. Real foams are not nearly this shear-thinning.

The resolution of the paradox of the unconventional foam behavior is still unclear. It appears to depend on gas trapping, however, as a way to counterbalance the effect of water injection rate on capillary pressure and drag on bubbles.

Previous Experimental Studies with Gas-Phase Tracers

Injection of gas-phase tracers with the foam, and measurement of tracer concentration in the effluent, have been used to estimate trapped-gas fraction during steady-state foam flow in porous media. Previous studies using this technique have employed different gas tracers and methods of interpretation, always with nitrogen as the main constituent of the foam. With distinct fractions representing flowing and trapped gas, in the absence of mass transfer between them and dispersion in the flowing gas, the analysis is simple: the time of breakthrough of tracer, in PV injected (at the average core pressure), represents the saturation of flowing gas in the core. Mass transfer (diffusion) of tracer between flowing and trapped gas greatly complicates the analysis of data, however.

Friedmann *et al.* (1991) used krypton gas as a tracer to estimate the trapped-gas fraction during steady-state flow of 95%-quality foam in a vertically mounted Berea sandstone core (30 cm long and 5 cm diameter). The trapped-gas fraction was estimated as the ratio of the times at which effluent tracer concentration was 10% of the injected

tracer concentration in two cases: co-injection of gas and surfactant solution, and co-injection of gas and brine without surfactant and at the same gas volume fraction. The authors state that effect of mechanical dispersion was the rationale for the use of 10% (instead of 50%) tracer concentration in the effluent. Using brine-gas flow as a reference in the calculation assumes that water saturation is the same in brine-gas flow as in foam flow, a dubious assumption. In fact, the breakthrough time in pore volumes PV of 10% of injected tracer concentration gives a good estimate of the saturation of flowing gas in foam under certain conditions, as described below. The authors concluded that 85% of the gas in the pore space was trapped during foam injection, a value which increased weakly with superficial gas velocity in the range 25-130 m/day. The authors attributed the asymmetric shape of the effluent tracer profiles to diffusion of tracer into trapped gas.

Radke and Gillis (1990) used two tracers (methane and sulfur hexafluoride) simultaneously in a Berea sandstone slab mounted horizontally. Water saturation was measured by scanning the core for microwave absorbance, which eliminated the need for a reference experiment with no surfactant present. All the experiments were conducted with atmospheric pressure at the outlet; the authors note that the pressure drop across the slab was small. The trapped-gas fraction was estimated by fitting a one-dimensional (1D) convection-diffusion model for each of the tracers to the measured effluent concentration profiles, taking into account the diffusion of the tracers into trapped gas. In the model as first given the diffusion of tracer into liquid films (lamellae) between bubbles is described, but in the final version of the model used to fit the data the resistance to tracer diffusion into the trapped gas is represented by an effective mass-transfer coefficient. A modified version of this model is described below. Methane is expected to have a larger mass-transfer coefficient than sulfur hexafluoride if their diffusion coefficients through lamellae between bubbles reflect their respective solubilities in water. The model assumes that at each axial position along the core the flowing and trapped gas can each be represented by a single concentration of each tracer. In other words, for each tracer, its concentration is uniform within flowing or trapped gas within each core cross-section at all times, though it does differ between flowing and trapped gas and does change with time and axial position long the core. By fitting the effluent data for two tracers injected simultaneously with the same flowing-gas fraction (but different mass-transfer coefficients) assumed for the two tracers in the model, the approach seeks to minimize uncertainty in the parameter values. Based on the fitted parameter values, Radke and Gillis concluded that for superficial velocities from 0.5 to 4 m/day and foam qualities from 80 to nearly 100%, the fraction of trapped gas was mostly greater than 70%, and in several cases almost 100%.

Recently, Tang and Kovscek (2004) employed the same dual-tracer technique and mass-transfer model of Radke and Gillis to estimate trapped gas in foam in Berea sandstone cores (52 cm long and 5.5 cm diameter) mounted horizontally at 120 psi back-pressure. Reported pressure drop across the core was small in all cases. Water saturation S_w was determined by scanning the core with X-ray computed tomography (CT). Carbon dioxide and methane were used as tracers. Bubble sizes were measured in the effluent along with tracer concentration. Tang and Kovscek presented a percolation model, in which pressure gradient, permeability, and bubble size combine to determine trapped-gas fraction, and fitted the model to their series of experiments. They found that trapped-gas fraction varied from 87 to 56% in their experiments; according to their model, this primarily reflected large changes in bubble size with injection rates.

Missing from previous studies has been a quantitative discussion of the uncertainty of estimates of trapped and flowing gases based on the statistical model fit to

effluent concentration data: that is, the range of trapped-gas fractions that could be employed to fit to the effluent data satisfactorily.

Recently, Nguyen *et al.* (2002) investigated diffusion of argon and ammonia gases across individual lamellae stabilized by 0.023 wt% sodium dodecyl sulfate (SDS) in the presence of 1.95 wt% NaCl. This study concluded that the primary resistance to transport of these gases across the lamellae was penetration of the surfactant monolayer on the two surfaces of the lamella, not solubility in or diffusion across the liquid in the lamella. An implication is that tracer diffusion rates across foam may not be simply related to solubility of the given gas tracer in water.

Nguyen (2004) also examined gas trapping in transparent two-dimensional glass micromodels with argon gas as a tracer. Trapped gas was determined directly by image analysis and indirectly by fitting a 1D mass-transfer model (described below) to the effluent tracer concentration profile. In the direct measurement, the area fraction of immobile bubbles in the micromodel images was averaged over each 1 cm of micromodel length. In the first cm of micromodel, trapped fraction varied from about 50 to 65% among the experiments; downstream of this point, trapped fraction varied from 60 to 70%. Nguyen concluded that, on the scale of the micromodel experiment, mass transfer of the tracer into trapped bubbles was slow because of the intervening lamellae. A fit to the data gave a relatively low mass-transfer coefficient and large dispersion coefficient, so that the trapped fraction was accurately reflected in the PV injected at which tracer effluent concentration was half of that injected. Values obtained this way from effluent tracer concentration agreed to within a few percent of those from image analysis. However, to obtain these data Nguyen had to first establish foam in the micromodel and then follow with gas-only injection, whereupon bubbles were displaced from a channel and a continuous gas path opened up. While he injected foam (gas and surfactant solution) into the micromodel, image analysis showed continual fluctuations in the flow path of foam; i.e. trapping and remobilization of bubbles. During this time the 1D mass-transfer model could not provide a satisfactory fit to the effluent concentration profile. Indeed, none of the models described in this report can correctly identify instantaneous trapped-gas fraction, which presumably controls gas effective relative permeability in foam, if it fluctuates among multiple paths on a sufficiently short time scale; all methods would include all the paths in the estimated trapped gas fraction because all paths would soon contain injected tracer. The CT method described below can identify some fluctuations not detectable using earlier methods.

Tracer Experiments at UT

Our apparatus for measuring flowing-gas fraction in foam corefloods using gas-phase tracers is shown in Fig. 2.17. It is essentially a conventional coreflood apparatus with a gas chromatograph (g.c.) as close as possible to the outlet of the core. It is similar to that used by others (Radke and Gillis, 1990; Tang and Kovscek, 2004) except that we have no scanning facility for measuring water saturation directly and we use only one gas-phase tracer. Our apparatus incorporates two advances over previous studies: First, we allow higher back-pressure (600 psi), closer to that of our other foam experiments. Second, one of the trickiest aspects of such experiments is breaking the foam and separating the surfactant solution before gas enters the chromatograph, while minimizing the apparatus volume downstream of the core. We accomplished this by injecting a small amount of ethanol just upstream of a T in the line. The ethanol effectively breaks the foam and causes the liquid to drain downward at the T, while gas rise upwards to enter the g.c. This foam-breaker adds less than 1 cc to the volume to the apparatus.

The core is held vertically in these experiments, with injection from the top, whereas in most previous studies (Radke and Gillis, 1990; Tang and Kovscek, 2004; Nguyen, 2004) the core was held horizontally so that it could be scanned. Pressure drop is measured in four sections along the length of the core, of length 2, 4, 4, and 2 in., respectively. Pressure gradients are much larger in our experiments than in those in Radke and Gillis and Tang and Kovscek, but in line with our other foam studies (*cf.* Fig. 1.1). Variable gas density (from pressure gradient along the core) is accounted for in the analysis of data, using a model described in Eqs. 2.1 to 2.4, below. Back-pressure is maintained at 600 psi to minimize the effects of gas expansion in the core. Foam is injected until steady state is attained, after which a portion of N₂ in the gas in the foam is replaced by He, which can be detected in the effluent by the gas chromatograph. Water saturation was not measured in these experiments, so water saturation S_w is a parameter to be fitted to the data. There is no foam generator upstream of the core, to minimize its effect on dispersion of the tracer. Surfactant concentration varied between 0.2 and 0.5 wt% sodium dodecyl sulfate (SDS) among these experiments.

Fig. 2.18 shows reproducibility in two experiments with flow through a foam generator, using N₂ for the foam and 10% He as the tracer. The surfactant was Shell Neodol 25-9, a nonionic surfactant used earlier by Jisung Kim in our group (Kim *et al.*, 2004; see Figs. 2.9 to 2.12 above). The reproducibility between the two runs is excellent, and surfactant was prevented from entering and damaging the g.c. The data illustrate the difficulty in accurately resolving the late portion of the tracer breakthrough curve, however, due to scatter in the data. The gaps in data are caused by the need periodically to pause the data-acquisition process for downloading data. The gaps are not significant if the front takes a longer time to come through, as illustrated in Fig. 2.19. This figure shows the breakthrough curve for He tracer in a Berea core sample with no foam present.

Our tracer results with foam bear a striking resemblance to an error-function curve, which suggests effects of dispersion without any trapped gas. Fig. 2.20 shows an example, along with a plot on probability axes. The effluent tracer profile reaches half of the injected concentration at about 0.83 PV, and the rest of the profile is remarkably symmetric about this point. The missing 0.17 PV may represent liquid saturation in the core. The implication is that either there is virtually no trapped gas in the core, or else mass transfer between the trapped and flowing gas is so rapid that the trapped gas is nearly indistinguishable from flowing gas. A problem with all methods of determining trapped-gas fraction using gas-phase tracers is that if mass transfer between flowing and trapped gas is sufficiently fast one cannot distinguish flowing from trapped gas. In Nguyen's experiments illustrated below, with the core held horizontally, tracer penetrated about half the core, mostly the upper portion of the core, in what may be an effect of gravity. It is possible that with the core held vertically in this experiment, tracer penetrates the entire core, rapidly equilibrating with nearby trapped gas, and giving the appearance of zero trapped gas fraction. We test this hypothesis further with an experiment where the core is held horizontally below.

The implication suggested above is faulty in one respect, however: dispersion produces a symmetric, error-function profile of concentration as a function of position at any fixed time; but it produces an asymmetric profile of concentration as a function of *time* at any *position* (e.g., outlet of the core in our effluent data), especially if the dispersion coefficient is large, as is the implication of the data in Fig. 2.20. In fact, our experiments indicate a substantial fraction of trapped gas, though this fraction cannot be determined with precision, due, evidently, to high rates of mass transfer between trapped and flowing gas over the time scale of the experiments.

Experimental Results and Discussion

All these experiments were conducted in a Boise sandstone core of permeability 964 md and porosity 29%. The core was 1 ft in length and 2 in. in diameter.

Table 2.1 lists the four experiments presented here. Sectional pressure gradients in the last four columns of Table 2.1 are used to calculate the average pressure in each section and the average pressure in the core, upon which the listed values of gas superficial velocity and foam quality are based. In each case there is lower pressure gradient in the first, 2-in., section of the core, and in most cases also in the second section. We chose a foot-long core in order to minimize entrance effects in our results, but our results show that using a longer core led to larger problems with mass transfer between trapped and flowing gas.

Case 1 involves injection of an 86%-quality foam at a total superficial velocity of 2.49 ft/d, with 0.5 wt% SDS in the aqueous phase. The effluent tracer data are shown in Fig. 2.21. The "global optimum fit" is a least-squares fit to all data. It gives an estimate of trapped-gas fraction $S_t = 0.85$. In keeping with the model described in the next section, S_t and S_f here refer to trapped and flowing gas *fractions* rather than saturations. Other fitted parameters are water saturation = 0.13, mass-transfer parameter $a_s k_e = 30 \times 10^{-3}$, and dispersivity = 0.2×10^{-3} ; these model parameters are described in connection with Eqs. 2.1 to 2.4 below. A least-squares fit to the breakthrough data only, up to 45% concentration, gives $S_t = 0.5$, $a_s k_e = 60 \times 10^{-3}$, and dispersivity = 10×10^{-3} . The difference between the two fitted values of S_t , 0.85 and 0.5, suggests a large uncertainty in flowing fraction (0.15 to 0.5, or variation by over a factor of 3). To test how wide a range of S_t values could be used to fit the data, Fig. 2.22 shows manual fits to the data with $S_t = 0.1$ and 0.9. The fit with $S_t = 0.9$ appears as good to the naked eye as the global optimum fit, though the fits using $S_t = 0.5$ and 0.1 are noticeably worse. One could conclude that the trapped-gas fraction is greater than 0.5 and could well be as high as 0.9.

Figs. 2.23 and 2.24 show the corresponding plots for Case 2, with 76%-quality foam injected at a total superficial velocity of 1.97 ft/d, with 0.2 wt% SDS in the aqueous phase. The global optimum fit (Fig. 2.23) gives an estimate of $S_t = 0.83$; other fitted parameters are $S_w = 0.10$, $a_s k_e = 23 \times 10^{-3}$, and dispersivity = 1×10^{-3} . A least-squares fit to the breakthrough data only, up to 70% concentration, gives $S_t = 0.53$, $a_s k_e = 18 \times 10^{-3}$, and dispersivity = 8×10^{-3} . In this case the optimal fit to breakthrough data fits all the data nearly as well as the global optimum fit; there is little sensitivity to the fitted value of S_t . Fig. 2.24 shows manual fits to the data with $S_t = 0.1$ and 0.9. The fit with $S_t = 0.9$ appears as good to the naked eye as the global optimum fit, though the fits using $S_t = 0.1$ is somewhat worse. One could conclude that the trapped-gas fraction could be as low as 0.5 or lower, and could well be as high as or higher than 0.9.

Figs. 2.25 and 2.26 show the corresponding plots for Case 3, with 66%-quality foam injected at a total superficial velocity of 0.67 ft/d, with 0.5 wt% SDS in the aqueous phase. The global optimum fit (Fig. 2.25) gives an estimate of $S_t = 0.43$; other fitted parameters are $S_w = 0.10$, $a_s k_e = 4.3 \times 10^{-3}$, and dispersivity = 3×10^{-3} . A least-squares fit to the breakthrough data only, up to 90% concentration, gives $S_t = 0.7$, $a_s k_e = 8 \times 10^{-3}$, and dispersivity = 5×10^{-3} . In this case there is very little difference between the optimal fit to all data and to breakthrough data only. Fig. 2.26 shows manual fits to the data with $S_t = 0.1$ and 0.9. The fit with $S_t = 0.9$ appears as good to the naked eye as the global optimum fit, and even the fit using $S_t = 0.1$ is nearly as good as the others. One can say very little about the magnitude of the trapped-gas fraction from this experiment.

The trend from Cases 1 to 3 shows declining precision in the fitted value of S_t as the injection rate decreases, i.e. as the time the gas spends in the core increases. This suggests that mass transfer is relatively rapid in these experiments, and slowing down the injection rate allows mass transfer to nearly obliterate the effect of trapped gas on the effluent profile.

Previous studies were mostly conducted in cores held horizontally rather than vertically as in these experiments. The CT study described in the next section shows that in that study gas moved mostly through the upper portion of the core. Mass transfer within this region was relatively rapid, but much slower between the upper region and the rest of the core. The effluent data in that study showed less apparent effect of mass transfer on the results than here. (There were other differences between the studies: the core in the CT study was shorter, and the injection rates higher (*cf.* Tables 2.1 and 2.2). Both these effects would also tend to reduce the effects of mass transfer on tracer effluent.)

To test the effect of core orientation, in Case 4 the core was oriented horizontally, with 78%-quality foam injected at a total superficial velocity of 2.06 ft/d, with 0.2 wt% SDS in the aqueous phase.. Though the conditions are similar to Case 2, the pressure gradient is significantly lower (Table 2.1), suggesting there may be an affect of gravity override with the core oriented horizontally. Figs. 2.27 and 2.28 show the effluent data and model fits. The global optimum fit (Fig. 2.27) gives an estimate of $S_t = 0.8$; other fitted parameters are $S_w = 0.10$, $a_{sk_e} = 20 \times 10^{-3}$, and dispersivity = 6×10^{-3} . A least-squares fit to the breakthrough data only, up to 60% concentration, gives $S_t = 0.5$, $a_{sk_e} = 11 \times 10^{-3}$, and dispersivity = 10×10^{-3} . Again, there is very little difference between the optimal fit to all data and to breakthrough data only, though neither fit is as good as in Cases 2 or 3. Fig. 2.28 shows manual fits to the data with $S_t = 0.1$ and 0.9. The fit with $S_t = 0.9$ appears as good to the naked eye as the global optimum fit, and but the fit using $S_t = 0.1$ is noticeably worse. One could conclude that the trapped-gas fraction could be as low as 0.5 and as high as 0.9 or higher. There is no qualitative difference between the ability of the model to distinguish the trapped-gas saturation in the presence of mass transfer in this case than in Case 2, with the core oriented vertically.

Strategies for reducing the effects of mass transfer in future studies could include

- reducing gas residence time in the core by using a shorter core. However, this would increase the artifact from the entrance region of the core (Table. 2.1).
- reducing gas residence time in the core by increasing gas injection rate. It would be preferable, however, to be able to set gas and liquid flow rates to be representative of the field, rather than to satisfy the needs of measuring trapped-gas saturation accurately.
- choosing a different gas tracer, with slower mass transfer to trapped gas. The study of diffusion of gas tracers through foam films of Nguyen *et al.* (2002) suggests that choosing the best gas-phase tracer is not as simple as choosing the one with the lowest solubility in water. But it is quite possible that there is a tracer with slower diffusion through foam films than He.

The difficulty in resolving trapped-gas fraction from tracer effluent data in the presence of rapid mass transfer between trapped and flowing foam suggests that use of dual gas tracers (Radke and Gillis, 1990; Tang and Kovscek, 2004), one of which has relatively rapid transport with trapped gas, would not improve the fit of the trapped-gas saturation. The effluent data for the rapidly diffusing component could be fit with a

variety of trapped-gas fractions, and thus these data would give relatively little information relevant to trapped-gas saturation.

Foam Yield Stress

The trapping of foam in porous media depends ultimately on the yield stress of foam in porous media, which depends on bubble shapes and curvatures in the pore space. Earlier modeling of this process (Rossen, 1988, 1990 a-d; Xu and Rossen, 2003a) was restricted to two dimensions (2D), and left some doubt as to whether there was a minimum pressure gradient for foam flow at all in 3D (Rossen, 1990d). In a collaboration with Prof. Denis Weaire and Dr. Simon Cox of Trinity College, Dublin, calculations have now been extended to 3D (Cox *et al.*, 2004) and confirm the earlier finding that there is a minimum pressure gradient required to maintain foam flow in 3D porous media, even in the limit of zero velocity; see Figs. 2.29 and 2.30. Even in pores that are radially symmetric and symmetric front-to-back, two forms of symmetry-breaking alter the passage of the lamella through the pore. First, if the pore is wide and has a sharp angle at the pore body, the lamella makes a jump across the pore body; as a result, the lamella spends more than half its time bulging forward, resisting forward movement. As a result, in a population of moving lamellae, there is net average resistance per lamella resisting flow: an effective yield stress to the flowing foam. Second, even radially symmetric pores the lamellae jump spontaneously to radially asymmetric shapes (Fig. 2.29). This alters the value of the yield stress, but in most cases not its existence. Details are in Cox *et al.* (2004).

Direct Observation of Tracer Distribution Through CT Imaging

In his PhD research at the Technical University of Delft (TUD), Dr. Quoc Nguyen performed experiments with CT scanning and Xe, a gas-phase tracer that is visible in CT. The CT images show clearly that the standard 1D model used to interpret tracer effluent profiles is incorrect in its assumptions. Since Dr. Nguyen's arrival at UT, in cooperation with Dr. Nguyen's PhD advisors at TUD (Prof. Peter Currie and Dr. Pacelli Zitha), we have extended his work and compared the *in situ* tracer distribution from CT images to the trapped-gas saturation estimated from fitting the effluent tracer profile to the 1D mass-transport model, augmented here for the effect of pressure variation along the core. We determined the effluent profile indirectly from the CT images in two ways: by imaging the tracer concentration in the flow line downstream of the core, and using a mass balance on tracer in the core. Estimates of trapped-gas fraction using the effluent data and the standard 1D model vary by as much as 0.2 among reasonable fits to the effluent data, and flowing gas fraction by as much as a factor of 1.5 or 2. This casts doubt on the precision of fitting trapped-gas fraction to tracer-effluent data. The experiments span a range of foam qualities and injection rates in Bentheim sandstone. Model-derived estimates of trapped-gas fraction decrease with increasing gas injection rate and increase weakly with increasing liquid injection rate in our experiments. The CT images show a shift to a wider variety of fluctuating flow paths as liquid or gas injection rate increases.

These results and the new analysis of results is described in detail in the remainder of this section on Task 2.

Experimental

The X-ray CT apparatus, foam core-flood setup, and materials are described in detail elsewhere (Nguyen, 2004). A schematic is shown in Fig. 2.31. Nguyen used a

Bentheim sandstone core, 15 cm long and 4.2 cm diameter, mounted horizontally. Four pressure ports along the core allowed pressure differences to be determined in three sections along the core, of length 40, 30 and 80 mm, respectively: these sections are denoted 1, 2 and 3. There was no foam generator upstream of the core. All experiments were conducted in a thermostat room at $20 \pm 1^\circ\text{C}$. Analytical grade nitrogen (N_2) and xenon (Xe) were used to make calibrated gas mixtures of N_2 and Xe .

The experiments were performed with a surfactant solution containing sodium dodecyl sulfate (analytical reagent grade, M 288, purchased from IFraChem) at a concentration of 0.023 wt%, in the presence of 1.95 wt% NaCl. The critical micelle concentration of the SDS surfactant is about 0.0144 wt% for this salt concentration, as determined from surface-tension measurements using the Wilhelmy-Plate method. All experiments were conducted in the same Bentheim sandstone core, of permeability 1010 md and porosity 22.1%. The surfactant formulation is the same as and the core is similar to that in other CT studies of liquid injection following foam (Nguyen, 2004; Nguyen *et al.*, 2003, 2005; Zitha *et al.*, 2003).

Nitrogen and surfactant solution were injected into the saturated core until reaching a steady state as indicated by (a) the sectional pressure drop profiles, and (b) the average CT values for liquid saturation (no Xe present) of the fluid system. The latter was determined from a set of seven image planes, slicing the core vertically, and parallel to its axis. The nitrogen stream was then switched to the tracer-gas mixture while surfactant injection continued, and the sequence scanning done to produce successive sets of images of the tracer displacement. Each sequence scan included nine CT slices 4 mm thick, with a fixed distance of 0.5 mm between two adjacent slices. Since the CT slice arrangement was symmetric, we denote the slice position as $P = n$, with $n = 0$ corresponding to the central slice on the plane of the core axis, and ± 1 to 4 to slices at increasing distances from the core axis. The equilibrium saturation of tracer over the entire core was signaled by constant CT values of the images, which typically took 10 to 14 PV, depending on injection rate. The experiments were conducted in two series: varying gas injection rate at fixed liquid injection rate, and varying liquid injection rate at fixed gas injection rate. Details of injection rates and foam qualities used for both types of sandstone cores are presented in Table 2.2. Sectional pressure drops are given in Table 2.3. The same sandstone core was used in all experiments. The procedure for recovering the core between experiments is described in Nguyen (2004) and Nguyen *et al.* (2003).

Original Analysis of Data

To quantify the trapped-gas fraction from his CT images, Nguyen (2004) averaged the concentration of tracer in several core cross-sections as a function of time. He then estimated the fraction of flowing gas in each cross-section as the fraction of a normalized concentration of 1 achieved in an initial, rapid rise, which he took to be due to convection. The remaining, slower rise in concentration he took to be diffusion into trapped gas in the cross-section. In that way, Nguyen obtained an estimate of the trapped- and flowing-gas fractions in each voxel. This approach is based on an assumption that the concentration rise from convection in the cross-section is rapid and that from diffusion is slow. If flowing and trapped gas are in intimate contact, however, diffusion of tracer into trapped gas slows the rise of tracer concentration in the flowing gas, while the initial rise in tracer concentration from diffusion into the trapped gas adjacent to flowing gas can be rapid. Thus, unless diffusive mass transfer is slow between flowing and trapped gas, there may be no fundamental shift in the rate of

concentration rise that can be simply identified with a shift from convective to diffusive mass transfer. Moreover, a 1D model for mass transfer (Eq. 2.6 below) suggests that the concentration of tracer at the break in slope is associated with the rate of mass transfer, not the volume of flowing or trapped gas. We are still investigating whether a modified version of this approach may give an dependable estimate of flowing-gas fraction. For the new analysis of data, however, we examined the accuracy of the conventional method of fitting effluent data to a mass-transfer model, by two means: first, examining the variability of the estimate of flowing-gas fraction from the model fit to the data; and, second, by examining the accuracy of the assumptions in the mass-transfer model using Nguyen's CT data.

Reconstruction of Effluent Tracer Profile

A unique aspect of this work is the direct comparison of tracer effluent concentration profiles with *in situ* tracer distribution. There was no direct measurement of effluent concentration during these experiments - no gas chromatograph or mass spectrometer downstream of the core (Fig. 2.31). Two methods were then used to reconstruct the effluent tracer concentration profile from the CT images. The first method is based on the CT value of the effluent in a small volume of the channel (0.8 cm long and 0.25 cm diameter) downstream of the outlet endcap as shown in Fig. 2.31. This channel is captured in the central CT image. The determination of tracer concentration within individual voxels of the channel region follows the same procedure as for *in situ* tracer concentration. Averaging voxel concentrations over the 365 voxels within the channel gives the effluent tracer concentration. This region is not shown in the CT images of the core itself shown below.

Independently, the effluent tracer profile was obtained from a mass balance for tracer over the whole core. First, total mass of tracer in the core was determined as a function of time at a series of discrete times by converting the CT value in individual voxels over all nine axial CT images into concentrations, and summing over all voxels. The local tracer fractions are converted to mass concentrations using average core porosity, the ideal gas law, and local pressure, interpolated linearly between values at the pressure taps. At time t , the produced mass of tracer over a time interval Δt is the difference between the mass of tracer injected during this time interval and the change in the mass of tracer within the core during this interval: Tracer concentration in the effluent can be determined from the mass flow rate in the effluent given the flow rate and outlet pressure. Because the mass flow rate of tracer out of the core is estimated from the difference between potentially noisy data at different times, the inferred value of effluent concentration is expected to have some noise as well.

Mass Transfer Between Flowing and Trapped Gas

Determining trapped and flowing gas from tracer effluent profiles is complicated by mass transfer between flowing and trapped gas. The diffusion coefficient for gases is typically higher than 10^{-6} m²/s (Forsythe, 1954), which would give extremely rapid transfer between flowing and trapped gas. The liquid films between gas bubbles provide the major resistance to gas diffusion in foam. Nguyen (2004) measured the resistance to gas diffusion through foam films for Ar gas and obtained a mass-transfer coefficient for transport across a single foam film of 3.5×10^{-4} m/s. His analysis shows that almost all this resistance is due to penetration of the surfactant monolayers on the two lamella surfaces, not to diffusion through the liquid in the film. If lamellae were spaced at

intervals of 200 μm along a capillary, the effective diffusion coefficient in the capillary would be about $(3.5 \times 10^{-4})(200 \times 10^{-6}) = 7 \times 10^{-8} \text{ m}^2/\text{s}$. The true value of the effective diffusion coefficient through trapped gas in porous media could be higher or lower than this rough estimate: higher, if one allows for larger bubbles, or for breaking and reforming of lamellae; lower, if one allows for diffusion through lamellae in throats much narrower than pore bodies and for tortuosity in the porous medium.

To see how rapidly gas in flowing foam could diffuse outwards into trapped gas, consider a cylindrical channel of flowing foam, of diameter 200 μm (representing a one-pore-wide flowing pathway), surrounded by an infinite body of stagnant, trapped gas. Suppose for simplicity that the trapped gas is initially at zero concentration of tracer, and abruptly starting at time $t = 0$ the inner surface of the trapped gas (i.e., the outer surface of the flowing channel) is at a concentration of tracer of 1. This unsteady diffusion problem is solved by Carslaw and Jaeger (1959). For a diffusion coefficient of $7 \times 10^{-8} \text{ m}^2/\text{s}$ for the trapped gas, within a period of 1 min. tracer would have reached a concentration of at least 0.5 to a diameter of about 1.2 mm. This region of high tracer concentration represents an increase in volume invaded by tracer by a factor of 36 over the volume in which gas actually flows. Meanwhile, the advance of tracer in the flowing gas itself is slowed and dispersed by mass transfer to the trapped gas. It may be difficult to distinguish truly flowing gas from the much larger volume of nearby trapped gas over a tracer experiment lasting many minutes.

Standard 1D Model for Interpreting Tracer Effluent Data

The standard model for analyzing tracer effluent data (Radke and Gillis, 1990) is extended here to allow for nonuniform pressure along the core. Consider a cylindrical homogeneous porous medium of length L and porosity ϕ . Foam flows at steady state through this medium at a nominal gas superficial velocity U_o , with a steady (though possibly nonuniform) pressure drop and uniform and constant liquid (S_w) and gas (S_g) saturations. Because pressure P varies along the core, local gas superficial velocity U varies with P according to $U = U_o(P_o/P)$, where U_o is superficial velocity at a reference pressure P_o , defined below. Once steady state is achieved, the gas is switched to a gas mixture having a fixed tracer mass fraction. The injection rate is maintained unchanged so as not to disturb the steady-state trapped-gas structure. S_f and S_t refer to flowing and trapped gas, respectively; α_f the mass fraction tracer in the flowing gas, and α_t the mass fraction of tracer in the trapped gas. Since the liquid saturation S_w , measured with CT (Nguyen, 2004), is nearly the same (13%) in all experiments discussed here, for convenience, liquid is treated as merely an additional part of the solid matrix, as though gas were the only phase in the medium (i.e., $S_f + S_t = 1$, and porosity ϕ is rescaled as $[\phi(1-S_w)]$). Thus, below, S_t and S_f refer to tracer volume fractions in the gas phase, not saturations. Implicit in this derivation is the assumption that tracer is not stored to a significant extent within the liquid phase.

The transport of the tracer gas can be described by a one-dimensional convection-dispersion equation coupled with an equation describing the transfer of the tracer from flowing gas into trapped gas:

$$\begin{cases} \phi S_f \rho_g \frac{\partial \alpha_f}{\partial t} + \phi S_t \rho_g \frac{\partial \alpha_t}{\partial t} + \frac{\partial (U \rho_g \alpha_f)}{\partial x} = \frac{\partial}{\partial x} \left(\phi S_f \rho_g D \frac{\partial \alpha_f}{\partial x} \right) \\ \frac{\partial \alpha_t}{\partial t} = a_s k_e (\alpha_f - \alpha_t) \end{cases} \dots\dots\dots (2.1)$$

where ρ_g is the gas density; a_s is the specific area between trapped and flowing gases, with units of area per unit volume of trapped gas; k_e is the effective mass-transfer coefficient of the tracer through this area; and D is the dispersion coefficient, expressed as

$$D = D_g + \frac{\lambda U}{\phi S_f} \dots\dots\dots (2.2)$$

where D_g is the effective diffusivity of gas in the porous medium and λ is the dispersivity. Assuming ideal-gas behavior, the effect of pressure can be expressed explicitly:

$$\begin{cases} \phi S_f P_d \frac{\partial \alpha_f}{\partial t} + \phi S_t P_d \frac{\partial \alpha_t}{\partial t} + U_o \frac{\partial \alpha_f}{\partial x} = \frac{\partial}{\partial x} \left([\phi S_f P_d D_g + \lambda U_o] \frac{\partial \alpha_f}{\partial x} \right) \\ \frac{\partial \alpha_t}{\partial t} = a_s k_e (\alpha_f - \alpha_t) \end{cases} \dots\dots\dots (2.3)$$

where ϕ is porosity and P_d is dimensionless pressure, (P/P_o) , where the reference pressure P_o is taken as the average pressure integrated over the core. Without loss of generality, one can renormalize α_f and α_t to a value of 1 at the injected tracer mass fraction. For the calculations here local pressure P is interpolated linearly between the pressures measured at the pressure taps. The terms in the first equation in Eqs. 2.1 and 2.3 represent, respectively, accumulation of tracer in the flowing gas, accumulation in trapped gas, convection, and diffusion/dispersion. The model is similar to the final equations of Radke and Gillis (1990), except that pressure variation is accounted for here explicitly. Like that model, it assumes that two tracer mass fractions α_f and α_t characterize the flowing and trapped gas, respectively, at each axial position x , and neglects axial diffusion through trapped gas. The following initial and boundary conditions are used in this study:

$$\begin{aligned} \alpha_f(x, 0) = \alpha_t(x, 0) = 0 \\ \alpha_f(0, t > 0) = 1 + \frac{\phi D}{LU} \frac{\partial \alpha_f}{\partial x} \Big|_{x=0} \dots\dots\dots (2.4) \\ \frac{\partial \alpha_f(t > 0)}{\partial x} \Big|_{x=L} = 0 \end{aligned}$$

Eqs. 2.3 are solved numerically for $\alpha_f(x,t)$ and $\alpha_t(x,t)$, using a fully implicit discretization scheme (Hirsch, 2000; Nguyen, 2004), given four parameters λ , D_g , S_f , and the product $(a_s k_e)$. The parameters are determined by fitting the model to the reconstructed effluent tracer profiles. The fitting procedure used here is based on a gradient-based optimization scheme described in detail elsewhere (Leuenberger, 1979). In this scheme, if a proposed change in model parameters makes no significant improvement in the fit to data, the

given parameter is left unchanged. As shown below, the tracer profile determined directly from the downstream tubing was less noisy than that estimated from a mass balance on the core, though the trends agree well. The parameter-fitting routine had problems converging when fit to the relatively noisy effluent-concentration curve based on a mass balance on the core. Therefore the parameters were fit to the effluent data determined from the CT image of the downstream tubing. The fit to the data was not sensitive to the value of dispersion coefficient. Fitted values of λ and D_g were close to $2 \cdot 10^{-4}$ m and 10^{-7} m²/s, respectively, in all cases, in part because the fitting routine rejects changes that make no significant improvement in the fit to the data. Tang and Kovscek (2004) also note the values of dispersion coefficient did not have much effect on the fit to their effluent data. Our fit was sensitive to the values of S_f and the product ($a_s k_e$).

Solution in Limit of Negligible Dispersion. If dispersion can be neglected, Eqs. 2.3 can be combined as follows:

$$S_f \frac{\partial \alpha_f}{\partial t} + \frac{U_o}{\phi P_d} \frac{\partial \alpha_f}{\partial x} = -(1 - S_f) a_s k_e (\alpha_f - \alpha_i) \quad \dots \dots \dots (2.5)$$

This is a first-order partial differential equation, leading to a solution where characteristics for the mobile phase have constant and uniform velocity $(dx/dt)_{char} = U_o/(\phi P_d S_f)$ and α_f is not constant along these characteristics (Lake *et al.*, 2002). In particular, for the characteristic corresponding to the leading edge of the tracer front, α_i is always zero, and one can immediately solve for concentration at the front as a function of time as it moves along the core:

$$(\alpha_f)_{front} = \exp\left(-\frac{1 - S_f}{S_f} a_s k_e t\right) \quad \dots \dots \dots (2.6)$$

One can convert this equation to a dependence on position x using the characteristic velocity $(dx/dt) = U_o/(\phi P_d S_f)$.

Because characteristic velocity is unaffected by mass transfer with the trapped gas, the leading edge of the tracer front is not slowed by mass transfer between trapped and flowing foam, though if $([(1 - S_f)/S_f] a_s k_e t)$ is sufficiently large one may not be able to distinguish this breakthrough from background noise. The breakthrough time is $(L \phi P_d S_f / U_o)$, where, as noted, ϕ reflects only the gas-filled pore space. As long as $([(1 - S_f)/S_f] a_s k_e t)$ is not too large, there is a jump from zero tracer concentration to a much larger value upon breakthrough of tracer in the effluent. To the extent that the 1D model describes the transport of tracer in foam, if dispersion is not significant, if mass transfer not too rapid, and water saturation is known, the method of Friedmann *et al.* (1991) correctly identifies flowing gas fraction in the foam from the breakthrough time of tracer in the effluent. Taking a value of tracer concentration at 10% of that injected, as they did, helps avoid the effect of decreasing tracer concentration at the front predicted by Eq. 2.6 and also any small effects of dispersion giving a small rise in tracer concentration before the main front.

Results and Discussion

Experiments were conducted with five different foam injection rates and nominal qualities in the Bentheim sandstone core. See Table 2.2 for nominal foam qualities and injection rates and Table 2.3 for sectional pressure drops for all cases.

Base Case: Foam A. In situ tracer distribution. Foam A has nominal total superficial velocity 5.71 m/d and foam quality 90.9% (Table 2.2; "nominal" values apply at outlet pressure). The sectional pressure gradients (*cf.* Table 2.3) are 87, 103, and 140 psi/ft (285, 336.7, and 456.3 psi/m) in sections 1, 2 and 3 respectively. Foam is stronger as one moves downstream, but strong foam is present in all core sections. At the core inlet, where pressure is approx. 73 psi, total superficial velocity is 1.13 m/d and foam quality is 67%. The total pressure drop across the core with Foam A, 58.0 psi, remained nearly constant during the foam injection with tracer.

Fig. 2.32 shows 5 of the 9 axial CT images of the displacement of steady-state Foam A by Foam A with tracer, at three dimensionless times (0.54, 0.86, and 1.15 PV, corresponding to 980, 1590, and 2120 s). Dimensionless time is defined here as pore volumes of gas injected, divided by the volume of gas-occupied pore space, at the average pressure in the core. The inlet and outlet endplates are shown at the extreme left and right of each image. The uniform dark red color of the injection endplate in all figures reflects uniform penetration of tracer along the endplate.

The images in the central plane $P = 0$ resemble its neighboring planes $P = \pm 1$ and ± 2 , which are not shown. Consider the first image series in Fig. 2.32 taken at 0.54 PV. The tracer penetrates about 1 cm deep into the core from the inlet, relatively uniformly over the cross-sectional area except for a region near the center of the endplate. Further downstream, tracer is present in the upper portion of the cylindrical core, and appears to have reached the outlet by this time. By 0.86 PV a front of high tracer concentration has advanced further along the top of the core, and the tracer front is also advancing slowly down from the top and in from the inlet. At 1.15 PV these trends continue: the front of high tracer concentration has advanced still further along the top of the core, and the tracer front continues to advance slowly down from the top and in from the inlet endplate. If the advance of tracer about 2 cm into the core from the inlet at 1.15 PV (2120 s) reflects diffusion of tracer into trapped gas without convection, it suggests a diffusion coefficient of tracer through foam of about 2×10^{-7} m²/s. This is of the same order of magnitude as the rough estimate of the diffusion coefficient through trapped foam above.

Fig. 2.33 shows cross-sectional CT images reconstructed from the axial images at roughly 1 cm distances along the core at 1.15 PV. In this case 13 axial CT images were taken at somewhat closer spacing than in the other cases. Except near the inlet, a high concentration of tracer occupies between 30 to 50% of the core, along the top and sides, depending on the cutoff in tracer concentration used.

One can immediately see one shortcoming of the 1D model (Eqs. 2.3) from these images: A significant portion of tracer in the core at times up to about 1 PV reflects invasion (probably diffusion) of tracer into trapped gas from the injection endplate. This retention of tracer in the core is not accounted for in the 1D model.

Examining tracer cross-sections over time also reveals that tracer penetrates the upper portion of the core in separate, narrower pathways in intimate contact with the trapped gas around it. Fig. 2.34 shows cross-sections at one location over a series of times. Within the upper region penetrated by tracer, tracer breaks through in individual locations spaced very roughly 0.3 (vertically) to 1 cm (horizontally) apart. The rough calculations on mass-transfer rate above suggest that differentiating between convection

and diffusion in these smaller regions may be difficult. In other words, it may be difficult to say for sure what fraction of the roughly 1/3 to 2/3 of this core eventually occupied by tracer represents convection and what fraction diffusion into adjacent trapped gas, based on the effluent profile.

Effluent tracer profiles for Foam A. Fig. 2.35 shows the effluent concentration profiles reconstructed from the CT images using the two methods (direct imaging of downstream tubing and material balance on the core) as well as the optimal fit the parameters in Eqs. 2.3 to these data. The two methods of reconstructing the effluent data agree well, especially up to about 1 PV. The fit of the model to the data is good. The fitted parameters are $S_t = 0.60$ and $a_s k_e = 7 \times 10^{-4} \text{ s}^{-1}$. The model predicts a sharper concentration rise at tracer breakthrough than in either reconstructed data set. The breakthrough of tracer in the model corresponds well to the flowing-gas saturation of 40% from the model fit. The flowing-gas saturation inferred from the model corresponds roughly to the upper fraction of the core through which tracer appears to be moving in Figs. 2.32 to 2.34.

Fig. 2.35 also shows an alternate fit to the data with $S_t = 0.47$, $a_s k_e = 9 \times 10^{-4}$, $D_g = 10^{-7}$, and $\lambda = 10^{-3}$. This fit minimizes the sum of squared errors in the breakthrough portion of the data, i.e. for concentrations less than 0.75 of injected concentration. Nonetheless it provides a reasonable fit to the entire effluent curve, and a better fit to the breakthrough of tracer. This sum of squared errors increases slightly in the manual fit (i.e. no optimal fitting procedure applied) shown in Fig. 2.36. Fig. 2.36 indicates that a good fit could also be obtained with $S_t = 0.39$ and $a_s k_e = 6.9 \times 10^{-4}$. Thus a 50% increase in flowing gas fraction over the global optimal value ($S_f = 0.61$ compared to 0.40 for the global optimal fit) still provides a reasonable fit to the entire effluent curve, and a better fit to the breakthrough of tracer. The 1D model value of S_t then can be said to have an uncertainty of at least 0.2, i.e., the difference between the optimal fit to all data and the manual fit to the initial breakthrough data. Nguyen (2004) originally estimated trapped-gas saturation at 77% based on analysis of the rise in cross-section average tracer concentration in the core.

Fig. 2.37 shows the tracer fraction in the flowing and trapped regions along the core, respectively, estimated by the global optimum fit of the 1D model to effluent data, at values of dimensionless time corresponding roughly to Fig. 2.32. If one associates the region near the top of the core, where tracer advances fastest in Fig. 2.32, as the flowing-gas region in the model, which according to the model occupies 40% of the volume of the core, it is clear from comparison of Figs. 2.32 and 2.37 that the 1D model overestimates the tracer fraction in the flowing region. It also misses the region of tracer penetration near the core inlet and the wide variation of tracer fraction within the trapped-foam region.

Effect of Gas Injection Rate - Foams B and C

In situ tracer concentration. Foam B has a gas injection rate twice that in Foam A and the same liquid injection rate (Table 2.2), with nominal superficial velocity 10.9 m/d and quality 95%. Pressure gradient is much higher than with Foam A: 93 psi across the core compared to 58 psi (Table 2.3). Because of gas compression, total superficial velocity at the inlet is 1.93 m/d and quality there is 73%. It is hard to compare gas mobilities in Foam A and Foam B because of the greater effect of compression on gas superficial velocity over much of the core with Foam B.

The displacement of the steady-state Foam B by Foam B with tracer is shown in Fig. 2.38 at three different dimensionless times (0.32, 0.81, and 1.59 PV, i.e. 350, 890,

and 1730 s). Fig. 2.39 shows reconstructed cross-section images at a dimensionless time of 2.14 PV. The structure of the region occupied by tracer at the top and sides of the core is similar to that observed with Foam A (Figs. 2.32 and 2.34). This region grows slowly downward as injection of tracer continues. The boundary between the tracer region at the top of the core and the tracer-free region below it is sharper than with Foam A (*cf.* Figs. 2.32, 2.33, 2.38 and 2.39). The region of high tracer fraction advances along the top of the core more rapidly than in Foam A (*cf.* Fig. 2.32 at 0.86 PV and Fig. 2.38 at 0.81 PV).

It appears from the image in Fig. 2.38 at $P = -2$ and 0.81 PV that tracer is flowing at one location below the middle of the core: the sharply defined region of high tracer concentration. This region shows no evidence of further advance (beyond what could be ascribed to diffusion) at 1.59 PV (region indicated by white arrow). If the presence of this region reflects convection at this location before 0.81 PV, it appears to have ceased by 1.59 PV.

Foam C has a gas injection rate three times that of Foam A, a nominal superficial velocity of 16.1 m/d and quality of 97%. Pressure drop across the core is 86 psi, slightly less than for Foam B. At the inlet, superficial velocity is 2.8 m/d and foam quality 81%. The near-constancy of pressure gradient upon a 50% increase in gas injection rate for Foam C suggests that it is in the high-quality regime (Fig. 1.1), though foam quality changes substantially along the core due to gas expansion. The slightly lower pressure gradient at 50% higher gas injection rate means that gas mobility is over 50% higher for Foam C than Foam B. This reflects a combination of shear-thinning rheology of foam and an increase in bubble size.

The increase in gas-injection rate produces some changes in the distribution of tracer within the core. Fig. 2.40 shows selected axial CT images of the tracer displacement of Foam C at dimensionless times 1.41 and 2.15 PV (1170 and 1780 s), which appears similar to that for Foam A (Fig. 2.32) and Foam B (Fig. 2.38). But the region of high tracer concentration advances more rapidly across the top of the core (perhaps in a narrower region near the top) than in Foam B (*cf.* Foam B at 1.59 PV and Foam C at 1.41 PV). At higher gas injection rate, there is less time for diffusion of tracer from flowing to trapped gas at the same value of dimensionless time. Assuming the invasion of tracer about 2 cm into the core from the inlet at 1.41 PV (1170 s) results purely from diffusion into trapped gas, one estimates a diffusion coefficient of order $3 \times 10^{-7} \text{ m}^2/\text{s}$, in rough agreement with the estimate for Foam A. Between 1.41 and 2.15 PV, however, a different mechanism of tracer transport appears active. By 2.15 PV, tracer has advanced about 5 cm along the bottom of the core. If this were due purely to diffusion into trapped gas during these 1780 s, the diffusion coefficient must be of order $1.5 \times 10^{-6} \text{ m}^2/\text{s}$, 5 times larger than estimated from the earlier time. We conclude that convection, not evident at earlier times, has transported tracer along the bottom of the core during this period, and that this convection started, or changed its rate, between 1.41 and 2.15 PV injection. Thus as gas injection rate increases from Foam A to B to C, there is a shift toward more gas flow along the bottom of the core: i.e., more variety in gas flow paths. From Foam A to Foam B there is an increase in pressure gradient, but not from Foam B to Foam C. It is not clear how bubble size may vary among these cases.

Fig. 2.41 shows the tracer fraction averaged across core cross sections at $X \equiv x/L = 0.2, 0.5$ and 0.9 , as a function of dimensionless time, for Foam C. From this curve, it appears that after 4 PV injection, perhaps 40% of the core volume is not yet penetrated by tracer.

Effluent tracer profiles for Foams B and C. Fig. 2.42 shows the two reconstructed effluent tracer profiles for Foam B. The reconstructed effluent data show

some scatter, but excellent agreement in their overall trends. Also shown is the 1D model global optimum fit with $S_t = 0.56$ and $a_s k_e = 10^{-3} \text{ s}^{-1}$. The model gives an excellent fit to the data, through the middle of the scatter. The fitted trapped-gas saturation $S_t = 0.56$ is a little lower than the optimal estimate of 0.60 for Foam A, while the fitted value of $a_s k_e$ for Foam B is a bit higher than that for Foam A ($7 \times 10^{-4} \text{ s}^{-1}$). Small difference in mass-transfer parameter could easily result from differences in bubble size or foam structure. Fig. 2.42 also shows an optimal fit to only the breakthrough data (concentration less than 70% of injected concentration), which, as in Fig. 2.36, gives a reasonable fit to all the data, but with a lower value of S_t , 0.48. There is virtually no difference in the fits, except that the latter gives a slightly better fit to the breakthrough portion of the data. Again, there is uncertainty in the trapped-gas fraction S_t based on the 1D-model fit to the effluent data. Attempts to fit the data manually with a lower value of S_t gave noticeably worse fits to the data, however.

Fig. 2.43 shows the global optimal fit to the reconstructed effluent data for Foam C, with $S_t = 0.47$ and $a_s k_e = 10^{-3} \text{ s}^{-1}$. As in other cases there is some scatter in the effluent data, but excellent agreement in the trend, and the model provides a reasonable fit, though it overshoots effluent concentration after breakthrough until about 1 PV, then underestimates effluent concentration until about 2 PV. Fig. 2.43 also shows the optimal fit to the breakthrough data only (tracer fraction less than 80% of injected), with $S_t = 0.36$, which to the naked eye provides at least as good a fit to all the data. Fig. 2.44 compares the global optimum fit to a manual fit with S_t as low as 0.33. Again, the fit with lower S_t is at least as good to the naked eye as the global optimum fit.

Fig. 2.45 shows the local resident average fraction of tracer at the same three positions as in Fig. 2.40, from the global optimal fit of the 1D model to the effluent data for Foam C. At 4 PV, for instance, the 1D model infers that tracer occupies about 95% of the pore space throughout the core. The 1D model greatly overestimates the amount of tracer in the core at this time, in spite of the apparently satisfactory fit to the trend of the data in Fig. 2.43.

In spite of the uncertainty, there is clearly a decreasing trend in estimated trapped-gas fraction as gas injection rate increases: from 0.6 to 0.56 to 0.47 for Foams A, B and C using the global optimum fits, or 0.47, 0.48, 0.36 from the optimal fits to the breakthrough data. It is hard to discern a trend with pressure gradient $|\nabla P|$ in the data, because $|\nabla P|$ is nearly the same for Foams B and C, between which the biggest change in estimated trapped-gas saturation occurs.

CT scans also identify a change in where gas flows that is not observable from effluent data and the 1D model fit alone: more gas flows along the bottom of the core as gas injection rate increases.

Effect of Liquid Injection Rate - Foams D and E

In situ tracer concentration. Foam D has the same gas injection rate as Foam B, but with twice the liquid injection rate (Table 2.2). This foam induced an overall pressure drop of 90 psi, slightly lower than that in Foam B. The gas mobility thus is similar to that in Foam B, while the liquid mobility is twice as great.

Fig. 2.46 shows the distribution of tracer with Foam D at 0.91 and 1.61 PV (960 and 1710 s) in image planes $P = 0$ and ± 3 . As in previous images, tracer advances along the top of the core. There is clearly either intermittent or slow convection along the bottom of the core as well, indicated by the horizontal white arrows in Fig. 2.46. Fig.

2.47 shows reconstructed cross-sections at 2.14 PV (2290 s). There is clearly a region of foam convection in the lower half of the core.

Foam E has a liquid injection rate four times higher than that for Foam B, with the same gas injection rate. The resulting pressure drop of 94 psi is comparable to those of Foam B and D. Gas mobility is similar to that in foams B and D, and liquid mobility is two or four times higher, respectively.

Fig. 2.48 shows complex behavior in the tracer displacement. Dimensionless times there (0.39, 1.03, 1.68 PV) correspond to 410, 1090, and 1780 s. At first (0.39 PV) there is convection both along the top and through the middle of the core. Later, convection shifts paths through the middle of the core. Three regions of high tracer concentration (white boxes at 0.39 PV) disperse and slowly move downstream in response to this shift.

A pressure gradient that does not vary with liquid injection rate, as in Foams B, D and E, is consistent with foam in the "low-quality regime" (Alvarez *et al.*, 2001). Rossen and Wang (1999) conjecture that the increase in liquid mobility upon increasing liquid injection rate in the low-quality regime is due to liquid replacing a portion of resident trapped gas, with no change in the mobility of flowing gas. The CT images of liquid saturation in steady state foam flow (Nguyen, 2004) for the same foam formulation in a similar Bentheim core show, if anything, a slight decrease in S_w from Foam B to D to E, in contradiction not only of the conjecture of Rossen and Wang but of other studies (Bernard, *et al.*, 1965; Sanchez and Schechter, 1989; de Vries and Wit, 1990; Friedmann *et al.*, 1991) that find that water relative permeability in foam is independent of the presence or strength of the foam. Water relative permeability increases by a factor of four from Foam B to Foam E, but water saturation does not appear to rise. Moreover, increasing liquid injection rate clearly does affect where gas flows, if not macroscopic gas mobility. More gas flows along the bottom of the core as liquid injection rate increases.

Effluent tracer profiles for Foams D and E. Fig. 2.49 shows the reconstructed effluent profiles for Foam D and the global optimal fit. Again there is scatter in the effluent data but excellent agreement on the trend of the data. The global optimum fit is satisfactory; it somewhat overestimates effluent tracer concentration from breakthrough to about 1 PV, and again from about 2 to 5 PV. The fitted value of S_t is 0.58. The fitted value for $a_e k_e$ for Foam D is about 1.5 times higher than that for Foam B. Fig. 2.49 also shows the optimal fit to the breakthrough data only (tracer fraction less than 80% of injected), giving a fit nearly indistinguishable from the global optimum fit, with a fitted value of $S_t = 0.5$. Fig. 2.50 compares the global optimum fit to a manual fit with $S_t = 0.40$. The fit to the early portion of the breakthrough curve is superior to the other fits, with a slightly worse fit from 1 to 4 PV. The variability in the estimate of S_t in this case is nearly as great in this case as with Foam A.

Fig. 2.51 shows the global and breakthrough optimal model fits to the reconstructed effluent profiles for Foam E. There is greater scatter, and the model fits are somewhat worse, in this case, but the fault is not all in the 1D model. A simple material balance on the core indicates that the area between the effluent curve and a dimensionless concentration of 1 represents the pore volumes of tracer left in the core at any given time. From this perspective, both sets of effluent data violate a material balance on the core - they both imply more than 1 PV of tracer left in the core at the end of the experiment. This paradox, that effluent data reconstructed from a putative material-balance on the core violates the same material balance, could be explained by two causes, both due to the relation between "pore volumes" of gas and pressure: fluctuations of pressure during

the experiment, and the imperfection of our piecewise-linear fit (between known pressures at pressure taps) to the true pressure gradient in the core. Any mismatch between local pressure in the core and that in the model would give an apparent violation of the material balance in the core in terms of pore volumes. The other assumptions in the mass balance (uniform and constant porosity and water saturation) are common to both the computation of the effluent profile from a mass balance and the 1D model, and would not explain the discrepancy between them.

Fig. 2.52 shows a manual fit with a significantly higher value of S_t : 0.84. Figs. 2.51 and 2.52 thus show that similar fits can be obtained with a variety of values of S_t : from 0.65 (Fig. 2.51) to 0.84 (Fig. 2.52). The inferred value of S_f varies by over a factor of 2, from 0.16 to 0.35.

The global-optimum fitted value of S_t for Foams B, D and E increases with increasing liquid injection rate from 0.56 to 0.58 and then to 0.65. The trend is not strong, especially considering the wide uncertainty in the value for Foam E. If real, this trend is in contradiction to the model for the low-quality regime of Rossen and Wang (1999), in which increasing water mobility results from replacement of part of the trapped gas by water as water superficial velocity increases. According to that conjecture, trapped-gas fraction should decrease slightly with increasing liquid injection rate. It is difficult to find a trend with pressure gradient in these data, because of the near-constancy of $|\nabla P|$ among these cases, as would be expected in the low-quality regime (Fig. 1.1).

The CT images tell a story different from that in the 1D model fits, and one that may contradict the model fits: comparison of Figs. 2.38, 2.46, and 2.48 shows a more even distribution of convection throughout the core as liquid injection rate increases: less convection through the upper region of the core, and more through the middle and bottom. Whether this would indicate an increase in flowing-gas fraction, in contradiction to the 1D model results, is not simply answered. It is possible that flowing-gas fraction decreases along the top of the core as it increases in the middle and bottom.

Discussion of CT Experiments

Effect of gravity. In all cases, tracer advances fastest in the upper part of the core, which suggests a gravity effect in this horizontally-mounted core. In a CT study of liquid injection after foam with the same foam formulations in similar core material (Nguyen, 2004; Nguyen *et al.*, 2003, 2005; Zitha *et al.*, 2003; see also following section), in many cases liquid fingered through the bottom of the core, also suggesting a gravity effect. If there is an effect of gravity here, it is a subtle one; for pressure gradient $|\nabla P|$ in the range of 50 to 90 psi/ft (167 to 300 psi/m), the pressure gradient is from 115 to 210 times larger than the gravitational-potential gradient. The model for gravity segregation of Stone (Stone, 1982; Shi and Rossen, 1998; Rossen and Van Duijn, 2004) suggests that a slight override zone might form even in such a case, but that model predicts that foam would propagate 4 to 8 m in such a core before the effect of gravity becomes dominant; *cf.* our core length of 15 cm. Xe is more dense than N_2 , and tracer fills the injection endplate in all cases, so the chance of gravity segregation within the gas phase can be discounted. The previous studies of Radke and Gillis (1990) and Tang and Kovscek (2004) also used horizontally mounted cores to allow scanning, with pressure gradients comparable to, or smaller than, those here.

Accuracy of the reconstructed effluent concentration data. Both methods of reconstructing effluent concentrations involve assumptions, apart from accuracy of the CT data themselves. The method of direct visualization of the downstream tubing

assumes that there is no bypassing of foam within the tubing. The mass balance on the core assumes that porosity and water saturation are uniform throughout the core and constant at steady state; pressure changes linearly between known values at pressure taps; and local pressure does not change once steady state is achieved. The assumptions in the two methods are independent of each other, however. The effluent data reconstructed from CT data by two independent methods each show some scatter, but agree well in their trend. Scatter is generally worse for the method based on a material balance on the core. The good fit in the trends derived from these two methods gives one confidence in the accuracy of those trends.

Consistency between the 1D model and CT images. The CT images reveal several phenomena not accounted for in the 1D model for tracer transport in foam:

- Tracer concentration is not uniform in the region in which, broadly speaking, tracer advances rapidly downstream in the core, i.e., the top of the core. It is not clear whether foam is flowing within this entire region, or advancing throughout the region at different velocities, or flowing through only part of it and rapidly diffusing to surrounding trapped gas within the region.
- Tracer concentration is not uniform within the trapped-gas fraction at each axial position.
- The 1D model cannot identify the shift in the spatial distribution of gas flow paths as injection rates vary: more tracer flows along the bottom of the core as gas or liquid injection rates increase.
- Tracer diffuses from the injection endplate into the core, increasing retention of tracer within the core in a way not accounted for in the 1D model.
- Whatever the short-term fluctuations of local gas velocity with foam, in some cases foam velocity fluctuates on time and length scales large enough to be observed in the CT images.
- In some cases, the 1D model overestimates the amount of tracer present in the core at moderately long times after breakthrough. In other words, it overestimates the rate of tracer transport from flowing into trapped foam.

The deficiencies in the mechanistic description of foam flow in the 1D model may explain the variability shown here in values of S_t derived from reasonable fits to the data. The basic deficiencies in the 1D model would not necessarily be rectified by use of simultaneous dual gas tracers (Radke and Gillis, 1990; Tang and Kavscek, 2004). The model might make the same sort of errors in modeling transport of both tracers. Moreover, as discussed above, the effluent data for the tracer with more-rapid mass transfer adds little information to the overall fit.

Implications for foam mobility. Assuming the 1D model is correct, estimates of S_f in these experiments differ by up to 50% (Foam A) to 100% (Foam E). The effect of this uncertainty on modeling gas mobility is large, especially if gas relative permeability scales with the third power of S_f .

Conclusions From CT Study

1. For the first time, we present CT images of *in situ* gas tracer fractions in foam flow in 3D porous media. Those images indicate shortcomings in the assumptions of the 1D mass-transport model for gas-phase tracer conventionally used to model tracer transport in foam in porous media:
 - Tracer concentration is not uniform within either the flowing or the trapped gas at each axial position along the core.
 - A significant amount of tracer diffuses into the core from the injection endplate during the time scale of these experiments.
 - Foam flow fluctuates over relatively long time and length scales in some cases.
2. Effluent tracer concentration can be reconstructed from the CT images in two ways: (a) from imaging tubing downstream of the core, and (b) from a mass balance on tracer in the core. The two methods each show some scatter in these experiments but agree well in the trend of the results.
3. A 1D transport model fits the reconstructed effluent data with a range of values of S_t , all consistent with the trend in the data. In particular, in most cases examined, fitting the breakthrough portion of the effluent data gives a lower value of trapped-gas fraction, still with a reasonable fit to the entire data set, than a least-squares fit to the entire effluent curve. In some cases, the 1D model overestimates the rate of tracer diffusion from flowing into trapped foam at moderately long times. Estimates of trapped-gas fraction can vary by as much as 0.2, and estimates of flowing-gas fraction differ by as much as 50-100%, among reasonable fits to the data. The effect on the inferred gas mobility could be large, depending on the model for gas relative permeability with foam.
4. The 1D model also cannot discern a trend in these experiments in *where* tracer flows as injection rates vary: more gas flows through the bottom of the core as gas or liquid injection rates increase.
5. The trapped-gas fraction S_t obtained from the global optimal fit to the five reconstructed effluent profiles decreases with increasing gas injection rate; it may increase weakly with increasing liquid injection rate. It is hard to distinguish effects of pressure gradient $|\nabla P|$ in our experiments, in part because $|\nabla P|$ is similar in most of the cases, in spite of significant changes in injection rates. This suggests that our experimental conditions may have been near the intersection of the low- and high-quality regimes, where increasing gas or liquid injection rates alone leaves $|\nabla p|$ unchanged (see Fig. 1.1).
6. The cases with increasing liquid injection rate appear to reflect the low-quality foam regime. If so, and if the fitted values of S_t are correct, then they contradict the conjecture of Rossen and Wang (1999) that trapped-gas fraction should decrease slightly with increasing liquid injection rate. One pair of cases with increasing gas injection rate may reflect the high-quality regime, but it is hard to know for sure because foam quality changes substantially along the core due to gas expansion.

CT Images of Liquid Injection After Foam

Nguyen also conducted a CT study of liquid injection after foam (Nguyen, 2004; Nguyen *et al.*, 2003). The mobility of liquid injected after foam is key to liquid

injectivity in SAG foam processes and foam-acid well-stimulation processes. A modeling study of the role of gas trapping in this process begins this report on Task 2.

In cooperation with colleagues at The Technical University of Delft (Prof. Peter Currie and Dr. Pacelli Zitha), who supervised Dr. Nguyen's PhD work at TUD, we helped to analyze these results after Dr. Nguyen arrived at UT. The experimental details are similar to those for the study described above, except that N₂ was the only gas. The contrast between X-ray absorbance for water and gas is the basis for imaging changes in water saturation upon injection of surfactant solution or surfactant-free brine following foam injection. In this case the CT slice thickness was 3 mm.

Fig. 2.53 shows axial CT images of the invasion of liquid into a foam-filled core. Fig. 2.54 shows reconstructed cross-section images at one location over several values of dimensionless time, and Fig. 2.55 shows the cross-section images at several locations at one time.

Details of this work are in Nguyen *et al.* (2005). The conclusions of this work area as follows:

1. Liquid, whether surfactant solution or brine, fingers through foam rather than displacing it. In a foam-acid diversion process, significant volumes of acid would not contact the formation or remove damage outside of these fingers within foam-filled layers.
2. The primary factors that affect ultimate apparent liquid mobility in a foam-acid diversion process in a given formation are the number and width of liquid fingers and the liquid saturation within the fingers. Thus experiments that interpret Δp measurements in terms of an average liquid mobility through trapped foam do not represent the process accurately. One-dimensional (1D) mathematical models that do not account for fingering, such as that described at the beginning of this section on Task 2, cannot accurately scale-up a foam-liquid diversion process, though, as shown above, they can be fitted to laboratory experiments. Those same models, applied in 2D or 3D, might be able to resolve the fingering process and permit scale-up.
3. In particular, 1D models predict that brine injection displaces the surfactant that stabilizes foam more rapidly than it does. In these experiments, post-foam brine injection was not qualitatively less effective than post-foam surfactant injection, though there were differences in both post-foam $|\nabla p|$ and finger pattern. Remarkably, gas saturation within the liquid finger was about the same with post-foam brine and surfactant injection.
4. The fingering process results because liquid has a much higher mobility in a region of high liquid saturation than flowing through trapped foam. Gas expansion and gas dissolution into the liquid are expected to have strong effects on the fingering process as observed in the laboratory. Unlike conventional viscous fingering with incompressible fluids, fingers or branches that lose the competition to a larger finger may later disappear due to gas expansion.
5. The formation of the finger is at least partly stochastic. In different experiments in the same core, with similar initial foam states, the liquid finger took markedly different paths through the core. Liquid injected after foam does not simply follow the path of mobile gas in the foam, as seen from comparison of gas-tracer images taken during foam flow and post-foam liquid saturation distribution. Gravity may have played a role in the path of the liquid finger in some cases, but no consistent trend could be discerned.

6. Pressure drop may increase at the start of post-foam liquid injection even if the volumetric injection rate of liquid is less than that of the foam at the injection point.
7. Rock heterogeneity played a complex role in these experiments. Foam was strongest in a core with higher average permeability, with layers parallel to the flow. In this core, a large finger formed near the inlet but did not rapidly spread to the outlet. Instead, for long times, injected liquid traveled the length of the finger and then spread across the core cross-section. This cannot be ascribed to a fixed anomaly in the core. In a core with one sharp, narrow, low-permeability layer perpendicular to the flow, a large liquid finger formed up to this layer and then evidently dispersed downstream of it.
8. *In situ* imaging, combined with two- or three-dimensional modeling, is essential to unraveling the mechanisms of the foam-acid diversion process.

Network Modeling of Gas Trapping

Gas trapping is important to foam mobility to the extent that it affects gas mobility through an effective gas relative-permeability function. There is no way to distinguish the effects of relative permeability and viscosity with foam in the laboratory, because only mobility can be measured. Therefore, we collaborated with colleagues Prof. Yannis Yortsos and PhD student (now post-doctoral fellow) Min Chen at the University of Southern California on a network model for gas trapping and mobility. Prof. Yortsos's research program at USC has developed a computer program to model the flow of a fluid with a yield stress in a pore network. The fluid is modeled as a Bingham plastic, which means that the resistance to flow of individual liquid films or lamellae are averaged across the fluid and represented by the yield stress of the Bingham plastic.

Results are presented in detail in Chen, *et al.* (2005). The work is in its early stages. Preliminary conclusions for flow of a Bingham plastic in a 2D square pore network are as follows: The fraction of the sites through which the fluid (Bingham plastic, or gas in foam) flows increases rapidly with the applied gradient above the threshold pressure gradient for flow. A "relative permeability" concept can be introduced to express the flow rate as a function of the fraction of the pore network through which the fluid flows ("flowing fraction" in foam terminology). This relation is reasonably fitted with a cubic power law, though this fit is mostly made at high fractions of flowing fluid; the fit may not be as good near the threshold for flow and low flowing fractions that characterize foam flow .

In many cases there is quadratic relation between flow rate and pressure gradient above the threshold gradient for flow. When the radii of the pore throats are widely varying, as expected in typical porous media, the quadratic regime is small and the relation between flow rate and pressure drop is effectively a straight line with an effective minimum threshold equal to the arithmetic mean of the threshold distribution.

Conclusions from Task 2 - Gas Trapping

1. A new model for gas trapping has been incorporated into a foam simulator. In this model, trapped-gas saturation is a function of pressure gradient, fit to data for liquid relative permeability following foam injection and the gas relative-permeability curve. This model can fit steady-state data for the two strong-foam flow regimes and in limited trials it also fits the transition period between foam injection and injection of liquid following foam. The simulator would be most helpful in modeling liquid injectivity in SAG foam processes.

2. Coreflood experiments have measured the average liquid saturation in a core during liquid injection following foam. Liquid saturation rose more upon liquid injection than had been previously thought. In this study the liquid relative-permeability function that applied to foam flow was also reasonably accurate during post-foam liquid injection. However, data implied that liquid does not uniformly sweep the core, but only contacts a portion of trapped gas.
3. Further CT studies of liquid injection after foam confirm that liquid fingers through foam rather than displacing it. This casts doubt on the ability of simulators to scale-up laboratory data unless applied in 2D or 3D on a scale fine enough to resolve the fingers. Because of this fingering, surfactant-free brine injected after foam does not displace the surfactant solution initially present or destroy foam as rapidly as predicted in 1D models.
4. A bundle-of-tubes model that accounts for foam yield stress and gas trapping can account for the anomalous behavior in the low-quality regime seen some experiments in Task 1 and other experiments with CO₂ foam. Pressure gradient can decrease upon increasing liquid superficial velocity in the low-quality regime because the drag on bubbles decreases as the liquid film between the bubble and the pore wall thickens. A pressure gradient that does not decrease with increasing liquid injection rate may reflect sensitivity of gas trapping to pressure gradient.
5. The yield stress of foam is the origin of gas trapping and relative-permeability effects with foam. Three-dimensional modeling, extending inconclusive work in 2D, confirms that there is an effective yield stress for trains of lamellae moving through porous media.
6. Direct CT imaging of gas-phase tracer concentration *in situ* during corefloods shows that the 1D model used to infer trapped- and flowing-gas fractions from gas tracer effluent data have several shortcomings:
 - Tracer concentration is not uniform within either the flowing or the trapped gas at each axial position along the core.
 - A significant amount of tracer diffuses into the core from the injection endplate during the time scale of these experiments.
 - Foam flow fluctuates over relatively long time and length scales in some cases.
 - 1D models cannot distinguish changes in the spatial distribution of gas flow paths that are evident from CT imaging.

In the cases examined, flowing-gas fractions inferred from the 1D model can vary by as much as a factor of 2 among reasonable fits to the data.

7. In spite of the uncertainty in individual estimates of trapped-gas fraction, some trends are evident in our data. The trapped-gas fraction S_t obtained from the 1D model fit to the five experiments shown here decreases with increasing gas injection rate; it may increase weakly with increasing liquid injection rate. It is hard to distinguish effects of pressure gradient $|\nabla P|$ in our experiments, in part because $|\nabla P|$ is similar in most of the cases, in spite of significant changes in injection rates. This suggests that our experimental conditions may have been near the intersection of the low- and high-quality regimes, where increasing gas or liquid injection rates alone leaves $|\nabla p|$ unchanged.
8. The cases with increasing liquid injection rate appear to reflect the low-quality foam regime. If so, and if the fitted values of S_t are correct, then they contradict the conjecture of Rossen and Wang (1999) that trapped-gas fraction should

- decrease slightly with increasing liquid injection rate. There is significant uncertainty in the fitted values of S_t for these cases, however. One pair of cases with increasing gas injection rate may reflect the high-quality regime, but it is hard to know for sure because foam quality changes substantially along the core due to gas expansion.
9. Data from several new gas-tracer experiments without the benefit of CT can be fit with a wide variety of values of trapped-gas fraction. The reason appears to be that mass transfer between flowing and trapped gas is rapid in these experiments on the time scale of the coreflood. Strategies for minimizing this problem in future studies include use of other tracer gases or shorter cores, though use of shorter cores increases the influence of the entrance region where foam is not at steady state.

TASK 3: FOAM GENERATION

Initial Experiments: Foam Generation as a Jump Between Steady States

In steady gas-liquid flow in homogeneous porous media with surfactant present, there is often observed a critical injection velocity or pressure gradient ∇p^{\min} at which "weak" or "coarse" foam is abruptly converted into "strong foam," with a reduction of one to two orders of magnitude in total mobility: i.e., "foam generation" (Ransohoff and Radke, 1988; Rossen and Gauglitz, 1990; Tanzil *et al.*, 2001; Friedmann *et al.*, 1991; Friedmann *et al.*, 1994; Shi, 1996). Once foam generation is obtained, one can reduce injection rates and maintain strong foam; see Fig. 3.1. In collaboration with colleagues Dr. Phillip Gauglitz at Battelle Pacific Natural Resources and Francois Friedmann of ChevronTexaco, we have extended earlier research on foam generation with extensive data for a variety of porous media, permeabilities, gases (N_2 and CO_2), surfactants, and temperatures. Unlike most previous studies, these experiments were conducted with fixed pressure drop across the core or sandpack, rather than fixed injection rates. As a result, one observes not only the "coarse foam" with low pressure gradient and "strong foam" with high pressure gradient, but an unstable transient regime between them, as illustrated in Fig. 3.2.

Similar experiments were conducted with N_2 and CO_2 , many surfactant formulations and porous media ranging from consolidated cores to high-permeability beadpacks. The results correlating ∇p^{\min} with permeability of the medium are summarized in Fig. 3.3. As shown in Fig. 3.3, in beadpacks and sandpacks, ∇p^{\min} was seen to vary with permeability k as $(1/k)$ over $2\frac{1}{2}$ orders of magnitude in k . The relation between ∇p^{\min} and k is more complex in consolidated media, in part because the relations between permeability, pore-throat size and pore length are more complex. This scaling of ∇p^{\min} with $(1/k)$ implies that foam generation scales with pore-throat radius and with the length of some sort of pore cluster, not the length of the medium.

Finite values of ∇p^{\min} were observed for CO_2 foams (Fig. 3.3). ∇p^{\min} was under 1 psi/ft, however, easily attainable in the field. ∇p^{\min} was a factor of 20 lower with CO_2 than with N_2 foams under similar conditions. Part, but not all, of this difference can be explained by the lower surface tension with dense CO_2 .

The unstable regime at values of $|\nabla p|$ intermediate between coarse and strong foam (Fig. 3.2) is particularly interesting; see Figs. 3.4 and 3.5. This regime manifests its instability in fluctuating flow rates at fixed $|\nabla p|$, and, at least sometimes, in $|\nabla p|$ that is not uniform. Some field applications of foam place limits on injection-well pressure, and therefore limit $|\nabla p|$ in the foam bank. These field applications may be constrained to

operate in this unstable regime. It important to determine how this instability, that appears as fluctuations in time in a 1D experiment, would appear in 3D - for instance, possibly as fluctuating regions in space within a foam bank.

For a given surfactant formulation and porous medium, it appears that there is one continuous surface of $|\nabla p|$ as a function of flow rates of liquid and gas, shown schematically in Fig. 3.6. There is low $|\nabla p|$ with coarse foam. At the onset of foam generation this surface folds over (*cf.* Fig. 3.2) to form an intermediate "transient" regime that is unstable, folding back to form the steady-state strong-foam regime at higher $|\nabla p|$. It is this upper surface that one observes in studies of the low-quality and high-quality steady-state strong-foam regimes (Alvarez *et al.*, 2001; *cf.* Fig. 1.1). The appearance of this folding surface is similar to that observed in "catastrophe theory" for dynamic systems with multiple steady states (Poston and Stewart, 1978).

Detailed results are in Gauglitz *et al.* (2002).

Incorporation of Mechanisms into Population-Balance Simulator: Steady State Behavior

We incorporated insights from our these experiments into a population-balance foam model and analyzed the behavior of this model at steady state. Specifically, we incorporated a foam-generation algorithm where the rate of foam creation increases with increasing pressure gradient into a population-balance model for foam (*cf.* Falls *et al.*, 1988; Friedmann *et al.*, 1991; Kovscek *et al.*, 1997; Bertin *et al.*, 1998; Myers and Radke, 2000).

Model Description

It is not clear exactly how the rate of lamella creation in porous media depends on pressure gradient and other factors. We employ the following simple relationship:

$$r_g = C_g |\nabla p|^m \dots\dots\dots(3.1)$$

where r_g is the rate of lamella creation, $|\nabla p|$ is pressure gradient in Pa/m, and C_g and m are model parameters. For $m > 1$, the rate of lamella creation increases steeply with increasing pressure gradient. Eq. 3.1 incorporates some, but not all, of the implications of the theory of Rossen and Gauglitz (1990). There, lamella creation depends on pressure gradient, but also on water saturation or capillary pressure, which governs the presence of lenses or lamellae present to be mobilized. Also, it is not clear from theory whether or not the rate of lamella creation should level off at high pressure gradient. (As shown below, for fine-textured foams at high $|\nabla p|$ other mechanisms dominate behavior and this issue is not crucial.)

Beyond that, our approach shares many features with previous Population Balance models (Falls *et al.*, 1988; Friedmann *et al.*, 1991; Kovscek *et al.*, 1997; Bertin *et al.*, 1998; Myers and Radke, 2000). Foam coalescence is governed by limiting capillary pressure, P_c^* (Khatib *et al.*, 1988; Rossen and Zhou, 1995). The capillary-pressure function $P_c(S_w)$ implies that there is a water saturation S_w^* corresponding to $S_w(P_c^*)$. No one knows how the rate of coalescence (lamella destruction) should depend on S_w or P_c , as long as it diverges toward infinity as $S_w \rightarrow S_w^*$ or $P_c \rightarrow P_c^*$. Different foam models use different functions to express this divergence (Kovscek *et al.*, 1997; Bertin *et al.*, 1998; Myers and Radke, 2000)). We adopt the following expression:

$$r_c = C_c n_f \left(\frac{1}{S_w - S_w^*} \right)^n \dots\dots\dots (3.2)$$

where r_c is the rate of foam coalescence and n_f number of lamellae in a unit volume. C_c and n are model parameters. Others include also a term for the rate of lamella transport into "termination sites" where they are destroyed (Kovscek *et al.*, 1997; Bertin *et al.*, 1998; Myers and Radke, 2000).

In steady-state flow, the rate of lamella creation is the same as the rate of lamella destruction, i.e., $r_g = r_c$. Equating Eqs. 3.1 and 3.2 gives, for steady state,

$$n_f = \left(\frac{C_g}{C_c} \right) (\nabla p)^m (S_w - S_w^*)^n \dots\dots\dots (3.3)$$

Hirasaki and Lawson (1985) suggest a shear-thinning gas viscosity in the presence of foam:

$$\mu_g^f = \mu_g^o + \frac{C_f n_f}{u_g^{1/3}} \dots\dots\dots (3.4)$$

where μ_g^o is gas viscosity in the absence of foam and C_f is a model parameter. Parameter C_f varies widely among theoretical and experimental studies in tubes, beadpacks and rock (Xu and Rossen, 2003a).

Transport of gas is governed by Darcy's law:

$$u_g = \frac{k k_{rg}^f}{\mu_g^f} \nabla p \dots\dots\dots (3.5)$$

where u_g volumetric flux of gas phase, k permeability, and k_{rg}^f the effective gas relative permeability in the presence of foam.

Eq. 3.5 implies that both gas relative permeability (k_{rg}^f) and gas viscosity (μ_g^f) are affected by the presence of foam. Effective gas relative permeability is reduced by bubble trapping, and theory suggests that gas effective viscosity should include a yield-stress term (Falls *et al.*, 1989). A large fraction of gas phase is trapped during foam flow (Radke and Gillis, 1990; Friedmann *et al.*, 1991; see also task 2 above) and clearly this alters effective gas relative permeability. Separating these two factors is complicated, however, because the yield stress is also the origin of gas trapping. Different Population Balance models treat these effects differently (Falls *et al.*, 1988; Friedmann *et al.*, 1991; Kovscek *et al.*, 1997; Bertin *et al.*, 1998; Myers and Radke, 2000). Some reduce gas mobility with foam by a factor that depends either linearly or nonlinearly on trapped-gas saturation, with the fraction of gas that is trapped either a constant or depending on bubble size or on pressure gradient. Most studies leave the yield stress out of the effective gas viscosity. Judging between these approaches is difficult, because there is no rigorous way to separate effective gas relative permeability and effective gas viscosity in laboratory gas-mobility data (Rossen, 1992).

Because the major focus of this work is foam generation, here we make a simplification:

$$u_g = \frac{k k_{rg}^o}{\mu_g^f} \nabla p \dots\dots\dots (3.6)$$

where k_{rg}^0 is gas relative permeability in the absence of foam and μ_g^f is given by Eq. 3.4. Thus C_f (Eq. 3.4) accounts both for a constant reduction in gas relative permeability with foam and for gas effective viscosity with foam.

Transport of liquid is governed by Darcy's law as well:

$$u_w = \frac{kk_{rw}(S_w)}{\mu_w} \nabla p \dots\dots\dots(3.7)$$

where u_w the volumetric flux (superficial velocity) of the liquid phase, $k_{rw}(S_w)$ the liquid-phase relative-permeability function, which is unaffected by foam (Bernard, *et al.*, 1965; Sanchez and Schechter, 1989; de Vries and Wit, 1990; Friedmann *et al.*, 1991), and μ_w the liquid viscosity, which likewise is unaffected by foam.

Relative-permeability functions for gas and liquid phases in the absence of foam were estimated by curve-fitting data for unconsolidated sandpack (Collins, 1961):

$$k_{rg} = \left(\frac{1 - S_w - S_{gr}}{1 - S_{wc} - S_{gr}} \right)^{2.2868} \dots\dots\dots(3.8)$$

$$k_{rw} = 0.7888 \left(\frac{1 - S_w - S_{wc}}{1 - S_{wc} - S_{gr}} \right)^{1.9575} \dots\dots\dots(3.9)$$

These relative-permeability functions are applied throughout this study. Fit to sandpack data, we estimate $S_{wc} = 0.04$ and $S_{gr} = 0$.

This model has five adjustable parameters (C_g , m , C_c , n , and C_f): two for lamella creation, two for lamella destruction, and one for effective gas mobility as a function of bubble size. With this simple model, we explore whether or not a foam model based on lamella creation triggered by pressure gradient can fit experimental data, what this model predicts, how predictions compare with existing knowledge on foam flow, and implications for modeling foam applications.

Results of Steady-State Analysis

Initially, we analyzed the model only for its steady-state behavior. Simulations of dynamic foam displacements using this model are reported below. The model is not yet predictive or complete. Some of its simplifications and shortcomings are described by Kam and Rossen (2003). In addition, it shares with all population-balance models the inherent ambiguity arising from the inability to distinguish effective gas relative permeability and gas viscosity, or separately measure lamella creation and lamella destruction rates, in porous media. Nonetheless, one can draw the following conclusions:

1. A population-balance model incorporating a lamella-creation function that depends on $|\nabla p|$ (Rossen and Gauglitz, 1990) fits the following features observed in foam-generation experiments (Gauglitz *et al.*, 2002):
 - a. There are three flow regimes (Fig. 3.7): a coarse-foam regime at low $|\nabla p|$, in which flow rate increases with increasing $|\nabla p|$; a transient regime at intermediate $|\nabla p|$, in which flow rate decreases with increasing $|\nabla p|$; and a strong-foam regime at high $|\nabla p|$, in which flow rate again increases with increasing $|\nabla p|$.

- b. A qualitative fit to laboratory data is obtained for the three foam regimes in consolidated core and a beadpack (*cf.* Fig. 3.7), in experiments with fixed $|\nabla p|$ and either fixed foam quality or fixed liquid injection rate.
 - c. The predicted minimum gas velocity for foam generation decreases as water fractional flow increases, in agreement with experiments. (The model disagrees with theory in that it predicts that the minimum pressure gradient for foam generation increases as liquid fractional flow increases.)
 - d. Both the minimum gas velocity and minimum pressure gradient for foam generation decrease as the formulation is altered to make the foam more stable, i.e. to give higher $|\nabla p|$ in the strong-foam regime.
 - e. The strong-foam state (Fig. 3.8) comprises a high-quality regime, in which $|\nabla p|$ is independent of gas flow rate, and a low-quality regime, in which $|\nabla p|$ is nearly independent of liquid flow rate (Alvarez *et al.*, 2001). The latter is observed if one imposes a lower limit on bubble size.
2. The details of the lamella-creation function have little effect on the high-quality and low-quality strong-foam regimes, which are controlled by other mechanisms. Therefore, a good model fit to steady-state strong-foam behavior is not itself proof of validity for the lamella-creation algorithm used in a population-balance model.
 3. If pressure gradient is plotted as a function of flow rates of gas and liquid, the model predicts a folding-over of this surface in an catastrophe (Poston and Stewart, 1978), where the transient regime originates (*cf.* Figs. 3.6 and 3.7). With current model parameters, the initial appearance of this feature would appear at extremely dry, high flow rates and would be hard to observe in the laboratory.
 4. The fractional-flow curves predicted by the model are complex, including both multiple-valued functions and isolated loops (Fig. 3.9). Predicting displacements from these curves (*cf.* Zhou and Rossen, 1995; Rossen *et al.*, 1999; Shan and Rossen, 2002) will require refinements in conventional fractional-flow theory. Some of those refinements are addressed below.

Critique of Foam Generation by Roof Snap-Off

At the start of this project, the consensus view among foam researchers was that the origin of foam in porous media is repeated snap-off by a process, described by Roof, when gas invades a liquid-filled pore throat. It was employed in most population-balance simulators (Kovscek *et al.*, 1997; Bertin *et al.*, 1998; Myers and Radke, 2000). Therefore we analyzed the evidence for this mechanism and published a critique of Roof snap-off as the prime mechanism of foam generation in homogeneous porous media (Rossen, 2003). The evidence that seems to support Roof snap-off as the key mechanism in foam generation is impressive: experimental studies in constricted glass tubes, etched-glass micromodels, and glass beadpacks; theoretical calculations; overall trends in gas mobility with liquid and gas injection rates; and success in simulations based on foam generation by Roof snap-off. A careful review of these individual mechanisms leads to the following conclusions, however:

- a. Studies of snap-off in glass tubes with a single constriction are not representative of porous media, because, in effect, the downstream pore body has infinite volume. Studies in glass micromodels show that at a given pore throat, once the downstream pore body fills with bubbles, Roof snap-off ceases. Moreover, studies in constricted tubes where gas and liquid are injected simultaneously are

- virtually guaranteed to produce snap-off, because virtually any liquid flow rate through the throat in the experiment would be greater than that observed in a corresponding throat in a porous medium.
- b. The most careful study of foam in etched-glass micromodels, that of Chambers and Radke (1990), concludes that Roof snap-off (called "constriction snap-off" there) is not an important mechanism of foam generation once the downstream pore body fills with bubbles.
 - c. The mechanism proposed by which snap-off produces foam generation in beadpacks cannot in fact explain the experimental observations of Ransohoff and Radke (1988), cited as evidence for the role of Roof snap-off in foam generation.
 - d. The theoretical calculations for snap-off rates in pore constrictions based on Roof snap-off (Kovscek and Radke, 1996, 2003) derive from initial or boundary conditions that do not apply in porous media. Without these unphysical initial or boundary conditions, snap-off does not occur in these models.
 - e. The commonly observed trends of gas mobility with injection rates of gas and liquid are better explained as a result of effects of foam coalescence rather than foam generation. Moreover, the trends cited in support of Roof snap-off occur only in the high-quality regime. If steady-state foam mobility were a direct reflection of foam generation by snap-off, then one could not explain the existence of the low-quality regime.
 - f. Similarly, the success of population-balance simulators based on foam generation by Roof snap-off is better explained by their accounting for foam coalescence at the limiting capillary pressure, which controls foam behavior at steady state. The same steady-state behavior is produced by models that do not incorporate snap-off but do incorporate the limiting capillary pressure. Therefore, the steady-state behavior does not uniquely confirm snap-off as the foam-generation mechanism.

Details of these lines of argument, and their implications, are in Rossen (2003).

Foam Displacements With Abrupt Changes in State

Foam generation is a phenomenon in which the flow of gas and liquid in a porous medium undergoes an abrupt change of regime (Fig. 3.1). In conventional experiments with gas and liquid injected simultaneously at fixed rates, the onset of foam generation can change the pressure drop across a core by a factor of tens or hundreds in a matter of minutes. On a field scale, this change is essentially instantaneous, and it would be modeled as an abrupt jump between two possible steady-state regimes. Foam generation then is an abrupt jump from a state of no-foam or coarse foam to a state of strong foam. There is limited evidence of a corresponding jump from strong foam to coarse foam as foam dries out at the limiting capillary pressure.

Furthermore, there is some evidence that the capillary-pressure function $P_c(S_w)$ may differ between these foam regimes. In particular, because in a strong foam some water is occupied in separating the gas bubbles, there is less water to occupy narrow pores; as a result, one would expect that at the same water saturation S_w , $P_c(S_w)$ would be higher in a strong foam than a coarse foam. There is some evidence for this (Khatib *et al.*, 1988; Kibodeaux and Rossen, 1997), but it is not clear how large an effect this would have in consolidated porous media.

In collaboration with Dr. Johannes Bruining of the Technical University of Delft, we investigated the implications of these abrupt changes on SAG foam displacements, i.e. displacements where gas and liquid are injected in alternating slugs. For calculations, we used a hypothetical local-steady-state foam model with two steady-state foam

regimes, "strong foam" and "no foam." This model is illustrated in Fig. 3.10. If there is no foam initially in the core, then the core is in the "no-foam" state. The no-foam regime reaches its limit at $S_w = 0.7$ (water fractional flow $f_w = 0.00999$), at which point no-foam abruptly reverts to strong foam (i.e. foam generation occurs). The strong-foam regime reaches its limit at $S_w = 0.37$ ($f_w = 0.0075$), at which foam abruptly reverts to no foam (i.e. remaining foam collapses abruptly). The strong-foam and no-foam behavior in this model is roughly consistent with that reported by Persoff *et al.* (1991), who found strong-foam behavior down to the limit of that study, $f_w = 0.004$. The jump between regimes is a conjecture added here for illustration. If there were a jump in the foam studied by Persoff *et al.*, it would occur at $f_w < 0.004$, lower than we assume here for illustration.

In addition, for some calculations we assume that when strong foam is present, the $P_c(S_w)$ function is 50% greater than the function that applies to "no-foam," as suggested by some studies. In other cases, the $P_c(S_w)$ function was the same for both states.

Rossen and Bruining (2004) present evidence supporting these conjectures and show the implications for foam displacements using fractional-flow theory and computer simulations. Their conclusions are as follows:

1. A number of experimental and theoretical studies suggest that the fractional-flow function $f_w(S_w)$ for some foam processes is either multi-valued in S_w or else comprises distinct fractional-flow curves for two or more foam regimes, with jumps between them when each regime reaches its limiting condition. Fig. 3.11 shows an example from Kibodeaux and Rossen (1997).
2. If the predicted or measured fractional-flow function includes portions where $(df_w/dS_w) < 0$, as in Fig. 3.11, these portions of the fractional-flow functions do not represent possible homogeneous steady-states and cannot be present within spreading waves with positive velocity. Any region at such a saturation, if present, would spontaneously split into zones of higher and lower saturation. In a displacement, such a fractional-flow function would behave as a system with two distinct fractional-flow functions, as illustrated in Fig. 3.10.
3. In cases with two distinct fractional-flow functions, the solution for a given displacement begins with consideration of the path of saturations that would be present in the traveling wave at the shock: in particular, equal capillary pressure at the jump between regimes. This leads one to identify the portions of the fractional-flow function that apply to the given displacement. Once one identifies the relevant portions of the fractional-flow curve, the standard graphical methods of fractional-flow analysis (Zhou and Rossen, 1995; Rossen *et al.*, 1999; Shan and Rossen, 2004) apply.
4. Differences between capillary-pressure functions for strong foam and coarse foam (or no-foam) are plausible and have experimental support. If such differences exist, they can exert a strong influence on field-scale displacements. For the data of Kibodeaux and Rossen (1997), an additional broad region of constant state is introduced, with much-different mobility control than with no difference in capillary pressures between strong foam and weak foam. It is therefore important to determine experimentally whether capillary pressure in porous media depends on the existence and state of the foam present. Figs. 3.12 and 3.13 show computed results for the model in Fig. 3.10, with and without a difference in $P_c(S_w)$ functions. A broad, low-mobility foam bank is present in one case that is absent in the other.

5. If one uses coreflood-derived transport properties directly, and foam affects the $P_c(S_w)$ function, accurate conventional finite-difference simulation can require extraordinarily large numbers of grid blocks. In one example, an estimated 5000 grid blocks would be required to give an accurate water saturation in the trapped-foam bank in a conventional finite-difference simulation. However, using the effective fractional-flow and capillary-pressure functions appears to eliminate this problem. Simulations with these upscaled functions gave the correct large-scale behavior, with the correct shocks.

Figs. 3.14 and 3.15 give the corrected graphical construction of the shock based on the data of Kibodeaux *et al.* (1997) assuming (Fig. 3.14) that $P_c(S_w)$ is independent of foam strength, and (Fig. 3.15) that $P_c(S_w)$ is greater for strong foam than coarse foam at the same water saturation. Whether $P_c(S_w)$ depends on foam state makes a huge difference to the upscaling of these coreflood results.

Pore-Level Mechanisms of Foam Generation

Understanding the role of pore-level mechanisms of foam generation in porous media is essential to predicting the success of foam generation at the macroscopic level. The three pore-level events that lead to foam formation are snap-off, leave-behind and lamella division (Ransohoff and Radke, 1988). As bubbles are created by any such mechanism, gas mobility falls and gas saturation increases, causing formation of new lamellae by snap-off and leave-behind as gas drains liquid-saturated pores. On the other hand, lamellae are stranded unless pressure gradient is sufficient to mobilize those that have been created. The initial state of the porous medium as surfactant is introduced (fully saturated with liquid, or already partially drained) also affects the different foam-generation mechanisms. To appreciate the roles of these mechanisms, their interaction at the pore-network level was modeled in a pore-network study that resulted from our continuing collaboration with Prof. Yortsos and Dr. Chen at the University of Southern California (Chen *et al.*, 2005).

Two paradoxes of our earlier modeling of foam generation were resolved by this work. The first paradox was how foam could continue to be generated by mobilization of lamellae and lamella division as lamellae move downstream. If lamellae are mobilized downstream, what replaces those lamellae near the core inlet? Shouldn't foam degrade over time near the core inlet, and that degraded region grow slowly downstream? Second, the model of Rossen and Gauglitz, as updated by Rossen *et al.* (1994), had a singularity at the percolation threshold. The two parts of the model, for continuous-gas and discontinuous-gas flow, diverged from each other at the percolation threshold.

Two-dimensional pore networks with up to 10,000 pores were considered, with rules for the formation and movement of foam lamellae by the three mechanisms enforced throughout. The study shows that strong foam generation by lamella mobilization and division and capillary fluctuations is possible without the necessity of repetitive Roof snap-off, supporting our current efforts at mechanistic modeling of foam generation (Rossen and Gauglitz, 1990; Gauglitz *et al.*, 2002; Kam and Rossen, 2003; Kam *et al.*, 2004). In the process, the study identified a new mechanism of snap-off and foam generation near the inlet of the medium (Fig. 3.16), which explained how lamellae are created there to replace those that are mobilized downstream. This mechanism of snap-off is distinct from Roof snap-off, discussed above. Gas mobility fluctuated significantly with time in the simulations (Fig. 3.17), in agreement with many experimental results. Minimum-pressure-gradient calculations led to results qualitatively similar to the theory of Rossen and Gauglitz (1988), without their questionable

assumption of a uniform $|\nabla p|$ in the pore network (Fig. 3.18), and without a divergence in the theory at the percolation threshold.

Population-Balance Simulator: Modeling Dynamic Displacements

The ultimate goal of studies of foam generation is to predict the process of foam generation using a simulator that can be applied on a field scale. In pursuit of this goal, we collaborated with Dr. Seung Kam, formerly of this research program, now at Adelaide University, Australia, in further development of a population-balance foam simulator (Kam *et al.*, 2004). This work followed up on steady-state analysis of a similar foam model described above (Kam and Rossen, 2003).

In this version of the model, the rate of lamellae creation is represented as follows:

$$r_g = C_g S_w (\nabla p)^m \dots\dots\dots(3.10)$$

where r_g is the rate of lamella creation per unit volume of gas phase, $|\nabla p|$ is the magnitude of pressure gradient, and C_g and m are model parameters. This algorithm differs from that described above (Eq. 3.1) by the factor S_w . The theory of Rossen and Gauglitz (1990) for foam generation implies that lamella creation depends on pressure gradient, but also on water saturation or capillary pressure, which governs the presence of lenses or lamellae available to be mobilized. Specifically, foam generation is easier at higher water saturation, because there are more liquid lenses on the pore network, and these lenses can be mobilized at lower $|\nabla p|$ because of their arrangement on the network.

Beyond that, the model is similar to that described above and used in many population-balance simulators (Falls *et al.*, 1988; Friedmann *et al.*, 1991; Kovsky *et al.*, 1997; Bertin *et al.*, 1998; Myers and Radke, 2000), and in particular to that of Kam and Rossen (2003).

We applied this model in simulating dynamic foam displacements. The results of the work are as follows:

For the first time, a population-balance model is fit to experimental data for both the three foam states (coarse foam, intermediate state, and strong foam) and the two strong-foam regimes (low-quality and high-quality); see Figs. 3.19 and 3.20.

Simulation results confirm the stability of the coarse-foam and strong-foam states to small perturbations, and the instability of the intermediate state. In the intermediate state, a perturbation in foam texture grows with time. See Figs. 3.21 to 3.23.

In modeling dynamic displacements, the population-balance model shows a transition from coarse foam to strong foam as injection rates increase at fixed foam quality, or as liquid fraction of injected fluids increases at fixed gas injection rate, in agreement with previous laboratory studies (Rossen and Gauglitz, 1990). Co-injection of gas and liquid at low injection rate results in coarse foam (Fig. 3.24), as expected from steady-state analysis of the model equations (Kam and Rossen, 2003). There is a peak in foam texture, at the leading edge of the gas bank, that degrades into steady-state coarse foam behind the front. As injection rate increases (Figs. 3.25 and 3.26) the peak in foam texture at the front rises higher. In a separate simulation (not shown) for a injection at 5.79 times the original injection rate in a pack twice as long (2 ft instead of 1 ft), strong foam results before the gas bank reaches the outlet. This injection rate is only a little lower than that predicted by steady-state analysis (6.03 times the injection rate in Fig. 3.24). For injection at 6.27 times the original injection pressure, strong foam is created at the inlet of the medium (Fig. 3.27).

In steady co-injection of gas and surfactant solution, if a bank of low-quality-regime strong foam forms, the kinetics of foam generation and destruction affect the length of the entrance region in which foam forms (Fig. 3.28). Thus the length of the entrance region can be used to calibrate the kinetic parameters in the model. The displacement front is practically unaffected by the magnitude of the kinetic parameters, though. The displacement front, and the bank behind it, are essentially what one would have predicted from local-steady-state principles, if one knows which steady state obtains in the foam bank. Local-steady-state modeling would fit the displacement on the large scale.

When coarse foams are created, there is a narrow region of finer foam (smaller bubbles, larger n_f) predicted near the gas injection front (Figs. 3.24 to 3.26). This phenomenon has two important implications. First, it is possible that this transient peak in texture near the displacement front can perturb the system from one state to another, i.e. trigger "foam generation." These dynamics did not greatly alter the threshold injection rate for foam generation in this study, however. Second, gas viscosity varies within the displacement front, and this affects the change in water saturation across the front. Fronts can be sharper than estimated from fractional-flow theory assuming a constant gas viscosity at the steady-state value behind the displacement front.

The model described here is not yet predictive, and the parameter set fit to the data is not necessarily unique. Moreover, we had difficulty simulating displacements in the high-quality strong-foam regime, evidently because of numerical instabilities. Development of this simulator is not yet complete.

Further Experiments in Sandpacks

We continued our experiments examining foam generation with limited pressure gradient with a new student, following up on earlier research showing a minimum pressure gradient for foam generation and an unstable regime at intermediate pressure gradients (Gauglitz *et al.*, 2002; Kam and Rossen, 2002). A schematic of the apparatus, similar to one in Gauglitz *et al.* (2002), is shown in Fig. 3.29.

Our experiments were conducted in sandpacks, for the following reasons. The same trends in foam behavior are observed in sandpacks as in consolidated core, but at lower pressure gradient (Khatib *et al.*, 1988; Alvarez *et al.*, 2001; Gauglitz *et al.*, 2002). It is much more convenient to work in sandpacks than consolidated core, because at low pressure drop in a sandpack one does not need to apply back-pressure. Fluctuations in back-pressure are hard to eliminate completely, and they can introduce transient false pressure gradients into the apparatus, which can in turn trigger foam generation. The lack of elevated back-pressure does mean that gas compression can affect gas flow rate near the inlet at high pressure drops across the core. Gas flow rates are measured (though not directly controlled) by a Brooks Instruments Co. mass flow controller (Fig. 3.29). Pressure drop across the core is set by a conventional pressure regulator in the gas line. All experiments reported below were conducted with Bio-Terge AS-40 surfactant, except where noted.

Two Foam States

Following the approach of Gauglitz *et al.* (2002), we first conducted experiments with fixed liquid injection rate and fixed pressure drop across the core. In these experiments, the sandpack is initially saturated with brine. Then gas and brine are injected until steady state is achieved. Surfactant solution and gas are then injected at the same rates as brine and gas, for a sufficient period for surfactant solution to replace the

brine in the sandpack at a pressure gradient too low to create foam. Then pressure drop on the gas line is raised in a series of steps, while holding liquid injection rate fixed.

Fig. 3.29 shows a typical result, with 1 wt% surfactant in a 45.5 darcy sandpack, with a fixed liquid interstitial velocity of 1.75 ft/day and with pressure drop Δp across the core fixed at a series of steps of increasing Δp . At very low $|\nabla p|$ (point "a" in Fig. 3.29), gas flows freely with high mobility. This is the "coarse foam" state. At some point, however, an increase in pressure gradient leads to a decrease in gas interstitial velocity. If injection rates were fixed rather than pressure drop, one would observe foam generation at a gas interstitial velocity of about 70 ft/day, with a corresponding jump upward in $|\nabla p|$ to about 10 psi/ft. With fixed pressure gradient, though, the onset of foam generation is indicated by a decrease in gas flow rate rather than a marked increase in $|\nabla p|$.

Gas flow rate continues to decrease until the sandpack is nearly plugged to gas flow at a pressure gradient of about 1 psi/ft. Near points "b" and "c" in Fig. 3.29, gas flow rates fluctuate, suggesting that this intermediate state is inherently unstable. At a pressure gradient above 8 psi/ft, gas flow rate starts to increase to significant values again. This is the "strong foam" state. The "high-quality" and "low-quality" regimes discussed above are both portions of the strong-foam state. In the strong foam state, gas flow rate is again steady, suggesting that this is a stable steady state.

Fig. 3.30 shows the same foam formulation in the same sandpack, but with a higher liquid superficial velocity, 6.98 ft/day. Both the gas velocity and the pressure gradient are lower at the onset of foam generation than with the lower liquid injection rate. This is consistent with the model of Rossen and Gauglitz (1990) for foam generation in steady liquid-gas flow. In addition, the pressure gradient with strong foam is higher, as would be expected with a higher liquid injection rate.

In experiments in high-permeability sandpacks, one may not immediately recognize strong foam from the (relatively low) magnitude of the pressure gradient. Therefore it is helpful to plot effective gas relative permeability k_{rg}^{eff} . In this context, "effective gas relative permeability" means gas mobility times the viscosity of gas without foam. In other words, all the mobility reduction of foam is lumped into k_{rg}^{eff} . Fig. 3.31 shows the k_{rg}^{eff} values derived from Figs. 3.29 and 3.30. In the coarse-foam state, k_{rg}^{eff} is about 0.01; then it declines to below 0.0001 in the strong-foam state. At sufficiently high $|\nabla p|$, k_{rg}^{eff} increases again, reflecting shear-thinning rheology of foam and coarsening of foam at the limiting capillary pressure (Khatib *et al.*, 1988). There is no sharp, universal dividing point between strong foam and coarse foam, but typically k_{rg}^{eff} greater than 0.001 would reflect a relatively coarse foam, and k_{rg}^{eff} less than 0.0001 a relatively strong foam.

Figs. 3.32 and 3.33 show a similar comparison of the effect of liquid superficial velocity, in a pack of lower permeability (7.1 darcy). Liquid injection rate in Fig. 3.33 is near that at the higher permeability in Fig. 3.30. Comparison of Figs. 3.30 and 3.33 shows that reducing permeability requires a higher pressure gradient and higher gas velocity for foam generation, in agreement with the theory of Rossen and Gauglitz (1990). Comparing Figs. 3.32 and 3.33 shows again that foam is created at a lower $|\nabla p|$ and lower gas velocity at higher liquid interstitial velocity.

Figs. 3.32, 3.34 and 3.35 show the effect of surfactant concentration on foam generation. At 0.1 wt% surfactant (Fig. 3.24), foam generation requires both higher velocity and higher pressure gradient than at 1 wt% (Fig. 3.32). At 0.01 wt% (Fig. 3.35),

we were not able to go high enough gas rates to create a reasonably strong foam. Fig. 3.36 confirms that gas mobility is not low for any of the data in Fig. 3.35.

Thus, over the range of conditions tested, **foam generation occurs at lower pressure gradient and lower gas velocity at (a) higher liquid injection rates, (b) lower permeability, and (c) higher surfactant concentration.**

We obtained similar experiments with a different surfactant, MA-80I, not shown. This surfactant was used earlier by Gauglitz *et al.* (2002) (see Fig. 3.4 and 3.5) and applied in the field for aquifer remediation. These results also show foam generation at lower gas velocity in higher-permeability media.

Foam Generation in Flow Across Layer Boundaries

Experiments next focused on foam generation in flow across layer boundaries. In all cases sandpacks were prepared with a lower-permeability region upstream, and an abrupt transition to a higher permeability about midway through the sandpack. In all cases, the increase in permeability was by a factor of at least four, which modeling suggests should be sufficient to trigger strong-foam generation (Ransohoff and Radke, 1988; Falls *et al.*, 1988; Rossen, 1999). In all cases the pack is held vertically and fluids are injected from the top of the pack.

Steady-State Experiments in Layered Sandpacks. Fig. 3.37 shows the results with a sandpack of 8.5 darcy upstream and 41.1 downstream, for a jump of 4.8 in permeability at a location within section 2 (out of four) in the pack. Behavior is similar to that in Gauglitz *et al.* (2002) for a homogeneous pack, except that the pack remains nearly plugged at the maximum pressure gradient. Fig. 3.38 shows the sectional pressure drops in this experiment; the lower-case letters in both figures correspond to the same points. In the coarse-foam state (points a and b), most of the pressure drop occurs in the first section of the core, near the inlet. At the transition from coarse foam to the intermediate state (b to c), most of the pressure drop now occurs in section 2, where the transition in permeability is located and foam generation is expected. As in Gauglitz *et al.*, in the intermediate state the flow rate in the core is not constant in time; in particular, when nearly plugged, the core alternates between bursts of flow and plugging. At higher pressure drop (pt. d), some foam evidently has been displaced into the third section, and the total pressure drop is now shared between sections 2 and 3. At still higher pressure drop (not shown), there is significant pressure drop in sections 1, 2 and 3, but not 4. One might conjecture that the core will remain nearly plugged at yet-higher pressure drop until foam has propagated through section 4 and reached the end of the core.

Fig. 3.38 illustrates a difficulty in obtaining results just above the pressure gradient that triggers foam generation in our experiments. The upper-right plot shows the flow rate and total pressure drop across the pack at the transition between points b and c in Fig. 3.37 - i.e., the onset of foam generation. The gas mass-flow controller (Fig. 3.29) does not deliberately control gas injection rate in these experiments: its purpose is merely to measure gas flow into the apparatus. However, the pressure drop across the controller can be significant if gas flow rate is high. Just before the onset of foam generation, gas flow rate through the apparatus often is high, and most of the pressure drop through the apparatus as a whole (set by the pressure regulator upstream) is dissipated in the mass flow controller. At the onset of foam generation, gas flow rate decreases, less pressure drop is dissipated in the mass-flow controller, and more is applied to the sandpack itself. The higher pressure gradient in the pack triggers further foam generation, reducing flow rate, further reducing pressure drop across the controller, and further increasing pressure gradient in the pack. Eventually the system settles down to a steady state of low gas flow

rate, sometimes with a substantial increase in pressure gradient in the pack, upon only a slight change to the pressure regulator upstream. We measure pressure drop across the sandpack itself with a separate transducer, so our data accurately reflect actual pressure drop across the pack and accurately identify the pressure gradient at the onset of foam generation. But it is difficult to get data with this pressure drop just above the value the triggers foam generation.

Fig. 3.39 shows results from a similar experiment, with a lower liquid injection rate. Foam generation is triggered at a lower pressure drop across the core than in Fig. 3.27.

As discussed above, it is hard to interpret pressure-drop data alone in terms of coarse or strong foam; one needs to relate the pressure gradient to mobilities. Fig. 3.40 shows the effective gas relative permeability in both experiments, averaged over the sandpack, and lumping all resistance to gas flow into the relative permeability. Where the core appears to be plugged (pressure gradient greater than 2 psi/ft), the gas mobility is indeed greatly reduced by foam.

Dynamic SAG Displacements in Layered Sandpacks. Next we examined foam generation during gas injection into a beadpack saturated with surfactant solution (a "SAG" displacement). Again, pressure drop was held fixed rather than (gas) injection rate. In this case the permeability contrast within the beadpack was extreme: 1.2 darcy upstream and 97.8 darcy downstream. In this case there were five sections to the beadpack, and the transition in permeability was in section 3.

Fig. 3.41 shows the results for a pressure drop of 8.5 psi. and 0.1 wt% surfactant concentration. Behavior is complex. At the start, all pressure drop is in section 1, but this pressure drop falls rapidly as pressure drop rises in section 2. Pressure drop falls in section 2 as it rises in section 3. Foam generation evidently occurs in section 2, as gas flow rate Q_g reaches a minimum, but soon most of the resistance to flow in the pack is in section 3. Gas flow rate rises slowly in time. The foam evidently does not propagate to section 4, which never shows a significant pressure drop.

Fig. 3.42 shows similar results for an experiment with a lower pressure drop, 4 psi, across the beadpack. Results are qualitatively similar to Fig. 3.41. Fig. 3.43 shows a case similar to Fig. 3.41 but with 1 wt % surfactant rather than 0.1 wt %. Again, the results are qualitatively similar.

Behavior appears to be shaped by whether or not foam is convected forward or remains trapped in the given core section.

Layered-Pack Experiments: Effect of Surfactant Concentration. Fig. 3.44 shows results similar to those above for steady co-injection of liquid at fixed rate and gas at fixed pressure, with 1 wt% surfactant in the aqueous phase. The sandpack has 8.5 darcy upstream and 41.1 downstream, for a jump by a factor of 4.8 in permeability at a location within section 2 (out of four sections) in the pack. In this plot, region (a) is the coarse-foam region, point (b) the onset of foam generation, and point (c) the onset of a state of nearly complete plugging of the core (d). Behavior is similar to that in Gauglitz *et al.* (2002) for a homogeneous pack, except that the pack remains nearly plugged at the maximum pressure gradient; the strong-foam state is not observed. We note above that, based on sectional pressure drops, as pressure drop across the pack Δp increased, foam appeared to be mobilized and move downstream from section 2, where the permeability transition was located, to section 3, but not to section 4 in the range of Δp attempted in this experiment.

Fig. 3.45 shows the effective gas relative permeability, averaged over the sandpack, and lumping all resistance to gas flow into the relative permeability, in both this experiment and one at lower liquid injection rate for which the results were similar. Where the core appears to be plugged (pressure gradient greater than 2 psi/ft), the gas mobility is indeed greatly reduced by foam.

Figs. 3.46 and 3.47 show results for an experiment with the same liquid injection rate but 10x lower surfactant concentration, i.e. 0.1 wt% surfactant. In this case the layers have permeabilities 11.3 and 48.5 darcy upstream and downstream of the transition, respectively. It takes a somewhat higher gas velocity to trigger foam generation, but the pattern is the same as in Figs. 3.44 and 3.45. It is difficult to distinguish any difference in the pressure drop required to trigger foam generation at this lower surfactant concentration.

Figs. 3.48 and 3.49 show the results with 0.01 wt% surfactant. In this case there is little evidence of foam at any pressure drop, even with liquid injection rate markedly higher than in previous cases.

There is no strong effect of surfactant concentration down to 0.1 wt%, but a failure to create foam at 0.01 wt% surfactant concentration, even with high liquid injection rate and a sharp change in permeability in the pack.

Enhanced Foam Generation: Pulsed-Pressure and Alternate-Slug Injection

Theory and experiments indicate that in homogeneous porous media foam generation is triggered primarily by pressure gradient (Rossen and Gauglitz, 1990; Gauglitz *et al.*, 2002; Tanzil, 2001; Tanzil *et al.*, 2002; Kam and Rossen, 2003). Next we investigated whether lasting foam generation could be triggered by a ***temporary increase in pressure gradient in homogeneous sandpacks***. In all cases here surfactant concentration is 1 wt%. For comparison, Fig. 3.50 shows how gas interstitial velocity responds to pressure gradient in a homogeneous 18.6-d sandpack, with liquid superficial velocity fixed at 7.61 ft/d. Note that gas is plugged when a steady pressure gradient of about 1.5 psi/ft is imposed on the pack.

Figs. 3.51 and 3.52 illustrate an experiment where pressure gradients of 1.5 psi/ft were imposed repeatedly for brief periods. There is ***almost no change in the triggering of foam generation in this case***.

Figs. 3.53 and 3.54 show a different strategy, one of ***alternating liquid and gas injection without increasing pressure gradient***. One way to be sure of accomplishing this is to shut off injection of one phase while holding the other injection rate or pressure constant. In this case, gas injection was stopped twice in the coarse-foam state, in the hopes of triggering foam generation when gas injection resumed, as suggested by Gauglitz and Rossen (1990). Further, once foam formed and nearly plugged the pack, liquid injection was stopped twice to see if gas could be remobilized.

Foam generation is triggered at a much lower gas velocity, and also at a lower pressure gradient, than with steady co-injection of gas and liquid (Fig. 3.48). Stopping liquid injection hardly affected behavior in the state of foam plugging, however. Once gas is plugged, there is almost no difference in gas effective relative permeability between the case with no interruption in liquid injection (Fig. 3.50) and with liquid injection stopped for long periods (Fig. 3.52).

Next we considered the effects of ***pulsed-pressure injection in layered sandpacks***. As in previous experiments with layered packs, sandpacks were prepared with a lower-permeability region upstream, and an abrupt transition to a higher permeability in this case about 2/3 through the pack. The increase in permeability was by

a factor of at least four. In all cases the pack was held vertically and fluids were injected from the top of the pack.

As in previous experiments, we fixed liquid injection rate and pressure drop across the pack, and followed the following procedure: The sandpack is initially saturated with brine. Then gas and brine are injected until steady state is achieved. Surfactant solution and gas are then injected at the same rates as brine and gas, for a sufficient period for surfactant solution to replace the brine in the sandpack at a pressure gradient too low to create foam. Then pressure drop on the gas line is raised in a series of steps, while holding liquid injection rate fixed.

Fig. 3.55 shows the results with a sandpack with permeability 17.1 darcy upstream and 87.3 downstream, for a jump by a factor of 5.1 in permeability, at a location within section 2 (out of four) in the pack, with 0.1 wt% surfactant solution. One curve shows the result with experimental procedure described above ("conventional"). From the pulsed-pressure experiment, we raised pressure drop across the pack to 2 psi for about 6 minutes, gas flow decreases quickly until foam blocks the pack. After foam generation, both experiments match very well in intermediate and strong foam states. The only difference is that ***foam is triggered more easily in the pulsed-pressure experiment in this layered pack***. The effect of pulsed pressure is much stronger in heterogeneous porous media than in homogeneous media. Fig. 3.56 shows the effective gas relative permeability, averaged over the sandpack, and lumping all resistance to gas flow into the relative permeability. In both experiments, the gas mobility is greatly reduced by foam.

Fig. 3.57 shows the sectional pressure drops in the pulsed-pressure experiment. Gas flow rate increases quickly when 2 psi pressure is imposed for a time; then the gas flow rate falls quickly to almost zero. Near the end of the experiment, just after liquid injection was terminated, gas mobility increased greatly. The possible reasons are: (a) slow drying of the core, a rise in P_c , and foam collapse ((Khatib *et al.*, 1988); (b) slow drying of the core and a rise in P_c at the transition in permeability, causing foam generation there to cease (Rossen, 1999). Fig. 3.57 shows a big decrease in pressure drop in last two sections, and a slight decrease in section 2, where the boundary is located. The pressure drop in the first section is not much affected by the changes in the other sections.

These experiments were hampered by the experimental problem noted in connection with Fig. 3.38 above: it was difficult to obtain a steady state with lower pressure drop across the sandpack once strong foam had been triggered by the brief period of higher pressure drop. Strong foam reduced gas flow rate, which reduced gas pressure drop through the mass-flow controller, which increased pressure drop across the pack. However, it is clear that foam generation was triggered by the temporary rise in pressure gradient with the layered packs, in contrast to the homogeneous packs, in spite of the difficulty of settling back to a steady state of low pressure gradient.

We obtained substantially the same results with 1 wt% surfactant, shown in Figs. 3.58-3.60.

Figs. 3.61 to 3.64 illustrate an alternate strategy for enhancing foam generation: ***pre-saturating the sandpack with surfactant solution before injecting any gas***. Fig. 3.61 shows that ***at the lowest attainable values of pressure drop the gas flow rate is still virtually zero*** (note change of scale with previous figures). This experiment differs from the SAG experiments in that surfactant injection continues when gas injection begins. Fig. 3.62 shows the relative permeabilities in this experiment, which are extraordinarily low at all pressure drops examined. Fig. 3.63 shows that once strong foam is created, shutting off liquid injection for periods as long as 30 min. has little or no effect on gas

mobility. Of course, with gas flow rate so low, the sandpack does not dry out much during this period of liquid shut-in. One would expect that gas mobility would rise eventually if liquid injection were shut off indefinitely.

Conclusions from Task 3: Foam Generation

1. When this project began, the consensus view in foam research was that foam is created by Roof snap-off, governed liquid and gas velocities and the geometry of pore throats and pore bodies. A careful review of these individual studies cited in support of this mechanism shows that there is no substantial support for this mechanism for steady-state foam generation in homogenous porous media.
2. Experiments with N₂ and CO₂ foam in a variety of porous media show that there is a minimum pressure gradient ∇p^{\min} required to trigger foam generation in steady flow through homogeneous porous media. In beadpacks and sandpacks, ∇p^{\min} was seen to vary with permeability k as $(1/k)$ over 2½ orders of magnitude in k . The relation between ∇p^{\min} and k is more complex in consolidated media, in part because the relations between permeability, pore-throat size and pore length are more complex. ∇p^{\min} was a factor of 20 lower with CO₂ than with N₂ foams under similar conditions. Part, but not all, of this difference can be explained by the lower surface tension with dense CO₂.
3. If pressure gradient is fixed rather than injection rates, one observes an unstable state between coarse foam (or no foam) and strong foam. This state manifests its instability in fluctuating flow rates at fixed $|\nabla p|$, and, at least sometimes, in $|\nabla p|$ that is not uniform. This state may have practical importance in field applications with limits on injection pressure.
4. For a given surfactant formulation and porous medium, it appears that there is one continuous surface of $|\nabla p|$ as a function of superficial velocities of liquid and gas, shown schematically in Fig. 3.6. There is low $|\nabla p|$ with coarse foam. At the onset of foam generation this surface folds over to form an intermediate "transient" state that is unstable, folding back to form the steady-state strong-foam state at higher $|\nabla p|$. It is this upper surface that one observes in studies of the low-quality and high-quality steady-state strong-foam regimes (Alvarez *et al.*, 2001; *cf.* Fig. 1.1). The appearance of this folding surface is similar to that observed in "catastrophe theory" for dynamic systems with multiple steady states.
5. A population-balance model incorporating a lamella-creation function that depends on $|\nabla p|$ fits numerous features observed in foam-generation experiments: in particular, the three foam states referred to above, the two steady-state strong-foam regimes, and trends of foam generation with injection rates. This model indicates that the details of the lamella-creation function have little effect on the high-quality and low-quality strong-foam regimes, if strong foam is formed. Lamella creation (foam generation) is of course crucial to the question of whether strong foam is formed under given conditions.
6. The population-balance foam simulator, applied to dynamic foam displacements, confirms the stability of the coarse- and strong-foam states and the instability of the intermediate state. The model predicts a transition from coarse foam to strong foam as injection rates increase, in agreement with experiments. The model predicts that whether strong foam is ultimately created may depend on the transient growth of a zone of finer foam near the leading edge of the gas bank. Most of the model parameters can be fit to steady-state data; the remaining kinetic

- parameters can be fit to the length of the region near the core inlet in which foam is created.
7. Fractional-flow models can be modified to account for sudden changes in properties such as foam generation and foam collapse. After one accounts for the nature of the traveling wave at shock fronts one can apply the conventional methods of fractional-flow theory to such a displacement. Numerical simulations may encounter severe difficulties in accurately modeling the displacements with feasible numbers of grid block unless transport functions are properly upscaled. If foam collapses suddenly at a limiting capillary pressure, accurate prediction of foam behavior in the field depends on knowing whether capillary pressure changes at the moment of foam collapse.
 8. A pore-network model for foam generation resolves two paradoxes troubling our finding that foam is created by mobilization and division of lamellae by pressure gradient. First, the network model shows how new lamellae are created near the inlet of the porous medium to replace those mobilized and transported downstream. Second, the model reconciles the two halves of the theory of Rossen and Gauglitz (1990) at the percolation threshold.
 9. A series of experiments in sandpacks found several effective ways of enhancing foam generation. We conducted experiments in sandpacks to avoid the need for a back-pressure regulator, which can introduce spurious pressure fluctuations and mar experimental results. Other studies indicate that the same trends in foam behavior are observed in sandpacks as in consolidated core, but at lower pressure gradient.
 - a. In homogeneous sandpacks, foam generation occurs at lower pressure gradient and lower gas velocity at (a) higher liquid injection rates, (b) lower permeability, and (c) higher surfactant concentration.
 - b. Creation of strong foam was not always observed when predicted by theory in flow across sharp change in permeability, but foam generation did occur more easily in such cases than in homogeneous sandpacks. There was no strong effect of surfactant concentration down to 0.1 wt%, but a complete failure to create foam at 0.01 wt% surfactant concentration.
 - c. Fixed-pressure SAG displacements in layered packs were complex. Sometimes foam was mobilized downstream of the transition in permeability and sometimes not.
 - d. Temporarily increasing pressure gradient did not facilitate foam generation in homogeneous sandpacks, but did trigger lasting foam generation in layered packs.
 - e. When gas was injected following a slug of liquid, or into a pack pre-saturated with liquid, foam generation occurred at a lower pressure gradient than with steady co-injection of liquid and gas.

CONCLUSIONS

Task 1 - Interactions Between Foam and Polymer

1. For the polymers (xanthan and partially hydrolyzed polyacrylamide), oils (decane and 37.5° API crude oil), and surfactant (Bio-Terge AS-40, an alpha-olefin sulfonate) tested here, it appears from coreflood pressure gradient $|\nabla p|$ that

- polymer *destabilizes* foam somewhat, raising water saturation S_w and water relative permeability k_{rw} (Eq. 1.1). Any increase in pressure gradient $|\nabla p|$ observed results from the increased viscosity of the aqueous phase. In all cases examined, this increase is less than predicted from the increase in the viscosity of the aqueous phase alone.
2. For the same polymers and surfactant, polymer does not stabilize foam in the presence of decane or 37.5° API crude oil.
 3. Complex behavior, in contradiction to the expected two steady-state strong-foam regimes, was sometimes observed. At the limit of, or in the place of, the high-quality regime, there was sometimes an abrupt jump upwards in $|\nabla p|$ as though from hysteresis and a change of state. In the low-quality regime, $|\nabla p|$ was not independent of liquid superficial velocity, but *decreased* with increasing liquid superficial velocity. This curious behavior in the low-quality regime was also found in studies of CO₂ foam; an explanation is offered in the section on Task 2, below.
 4. Theory predicts that polymer should make the flow of foam more shear-thinning than without polymer. In the high-quality regime, where pressure gradient is controlled by water transport at fixed water saturation (Eq. 1.1), the shear-thinning nature of the aqueous polymer solution would make flow shear-thinning. In the low-quality regime, where rheology depends on the resistance to movement of gas bubbles, flow is predicted to be more shear-thinning because of the presence of polymer (Figs. 1.24 and 1.25). This is in addition to the shear-thinning effective viscosity of foam without polymer (Hirasaki and Lawson, 1985) and any relative-permeability effects of gas trapping and mobilization.

Task 2 - Gas Trapping

1. A new model for gas trapping has been incorporated into a foam simulator. In this model, trapped-gas saturation is a function of pressure gradient, fit to data for liquid relative permeability following foam injection and the gas relative-permeability curve. This model can fit steady-state data for the two strong-foam flow regimes and in limited trials it also fits the transition period between foam injection and injection of liquid following foam. The simulator would be most helpful in modeling liquid injectivity in SAG foam processes.
2. Coreflood experiments have measured the average liquid saturation in a core during liquid injection following foam. Liquid saturation rose more upon liquid injection than had been previously thought. In this study the liquid relative-permeability function that applied to foam flow was also reasonably accurate during post-foam liquid injection. However, data implied that liquid does not uniformly sweep the core, but only contacts a portion of trapped gas.
3. Further CT studies of liquid injection after foam confirm that liquid fingers through foam rather than displacing it. This casts doubt on the ability of simulators to scale-up laboratory data unless applied in 2D or 3D on a scale fine enough to resolve the fingers. Because of this fingering, surfactant-free brine injected after foam does not displace the surfactant solution initially present or destroy foam as rapidly as predicted in 1D models.
4. A bundle-of-tubes model that accounts for foam yield stress and gas trapping can account for the anomalous behavior in the low-quality regime seen some experiments in Task 1 and other experiments with CO₂ foam. Pressure gradient

- can decrease upon increasing liquid superficial velocity in the low-quality regime because the drag on bubbles decreases as the liquid film between the bubble and the pore wall thickens. A pressure gradient that does not decrease with increasing liquid injection rate may reflect sensitivity of gas trapping to pressure gradient.
5. The yield stress of foam is the origin of gas trapping and relative-permeability effects with foam. Three-dimensional modeling, extending inconclusive work in 2D, confirms that there is an effective yield stress for trains of lamellae moving through porous media.
 6. Direct CT imaging of gas-phase tracer concentration *in situ* during corefloods shows that the 1D model used to infer trapped- and flowing-gas fractions from gas tracer effluent data have several shortcomings:
 - Tracer concentration is not uniform within either the flowing or the trapped gas at each axial position along the core.
 - A significant amount of tracer diffuses into the core from the injection endplate during the time scale of these experiments.
 - Foam flow fluctuates over relatively long time and length scales in some cases.
 - 1D models cannot distinguish changes in the spatial distribution of gas flow paths that are evident from CT imaging.

In the cases examined, flowing-gas fractions inferred from the 1D model can vary by as much as a factor of 2 among reasonable fits to the data.
 7. In spite of the uncertainty in individual estimates of trapped-gas fraction, some trends are evident in our data. The trapped-gas fraction S_t obtained from the 1D model fit to the five experiments shown here decreases with increasing gas injection rate; it may increase weakly with increasing liquid injection rate. It is hard to distinguish effects of pressure gradient $|\nabla P|$ in our experiments, in part because $|\nabla P|$ is similar in most of the cases, in spite of significant changes in injection rates. This suggests that our experimental conditions may have been near the intersection of the low- and high-quality regimes, where increasing gas or liquid injection rates alone leaves $|\nabla p|$ unchanged.
 8. The cases with increasing liquid injection rate appear to reflect the low-quality foam regime. If so, and if the fitted values of S_t are correct, then they contradict the conjecture of Rossen and Wang (1999) that trapped-gas fraction should decrease slightly with increasing liquid injection rate. There is significant uncertainty in the fitted values of S_t for these cases, however. One pair of cases with increasing gas injection rate may reflect the high-quality regime, but it is hard to know for sure because foam quality changes substantially along the core due to gas expansion.
 9. Data from several new gas-tracer experiments without the benefit of CT can be fit with a wide variety of values of trapped-gas fraction. The reason appears to be that mass transfer between flowing and trapped gas is rapid in these experiments on the time scale of the coreflood. Strategies for minimizing this problem in future studies include use of other tracer gases or shorter cores, though use of shorter cores increases the influence of the entrance region where foam is not at steady state.

Task 3 - Foam Generation

1. When this project began, the consensus view in foam research was that foam is created by Roof snap-off, governed liquid and gas velocities and the geometry of pore throats and pore bodies. A careful review of these individual studies cited in support of this mechanism shows that there is no substantial support for this mechanism for steady-state foam generation in homogenous porous media.
2. Experiments with N₂ and CO₂ foam in a variety of porous media show that there is a minimum pressure gradient ∇p^{\min} required to trigger foam generation in steady flow through homogeneous porous media. In beadpacks and sandpacks, ∇p^{\min} was seen to vary with permeability k as $(1/k)$ over 2½ orders of magnitude in k . The relation between ∇p^{\min} and k is more complex in consolidated media, in part because the relations between permeability, pore-throat size and pore length are more complex. ∇p^{\min} was a factor of 20 lower with CO₂ than with N₂ foams under similar conditions. Part, but not all, of this difference can be explained by the lower surface tension with dense CO₂.
3. If pressure gradient is fixed rather than injection rates, one observes an unstable state between coarse foam (or no foam) and strong foam. This state manifests its instability in fluctuating flow rates at fixed $|\nabla p|$, and, at least sometimes, in $|\nabla p|$ that is not uniform. This state may have practical importance in field applications with limits on injection pressure.
4. For a given surfactant formulation and porous medium, it appears that there is one continuous surface of $|\nabla p|$ as a function of superficial velocities of liquid and gas, shown schematically in Fig. 3.6. There is low $|\nabla p|$ with coarse foam. At the onset of foam generation this surface folds over to form an intermediate "transient" state that is unstable, folding back to form the steady-state strong-foam state at higher $|\nabla p|$. It is this upper surface that one observes in studies of the low-quality and high-quality steady-state strong-foam regimes (Alvarez *et al.*, 2001; *cf.* Fig. 1.1). The appearance of this folding surface is similar to that observed in "catastrophe theory" for dynamic systems with multiple steady states.
5. A population-balance model incorporating a lamella-creation function that depends on $|\nabla p|$ fits numerous features observed in foam-generation experiments: in particular, the three foam states referred to above, the two steady-state strong-foam regimes, and trends of foam generation with injection rates. This model indicates that the details of the lamella-creation function have little effect on the high-quality and low-quality strong-foam regimes, if strong foam is formed. Lamella creation (foam generation) is of course crucial to the question of whether strong foam is formed under given conditions.
6. The population-balance foam simulator, applied to dynamic foam displacements, confirms the stability of the coarse- and strong-foam states and the instability of the intermediate state. The model predicts a transition from coarse foam to strong foam as injection rates increase, in agreement with experiments. The model predicts that whether strong foam is ultimately created may depend on the transient growth of a zone of finer foam near the leading edge of the gas bank. Most of the model parameters can be fit to steady-state data; the remaining kinetic parameters can be fit to the length of the region near the core inlet in which foam is created.
7. Fractional-flow models can be modified to account for sudden changes in properties such as foam generation and foam collapse. After one accounts for the nature of the traveling wave at shock fronts one can apply the conventional

- methods of fractional-flow theory to such a displacement. Numerical simulations may encounter severe difficulties in accurately modeling the displacements with feasible numbers of grid block unless transport functions are properly upscaled. If foam collapses suddenly at a limiting capillary pressure, accurate prediction of foam behavior in the field depends on knowing whether capillary pressure changes at the moment of foam collapse.
8. A pore-network model for foam generation resolves two paradoxes troubling our finding that foam is created by mobilization and division of lamellae by pressure gradient. First, the network model shows how new lamellae are created near the inlet of the porous medium to replace those mobilized and transported downstream. Second, the model reconciles the two halves of the theory of Rossen and Gauglitz (1990) at the percolation threshold.
 9. A series of experiments in sandpicks found several effective ways of enhancing foam generation. We conducted experiments in sandpicks to avoid the need for a back-pressure regulator, which can introduce spurious pressure fluctuations and mar experimental results. Other studies indicate that the same trends in foam behavior are observed in sandpicks as in consolidated core, but at lower pressure gradient.
 - a. In homogeneous sandpicks, foam generation occurs at lower pressure gradient and lower gas velocity at (a) higher liquid injection rates, (b) lower permeability, and (c) higher surfactant concentration.
 - b. Creation of strong foam was not always observed when predicted by theory in flow across sharp change in permeability, but foam generation did occur more easily in such cases than in homogeneous sandpicks. There was no strong effect of surfactant concentration down to 0.1 wt%, but a complete failure to create foam at 0.01 wt% surfactant concentration.
 - c. Fixed-pressure SAG displacements in layered packs were complex. Sometimes foam was mobilized downstream of the transition in permeability and sometimes not.
 - d. Temporarily increasing pressure gradient did not facilitate foam generation in homogeneous sandpicks, but did trigger lasting foam generation in layered packs.
 - e. When gas was injected following a slug of liquid, or into a pack pre-saturated with liquid, foam generation occurred at a lower pressure gradient than with steady co-injection of liquid and gas.

ACKNOWLEDGMENTS

In addition to the staff and students at The University of Texas at Austin, this project has benefited from several collaborations with the following individuals at other institutions:

- Prof. Peter Currie and Dr. Pacelli Zitha, Faculty of Civil Engineering and Applied Geosciences, the Technical University of Delft, Delft, The Netherlands
- Prof. Yannis Yortsos and Dr. Min Chen, Department of Chemical Engineering, The University of Southern California
- Dr. Hans Bruining, Faculty of Civil Engineering and Applied Geosciences, the Technical University of Delft, Delft, The Netherlands
- Dr. Seung I. Kam, Australian School of Petroleum, University of Adelaide, Australia
- Dr. Hans van Duijn, Dept of Mathematics and Computer Science, the Technical University of Eindhoven, Eindhoven, The Netherlands
- Prof. Denis Weaire and Dr. Simon Cox, Department of Physics, Trinity College, University of Dublin, Ireland
- Dr. Phillip Gauglitz, Battelle Pacific Northwest National Laboratory, Richland, WA
- Dr. Wayne Frenier and Dr. Stephen Davies, Schlumberger, Inc., Sugar Land, TX

REFERENCES

- Aarra, M. G., Ormehaug, P. A., and Skauge, A., "Foam for GOR Control – Improved Stability by Polymer Additives", paper presented at 9th European IOR Symp., The Hague, The Netherlands, Oct. 20-22, 1997.
- Alvarez, J. M., Rivas, H., and Rossen, W. R.: "A Unified Model for Steady-State Foam Behavior at High and Low Foam Qualities," *SPE J* (Sept. 2001), 325-333.
- Bernard, G. G., Holm, L. W., and Jacobs, W. L.: "Effect of Foam on Trapped Gas Saturation and on Permeability of Porous Media to Water," *SPE J* (1965), 195.
- Bertin, H. J., Quintard, M. Y., and Castanier, L. M.: "Development of a Bubble-Population Correlation for Foam-Flow Modeling in Porous Media," *SPE J* (Dec. 1998), 356-362.
- Bird, R. B., Stewart, W. E., and Lightfoot, E. N.: *Transport Phenomena*, 1st ed., Wiley, New York, 1960.
- Blaker, T., Celius, H.K., Lie, T., Martinsen, H.A., Rasmussen, L. and Vassenden, F.: "Foam for Gas Mobility Control in the Snorre Field: The FAWAG Project," paper SPE 56478 presented at the 1999 SPE Annual Technical Conference and Exhibition, Houston, TX, Oct. 3-6.
- Bretherton, F. P., "The motion of long bubbles in tubes", *J. Fluid Mech.* **10**, 160-188 (1961).
- Cannella, W. J., Huh, C., and Seright, R. S., "Prediction of Xanthan Rheology in Porous Media", SPE 18089, presented at 63rd Annual Tech. Conf. SPE, Houston, TX, Oct. 2-5, 1988.
- Carslaw, H. S., and Jaeger, J. C.: *Conduction of Heat in Solids*, 2nd ed., Clarendon Press, Oxford, 1959.
- Chambers, K. T., and Radke, C. J.: "Capillary Phenomena in Foam Flow Through Porous Media," in *Interfacial Phenomena in Oil Recovery*, N. R. Morrow, (ed.), Marcel Dekker, New York, 1990.
- Chen, M., Yortsos, Y. C., and Rossen, W. R.: "Insights on Foam Generation in Porous Media from Pore-Network Studies," *Colloids Surfaces A: Physicochem Eng. Aspects*, **256** (2-3), 181-189 (2005).
- Cheng, L.: "Simulation Studies of Foam-Acid Diversion," PhD dissertation, Department of Petroleum and Geosystems Engineering, The University of Texas at Austin, 2002.
- Cheng, L., Kam, S. I., Delshad, M., and Rossen, W. R.: "Simulation of Dynamic Foam-Acid Diversion Processes," *SPE J* (Sept. 2002), 316-324.
- Cheng, L., Reme, A. B., Shan, D., Coombe, D. A., and Rossen, W. R., "Simulating Foam Processes at High and Low Foam Qualities," paper SPE 59287 presented at the 2000 SPE/DOE Symposium on Improved Oil Recovery, Tulsa, OK, 3-5 April.
- Collins, R. E.: *Flow of Fluids Through Porous Materials*, Research & Engineering Consultants, Inc., Englewood, CO (1961).
- Chukwueke, V. O., Bouts, M. N., and Van Dijkum, C. E., "Gas Shut-Off Foam Treatment", SPE 39650 presented at SPE/DOE Improved Oil Recovery Symp., Tulsa, OK, Apr. 19-22, 1998.
- Cox, S.J., Neethling, S., Rossen, W.R., Schleifenbaum, W., Schmidt-Wellenburg, P., and Cilliers, J.J., "A Theory of the Effective Yield Stress of Foam in Porous Media: The Motion of a Soap Film Traversing a Three-Dimensional Pore," *Colloids Surfaces A: Physicochem Eng. Aspects* **245**, 143–151 (2004).

- Dalland, M., and Hanssen, J. E., "Enhanced Foams for Efficient Gas Influx Control", SPE 37217 presented at SPE Intern. Symp. Oilfield Chemistry, Houston, TX, 1997.
- De Vries, A. S. and Wit, K.: "Rheology of Gas/Water Foam in the Quality Range Relevant to Steam Foam," *SPE* (May 1990), 185-192.
- Falls, A. H., Hirasaki, G. J., Patzek, T. W., Gauglitz, P. A., Miller, D. D., and Ratulowski, J.: "Development of a Mechanistic Foam Simulator: The Population Balance and Generation by Snap-Off," *SPE* (Aug. 1988) 884-892.
- Falls, A. H., Musters, J. J., and Ratulowski, J.: "The Apparent Viscosity of Foams in Homogeneous Bead Packs," *SPE*. (May. 1989) 155.
- Forsythe, W. E., Smithsonian Physical Tables, 9th ed., Smithsonian Institution, Washington, DC, 1954, p. 644.
- Friedmann, F., Chen, W. H., and Gauglitz, P.A.: "Experimental and Simulation Study of High-Temperature Foam Displacement in Porous Media," *SPE* (Feb. 1991) 37-45.
- Friedmann, F., Hughes, T. L., Smith, M. E., Hild, G. P., Wilson, A., and Davies, S. N., "Development and Testing of a New Foam-Gel Technology to Improve Conformance of the Rangely CO₂ Flood", SPE 38837 presented at SPE Annual Tech. Conf., San Antonio, TX, Oct. 5-8, 1997.
- Friedmann, F., Smith, M. E., Guice, W. R., Gump, J. M., and Nelson, D. G.: "Steam-Foam Mechanistic Field Trial in the Midway-Sunset Field," *SPE* (Nov. 1994), 297-304.
- Gauglitz, P.A., Friedmann, F., Kam, S. I., and Rossen, W.R., "Foam Generation in Homogeneous Porous Media," *Chem. Eng. Sci.* **57**, 4037-4052 (2002).
- Ginley, G. M., and Radke, C. J., "Chapter 26: Influence of Soluble Surfactants on the Flow of Long Bubbles Through a Cylindrical Capillary", in *Oil-Field Chemistry: Enhanced Recovery and Production Stimulation*, J. K. Borchardt, and T. F. Yen, eds., Amer. Chem. Soc. Symp. Ser. 396, 480-501, 1989.
- Hanssen, J. E., and Dalland, M., "Increased Oil Tolerance of Polymer-Enhanced Foams: Deep Chemistry or Just "Simple" Displacement Effects?", SPE 59282 presented at SPE/DOE Improved Oil Recovery Symp., Tulsa, OK, Apr. 3-5, 2000.
- Hirasaki, G.J. and Lawson J.B.: "Mechanisms of Foam Flow in Porous Media: Apparent Viscosity in Smooth Capillaries," *SPE J* (April 1985), 176-190.
- Hughes, T. L., Friedmann, F., Johnson, D., Hild, G. P., Wilson, A., and Davies, S. N., "Large-Volume Foam-Gel Treatments to Improve Conformance of the Rangely CO₂ Flood", SPE 39649 presented at SPE/DOE Improved Oil Recovery Symp., Tulsa, OK, Apr. 19-22, 1998.
- Kam, S. I., Nguyen, Q. P., Li, Q., and Rossen, W. R.: "Dynamic Simulations With an Improved Model for Foam Generation," SPE 90938 presented at the 2004 SPE Annual Technical Conference and Exhibition held in Houston, Texas, U.S.A., 26-29 September.
- Kam, S. I., and Rossen, W. R., "A Model for Foam Generation in Homogeneous Porous Media," *SPE J* (Dec. 2003), 417-425.
- Kamisli, F., and Ryan, M. E., "Perturbation Method in Gas-Assisted Power-Law Fluid Displacement in a Circular Tube and a Rectangular Channel", *Chem. Eng. J.* **75**, 167-176 (1999).
- Khatib, Z.I., Hirasaki, G.J., and Falls, "Effects of Capillary Pressure on Coalescence and Phase Mobilities in Foam Flowing Through Porous Media," *SPE* (Aug. 1988), 919-926.

- Kibodeaux, K. R., and Rossen, W.R.: "Coreflood Study of Surfactant-Alternating-Gas Foam Processes: Implications for Field Design," paper SPE 38318 presented at the 1997 SPE Western Regional Meeting, Long Beach, CA, June 25-27.
- Kibodeaux, K. R., Zeilinger, S. C. and Rossen, W. R., "Sensitivity Study of Foam Diversion Processes for Matrix Acidization," paper SPE 28550, Proc. 1994 SPE Annual Technical Conference and Exhibition, New Orleans, LA, Sept. 26-28, 1994.
- Kim, J. S., Dong, Y., and Rossen, W. R., "Steady-State Flow Behavior of CO₂ Foam," SPE 89351 presented at the 2004 SPE/DOE Symposium on Improved Oil Recovery, Tulsa, OK, 17-21 April; accepted for publication by *SPE J.*
- Kovscek, A. R., Patzek, T. W., and Radke, C. J.: "Mechanistic Foam Flow Simulation in Heterogeneous and Multidimensional Porous Media," *SPE J.* (Dec. 1997), 511-526.
- Kovscek, A. R., and Radke, C. J.: "Gas-bubble Snap-Off Under Pressure-Driven Flow in Constricted Noncircular Capillaries," *Colloids Surfaces A: Physicochem. Eng. Aspects* **117**, 55-76 (1996).
- Kovscek, A. R., and Radke, C. J.: "Pressure-driven capillary snap-off of gas bubbles at low wetting-liquid content," *Colloids Surfaces A: Physicochem. Eng. Aspects* **212**, 99 (2003).
- Kutay, S. M., and Schramm, L. L., "Structure/Performance Relationships for Surfactant and Polymer Stabilized Foams in Porous Media", *J. Canadian Petrol. Tech.*, **43**, 19 (2004).
- Lake, L. W.: *Enhanced Oil Recovery*, Prentice Hall, Upper Saddle River, NJ, 1989.
- Lake, L. W., Bryant, S. L., and Araque-Martinez, A. N.: *Geochemistry and Fluid Flow*, Elsevier, Amsterdam, 2002.
- Luenberger, D. G.: *Introduction to Dynamic Systems. Theory, Models & Applications*. John Wiley and Sons, 1979.
- Mamun, C. K., Rong, J. G., Kam, S. I., Liljestrang, H. M., and Rossen, W. R., "Extending Foam Technology from Improved Oil Recovery to Environmental Remediation", SPE 77557 presented at SPE Annual Tech. Conf., San Antonio, TX, Sept. 29-Oct. 2, 2002.
- Myers, T. J. and Radke, C. J.: "Transient Foam Displacement in the Presence of Residual Oil: Experiment and Simulation Using a Population-Balance Model," *Ind. Eng. Chem. Res.* **39**, 2725-2741 (2000).
- Nguyen, Q. P.: "Dynamics of Foam in Porous Media," PhD dissertation, Technical University of Delft, 2004.
- Nguyen Q.P., Currie, P.K., and Zitha, P.L.J.: "Determination of Foam Induced Fluid Partitioning in Porous Media using X-ray Computed Tomography," paper SPE 80245 presented at the SPE International Symposium on Oilfield Chemistry held in Houston, TX, 2003.
- Nguyen Q.P., Currie, P.K., and Zitha, P.L.J., and Rossen, W.R.: "CT Study of Liquid Diversion with Foam" paper SPE at the 2005 SPE Production and Operations Symposium held in Oklahoma City, OK, 2005.
- Nguyen, Q.P., Zitha, P.L.J., and Currie P. K.: "Film Resistance to Gas Diffusion," *Journal of Colloid and Interface Science* 2002, **248**, 2, 467.
- Park, C. W., "Influence of Soluble Surfactants on the Motion of a Finite Bubble in a Capillary Tube", *Phys. Fluids*, **A 4**, 2335 (1992).

- Persoff, P., Radke, C.J., Pruess, K., Benson, S.M., and Witherspoon, P.A.: "A Laboratory Investigation of Foam Flow in Sandstone at Elevated Pressure," *SPE* (Aug. 1991) 185-192.
- Pope, G. A., Tsaur, K., Schechter, R. S., and Wang, B., "The Effect of Several Polymers on the Phase Behavior of Micellar Fluids", *SPEJ*, 816, Dec. 1982.
- Poston, T. and Stewart, I.: *Catastrophe Theory and Its Applications*, Dover Publications, Inc., Mineola, (1978).
- Radke, C. J., and Gillis, J. V.: "A Dual Gas Tracer Technique for Determining Trapped Gas Saturation During Steady Foam Flow in Porous Media," paper SPE 20519 presented at the 1990 SPE Annual Technical Conference and Exhibition, New Orleans, Sept. 23-26.
- Ransohoff, T. C., and Radke, C. J.: "Mechanisms of Foam Generation in Glass-Bead Packs," *SPE* (May 1988), 573-585.
- Ratulowski, J., and Chang, H.-C., "Transport of Gas Bubbles in Capillaries", *Phys. Fluids A*, **1**, 1642 (1989).
- Ratulowski, J., and Chang, H.-C., "Marangoni Effects of Trace Impurities on the Motion of Long Gas Bubbles in Capillaries", *J. Fluid Mech.*, **210**, 303 (1990).
- Romero, C., Alvarez, J. M., and Muller, A. J.: "Micromodel Studies of Polymer-Enhanced Foam Flow Through Porous Media," paper SPE 75179 presented at the 2002 SPE/DOE Improved Oil Recovery Symposium, Tulsa, OK, April 13-17.
- Rossen, W. R., "A Critical Review of Roof Snap-Off as a Mechanism of Steady-State Foam Generation in Homogeneous Porous Media," *Colloids Surfaces A: Physicochem Eng. Aspects*, **225** 1-24 (2003).
- Rossen, W.R., "Foam Generation at Layer Boundaries in Porous Media," *SPE Journal* (Dec. 1999), 409-412.
- Rossen, W.R., "Foams in Enhanced Oil Recovery," in R. K. Prud'homme and S. Khan, ed., *Foams: Theory, Measurements and Applications*, Marcel Dekker, New York, 1996, pp. 413-464.
- Rossen, W.R.: "Minimum Pressure Gradient for Foam Flow in Porous Media: Effect of Interactions with Stationary Lamellae," *J. Colloid Interface Sci.* **139**, 457-468 (1990d).
- Rossen, W.R.: "Rheology of Foam in Porous Media at the 'Limiting Capillary Pressure'," *Revue de l'Institut Français du Pétrole* **47**, 68-80 (1992).
- Rossen, W.R.: "Theory of Mobilization Pressure Gradient of Flowing Foams in Porous Media. I. Incompressible Foam," *J. Colloid Interface Sci.* **136**, 1-16 (1990a).
- Rossen, W.R.: "Theory of Mobilization Pressure Gradient of Flowing Foams in Porous Media. II. Effect of Compressibility," *J. Colloid Interface Sci.* **136**, 17-37 (1990b).
- Rossen, W.R.: "Theory of Mobilization Pressure Gradient of Flowing Foams in Porous Media. III. Asymmetric Lamella Shapes," *J. Colloid Interface Sci.* **136**, 38-53 (1990c).
- Rossen, W.R.: "Theories of Foam Mobilization Pressure Gradient," SPE 17358, presented at the 1988 SPE/DOE Enhanced Oil Recovery Symposium, Tulsa, OK, April 17-20, 1988.
- Rossen, W. R., and Gauglitz, P. A.: "Percolation Theory of Creation and Mobilization of Foam in Porous Media," *AIChE J.* **36** (1990), 1176-1188.
- Rossen, W.R., Shi, J. and Zeilinger, S.C., "Percolation Modeling of Foam Generation in Porous Media," *AIChE J.* **40**, 1082-1084 (1994).

- Rossen, W.R. and Wang, M.-W., "Modeling Foams for Acid Diversion," *SPE J* (June 1999), 92-100.
- Rossen, W.R., Zeilinger, S.C., Shi, J.-X., and Lim, M. T.: "Simplified Mechanistic Simulation of Foam Processes in Porous Media," *SPE J*, 4, 279-287 (Sept. 1999).
- Rossen, W.R. and Zhou, Z.H.: "Modeling Foam Mobility at the Limiting Capillary Pressure," *SPE Adv. Tech.* **3**, 146 (1995).
- Sabbadin, J., Le Moigne, J., and Francois, J., "Study of the Interaction between Surfactants and Polyacrylamide of Various Hydrolysis Degree", in *Surfactant in Solution*, Vol. 2, K. L. Mittal, and B. Lindman, eds., 1377-1390, Plenum Press, NY, 1984.
- Sanchez, J. M., and Schechter, R. S.: "Surfactant Effects on the Two-Phase Flow of Steam-Water and Nitrogen-Water Through Permeable Media," *J. Petr. Sci. Eng.* **3**, 185 (1989).
- Shan, D. and Rossen, W.R., "Optimal Injection Strategies for Foam IOR," *SPE Journal* **9** (June 2004), 132-150.
- Shi, J.-X.: "Simulation and Experimental Studies of Foam for Enhanced Oil Recovery," PhD dissertation, Department of Petroleum and Geosystems Engineering, The University of Texas at Austin, 1996.
- Shi, J.-X., and Rossen, W.R.: "Simulation of Gravity Override in Foam Processes in Porous Media," *SPEE* (1998), 148.
- Stone, H. L.: "Vertical Conformance in an Alternating Water-Miscible Gas Flood," paper SPE 11140 presented at the SPE Annual Technical Conference and Exhibition, New Orleans, LA, 1982.
- Sydansk, R. D., "Polymer-Enhanced Foam: Laboratory Development and Evaluation", SPE 25168 presented at SPE Intern. Symp. Oilfield Chemistry, New Orleans, LA, Mar. 2-5, 1993a.
- Sydansk, R. D., "Polymer-Enhanced Foam Propagation Through High-Permeability Sandpacks", SPE 25175 presented at SPE Intern. Symp. Oilfield Chemistry, New Orleans, LA, Mar. 2-5, 1993b.
- Tang, G. Q., and Kovscek, A. R.: "Measurement and Theory of Gas Trapping in Porous Media during Steady-State Foam Flow, SPE 90142 presented at the 2004 SPE Annual Technical Conference and Exhibition, Houston, TX, 26-29 September.
- Tanzil, D.: "Foam Generation and Propagation in Heterogeneous Porous Media," Ph.D. dissertation, Department of Chemical Engineering, Rice U., 2001.
- Tanzil, D., Hirasaki, G. J., and Miller, C. A.: "Conditions for Foam Generation in Homogeneous Porous Media," SPE 75176 presented at the 2002 SPE/DOE Symposium on Improved Oil Recovery, Tulsa, OK, 13-17 April.
- Teletzke, G. F., Davis, H. T., and Scriven, L. E., "Wetting Hydrodynamics", *Revue Phys. Appl.*, **23**, 989-1007, 1988.
- Thach, S., Miller, K. C., Lai, Q. J., Sanders, G. S., Styler, J. W., and Lane, R. H., "Matrix Gas Shut-Off in Hydraulically Fractured Wells Using Polymer-Foams", SPE 36616 presented at SPE Annual Tech. Conf., Denver, CO, Oct. 6-9, 1996.
- Rossen, W.R., and van Duijn, C.J.: "Gravity Segregation in Steady-State Horizontal Flow in Homogeneous Reservoirs," *J. Petr. Sci. Eng.* **43**, 99-111 (2004).
- Xu, Q.: "Theoretical and Experimental Study of Foam for Enhanced Oil Recovery and Acid Diversion," PhD dissertation, The University of Texas at Austin, 2003.
- Xu, Q., and Rossen, W. R., "Effective Viscosity of Foam in Periodically Constricted Tubes," *Colloids Surfaces A: Physicochem Eng. Aspects* **216**, 175-194 (2003a).

- Xu, Q., and Rossen, W. R., "Laboratory Study of Gas Trapping in Foam-Acid Diversion," SPE 84133 presented at the 2003 SPE Annual Technical Conference and Exhibition, Denver, CO, 5-8 Oct (2003b).
- Yang, S.H., and Reed, R.L.: "Mobility Control Using CO₂ Forms," paper SPE 19689, presented at the SPE Annual Technical Conference and Exhibition, San Antonio, TX, October 8-11, 1989.
- Zeilinger, S.C., Wang, M., Kibodeaux, K.R. and Rossen, W.R., "Improved Prediction of Foam Diversion in Matrix Acidization," paper SPE 29529, Proc. 1995 SPE Production Operations Symposium, Oklahoma City, OK, April 2-4, 1995.
- Zhou, Z. H., and Rossen, W. R.: "Applying Fractional-Flow Theory to Foam Processes at the 'Limiting Capillary Pressure'," *SPE Adv. Technol.*, **3**, 154 (1995).
- Zitha, P. L. J., Nguyen Q. P. and Currie, P. K., "Effect of Flow Velocity and Rock Layering on Foam Flow: an X-ray Computed Tomography Study," paper SPE 80530 presented at the SPE Asia Pacific Oil and Gas Conference and Exhibition held in Jakarta, Indonesia, 2003.
- Zhu, T., Strycker, A., Raible, C. J., and Vineyard, K., "Foams for Mobility Control and Improved Sweep Efficiency in Gas Flooding", SPE 39680 presented at SPE/DOE Improved Oil Recovery Symp., Tulsa, OK, Apr. 19-22, 1998.

TABLES

Task 1

Table 1.1: Asymptotic Constants for Power-Law Approximation

α	S	T
1.00	0.643	2.68
1.25	0.807	2.93
1.50	0.944	3.14
2.0	1.156	3.50
3.0	1.430	4.01
4.0	1.599	4.36
5.0	1.714	4.63

Table 1.2: Ellis Model Parameters Employed for Fig. 3 (from Cannella *et al.*, 1988)

C_p (ppm)	α	K (cp. sec ^{1/α-1})	μ_n (cp)
300	1.333	17	8.6
600	1.667	43	26.0
1200	2.083	195	102.0
1600	2.857	620	1000.

Task 2

Table 2.1 Pressure gradient and average pressure in tracer experiments w/o CT

case	Uw, ft/d	Ug* ft/d	ave P	Foam	Sectional ave. P (psig)				Sectional P gradient (psi/ft)			
			psi	qual, %	1	2	3	4	1	2	3	4
1	0.35	2.14	801.0	85.9	921.3	871.4	751.2	639.5	24.5	287.2	433.7	473.7
2	0.47	1.5	820.4	76.1	995.6	897.7	747.6	635.8	284.84	444.81	456.06	429.56
3	0.23	0.44	775.1	65.7	863.8	790.5	683.2	630.0	22.76	219.85	321.97	319.19
4	0.47	1.69	732.5	78.2	802.2	759.2	647.7	592.0	69.47	128.85	334.42	334.42

* at average pressure in core

Table 2.2 Experimental program

Injection Foam	Liquid rate (m/d)	Gas rate* (m/d)	Foam quality* (%)
<i>Foam A</i>	0.52	5.19	90.90
<i>Foam B</i>	0.52	10.38	95.24
<i>Foam C</i>	0.52	15.57	96.77
<i>Foam D</i>	1.04	10.38	90.90
<i>Foam E</i>	2.08	10.38	83.33

*at standard conditions (1 bar), i.e. conditions at core outlet

Table 2.3 Section pressure drop			
Foam type	Cross-section pressure (psi)		
	Section 1 (4 cm)	Section 2 (3 cm)	Section 3 (8 cm)
<i>Foam A</i>	11.4	10.1	36.5
<i>Foam B</i>	10.8	18.3	63.7
<i>Foam C</i>	11.7	16.3	57.8
<i>Foam D</i>	14.8	18.9	56.2
<i>Foam E</i>	12.1	20.7	61.5

FIGURES

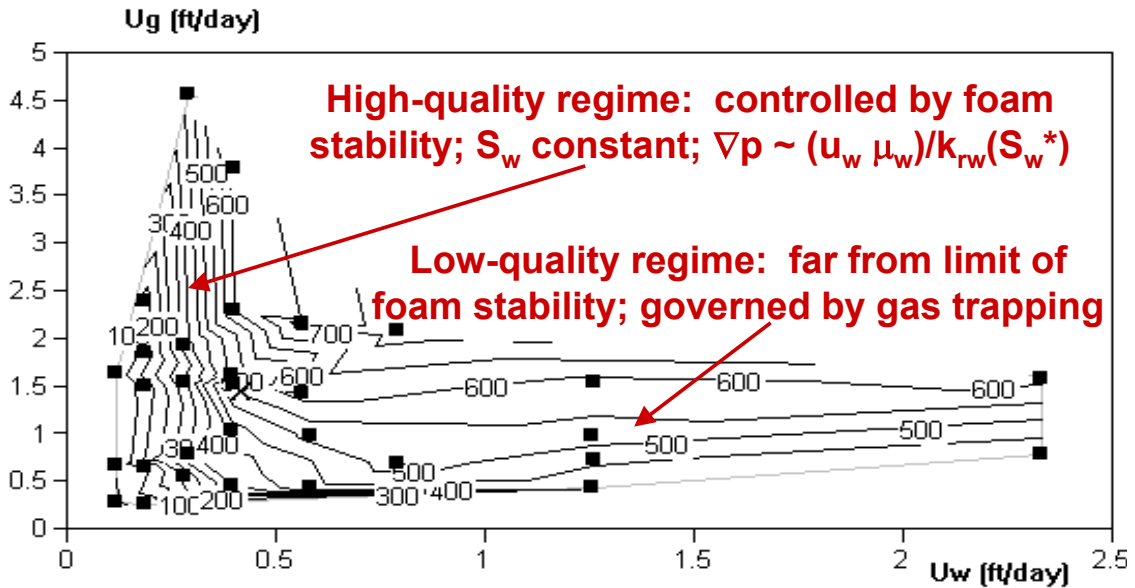


Fig. 1.1. Steady-state pressure gradient as a function of superficial velocities of gas (U_g) and water (U_w) for one N_2 foam formulation in a Berea core, from Alvarez *et al.* (2001), illustrating the two conventional steady-state strong-foam regimes. Dark dots represent individual steady-state data.

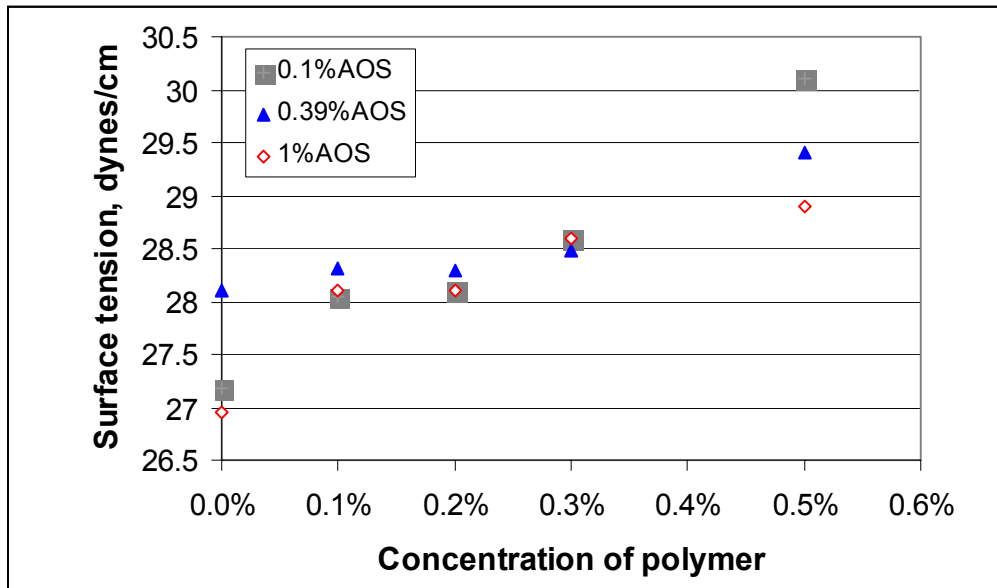


Fig. 1.2. Effect of wt% concentrations of Alcoflood 935 polyacrylamide polymer and Bio-Terge AS-40 surfactant on surface tension at room temperature. No added salt.

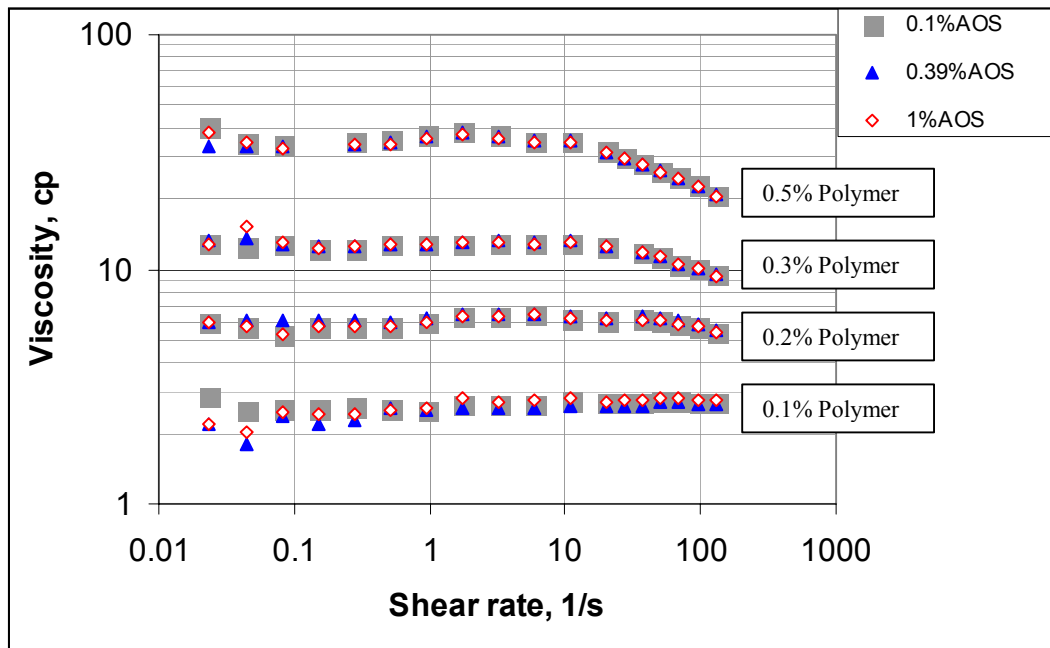


Fig. 1.3. Effects of shear rates and concentrations of polymer and surfactant on viscosity of surfactant and polymer solutions; 1 wt% NaCl in all cases.

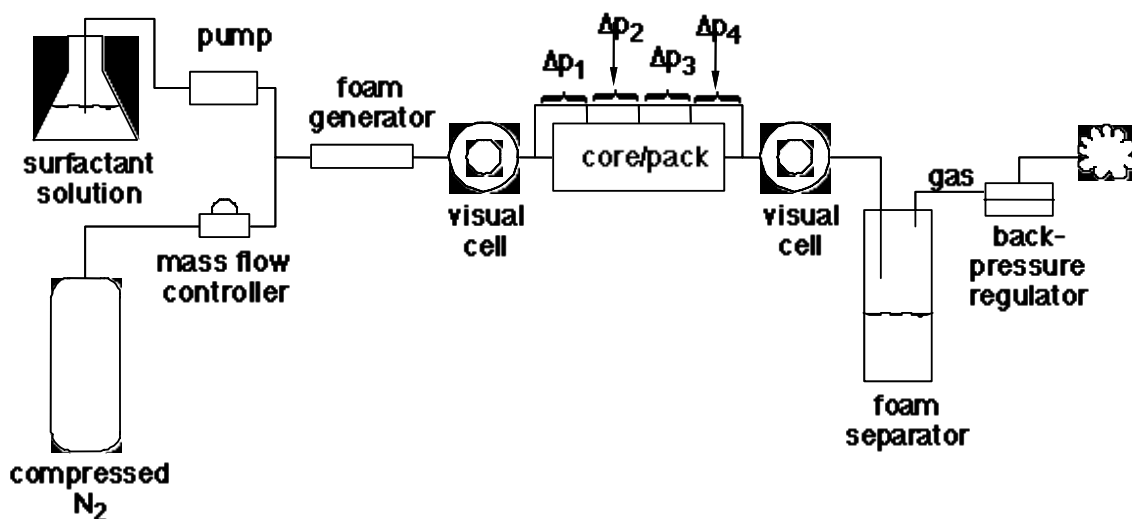


Fig. 1.4. Schematic of experimental coreflood or sandpack apparatus for studying foam in porous media. The general features shown here are reproduced in modified form in all the studies in this report.

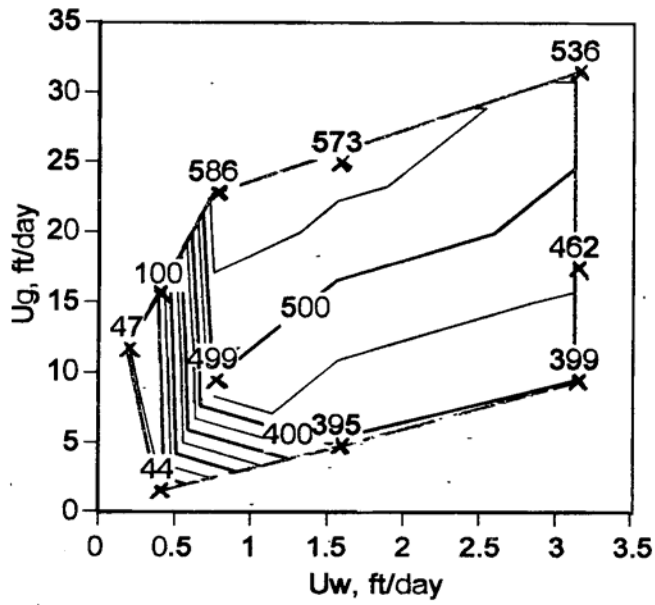


Fig. 1.5. Steady-state pressure gradient as a function of superficial velocities of gas (U_g) and water (U_w) for N_2 foam without polymer or oil in a 6.6-darcy sandpack. X symbols represent individual data, and the numbers above them the measured values of pressure gradient.

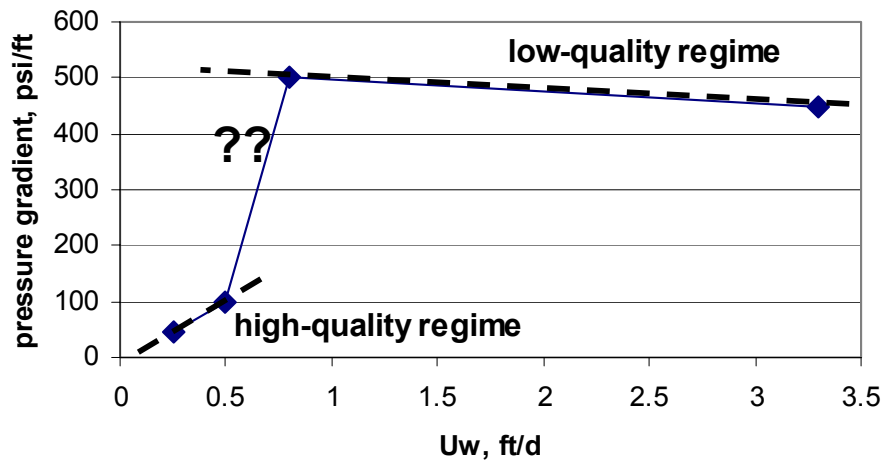


Fig. 1.6. Approximate transect through $|\nabla p|$ data of Fig. 1.5 at $U_g \sim 9$ ft/d, showing apparent abrupt jump between high-quality regime and low-quality regime.

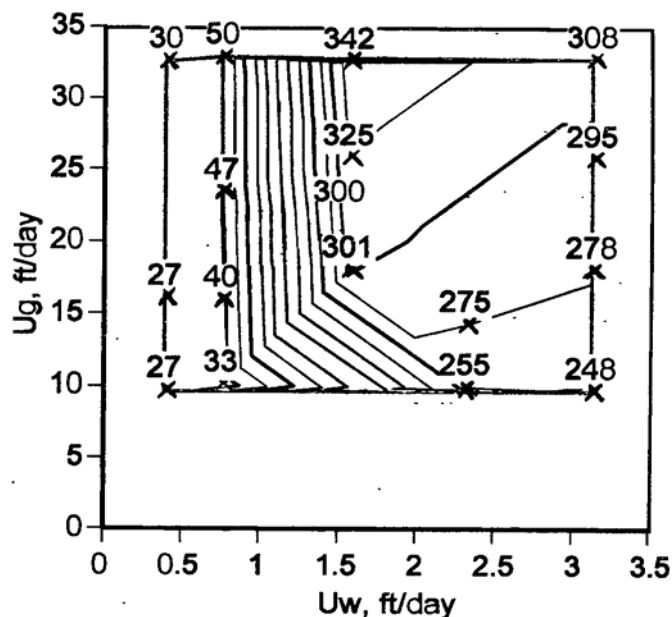


Fig. 1.7. Steady-state pressure gradient as a function of superficial velocities of gas (U_g) and water (U_w) for N_2 foam with 0.1 wt% low-MW polyacrylamide polymer in a 6.6-darcy sandpack. X symbols represent individual data, and the numbers above them the measured values of pressure gradient.

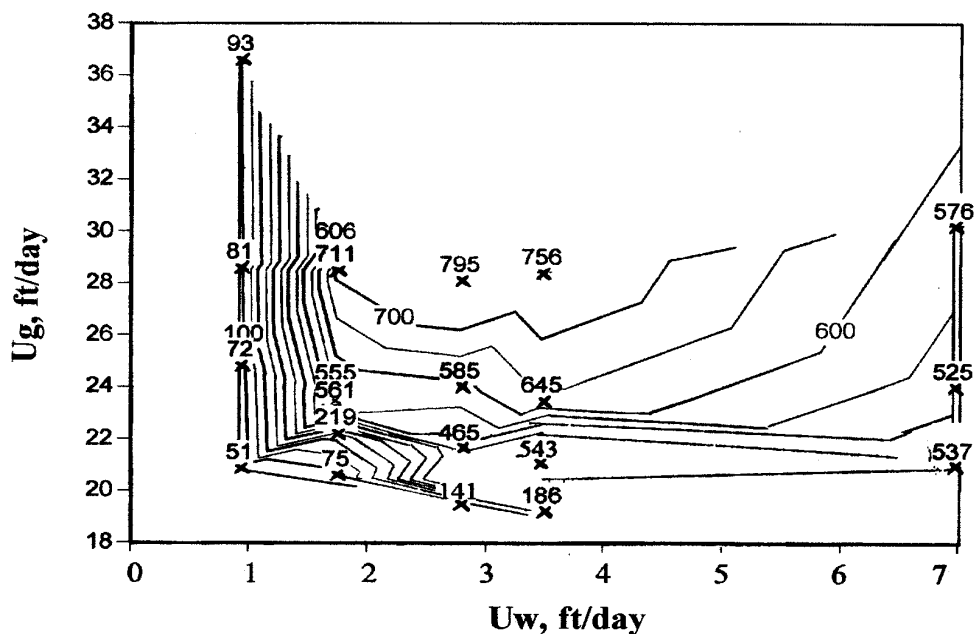


Fig. 1.8. Steady-state pressure gradient as a function of superficial velocities of gas (U_g) and water (U_w) for N_2 foam with 0.39 wt% active surfactant in brine with 0.01 wt% $CaCl_2$ and 0.25 wt% $NaCl$ in an 11.8-darcy sandpack.

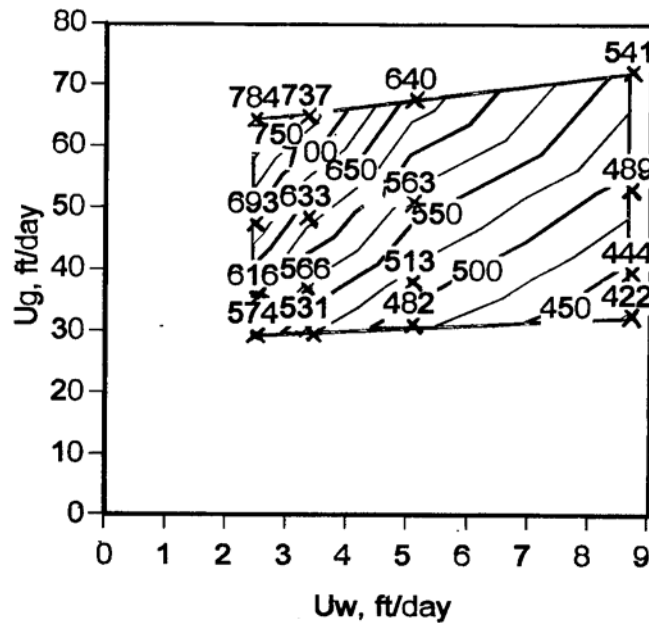


Fig. 1.9. Steady-state pressure gradient as a function of superficial velocities of gas (U_g) and water (U_w) for N_2 foam with 0.1 wt% high-MW polyacrylamide polymer in a 16.6-darcy sandpack. X symbols represent individual data, and the numbers above them the measured values of pressure gradient.

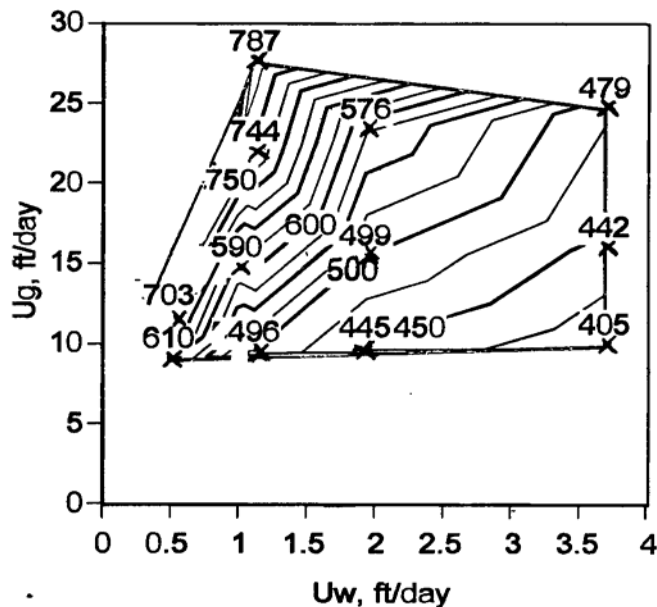


Fig. 1.10. Steady-state pressure gradient as a function of superficial velocities of gas (U_g) and water (U_w) for N_2 foam with 0.05 wt% xanthan polymer in a 16.6-darcy sandpack. X symbols represent individual data, and the numbers above them the measured values of pressure gradient.

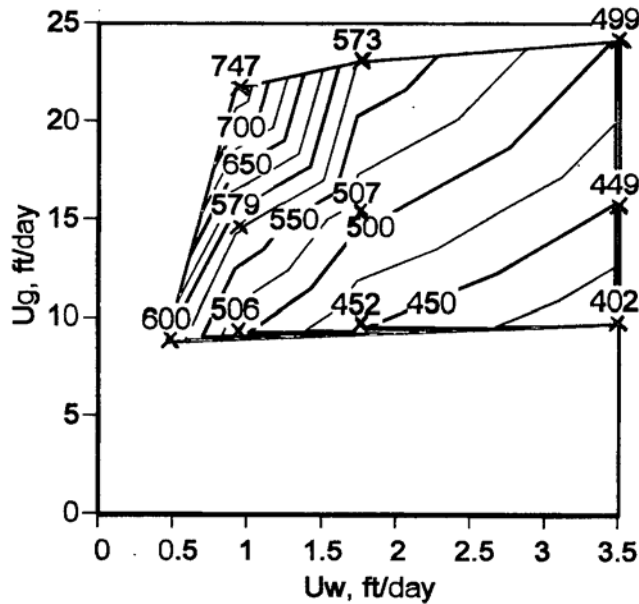


Fig. 1.11. Steady-state pressure gradient as a function of superficial velocities of gas (U_g) and water (U_w) for N_2 foam without polymer in a 16.6-darcy sandpack, into which polymer foam had previously been injected. X symbols represent individual data, and the numbers above them the measured values of pressure gradient.

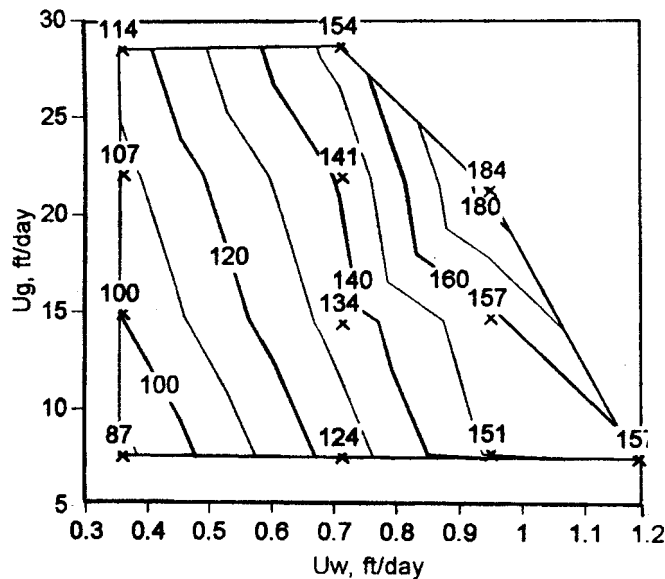


Fig. 1.12. Steady-state pressure gradient as a function of superficial velocities of gas (U_g) and water (U_w) for N_2 foam without oil or polymer in a 3.67-darcy sandpack. X symbols represent individual data, and the numbers above them the measured values of pressure gradient.

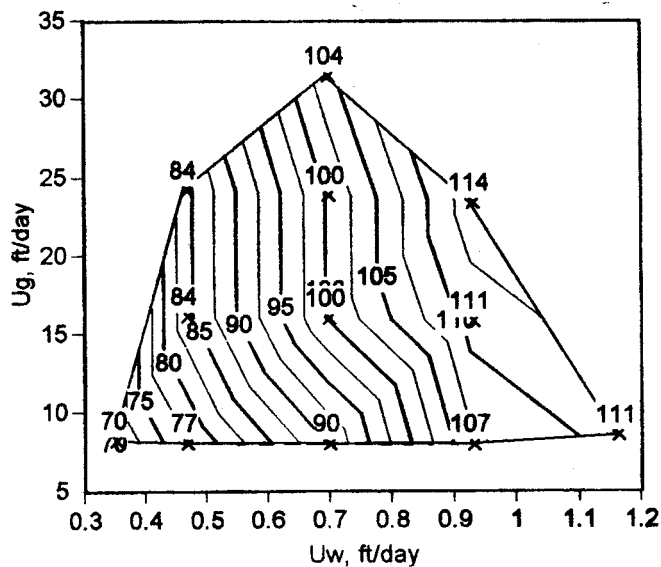


Fig. 1.13. Steady-state pressure gradient as a function of superficial velocities of gas (U_g) and water (U_w) for N_2 foam with decane but without polymer, in a 3.67-darcy sandpack. X symbols represent individual data, and the numbers above them the measured values of pressure gradient.

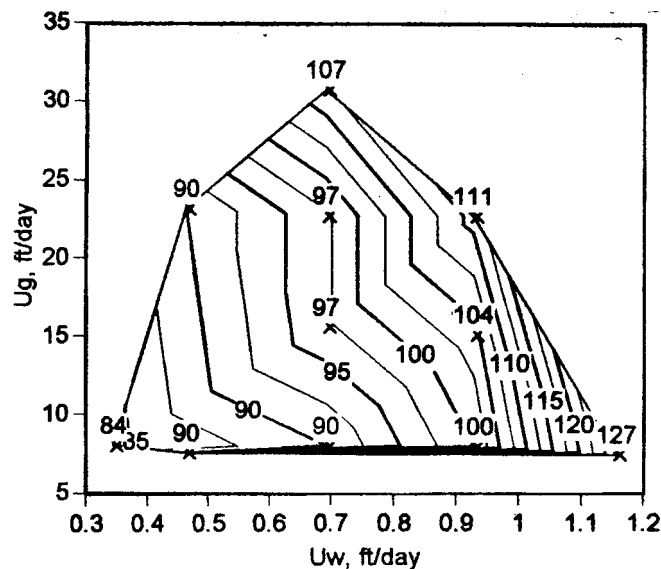


Fig. 1.14. Steady-state pressure gradient as a function of superficial velocities of gas (U_g) and water (U_w) for N_2 foam with both 0.05 wt% xanthan polymer and 22 vol% decane injected into a 3.67-darcy sandpack. X symbols represent individual data, and the numbers above them the measured values of pressure gradient.

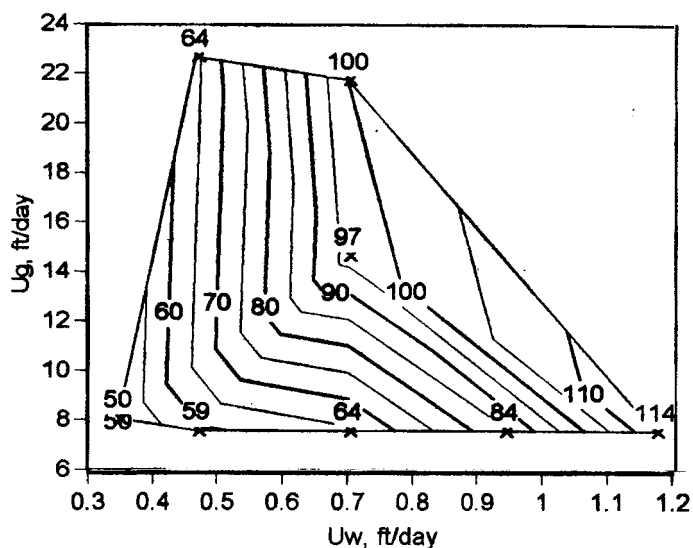


Fig. 1.15. Steady-state pressure gradient as a function of superficial velocities of gas (U_g) and water (U_w) for N_2 foam without polymer or oil in a 3.67-darcy sandpack, through which polymer and oil have both been injected previous. X symbols represent individual data, and the numbers above them the measured values of pressure gradient.

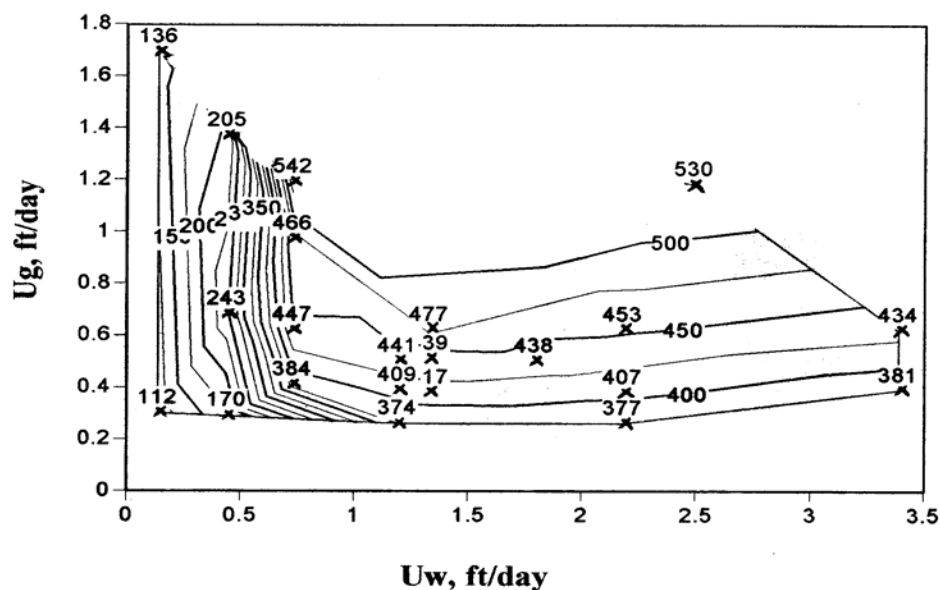


Fig. 1.16. Steady-state pressure gradient as a function of superficial velocities of gas (U_g) and water (U_w) for N_2 foam with 0.39 wt% active surfactant in brine with 1 wt% NaCl in the first Boise sandstone core.

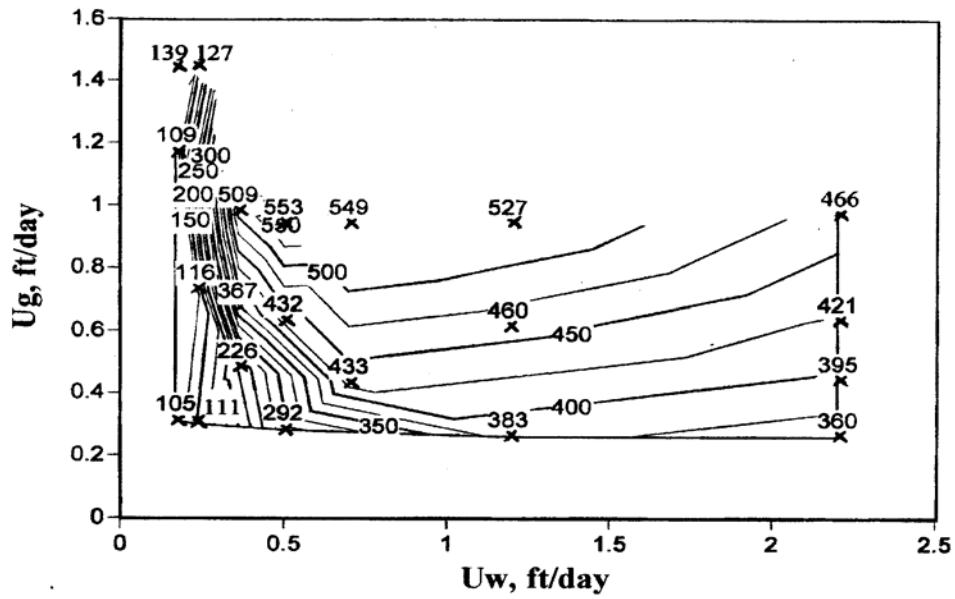


Fig. 1.17. Steady-state pressure gradient as a function of superficial velocities of gas (U_g) and water (U_w) for N_2 foam with 0.39 wt% active surfactant with 0.2 wt% Alcoflood 935 polymer in 1 wt% NaCl brine in the first Boise sandstone core.

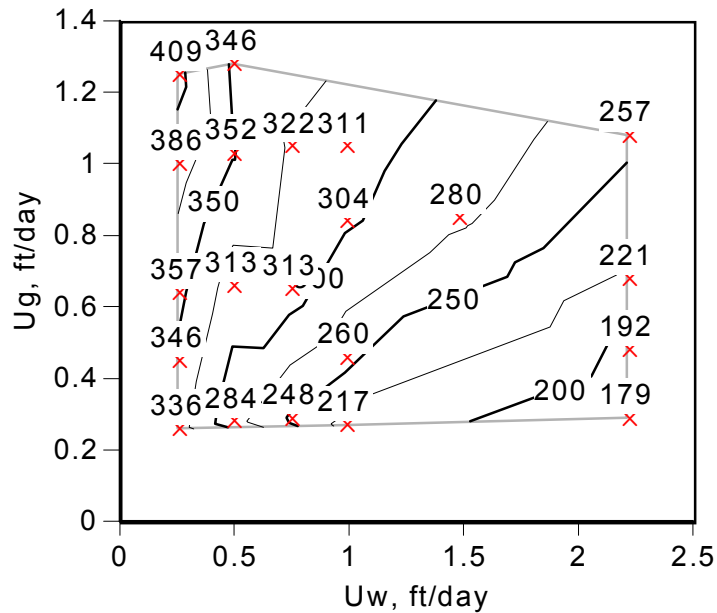


Fig. 1.18. Steady-state pressure gradient as a function of superficial velocities of gas (U_g) and water (U_w) for N_2 foam with 0.39 wt% active surfactant in brine with 1 wt% NaCl in the first Boise sandstone core, with decane injected simultaneously with the foam.

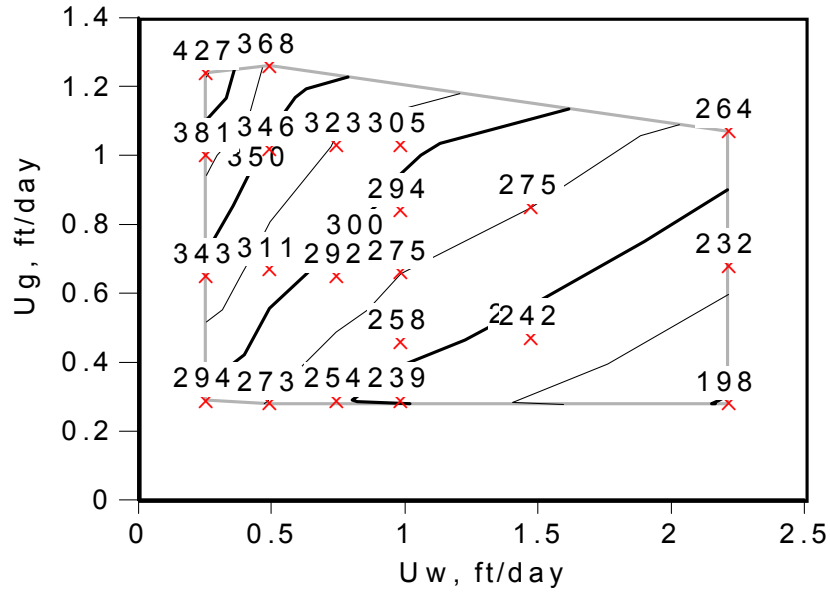


Fig. 1.19. Steady-state pressure gradient as a function of superficial velocities of gas (U_g) and water (U_w) for N_2 foam with 0.39 wt% active surfactant and 0.2 wt% Alcoflood polymer in brine with 1 wt% NaCl in the first Boise sandstone core, with decane injected simultaneously with the foam.

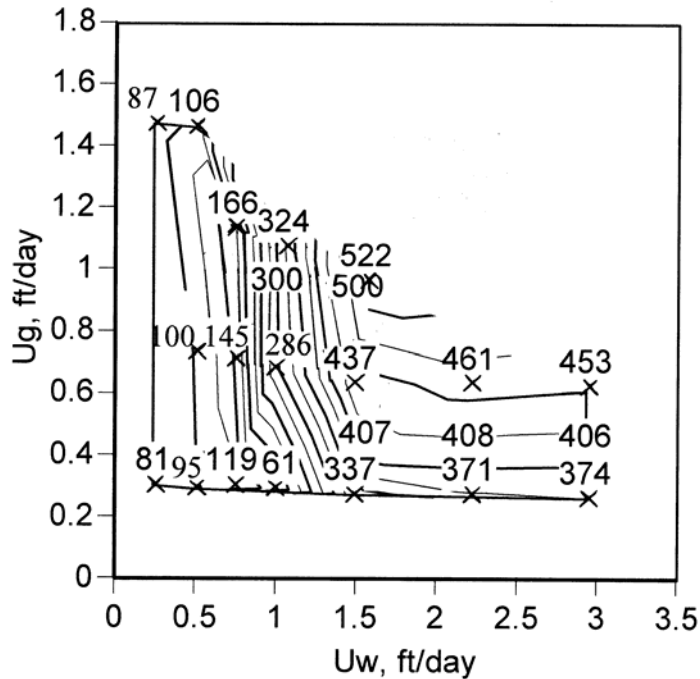


Fig. 1.20. Steady-state pressure gradient as a function of superficial velocities of gas (U_g) and water (U_w) for N_2 foam with 0.39 wt% active surfactant in brine with 1 wt% NaCl in the second Boise sandstone core.

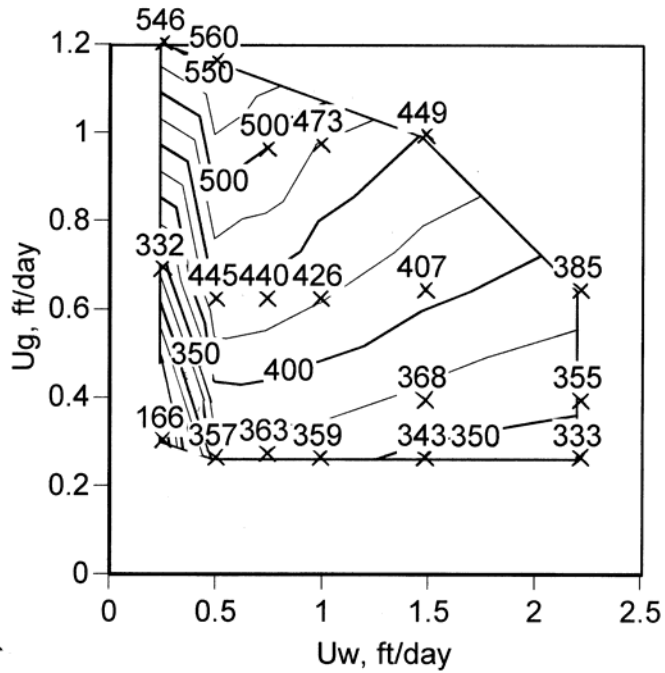


Fig. 1.21. Steady-state pressure gradient as a function of superficial velocities of gas (U_g) and water (U_w) for N_2 foam with 0.39 wt% active surfactant with 0.2 wt% Alcoflood 935 polymer in 1 wt% NaCl brine in the second Boise sandstone core.

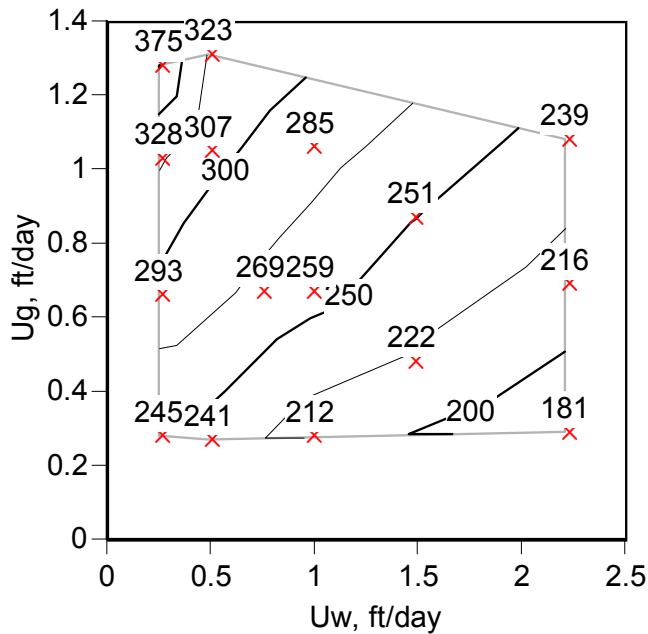


Fig. 1.22. Steady-state pressure gradient as a function of superficial velocities of gas (U_g) and water (U_w) for N_2 foam with 0.39 wt% active surfactant in brine with 1 wt% NaCl in the second Boise sandstone core, with 37.5° API crude oil injected simultaneously with the foam.

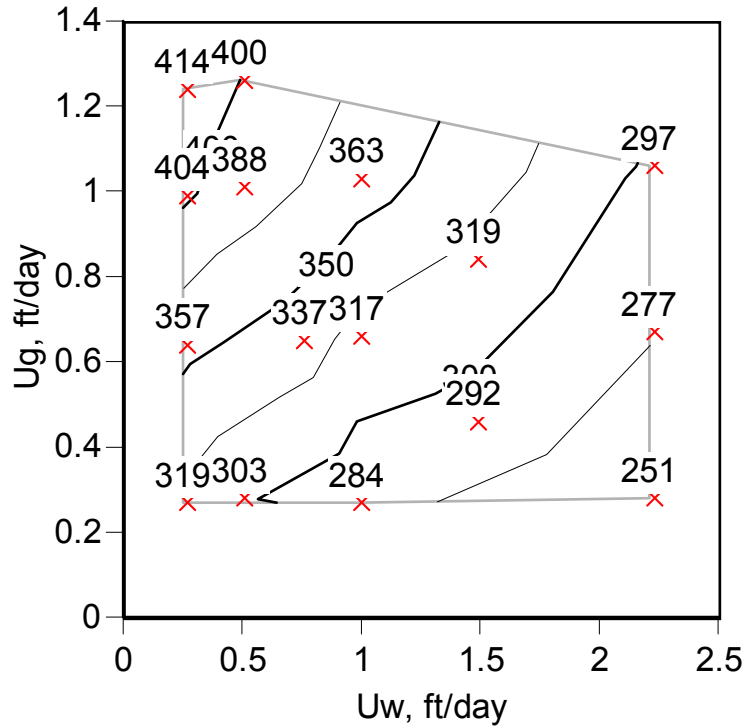


Fig. 1.23. Steady-state pressure gradient as a function of superficial velocities of gas (U_g) and water (U_w) for N_2 foam with 0.39 wt% active surfactant and 0.2 wt% Alcofluid polymer in brine with 1 wt% NaCl in the second Boise sandstone core, with 37.5° API crude oil injected simultaneously with the foam.

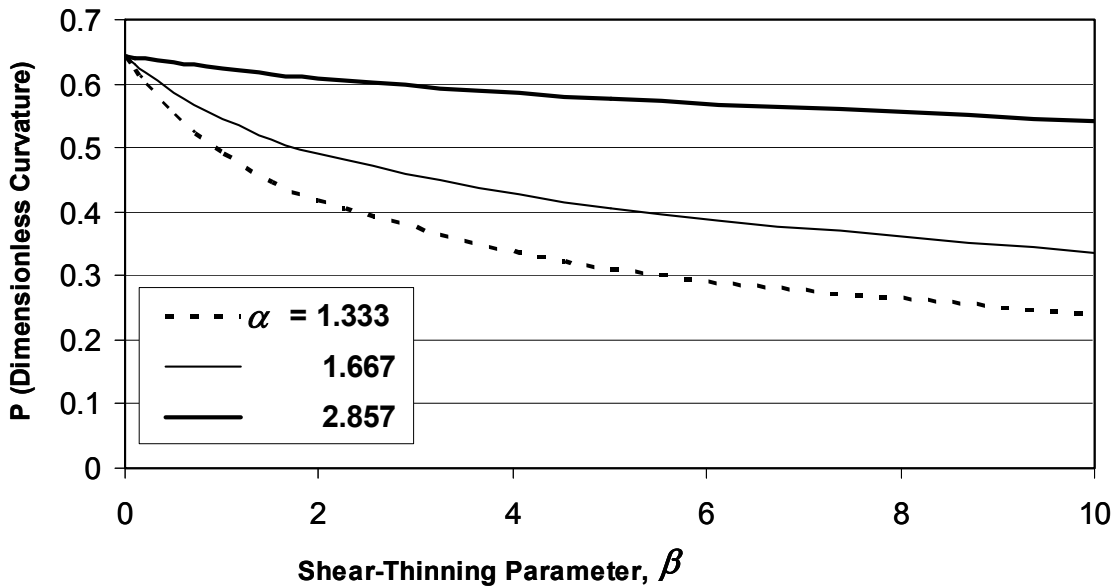


Fig. 1.24. Effect of parameters α and β on the dimensionless curvature P , which affects drag on bubbles in cylindrical tubes (Eq. 1.21).

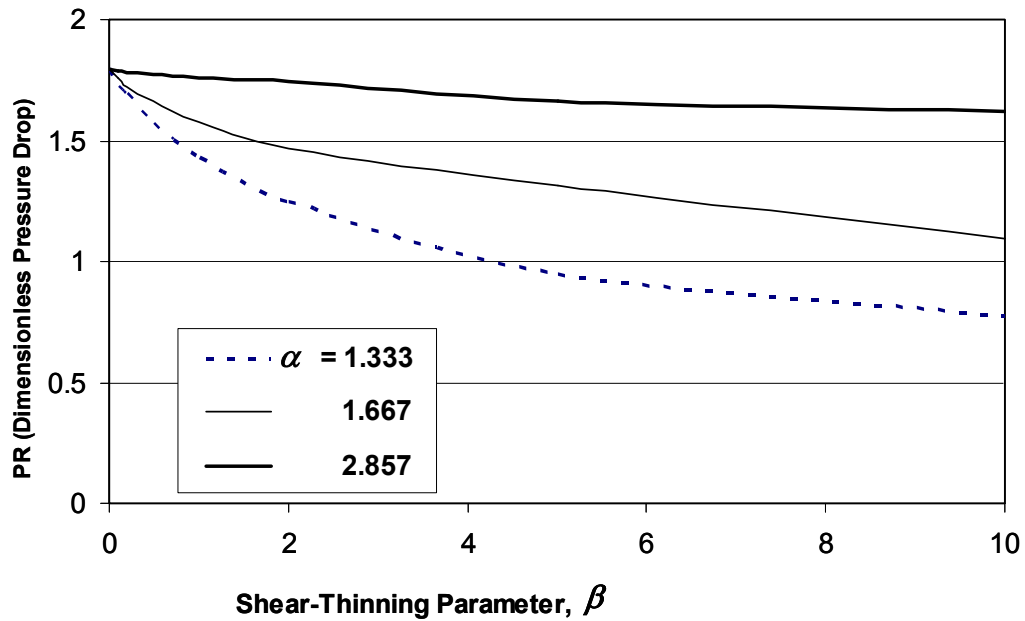


Fig. 1.25. Effect of parameters α and β on the product of parameters P and R, which affects drag on bubbles in cylindrical tubes (Eq. 1.21). Increasing velocity increases β , which reduces the product [PR], which then reduces the drag on bubbles below that expected for a foam made with a comparable Newtonian fluid. The more shear-thinning the fluid (the large the value of α), the stronger the effect.

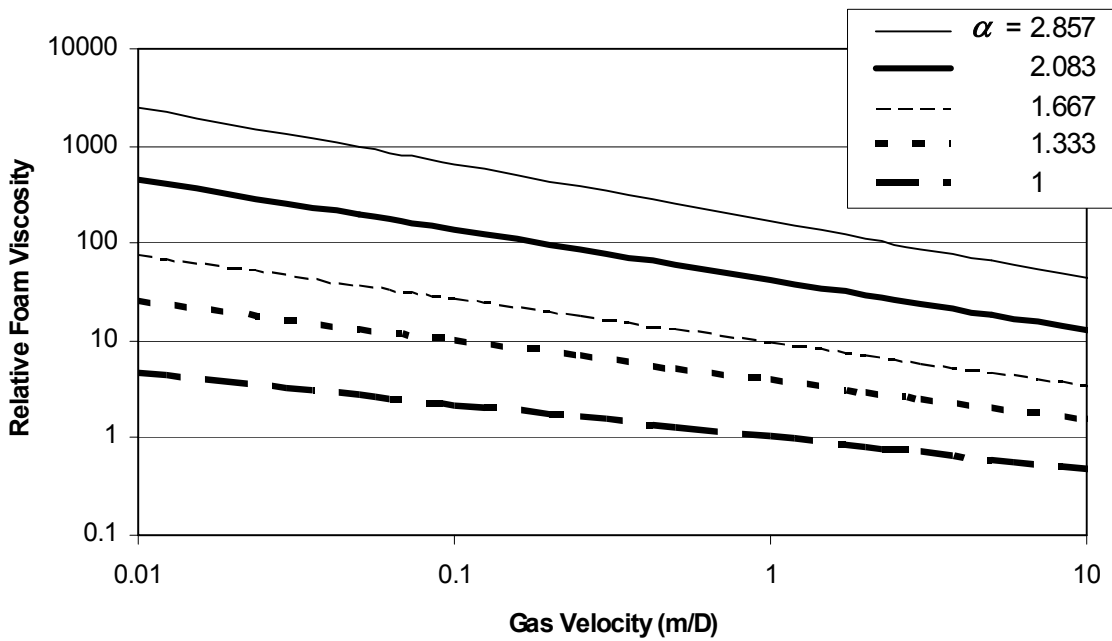


Fig. 1.26. Effect of gas velocity on foam viscosity.

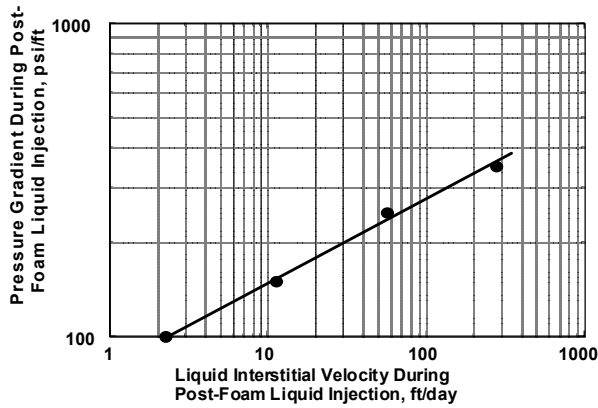


Fig. 2.1 Steady-state pressure gradient attained during injection of surfactant solution following foam for one foam formulation in Berea sandstone, from Rossen and Wang (1999).

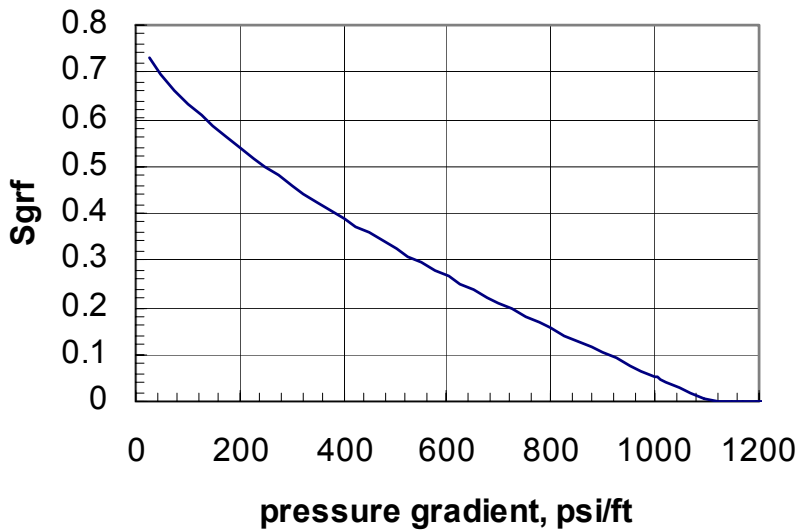


Fig. 2.2. Trapped-gas saturation with foam S_{gr}^f as a function of pressure gradient $|\nabla p|$, fit to data of liquid mobility during post-foam injection (Fig. 2.1).

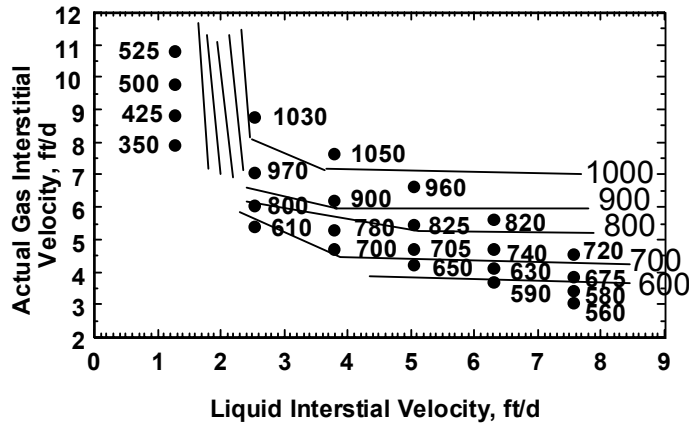


Fig. 2.3 Pressure gradient (psi/ft) as a function of gas and water interstitial velocities, from study of foam in a Berea sandstone (Rossen and Wang, 1999).

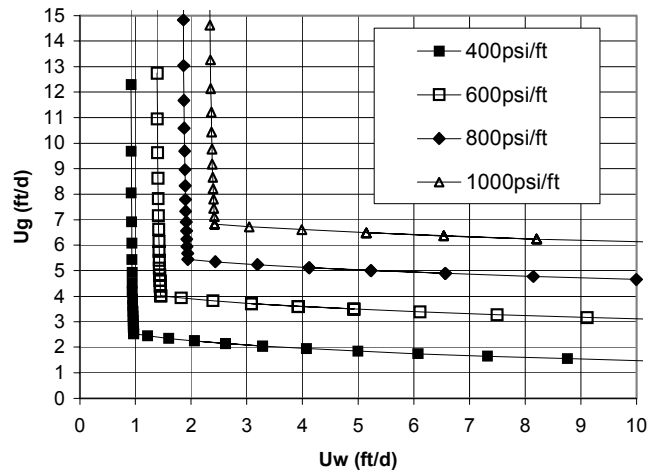


Fig. 2.4 Fit to the data of Fig. 2.3 using foam parameters that account for variation of S_{gr} with pressure gradient (Figs. 2.1 and 2.2); details are in Cheng *et al.* (2002).

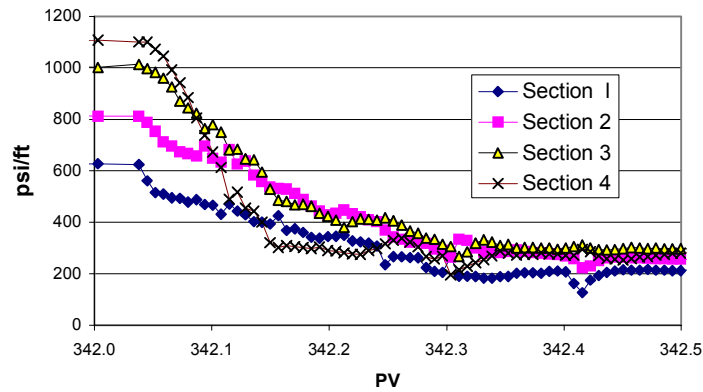


Fig. 2.5 Expanded view of decline of pressure gradient just after gas injection ceases; i.e. transition period between steady-state foam injection and quasi-steady-state liquid injection. Experimental data.

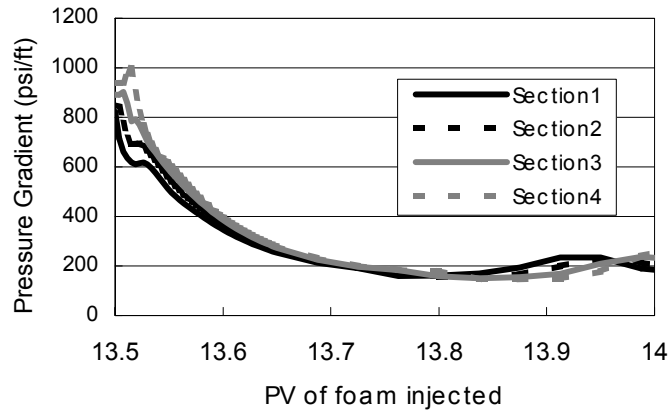


Fig. 2.6 Simulator fit to the coreflood data of Fig. 2.5. In the simulation, foam injection ceases after 13.5 PV injection.

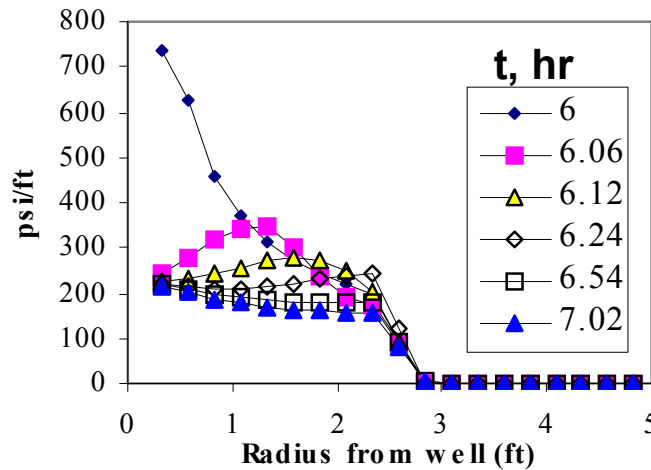


Fig. 2.7. Simulation of injection of liquid slug in radial flow following 6 hrs of foam injection, at the same volumetric rate of foam injection at the wellbore. Note that pressure gradient settles down in less than 15 minutes.

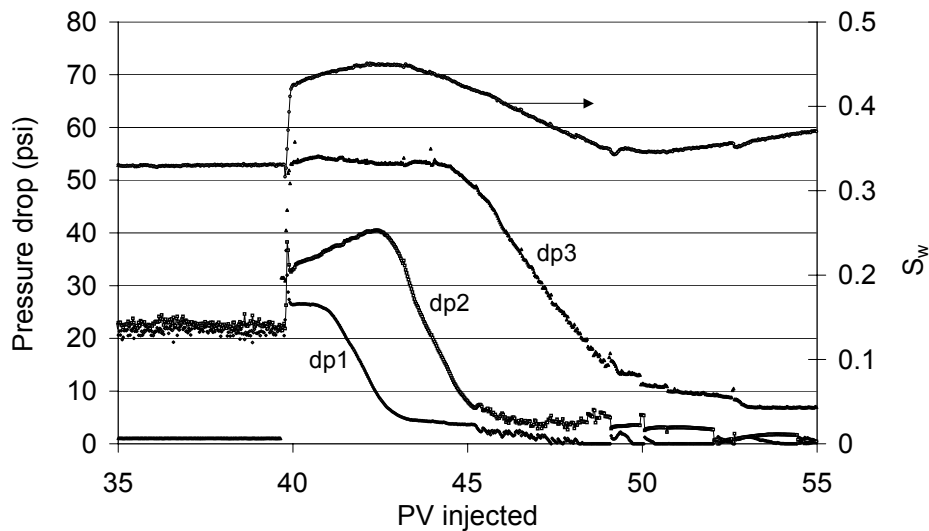


Figure 2.8. Data from coreflood experiment on gas trapping with foam. Shortly before 40 PV injection, gas injection ceases and liquid injection rate increases to approximate total volumetric injection rate of foam. Water saturation rapidly rises by about 10%, while pressure drops (dp) in all three sections of the core increase. The subsequent, slower rise in pressure drop in section 2 (dp2) is not fully understood. The subsequent rise, fall, and rise in water saturation S_w (top curve) during injection of liquid can be understood as the separate effects of gas dissolution and of expansion of gas still trapped as pressure falls in the core. Details are in Xu (2003) and Xu and Rossen (2003b).

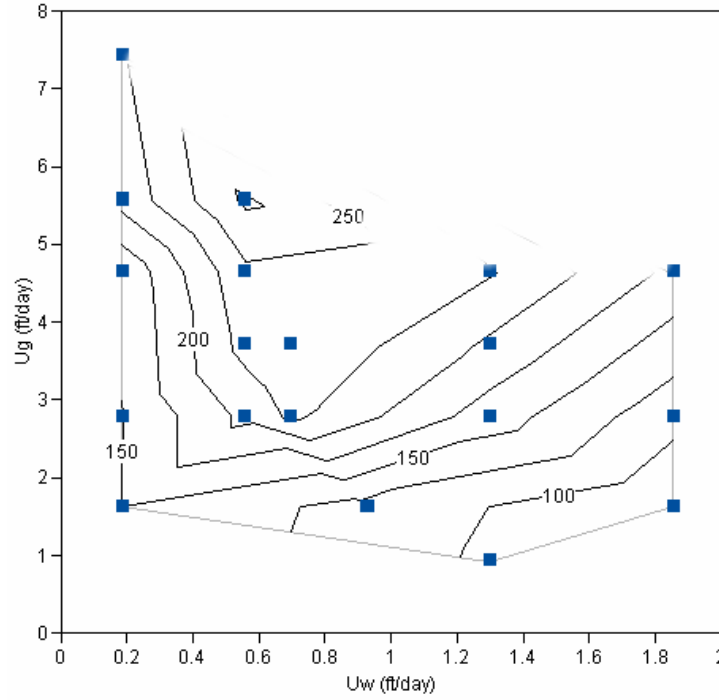


Fig. 2.9. Steady-state pressure gradient as a function of superficial velocities of gas (U_g) and water (U_w) for CO₂ foam at 2000 psi and room temperature in a Boise sandstone core. Dark dots represent individual data.

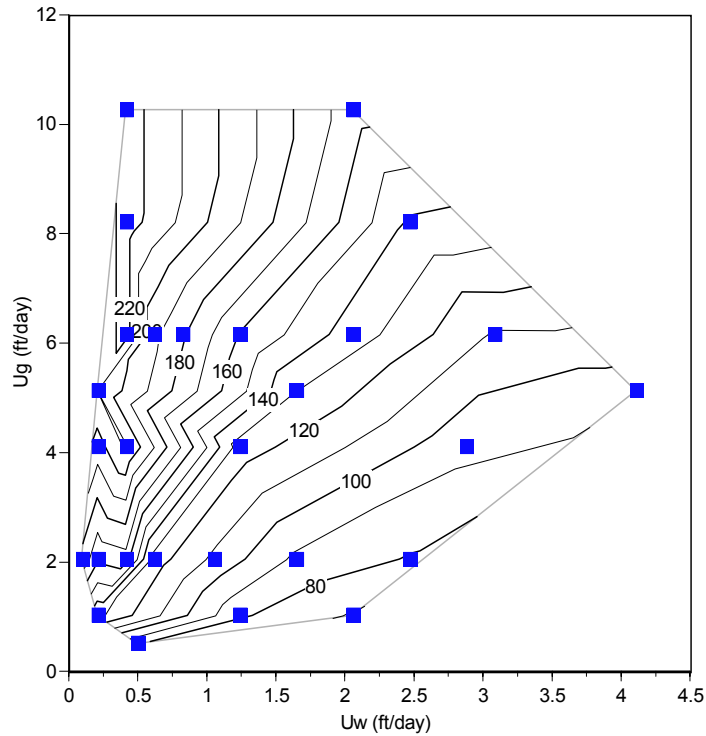


Fig. 2.10. Steady-state pressure gradient as a function of superficial velocities of gas (U_g) and water (U_w) for CO₂ foam at 2000 psi and room temperature in a sandpack. Dark dots represent individual data.

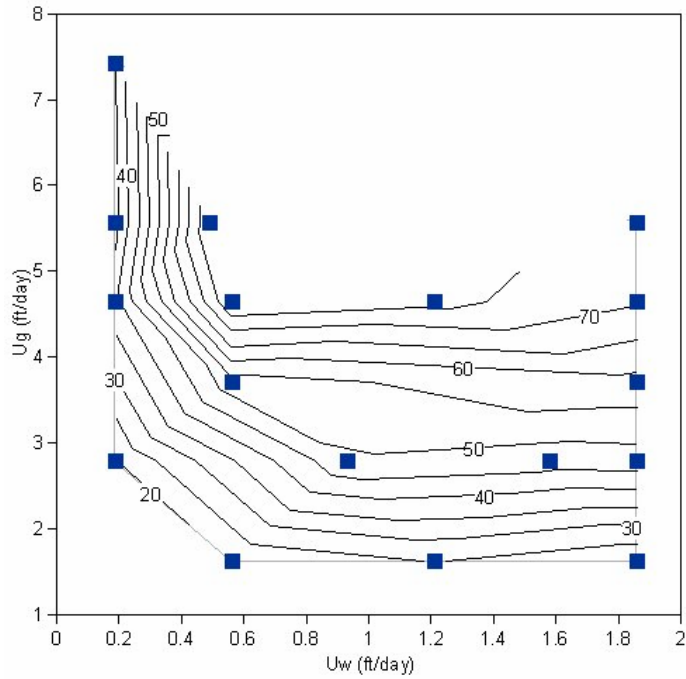


Fig. 2.11. Steady-state pressure gradient as a function of superficial velocities of gas (U_g) and water (U_w) for CO_2 foam at 2000 psi above the critical temperature of CO_2 in a Boise sandstone core. Dark dots represent individual data.

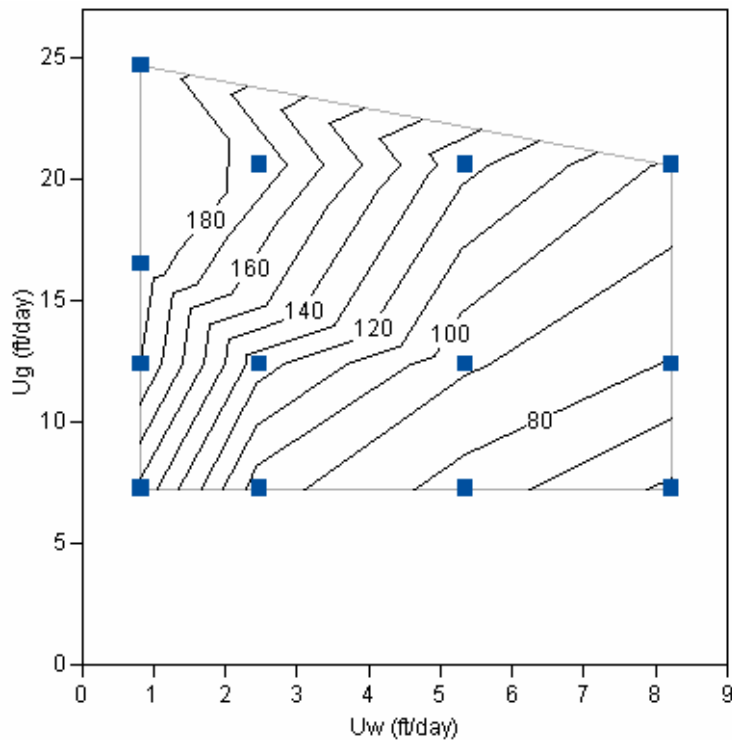


Fig. 2.12. Steady-state pressure gradient as a function of superficial velocities of gas (U_g) and water (U_w) for CO_2 foam at 2000 psi above the critical temperature of CO_2 in a sandpack. Dark dots represent individual data.

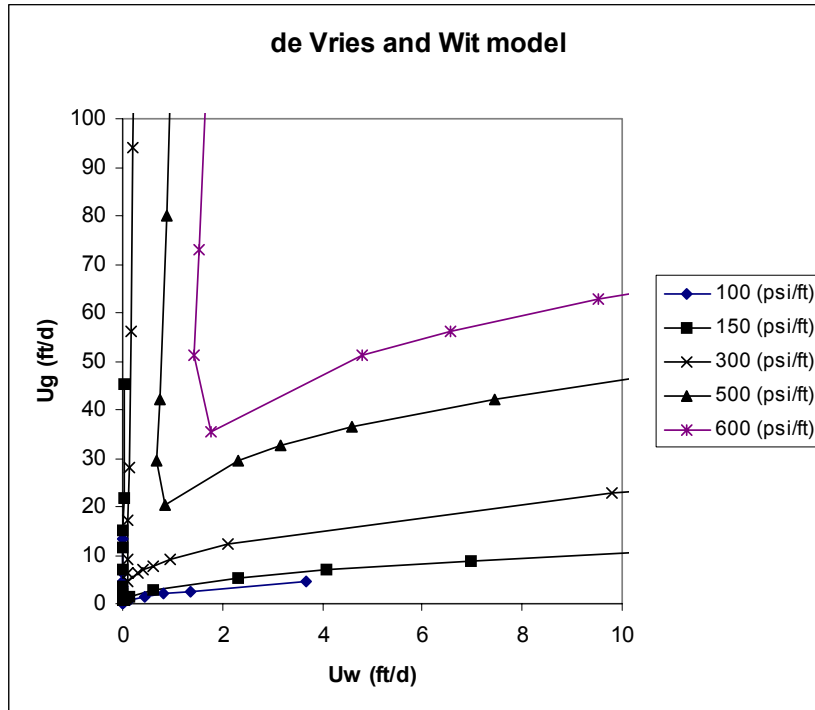


Fig. 2.13. Steady-state pressure gradient as a function of superficial velocities of gas (U_g) and water (U_w) for foam based on model of de Vries and Wit (1990). Symbols represent model-calculated values, not data.

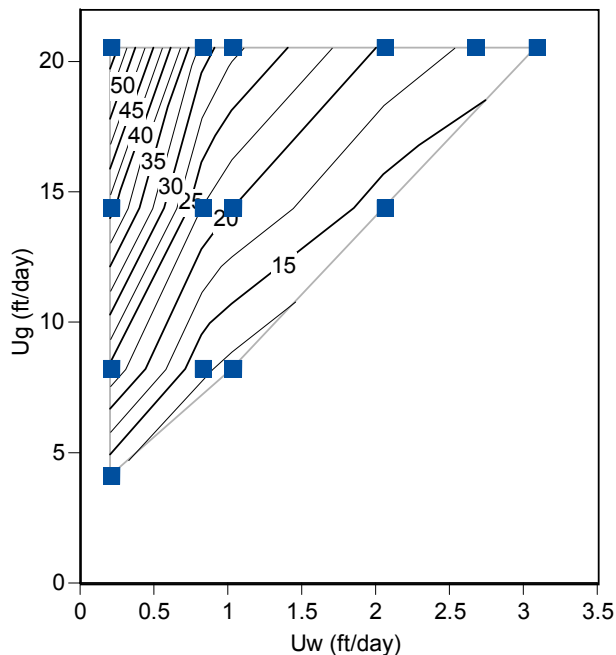


Fig. 2.14. Steady-state pressure gradient as a function of superficial velocities of gas (U_g) and water (U_w) for foam in the low-quality regime, based on model of Hirasaki and Lawson (1985), assuming foam flows through tubes of identical diameter, and that all water flows as Plateau borders between bubbles. Dark squares represent model-calculated values, not data.

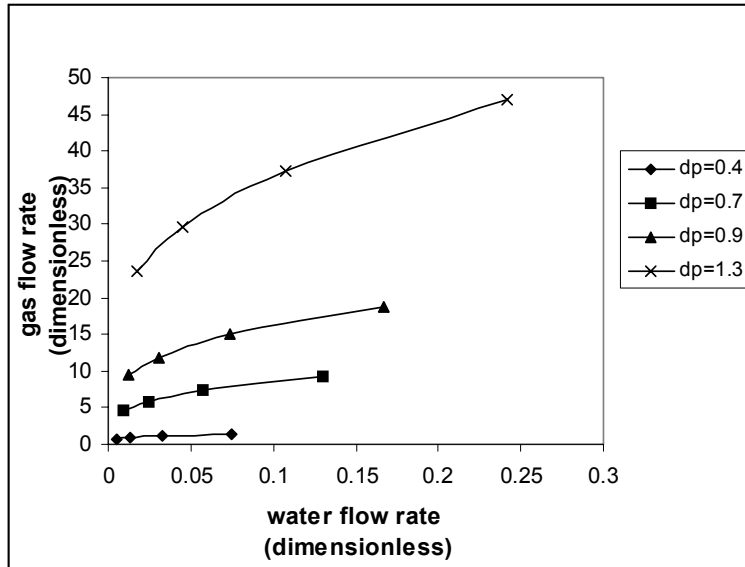


Fig. 2.15. Steady-state pressure gradient as a function of superficial velocities of gas (U_g) and water (U_w) for foam in the low-quality regime, based on combining the rheological models of Falls *et al.* (1989) and Hirasaki and Lawson (1985) with bundle-of-tubes model for foam of Rossen and Wang (1999). In this case 95% of the capillaries have a diameter within a factor of 3.4 of the mean. Symbols represent model-calculated values, not data.

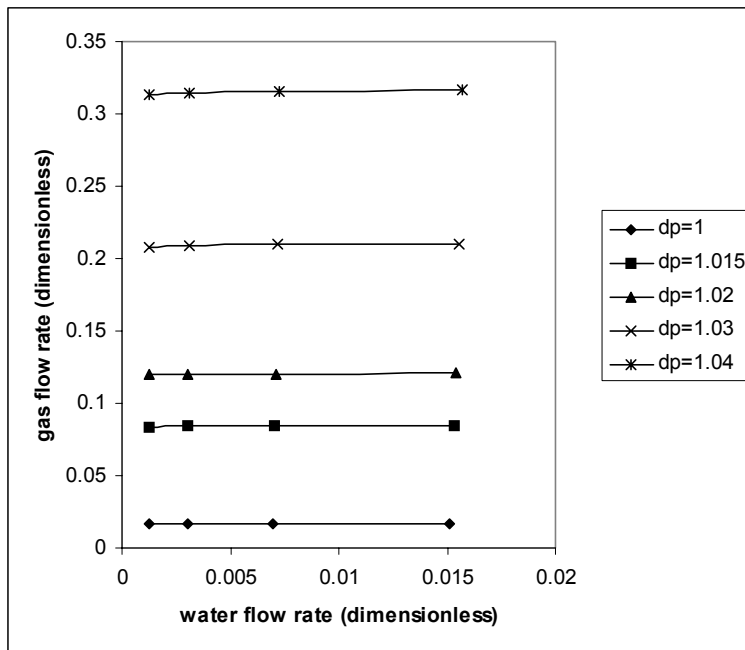


Fig. 2.16. Steady-state pressure gradient as a function of superficial velocities of gas (U_g) and water (U_w) for foam in the low-quality regime, based on combining the rheological models of Falls *et al.* (1989) and Hirasaki and Lawson (1985) with bundle-of-tubes model for foam of Rossen and Wang (1999). In this case 95% of the capillaries have a diameter within a factor of 1.02 of the mean. Symbols represent model-calculated values, not data.

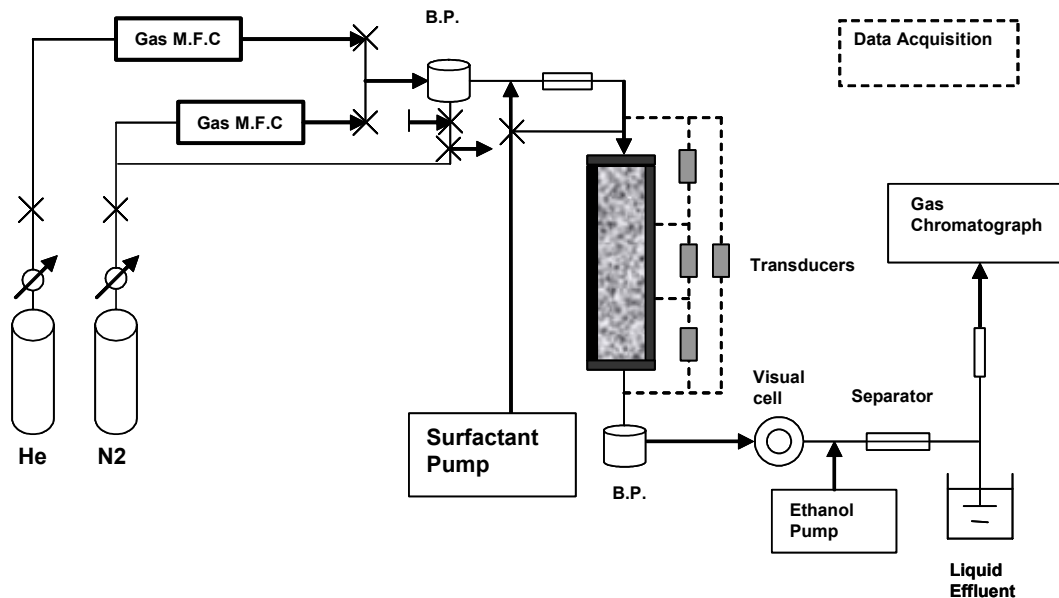


Fig. 2.17. Schematic of coreflood apparatus for estimating trapped- and flowing-gas saturations from breakthrough if gas-phase tracer in effluent.

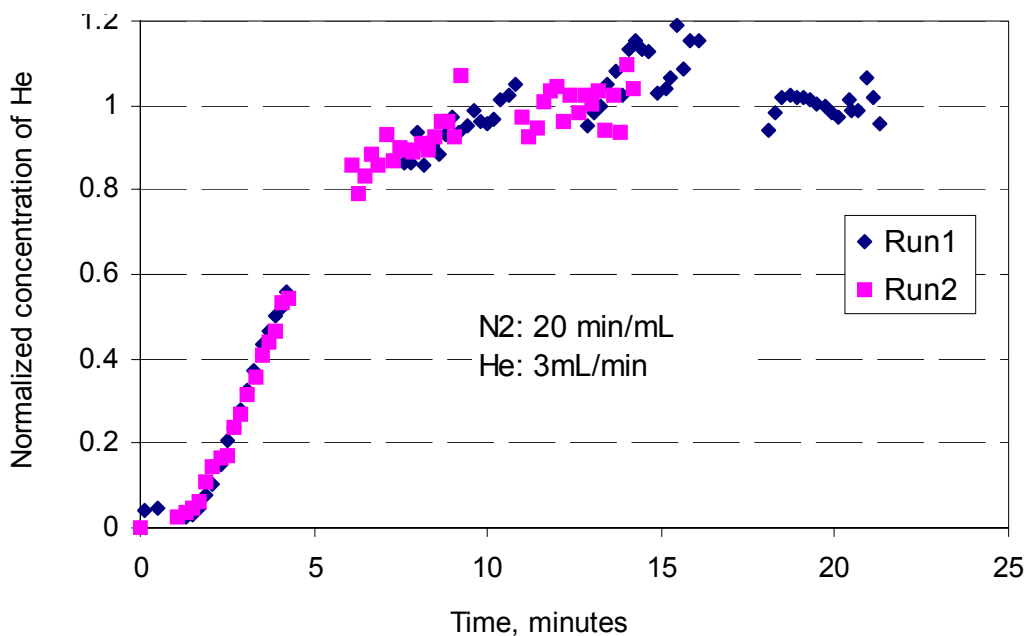


Fig. 2.18. Reproducibility in tracer breakthrough curve in two experiments with gas and liquid (surfactant solution) injection through a foam generator.

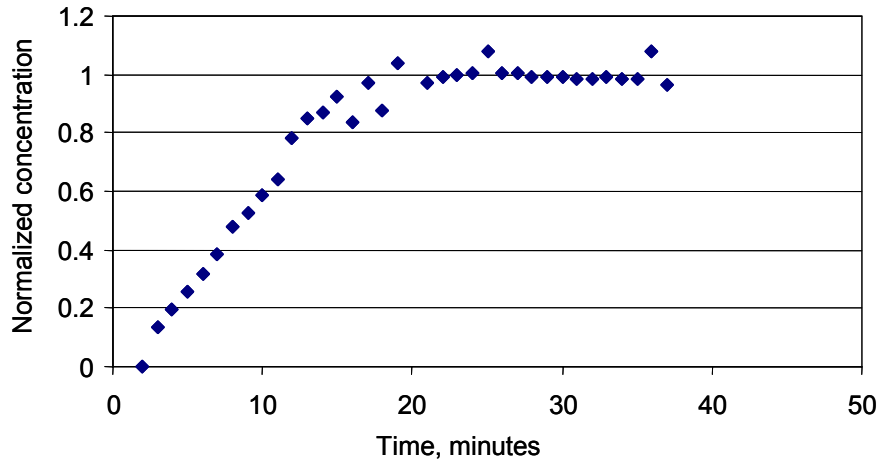


Fig. 2.19. Tracer breakthrough curve in experiment without foam in a Berea core.

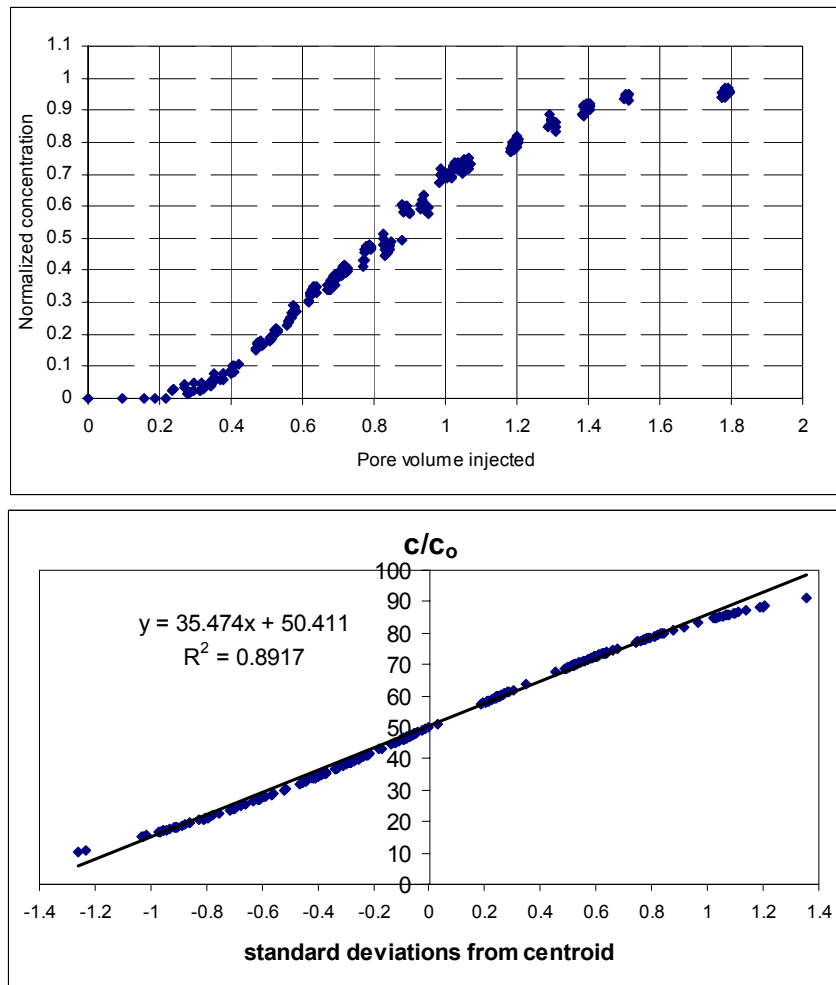


Fig. 2.20. Top: He tracer breakthrough curve from a foam-tracer experiment. Bottom: Plot of tracer-breakthrough data on probability axes. The nearly linear fit indicates close agreement with an error-function form, with either instantaneous equilibration with trapped gas, or negligible trapped-gas saturation. The centroid of the curve (point where tracer effluent concentration c reaches half the injected concentration c_0) is at 0.83 PV.

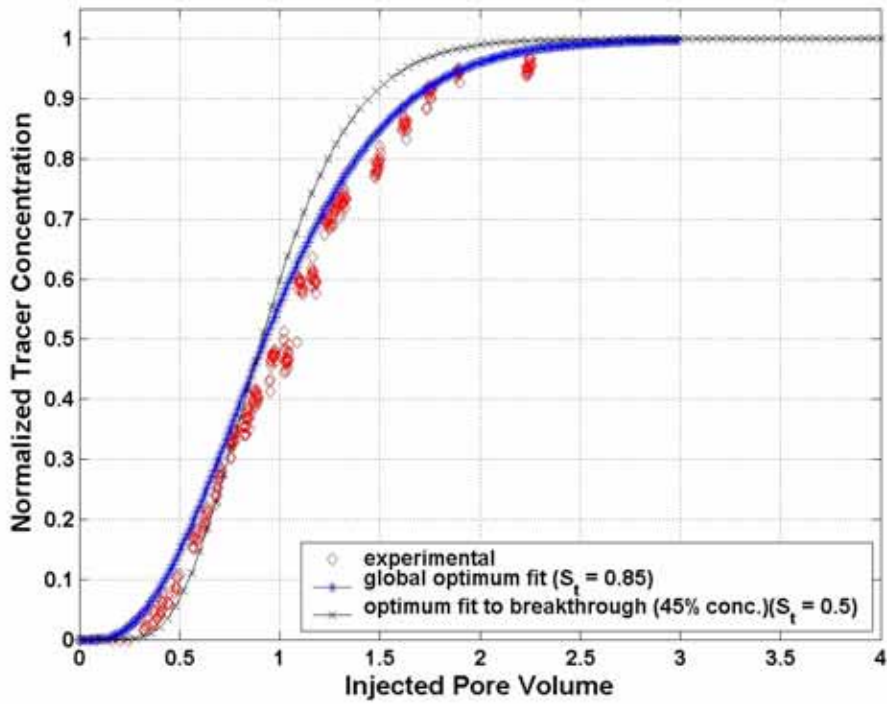


Fig. 2.21. Effluent tracer concentration (red symbols) and "optimal" (least-squares) model fits to data from Case 1 (Table 2.1).

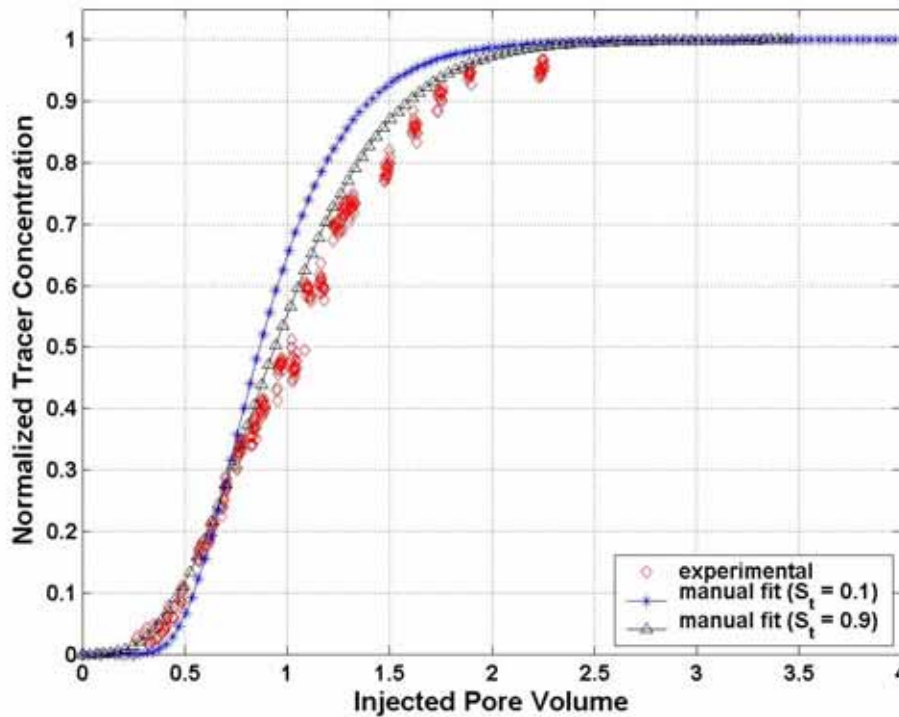


Fig. 2.22. Manual fits to data for Case 1 (Table 2.1) with S_t fixed at 0.1 and 0.9.

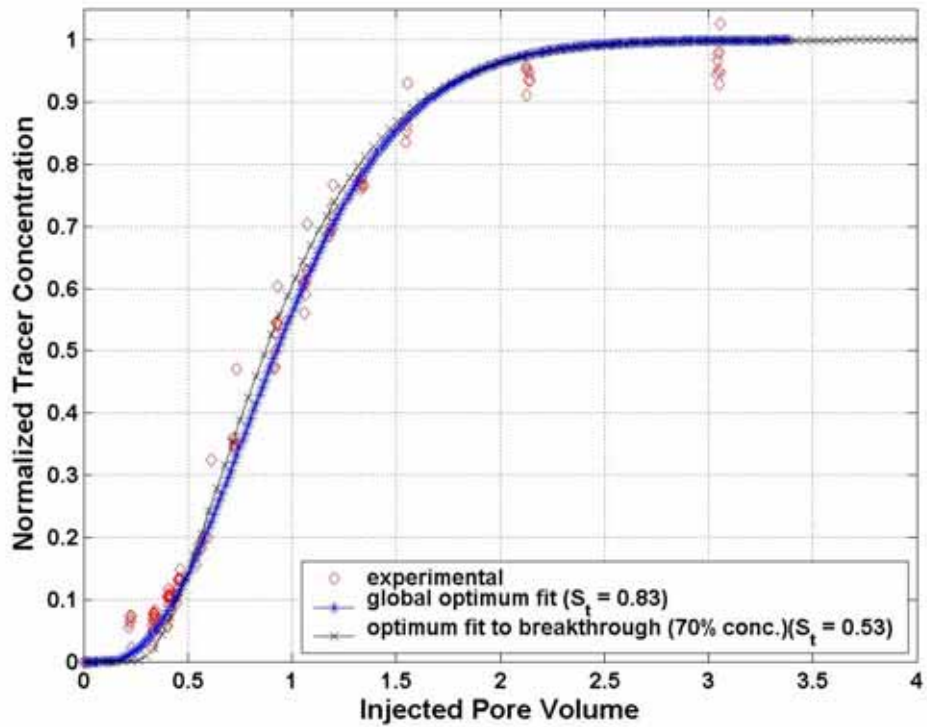


Fig. 2.23. Effluent tracer concentration (red symbols) and optimal model fits to data from Case 2 (Table 2.1).

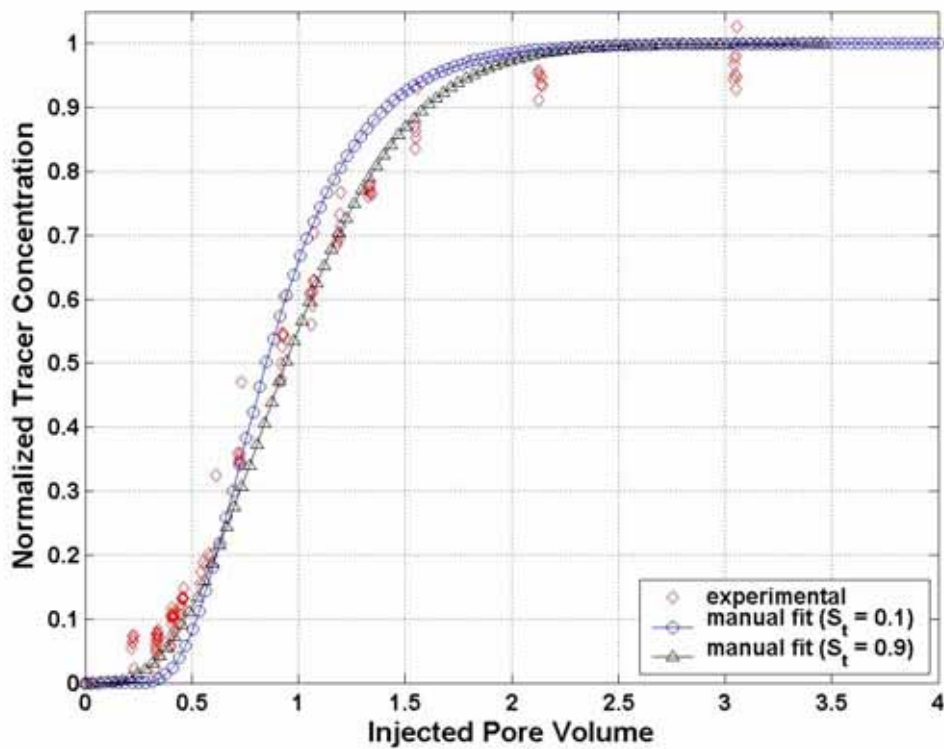


Fig. 2.24. Manual fits to data for Case 2 (Table 2.1) with S_t fixed at 0.1 and 0.9.

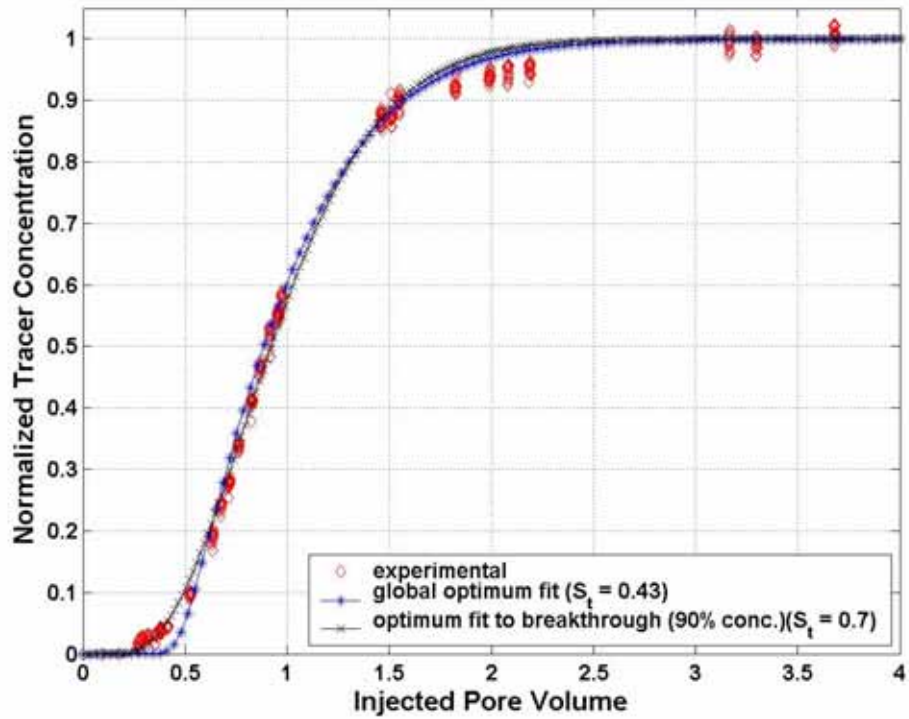


Fig. 2.25. Effluent tracer concentration (red symbols) and optimal model fits to data from Case 3 (Table 2.1).

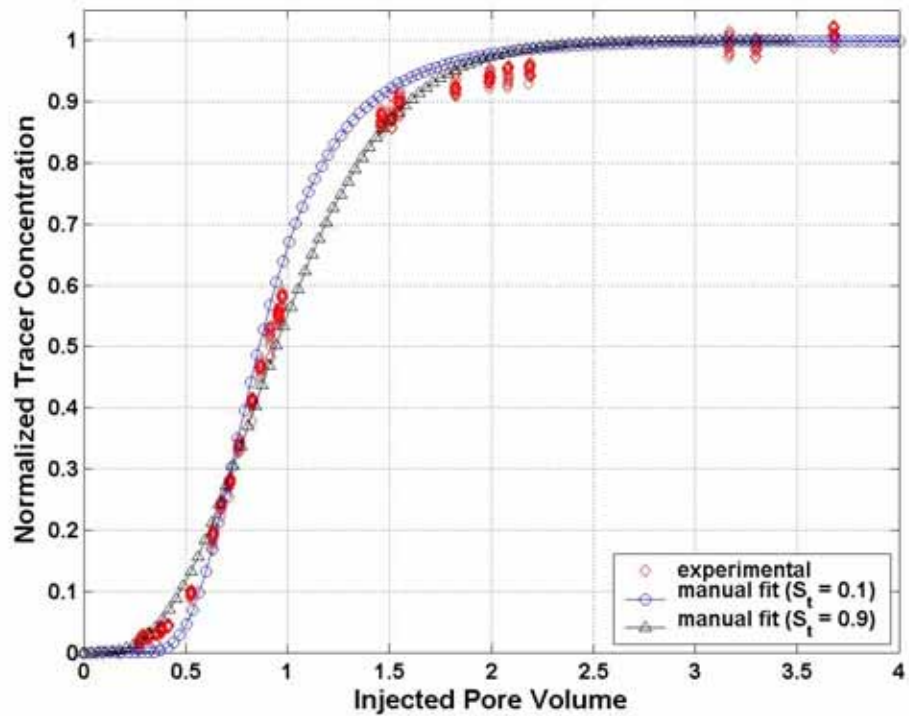


Fig. 2.26. Manual fits to data for Case 3 (Table 2.1) with S_t fixed at 0.1 and 0.9.

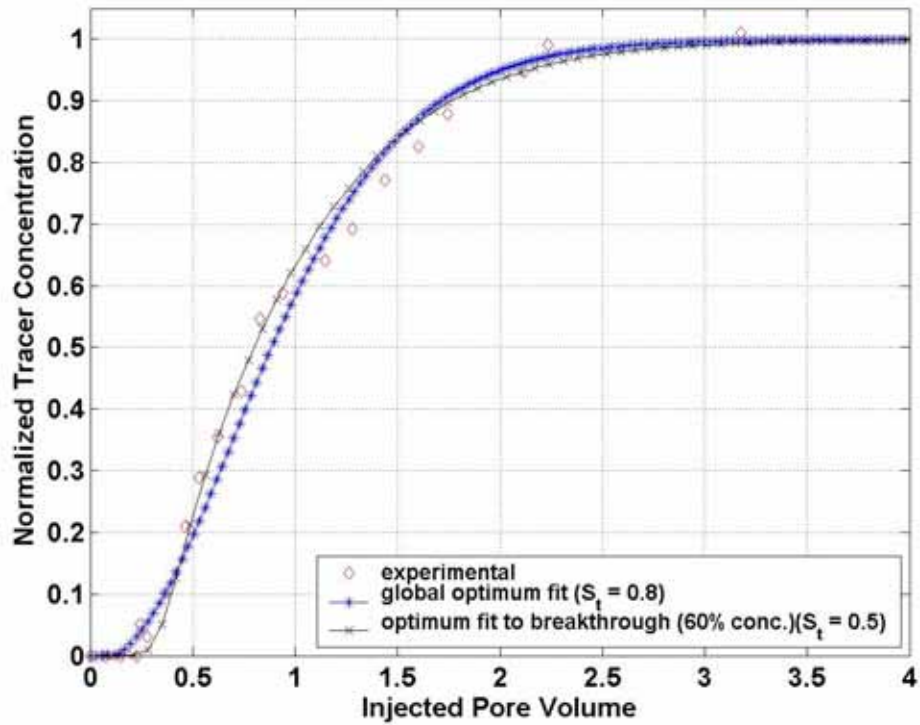


Fig. 2.27. Effluent tracer concentration (red symbols) and optimal model fits to data from Case 4 (Table 2.1).

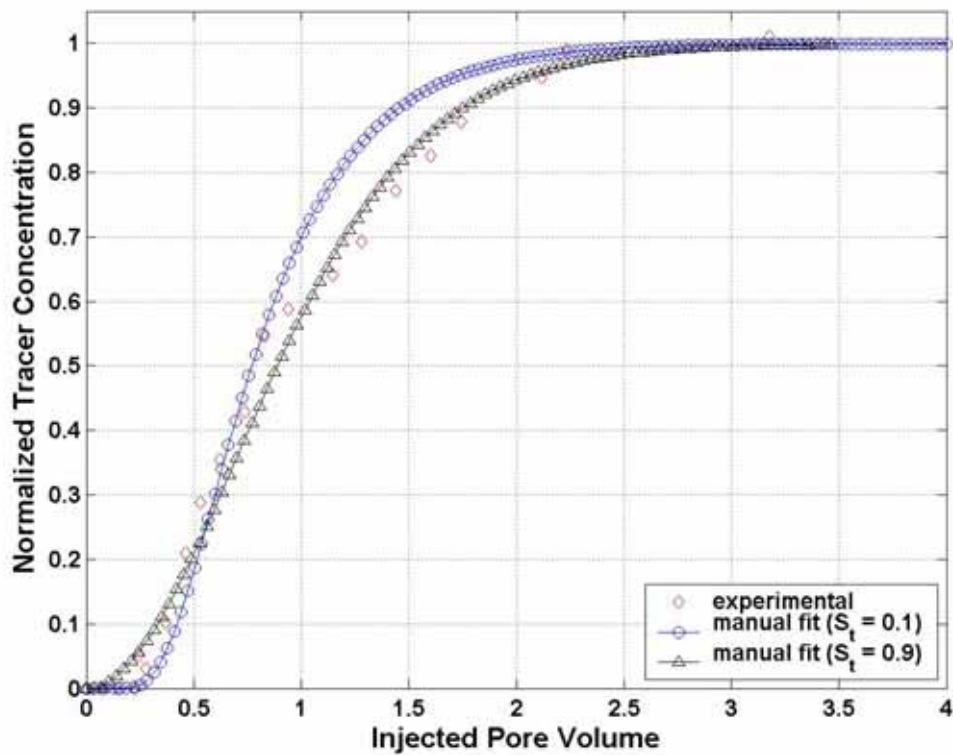


Fig. 2.28. Manual fits to data for Case 3 (Table 2.1) with S_t fixed at 0.1 and 0.9.

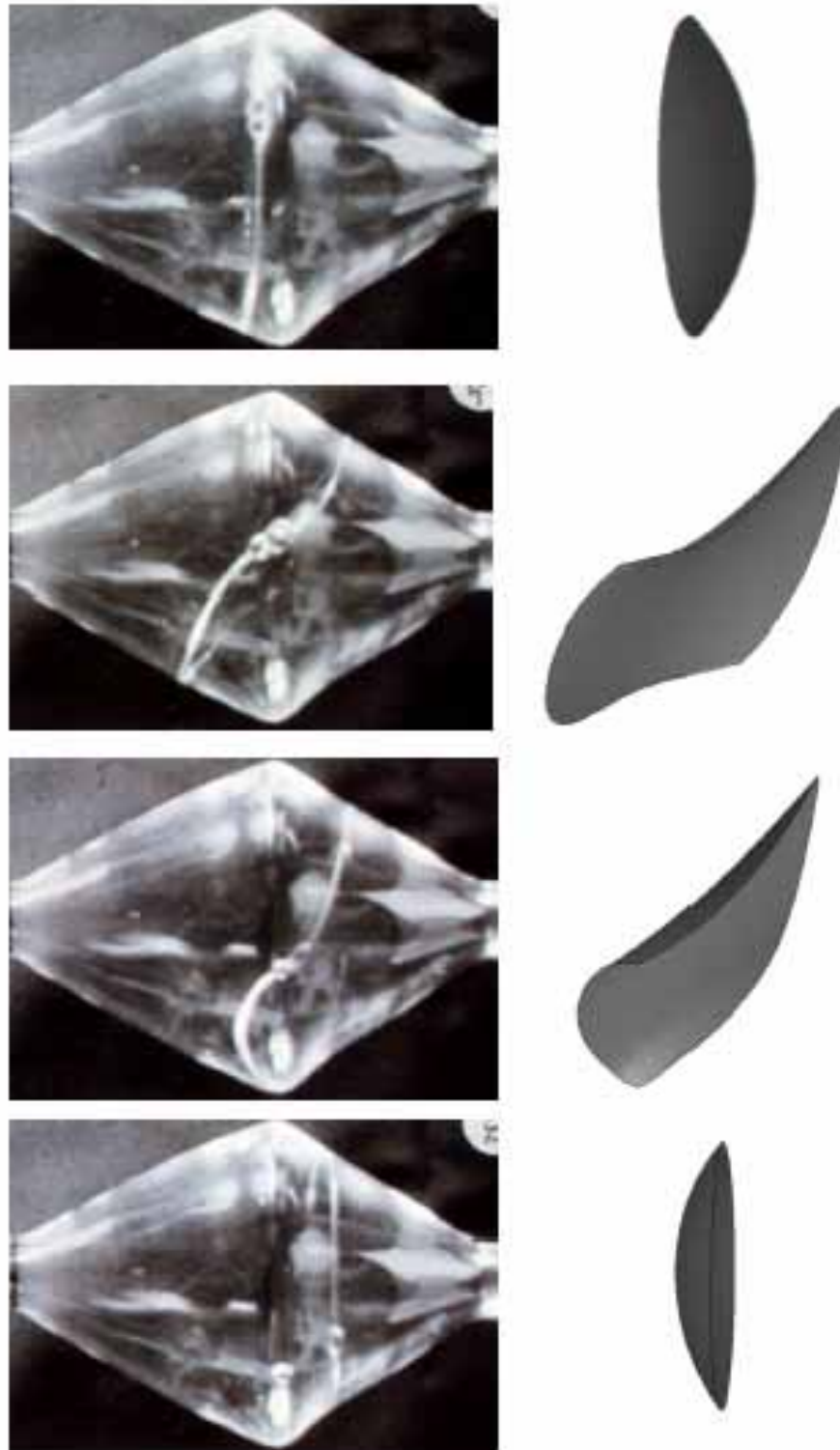


Fig. 2.29. Photographs of lamella traversing a biconical pore (left), and fit of computer model to these shapes (right).

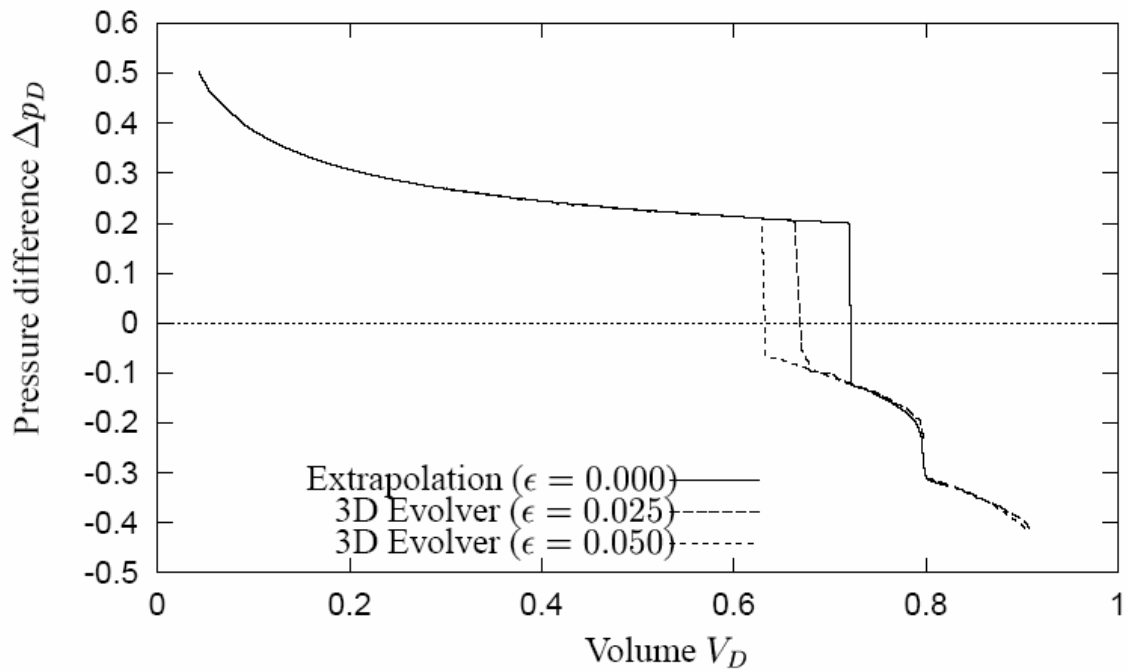


Fig. 2.30. Plot of dimensionless pressure drop across lamella as function of dimensionless time (equal to dimensionless volume behind lamella in pore), based on curvatures of surfaces determined by computer model illustrated in Fig. 2.29. The integral of this curve (area between the curve and horizontal axis) gives net resistance to flow of lamella. Asymmetry of this curve with respect to time means that there is a net resistance to flow for a train of lamellae moving through a porous medium comprising pores shaped like that in Fig. 2.29. Parameter ϵ is a measure of the amount of water occupying the corner at the pore body. Details are in Cox, *et al.*, 2004.

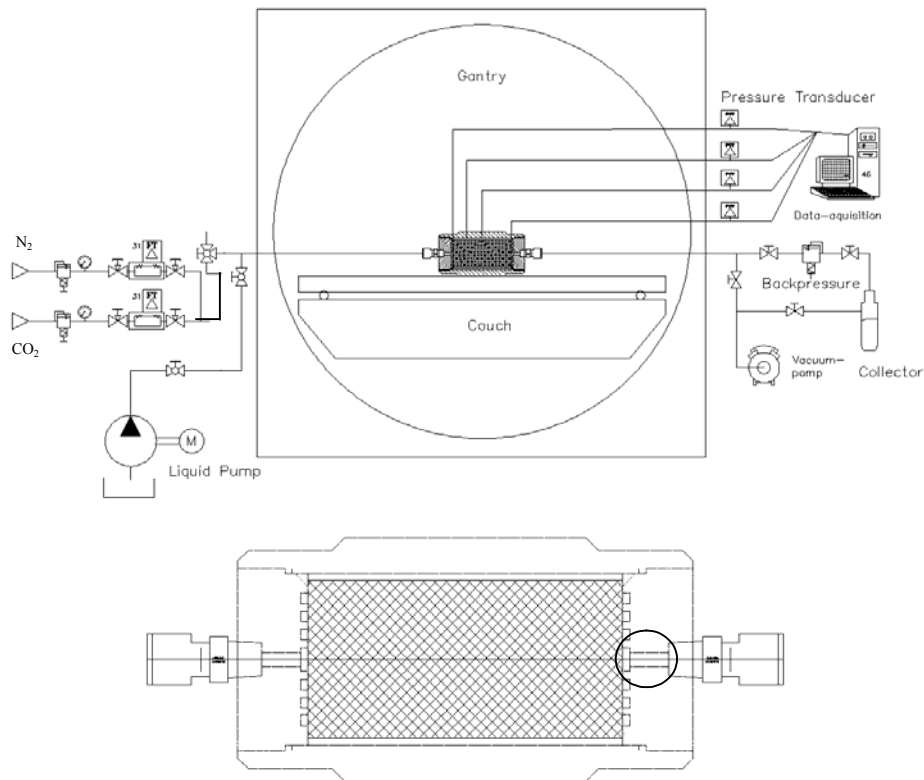


Fig. 2.31. Top: Schematic of CT coreflood apparatus. Bottom: Enlarged view of location of downstream tubing (denoted by the circle) where effluent tracer concentration is directly visible by CT in central image plane. Hatched area represents core.

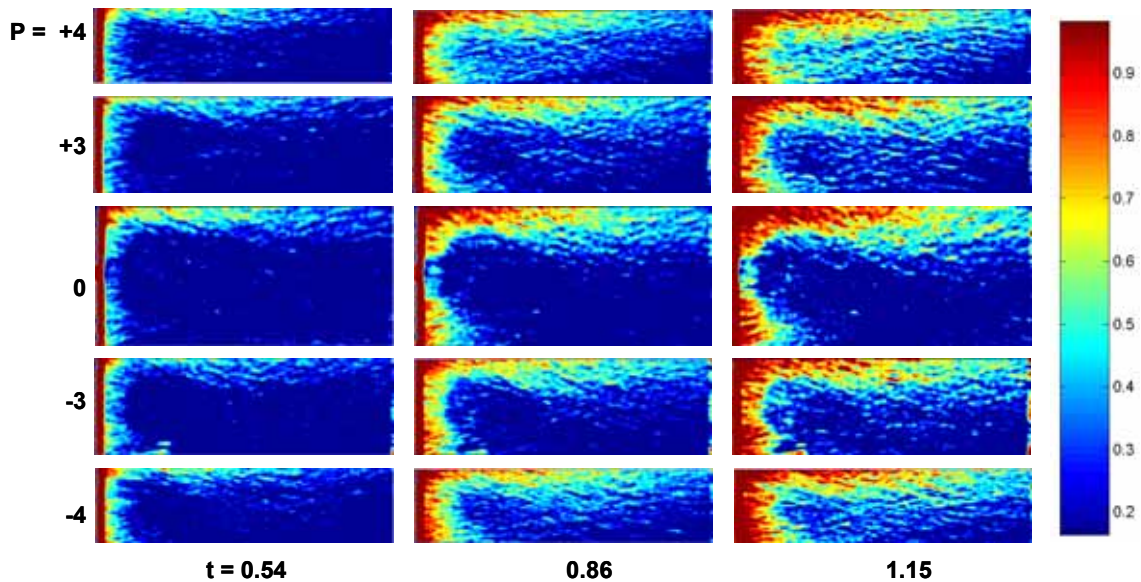


Fig. 2.32. Axial CT images of Foam A with Xe tracer displacing steady-state Foam A in 5 of 9 axial image planes ($P = +4, +3, 0, -3, -4$) at three dimensionless times. Color indicates Xe mass fraction in each pixel, according to the color bar on right. The same color bar applies to all CT images in this report.

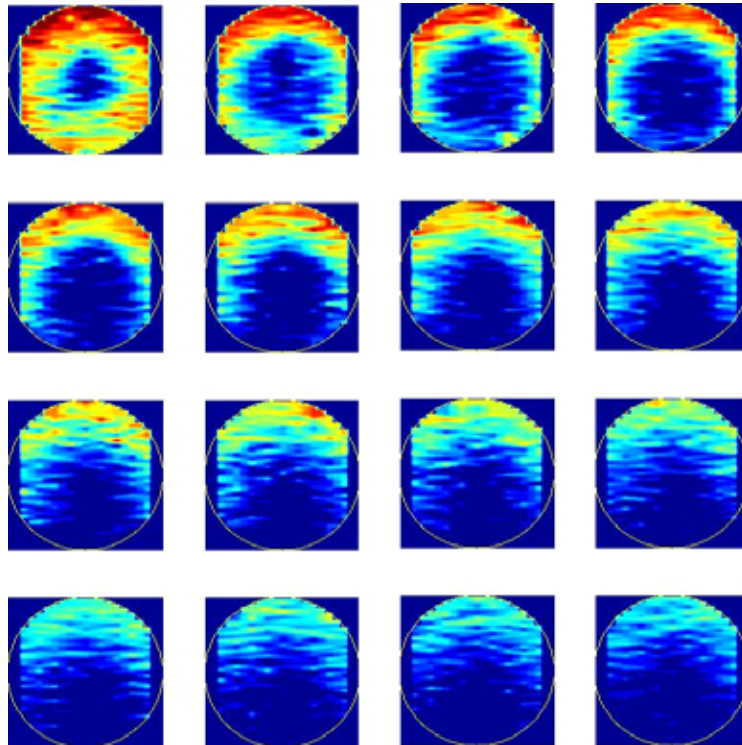


Fig. 2.33. Reconstructed cross-sectional CT images for tracer in Foam A at 1.15 PV injection. Cross-sections are spaced about 1 cm apart along the core.

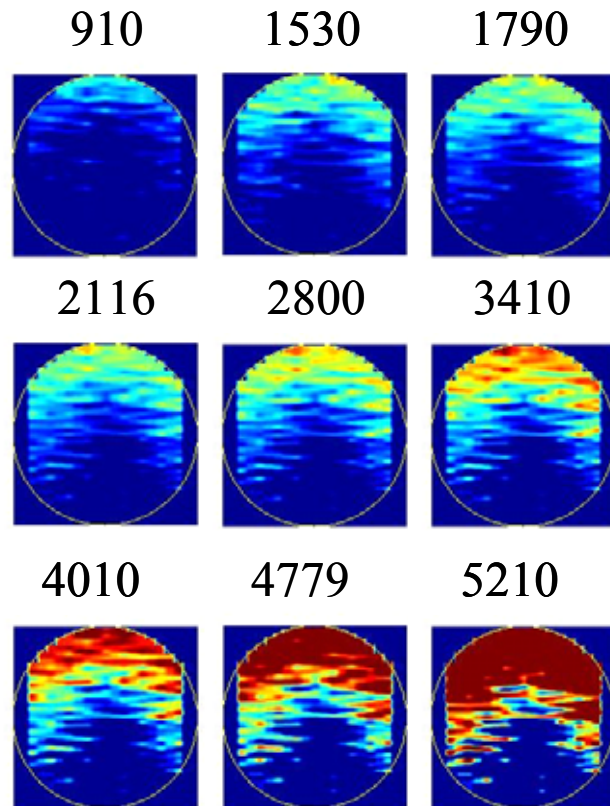


Fig. 2.34. Cross-sectional reconstruction of the data in Fig. 2.32, for a position about 3/4 of the way across the 15-cm-long core. Numbers represent the time into the coreflow in seconds. One pore volume injection corresponds to about 1470 s.

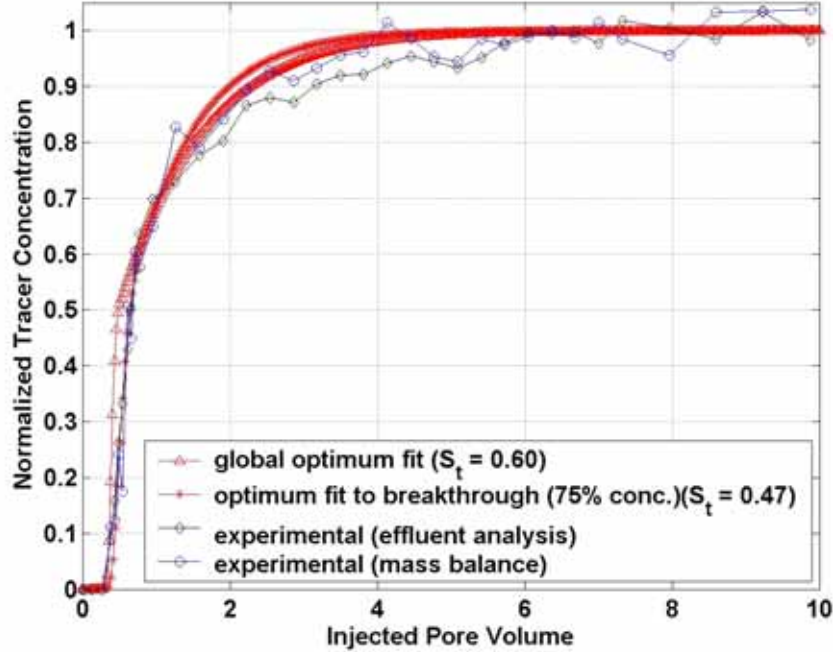


Fig. 2.35. Effluent tracer concentration for experiment with Foam A reconstructed by two methods: direct imaging of tubing downstream of core (*cf.* Fig. 2.31) ("effluent analysis") and mass balance on tracer in core. Also shown is the optimal fit of the 1D model (Eqs. (2.3)), based on minimizing squared deviations along the entire data set ("global optimum fit"), giving a fitted value of $S_t = 0.6$, and an optimal fit to the breakthrough of tracer (up to effluent concentration 75% of injected), giving a fitted value of $S_t = 0.47$.

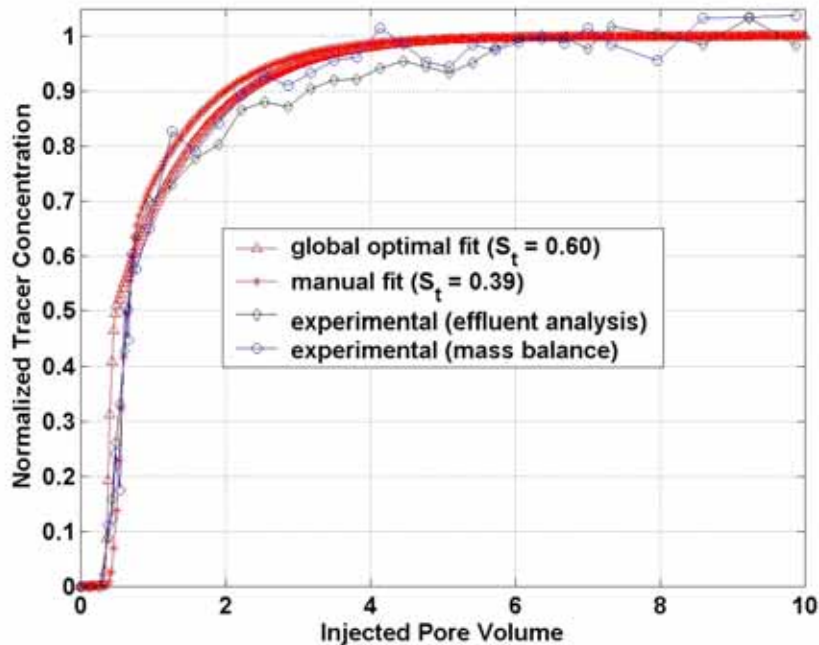


Fig. 2.36. Comparison of global optimal fit (with $S_t = 0.6$) to effluent tracer data for Foam A to manual fit to data with $S_t = 0.39$.

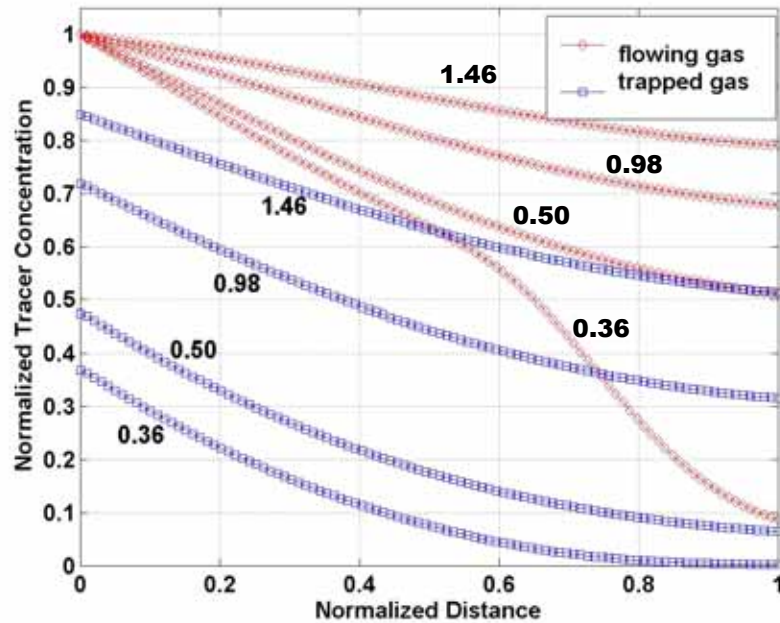


Fig. 2.37. Mass fractions of tracer in trapped and flowing gas along the core derived from global optimum fit of 1D model to effluent tracer concentration for Foam A; *cf.* Fig. 2.32. The 1D model estimates that flowing- and trapped-gas volume fractions are 0.4 and 0.6 of the gas phase, respectively.

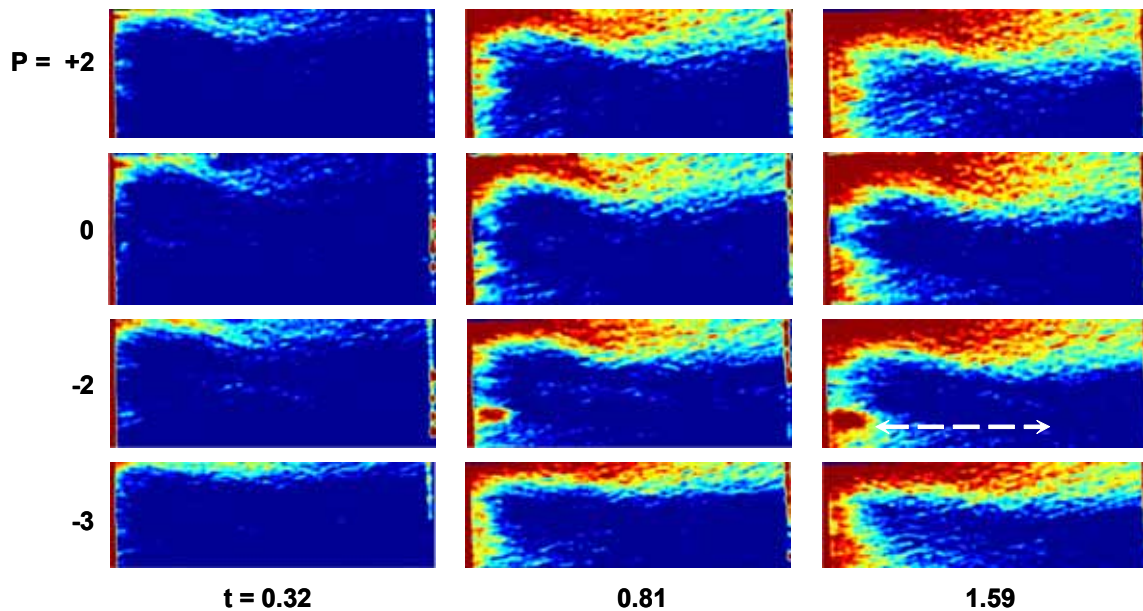


Fig. 2.38. Axial CT images of Foam B with tracer displacing steady-state Foam B at three dimensionless times.

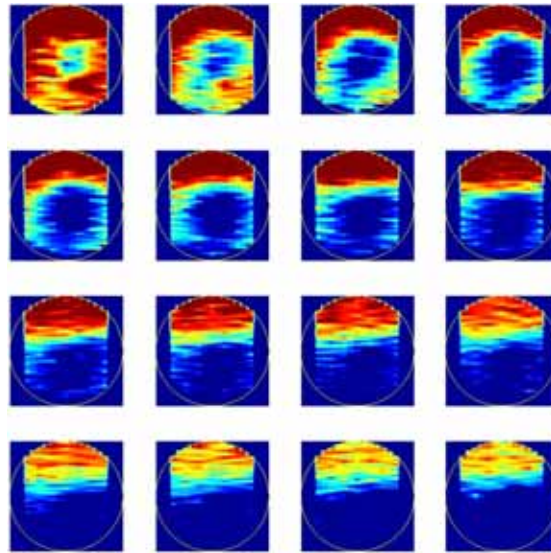


Fig. 2.39. Reconstructed cross-sectional CT images for tracer in Foam B at 2.14 PV injection. Cross-sections are spaced about 1 cm apart along the core.

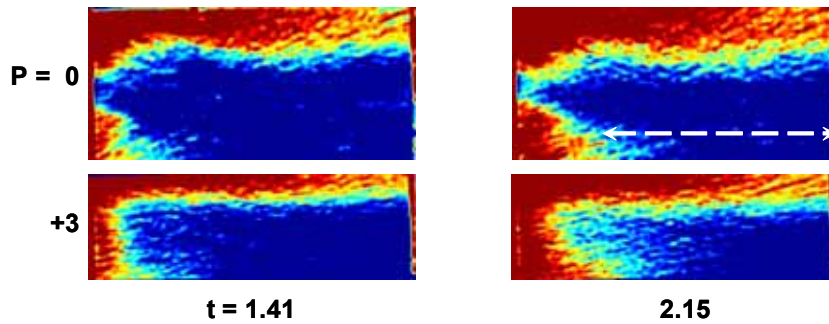


Fig. 2.40. Axial CT images of Foam C with tracer displacing steady-state Foam C at two dimensionless times.

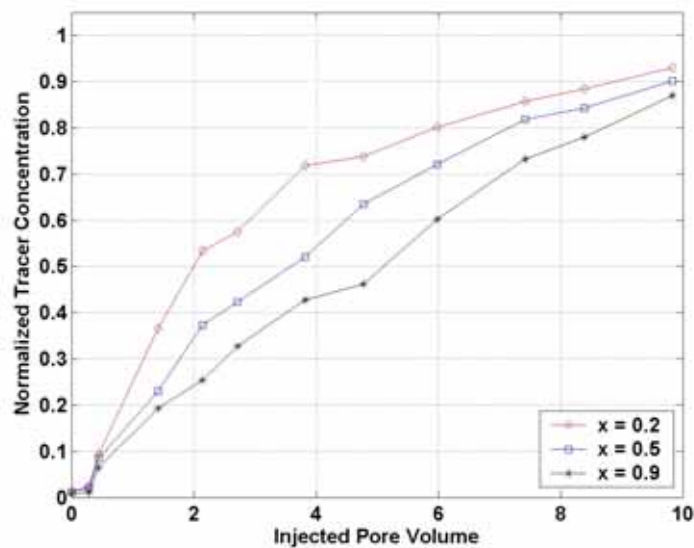


Fig. 2.41. Cross-section-average fraction of tracer in gas phase as a function of dimensionless time at three positions along core from CT images.

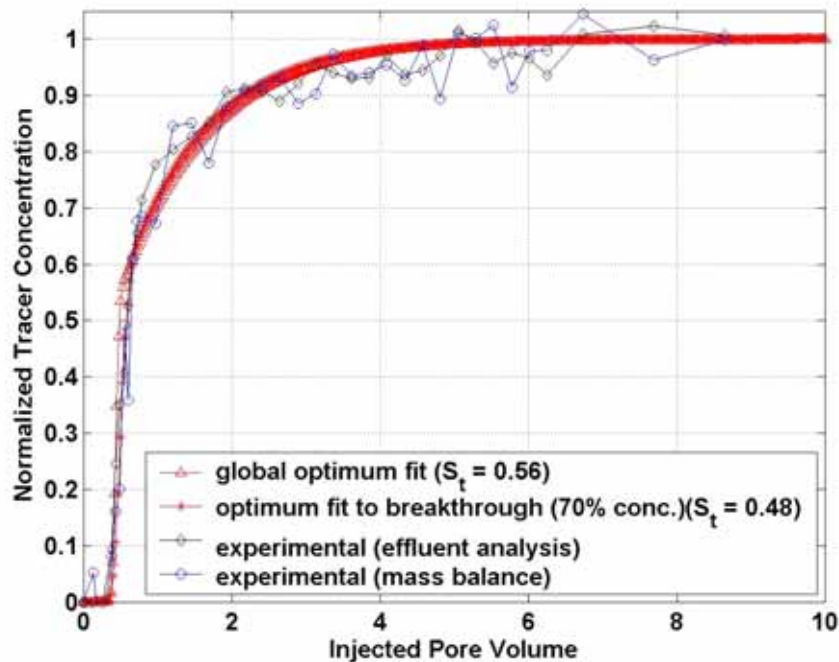


Fig. 2.42. Effluent tracer concentration data for Foam B. Also shown is the global optimal fit of the 1D model, with $S_t = 0.56$, and an optimal fit to the breakthrough of tracer (up to effluent concentration 70% of injected), giving a fitted value of $S_t = 0.48$.

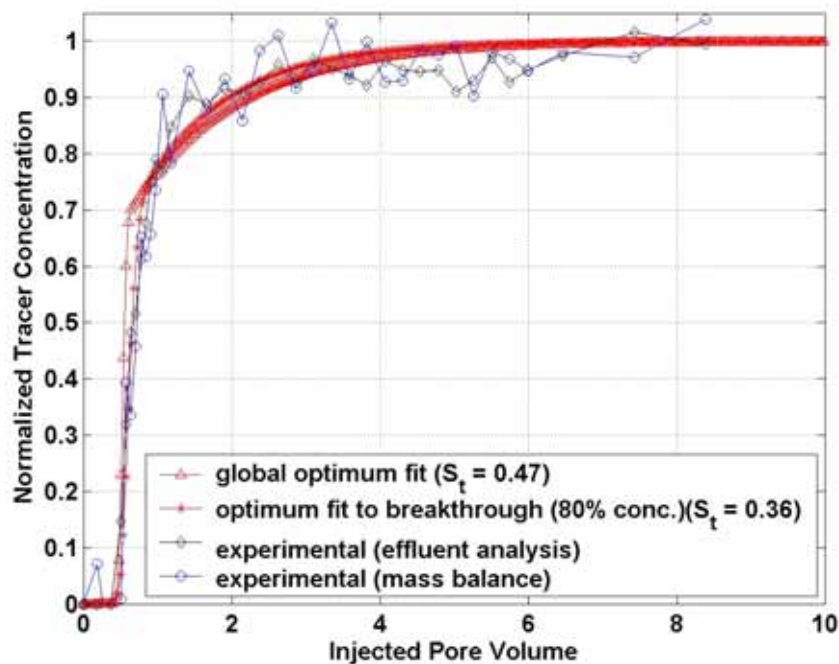


Fig. 2.43. Effluent tracer concentration data for Foam C. Also shown is the global optimal fit of the 1D model, with $S_t = 0.47$, and an optimal fit to the breakthrough of tracer (up to effluent concentration 80% of injected), giving a fitted value of $S_t = 0.36$.

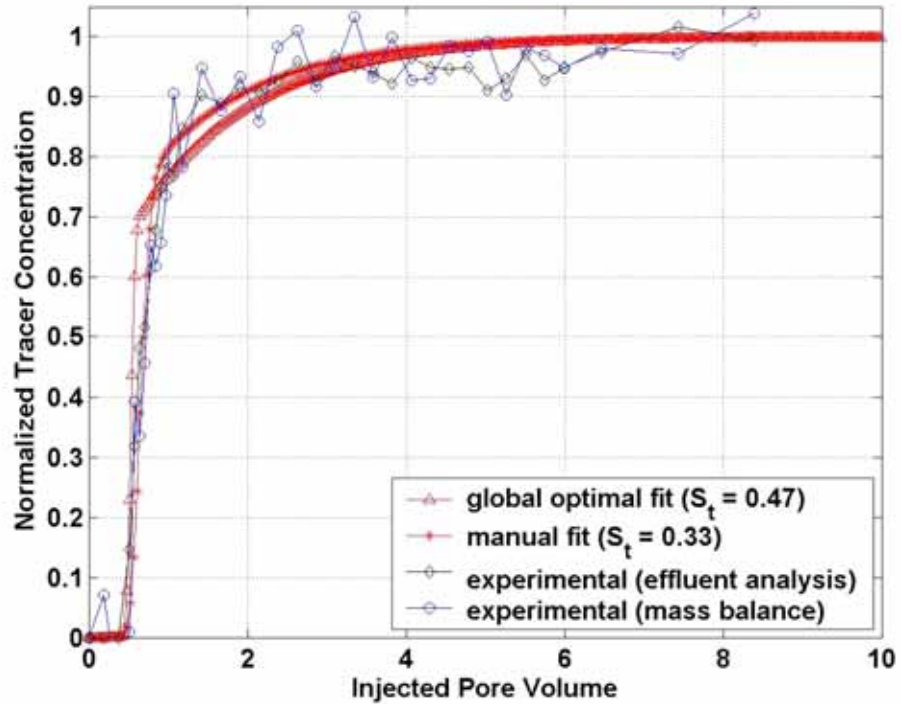


Fig. 2.44. Comparison of global optimal fit (with $S_t = 0.47$) to effluent tracer data for Foam C to manual fit to data with $S_t = 0.33$.

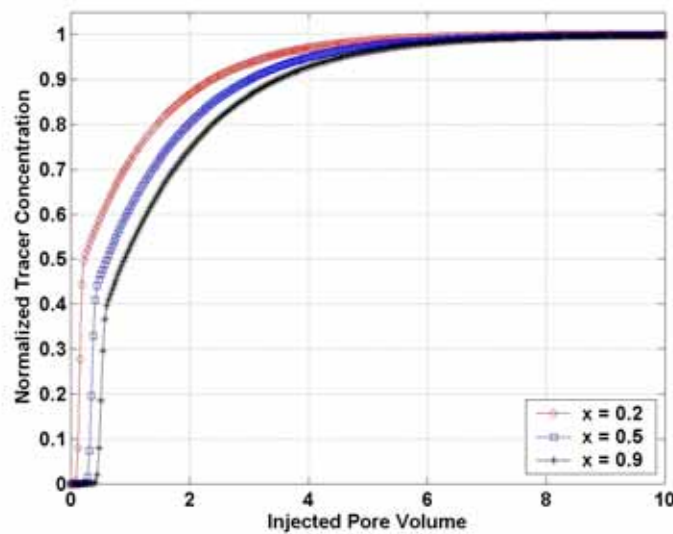


Fig. 2.45. Cross-section-average fraction of tracer in both trapped and flowing gas, derived from global optimum fit of 1D model to effluent data for Foam C (Fig. 2.43) at three locations along core; *cf.* Fig. 2.41.

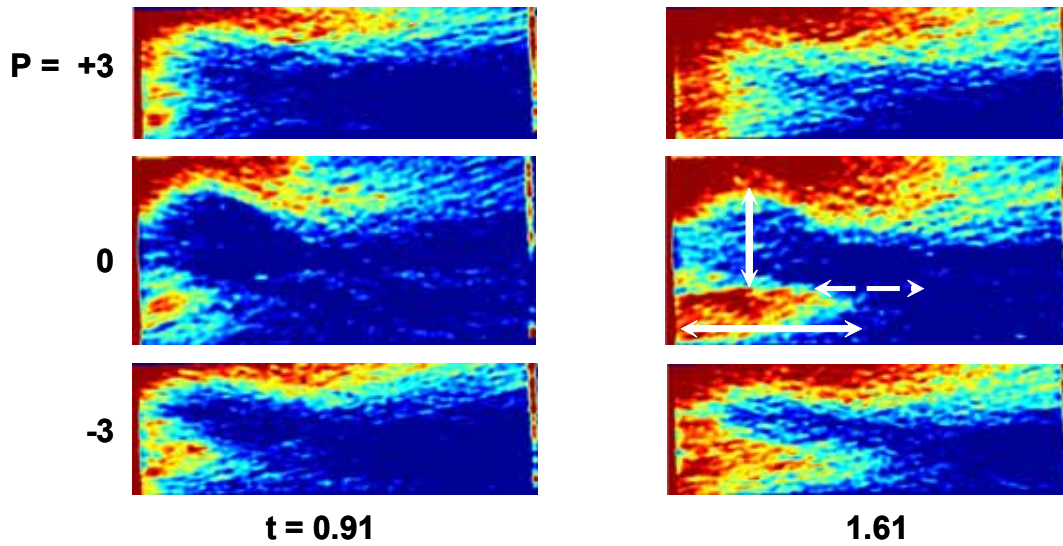


Fig. 2.46. Axial CT images of Foam D with tracer displacing steady-state Foam D at two dimensionless times.

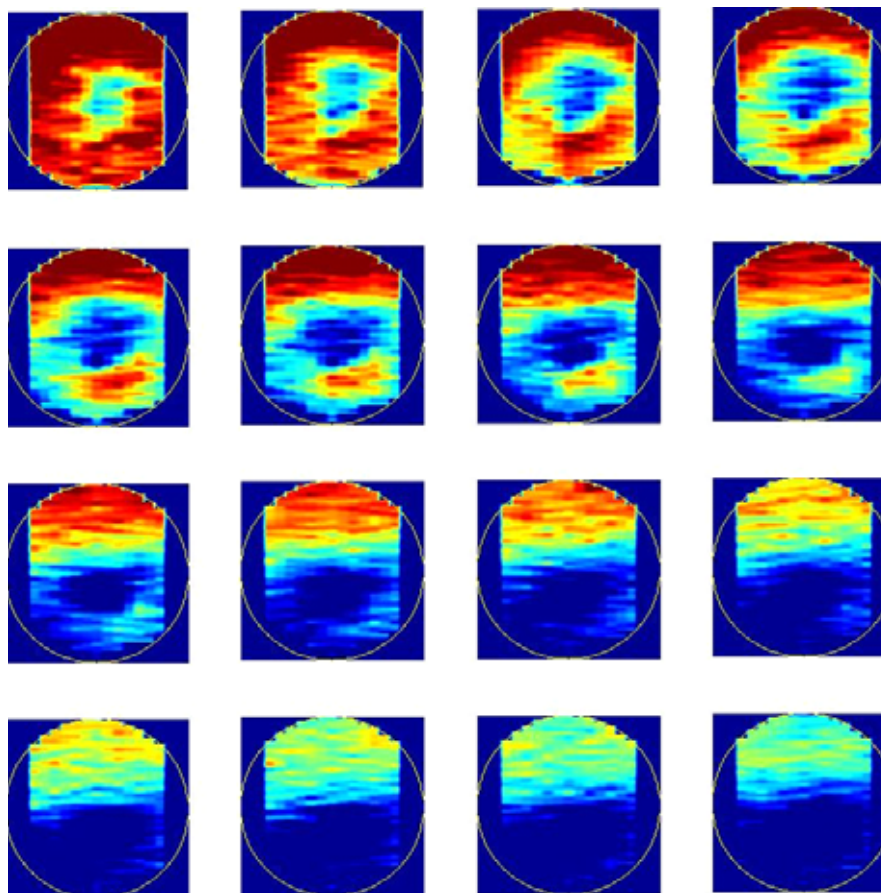


Fig. 2.47. Reconstructed cross-sectional CT images for tracer in Foam D at 2.14 PV injection. Cross-sections are spaced about 1 cm apart along the core.

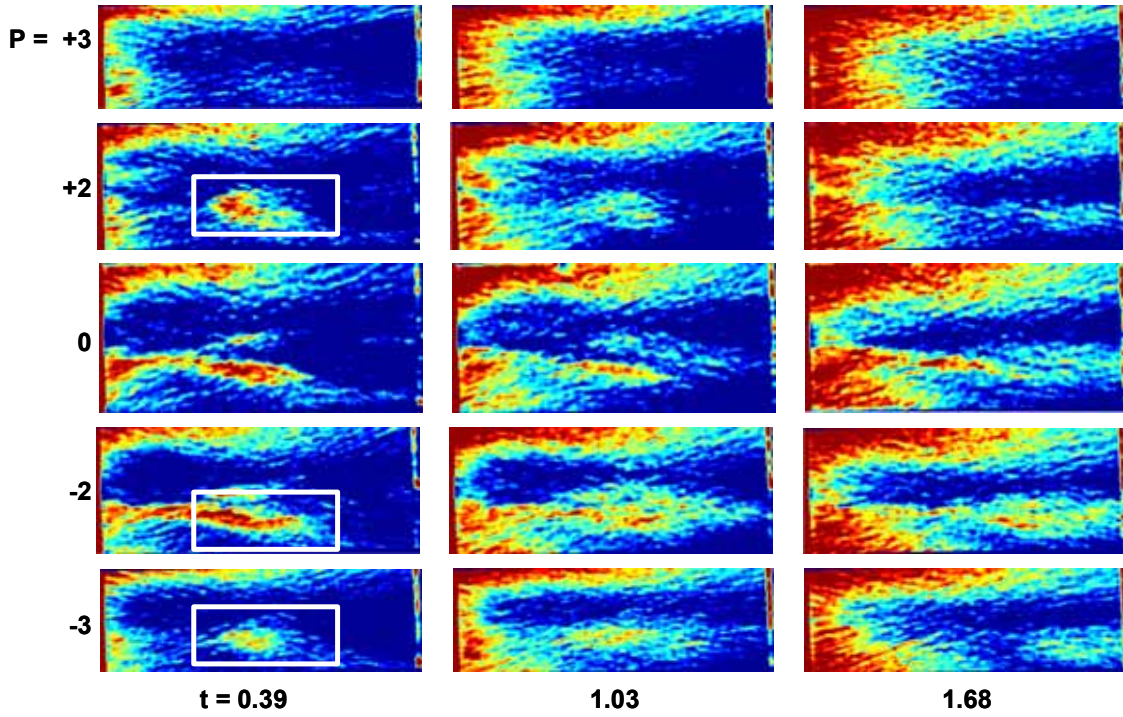


Fig. 2.48. Axial CT images of Foam E with tracer displacing steady-state Foam E at three dimensionless times.

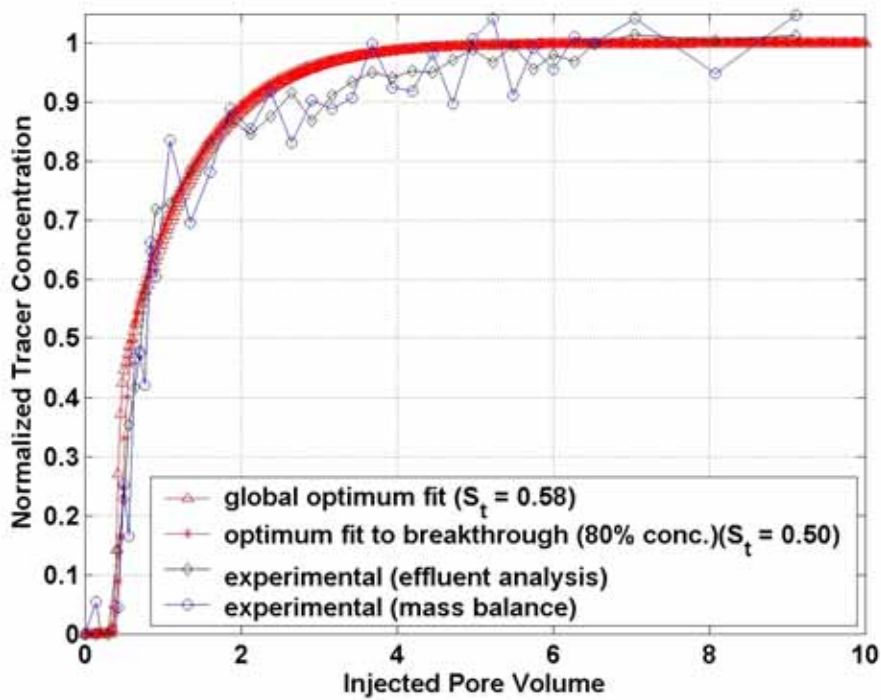


Fig. 2.49. Effluent tracer concentration data for Foam D. Also shown is the global optimal fit of the 1D model, with $S_t = 0.58$, and an optimal fit to the breakthrough of tracer (up to effluent concentration 80% of injected), giving a fitted value of $S_t = 0.50$.

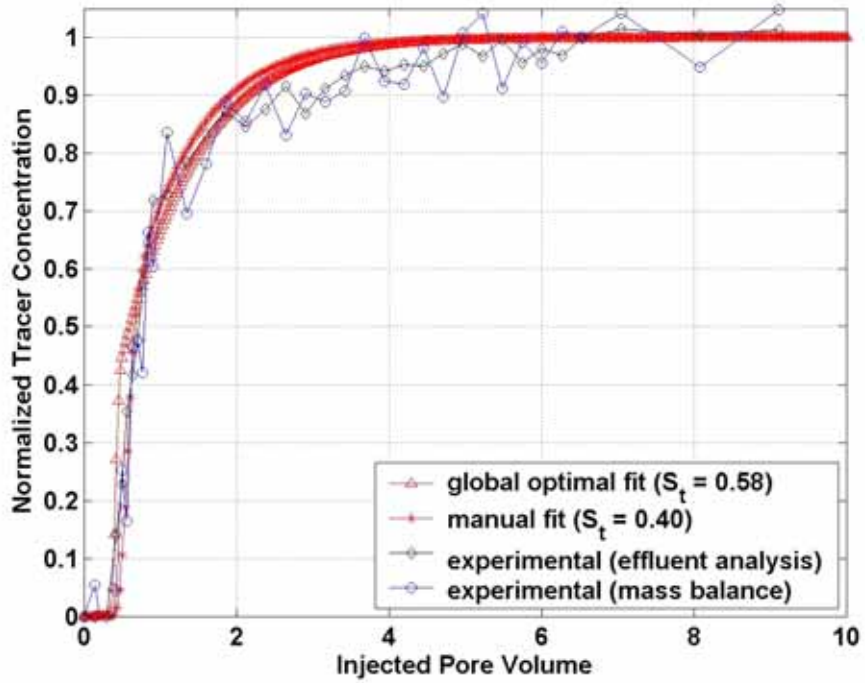


Fig. 2.50. Comparison of global optimal fit (with $S_t = 0.58$) to effluent tracer data for Foam D to manual fit to data with $S_t = 0.40$.

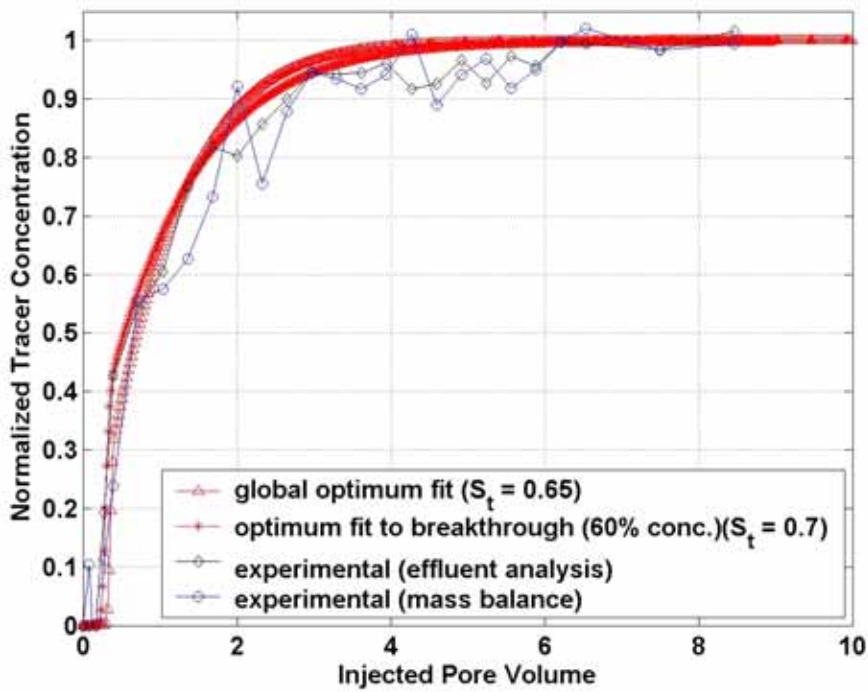


Fig. 2.51. Effluent tracer concentration data for Foam E. Also shown is the global optimal fit of the 1D model, with $S_t = 0.65$, and an optimal fit to the breakthrough of tracer (up to effluent concentration 60% of injected), giving a fitted value of $S_t = 0.70$.

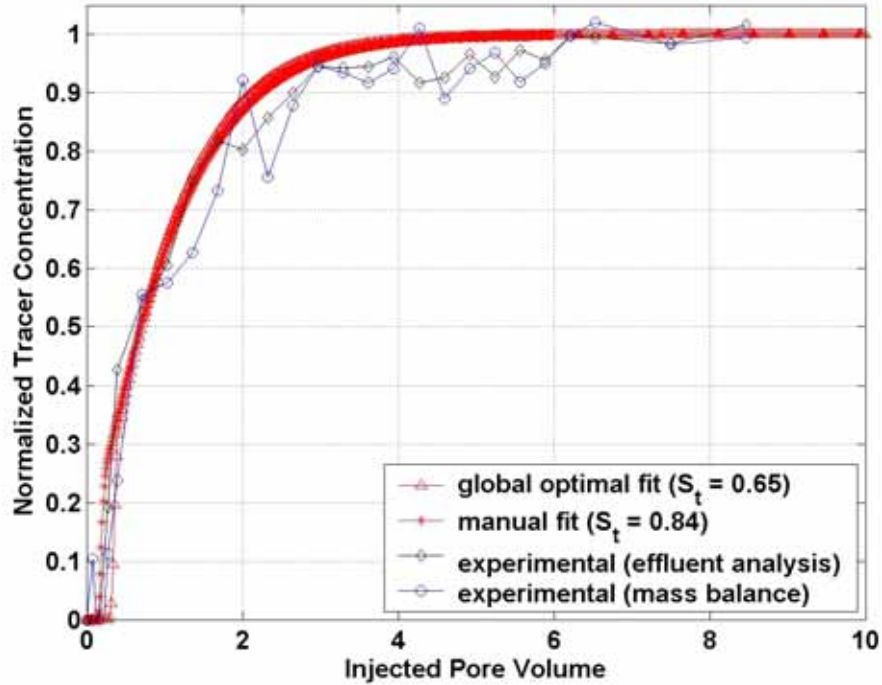


Fig. 2.52. Comparison of global optimal fit (with $S_t = 0.65$) to effluent tracer data for Foam E to manual fit to data with $S_t = 0.78$.

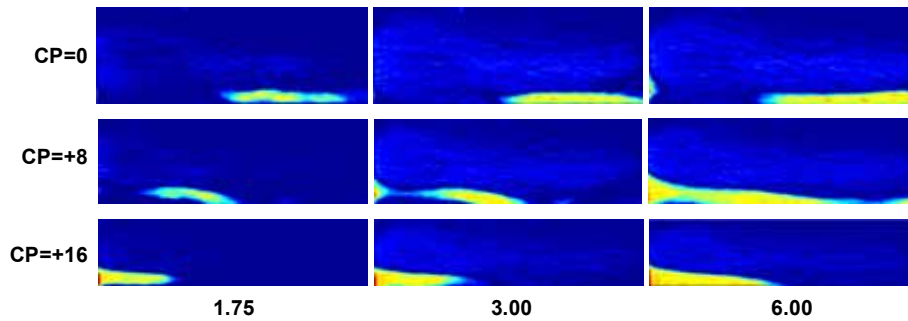


Fig. 2.53. Axial CT images of liquid saturation as surfactant solution displaces Foam A in a Bentheim core at dimensionless times 1.75, 3.00 and 6.00. The liquid finger has an asymmetrical structure spanning image planes from $P = 0$ to $P = +16$. Dark blue represents $S_w = 0$, light blue $S_w = 0.5$, yellow $S_w = 0.75$, and deep red $S_w = 1$.

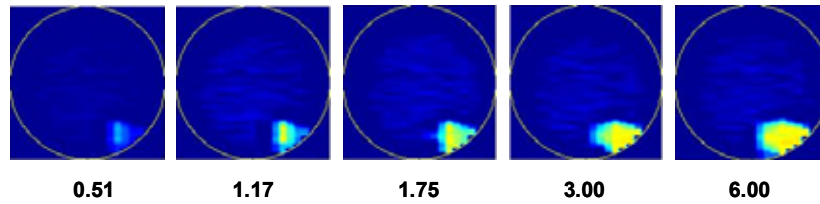


Fig. 2.54. Reconstructed cross-sectional CT images of liquid saturation at an axial position about 2 cm from the inlet, at various values of dimensionless time, as surfactant solution displaces Foam A in the Bentheim core.

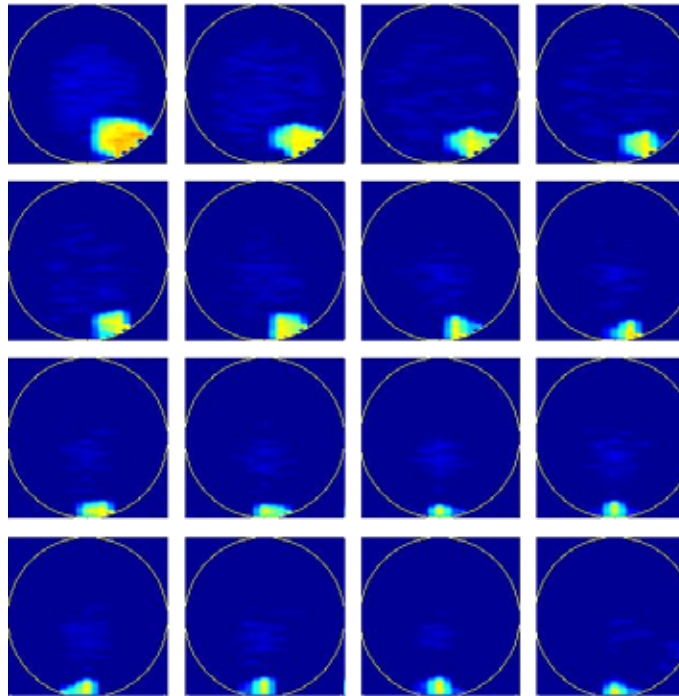


Fig. 2.55. Reconstructed cross-sectional CT images of liquid saturation as surfactant solution displaces Foam A in the Bentheim core, at equally spaced axial positions from the inlet to the outlet, at a dimensionless time of 3.00.

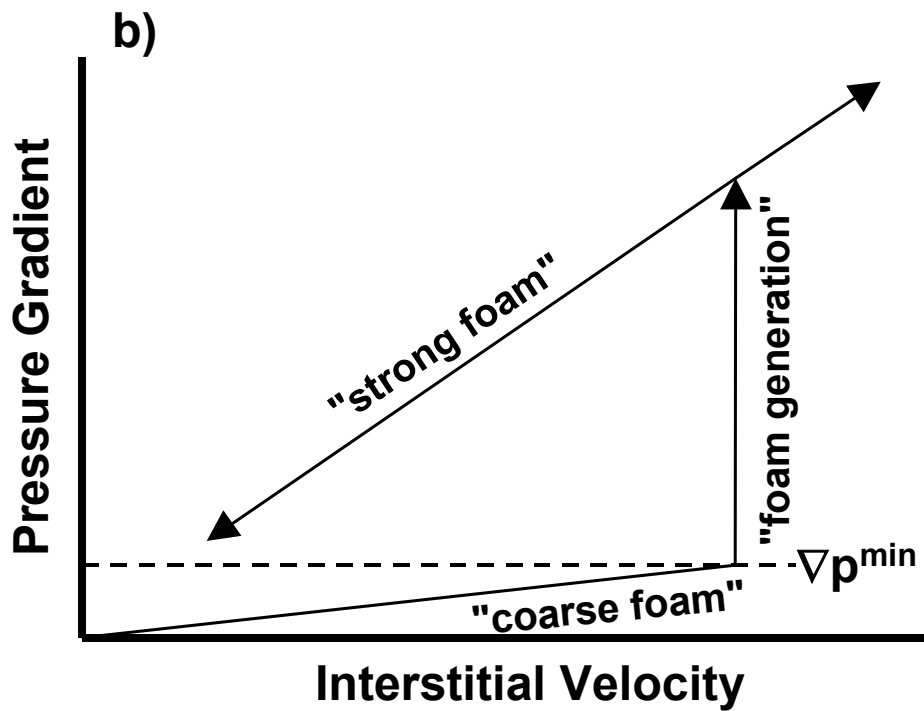


Fig. 3.1. Schematic of minimum pressure gradient for foam generation as seen in experiments at a fixed injection rate that is steadily increased; relation between pressure gradient and interstitial velocity.

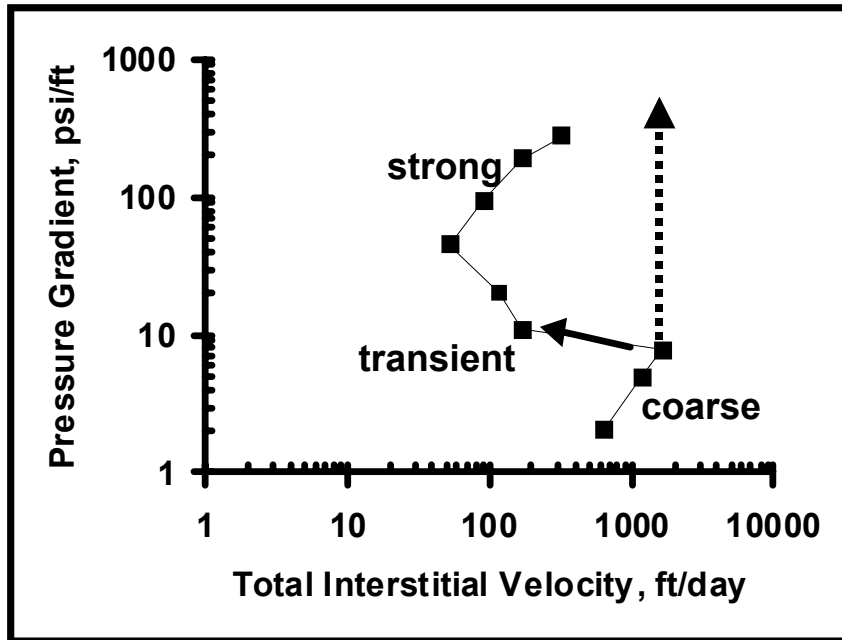


Fig. 3.2. Total interstitial velocity as a function of pressure gradient for one surfactant formulation in Boise sandstone. Dark arrow indicates start of foam generation in experiment with fixed pressure drop across core. Dotted arrow indicates sudden rise in pressure gradient that would be observed upon foam generation in an experiment at fixed injection rates (*cf.* Fig. 3.1).

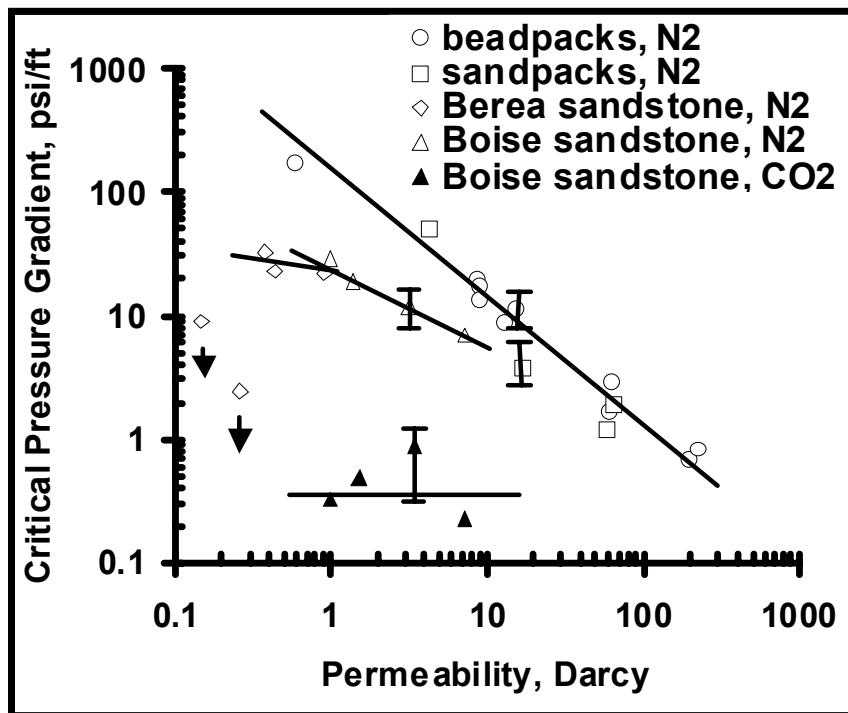


Fig. 3.3. Minimum pressure gradient for foam generation as a function of permeability for several N₂ and CO₂ foams.

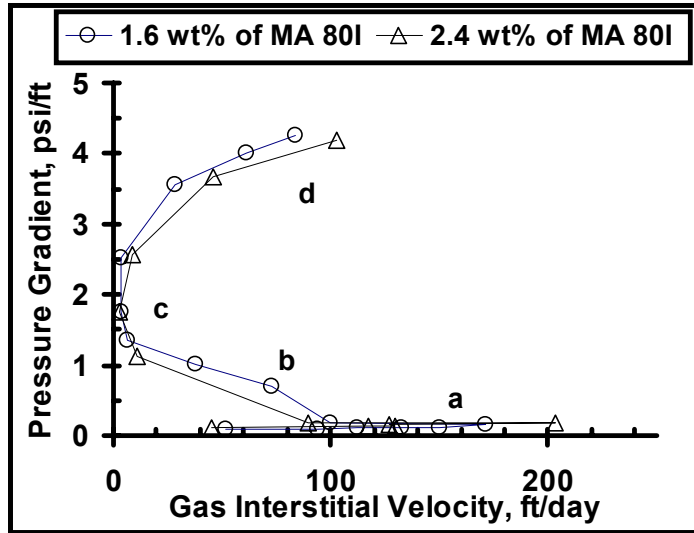


Fig. 3.4. Pressure gradient as a function of gas interstitial velocity for two experiments with gas injection at constant pressure drop and liquid injection at constant flow rate. (Interstitial velocity of liquid is set at 1.09 ft/day for surfactant MA 80I surfactant in a beadpack with $\phi=0.31$, $k=30.4$ Darcy).

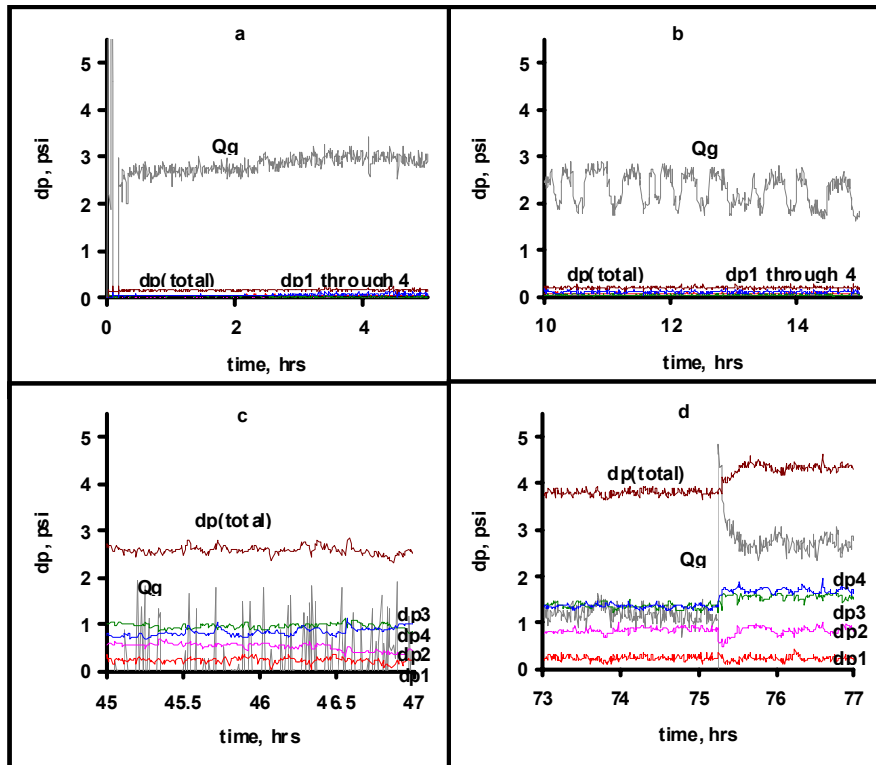


Fig. 3.5. Response of gas flow rate during the monotonic increase in pressure gradients in Fig. 3.4. Cases a, b, c, and d correspond to the points in Fig. 3.4. dp1 through dp4 indicate pressure drops in each section of the pack. Note instability of gas rate in intermediate regime (points b and c).

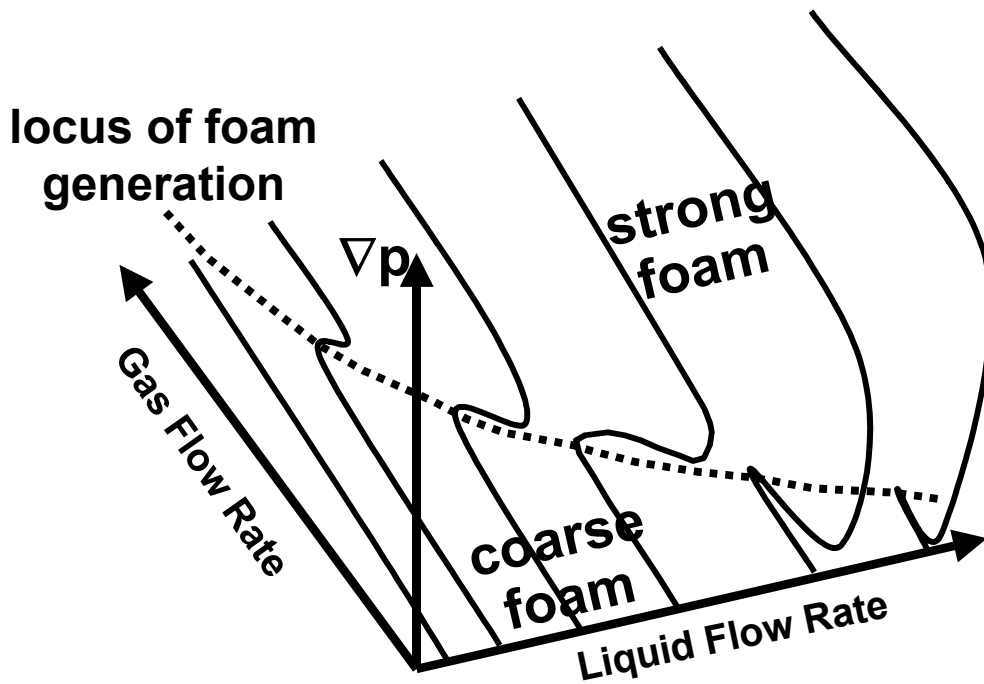


Fig. 3.6. Schematic of surface defining pressure gradient as function of injection rates of liquid and gas, locus of foam generation at folding of this surface, and coarse-foam and strong-foam regimes. Solid curves schematically represent data at fixed liquid flow rate.

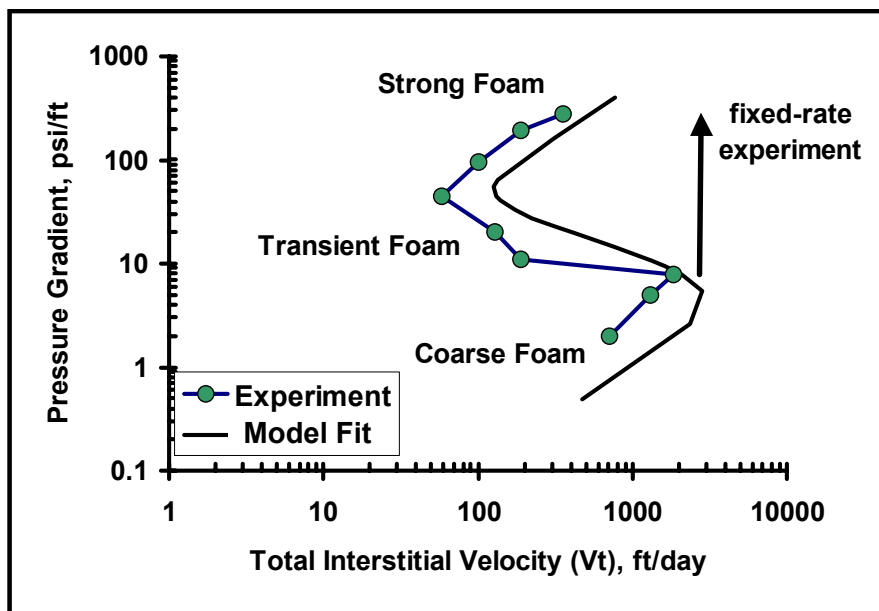


Fig. 3.7. Laboratory data for foam generation in a Berea core (Fig. 3.2) fit by a population-balance model that incorporates foam generation triggered by pressure gradient. In this example pressure gradient and nominal foam quality are held fixed in both the experiment and the model, and total flow rate responds to the creation and rheology of foam.

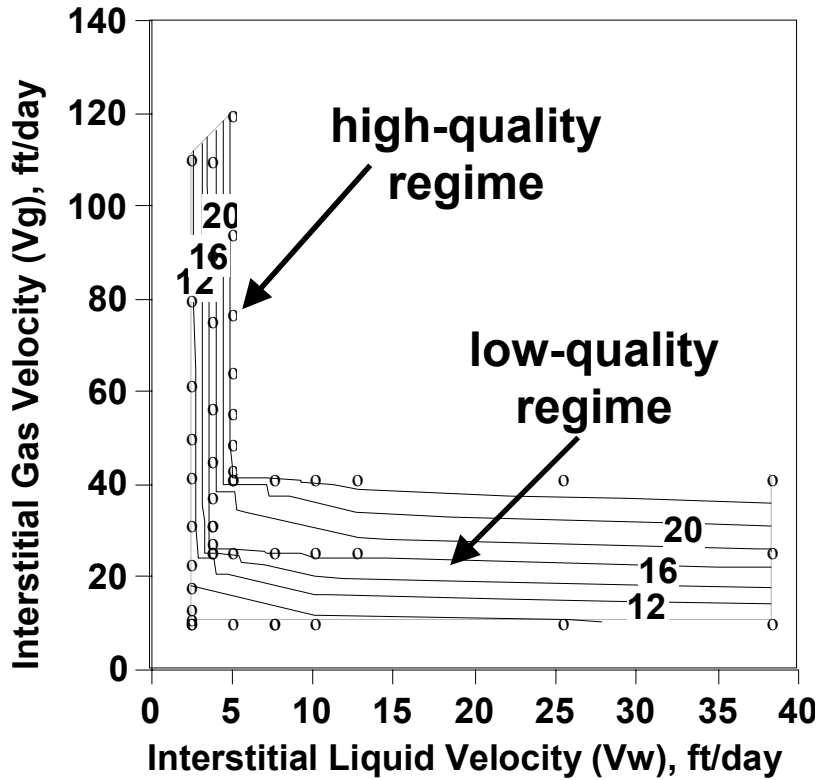


Figure 3.8. Steady-state pressure gradient as a function of interstitial velocities of gas and liquid in a beadpack predicted by a population-balance foam model that incorporates foam generation triggered by pressure gradient. Note high-quality regime (vertical ∇p contours at upper left) and low-quality regime (lower right). Circles represent points where model properties were calculated, not data points.

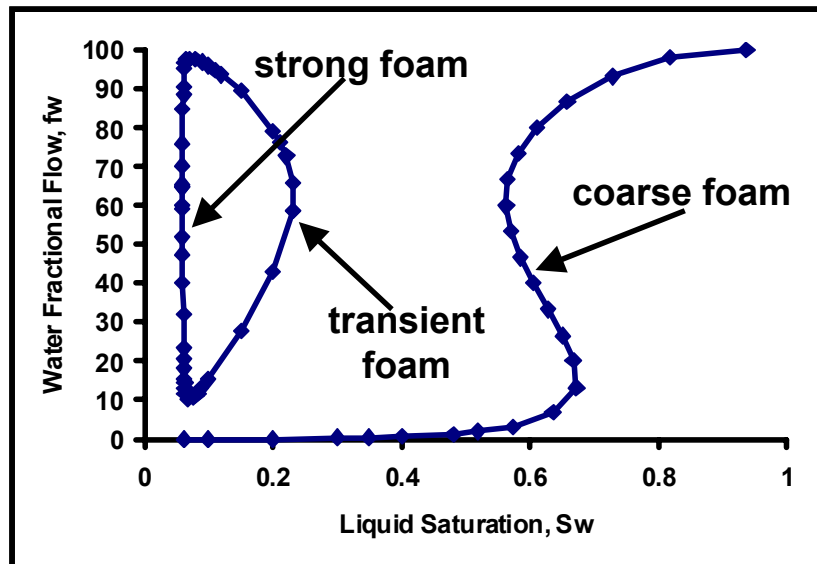


Figure 3.9. Example fractional-flow curve predicted by population-balance foam model that incorporates foam generation triggered by pressure gradient.

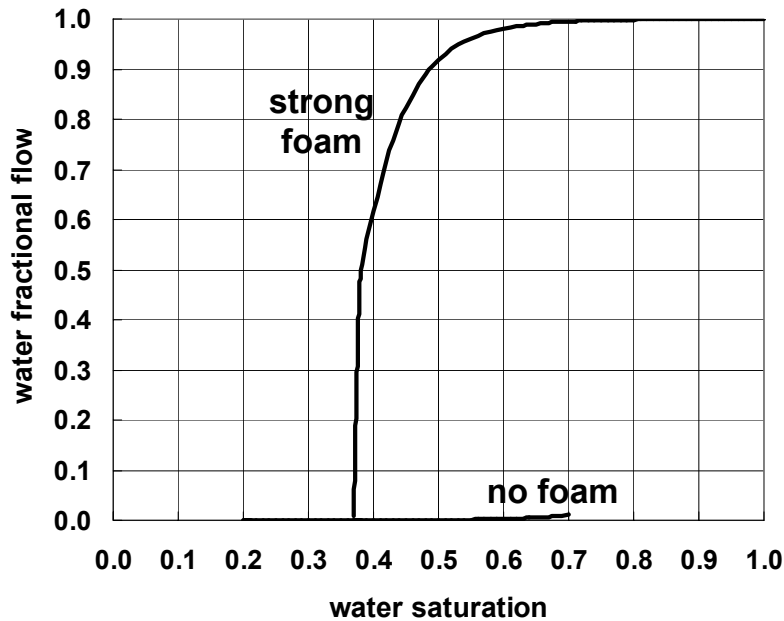


Fig. 3.10. Foam model used in study of foam displacement with abrupt changes of state, with two foam states, "strong foam" and "no foam." Strong foam reverts to no-foam (foam collapse) if S_w falls below 0.37 (corresponding to the "limiting capillary pressure"); no-foam reverts to strong foam for $S_w > 0.7$ (foam generation). The strong-foam curve ends at $f_w = 0.0075$; there is a jump between curves below this point not obvious on this scale. Model details are in Rossen and Bruining (2004).

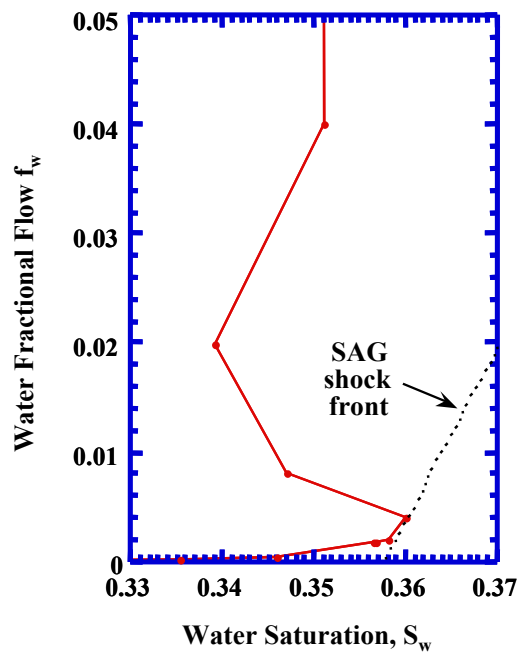


Fig. 3.11. Experimental $f_w(S_w)$ curve for strong foam from Kibodeaux and Rossen (1997) including shock (incorrectly) suggested by them for SAG displacement.

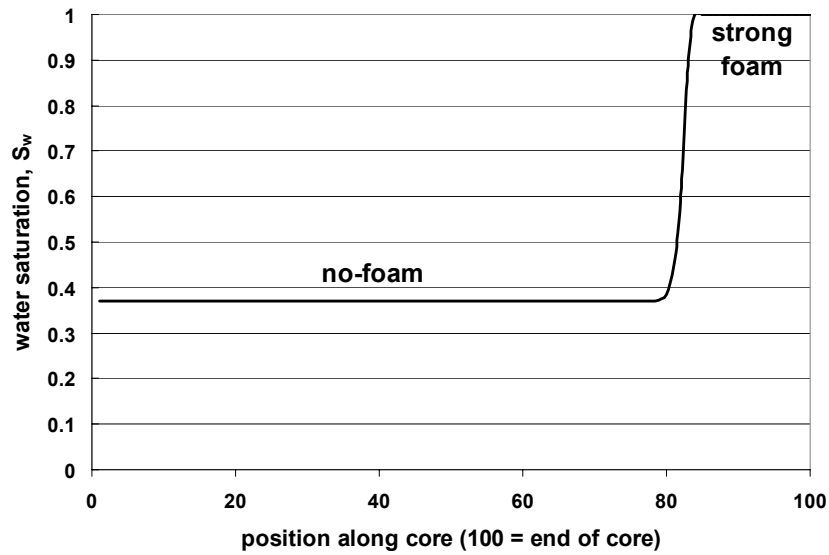


Fig. 3.12. Finite-difference simulation of gas injection into a liquid-saturated medium, with no difference in capillary-pressure functions between strong foam and no-foam, after 0.514 PV gas injection. In this case, 100 grid blocks represent a 0.6-m long core. In this example, foam collapses completely at the shock front at the leading edge of the gas bank.

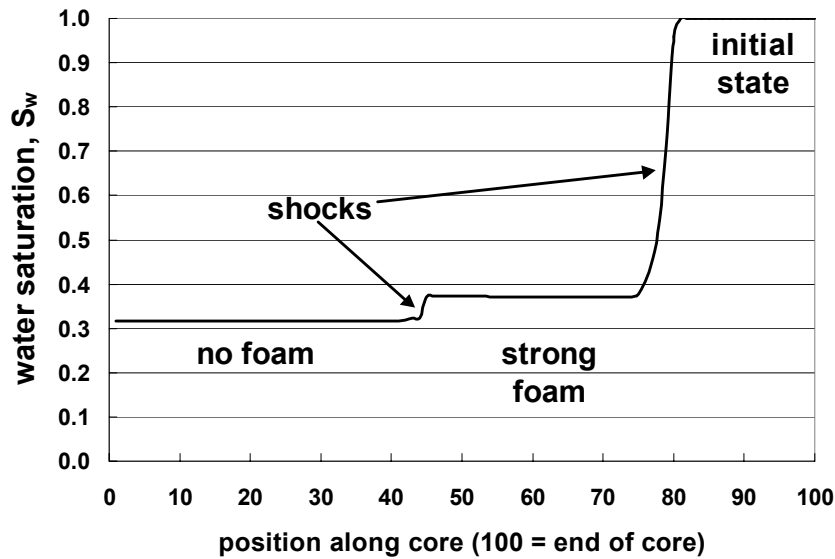


Fig. 3.13. Finite-difference simulation of gas injection into a liquid-saturated medium, with higher capillary pressure for strong foam, after 0.514 PV gas injection. The only difference with Fig. 3.12 is that here there is a higher $P_c(S_w)$ function for strong foam than no-foam; this introduces an additional foam bank into the displacement.

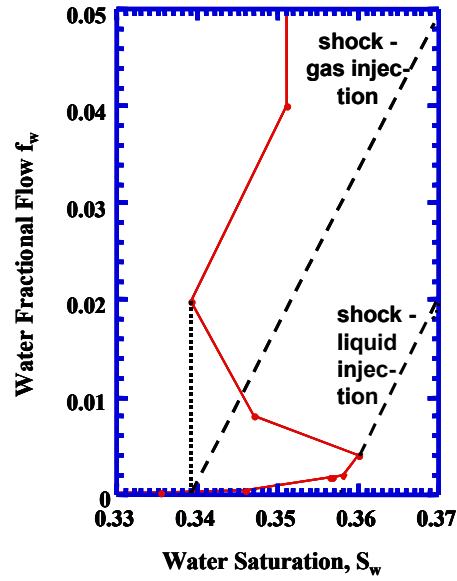


Fig. 3.14. Revised construction of shocks based on fractional-flow data of Kibodeaux and Rossen (1997) (*cf.* Fig. 3.11), assuming equal capillary pressure for strong and weak foam. Shock for gas injection would occur to lower portion of fractional-flow curve at same capillary pressure as the lowest- S_w point on the upper portion of curve (just before (df_w/dS_w) reverses sign). This results in poorer mobility control than suggested by Kibodeaux and Rossen based on their graphical construction in Fig. 3.11. The shock for a process of liquid injection after foam would occur from lower portion of fractional-flow curve to portion of curve at much higher fractional flow (not shown on this scale).

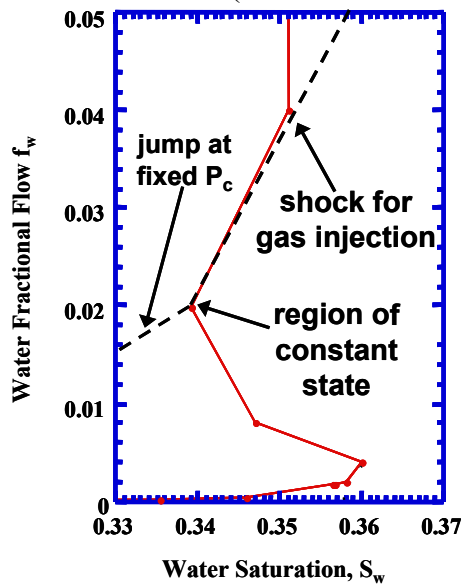


Fig. 3.15. Revised construction of shock for gas injection based on fractional-flow data of Kibodeaux and Rossen (1997) (*cf.* Fig. 3.11), assuming higher capillary pressure for strong foam. In this case there is an intermediate region of constant state of strong foam (*cf.* Fig. 3.13) at much lower mobility than any bank in Fig. 3.14. Mobility control would be significantly more effective than suggested by Kibodeaux and Rossen based on their graphical construction, and greatly more effective than suggested by Fig. 3.14.

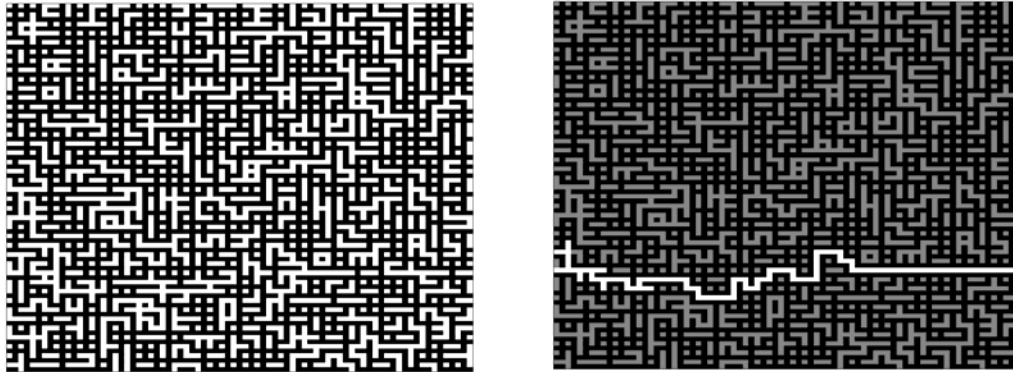


Fig. 3.16. Two snap-shots of lamella positions (dark black lines) from one network simulation at different times, illustrating how foam can be created by capillary fluctuations and mobilization near a core inlet. At the left, gas flow is completely blocked. Mobilization of lamellae leads to a path illustrated on the right (where the remainder of the gas is shaded gray), with no lamellae blocking flow. As a result, ∇p is briefly low in the gas phase, much lower than in the liquid phase. This causes capillary pressure to fall near the inlet and trigger snap-off, which returns the medium to the state shown on the left. This mechanism of snap-off, triggered by low P_c , is distinct from Roof snap-off discussed earlier in this report.

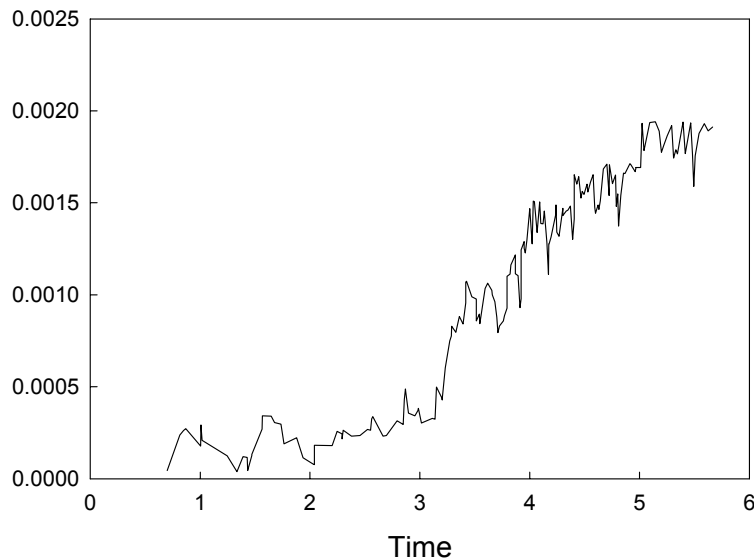


Fig. 3.17. Gas flow rate as a function of time in a network simulation of foam mobilization and generation. At the end of the cycle, a continuous gas path opens, $|\nabla p|$ falls to repeat the cycle, new lamellae are generated by capillary pressure, and the process is repeated indefinitely.

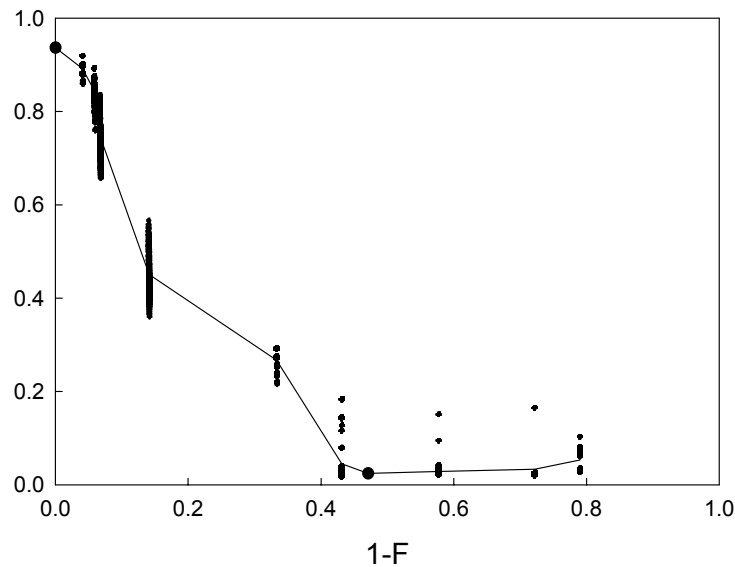


Fig. 3.18. Plot of minimum pressure gradient required to mobilize lamellae as a function of fraction of throats not currently blocked by lamellae ($1-F$). Individual points represent individual network realizations, and the solid line represents the average result at each value of ($1-F$). Mobilization is a key step in foam generation (Rossen and Gauglitz, 1990). Theory predicts a minimum pressure gradient for mobilization at the percolation threshold, which for square networks as in this study is at 0.5. Previously, however, theory was limited by its questionable assumption of uniform $|\nabla p|$ in the pore network, an assumption not needed in this study.

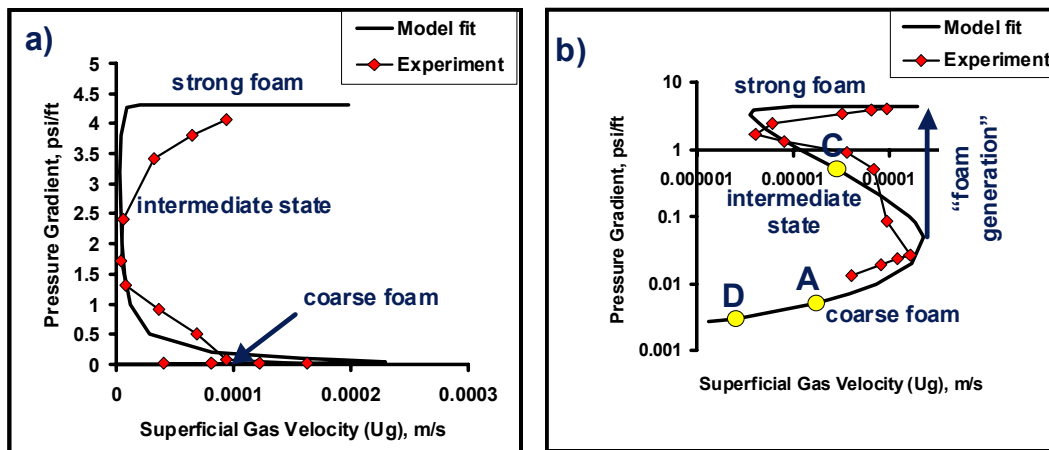


Fig. 3.19. Population-balance model fit (smooth curve) to data (dark diamonds) in which liquid injection rate and pressure drop were fixed across a 1-ft beadpack; a) linear axes. b) log-log axes. Points A, C and D, with pressure gradients of 0.005, 0.5 and 0.003 psi/ft, respectively, correspond to the conditions in Figs. 3.21, 3.23 and 3.24, respectively, below.

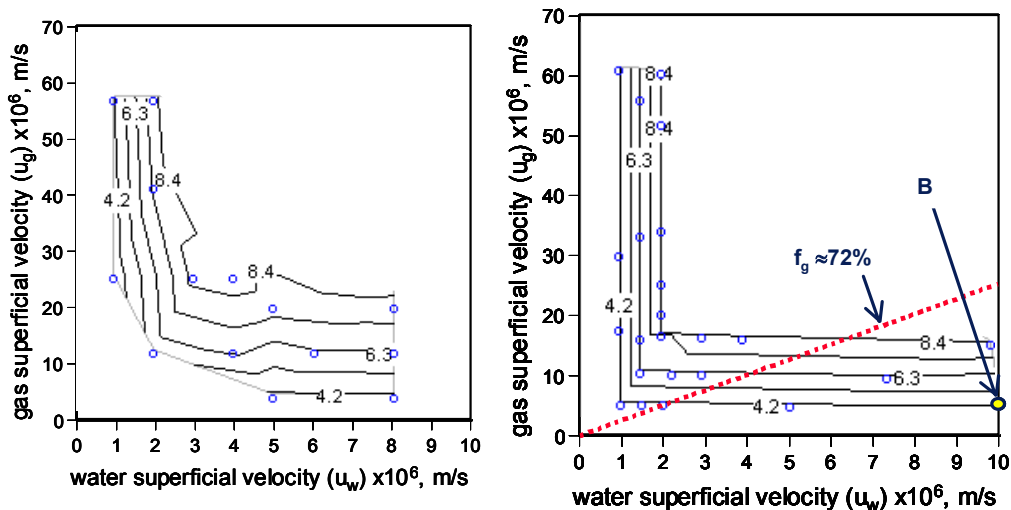


Fig. 3.20. Pressure gradient (psi/ft) as a function of gas and water superficial velocities U_g and U_w in the strong-foam state, for the same surfactant formulation and porous medium as Fig. 3.19. Left: experimental data (open circles). Right: model fit (open circles calculated values). Point B corresponds to the conditions of Fig. 3.22, below. Line represents a fixed foam quality of 72%, the conditions in Figs. 3.24 to 3.27.

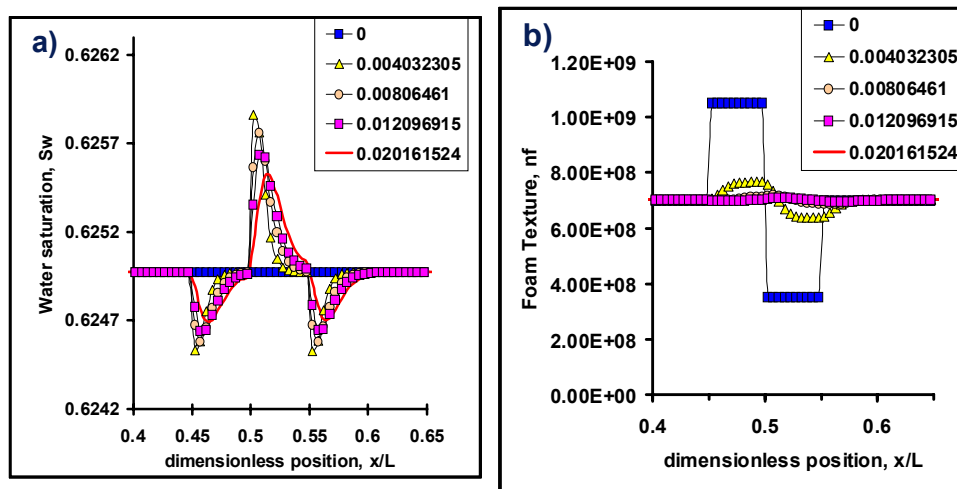


Fig. 3.21. Response of a coarse foam to perturbation in foam texture n_f . Times listed are time since perturbation, in PV injected. There is no initial perturbation in water saturation. Perturbations in S_w and n_f both decrease with time, indicating a stable steady state. Steady-state properties correspond to point A in Fig. 3.19. 200 grid blocks.

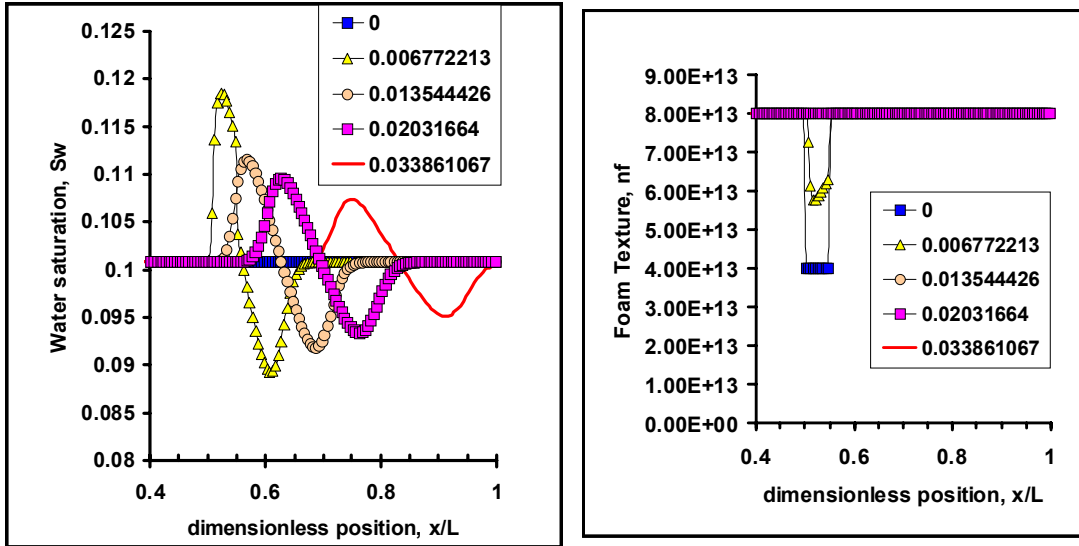


Fig. 3.22. Response of a low-quality-regime strong foam to perturbation in foam texture n_f . Times listed are time since perturbation, in PV injected. There is no initial perturbation in water saturation. Perturbations in S_w and n_f both decrease with time, indicating a stable steady state. Steady-state properties correspond to point B in Fig. 3.20. 200 grid blocks.

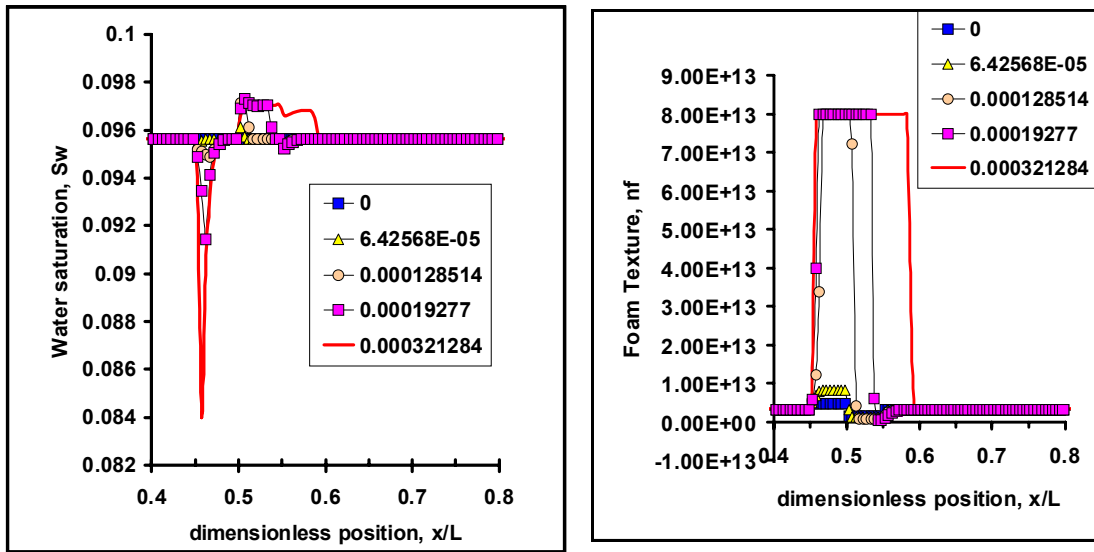


Fig. 3.23. Response of foam in the intermediate state to perturbation in foam texture n_f . Times listed are time since perturbation, in PV injected. There is no initial perturbation in water saturation. The perturbation in S_w grows in magnitude, indicating an unstable steady state, while n_f reaches its limiting upper value defining the low-quality strong-foam state. Steady-state properties correspond to point C in Fig. 3.19. 200 grid blocks.

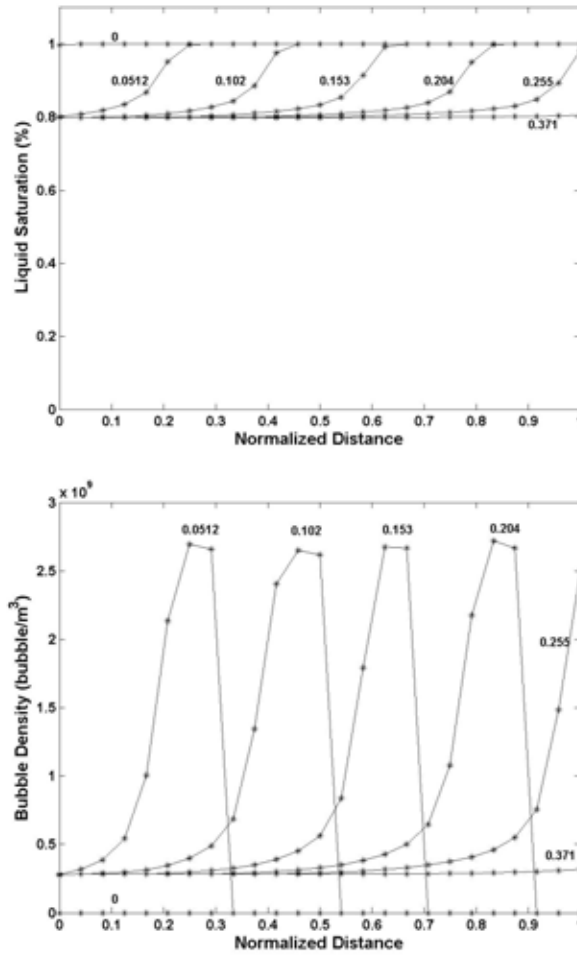


Fig. 3.24. Simulation of co-injection of gas and liquid into a medium saturated with surfactant solution, leading to a coarse-foam state. $U_g = 2.57 \times 10^{-6}$ m/s, $U_w = 1.0157 \times 10^{-6}$ m/s ($U_t = 1.02$ ft/d, $f_g = 0.72$). Steady-state properties correspond to point D in Fig. 3.19. 25 grid blocks, and capillary-pressure gradients neglected.

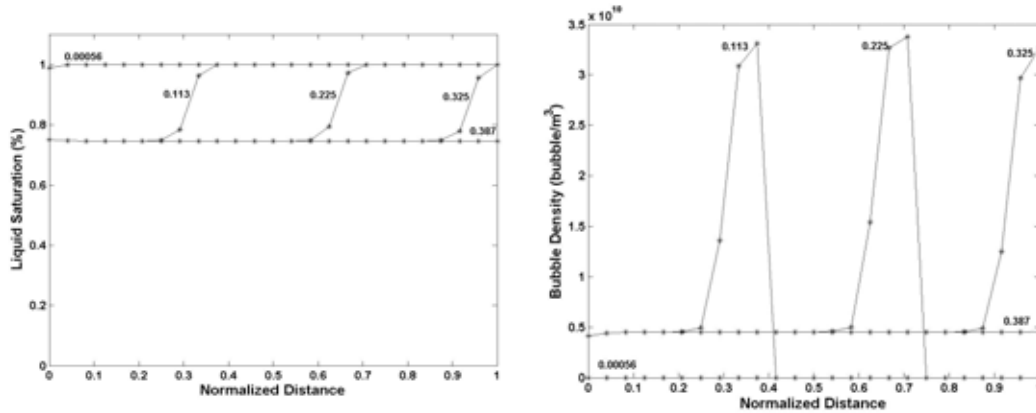


Fig. 3.25. Simulation of co-injection of gas and liquid into a pack saturated with surfactant solution at the same foam quality as Fig. 3.24, at 2.86 times higher injection rate than Fig. 3.24 (2.91 ft/d). 25 grid blocks, and capillary-pressure gradients neglected.

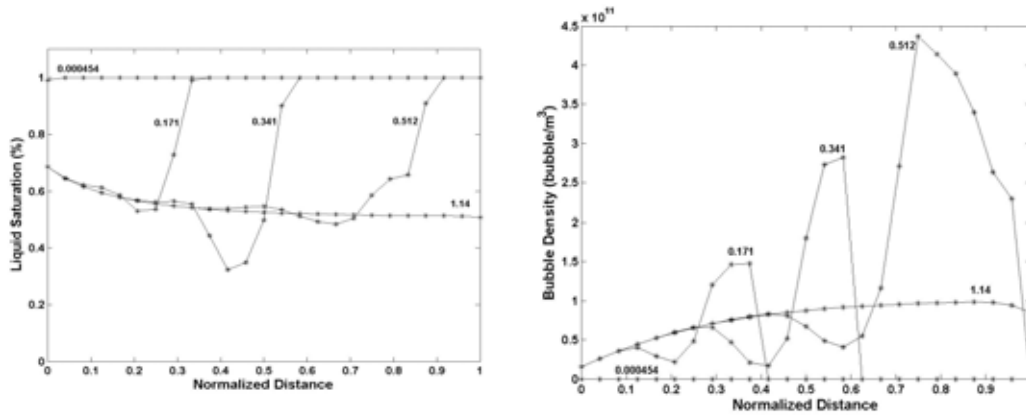


Fig. 3.26. Simulation of co-injection of gas and liquid into a pack saturated with surfactant solution at the same foam quality as Fig. 3.24, at 5.79 times higher injection rate than Fig. 3.24 (5.89 ft/d). 25 grid blocks, and capillary-pressure gradients neglected.

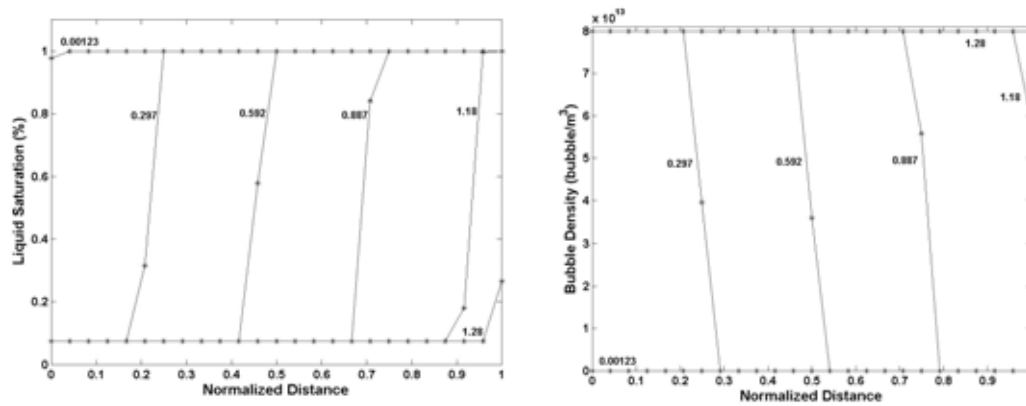


Fig. 3.27. Simulation of co-injection of gas and liquid into a pack saturated with surfactant solution at the same foam quality as Fig. 3.24, at 6.27 times higher injection rate than Fig. 3.24 (6.37 ft/d). 25 grid blocks, and capillary-pressure gradients neglected.

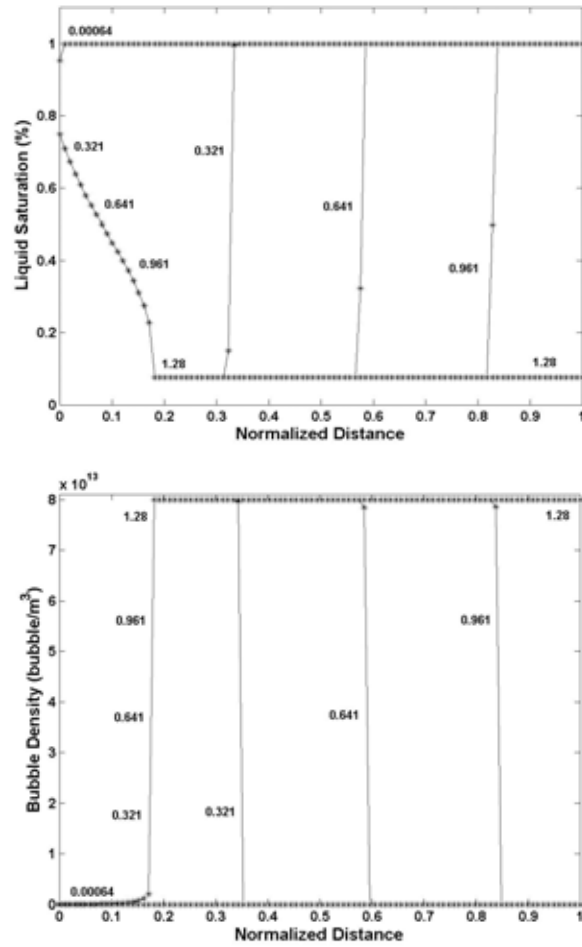


Fig. 3.28. Simulation of a case similar to Fig. 3.27, with both C_c and C_g (Eqs. 3.10 and 3.2) 10 times smaller than in Fig. 3.27. Note the finite region near the inlet in which strong foam is created.

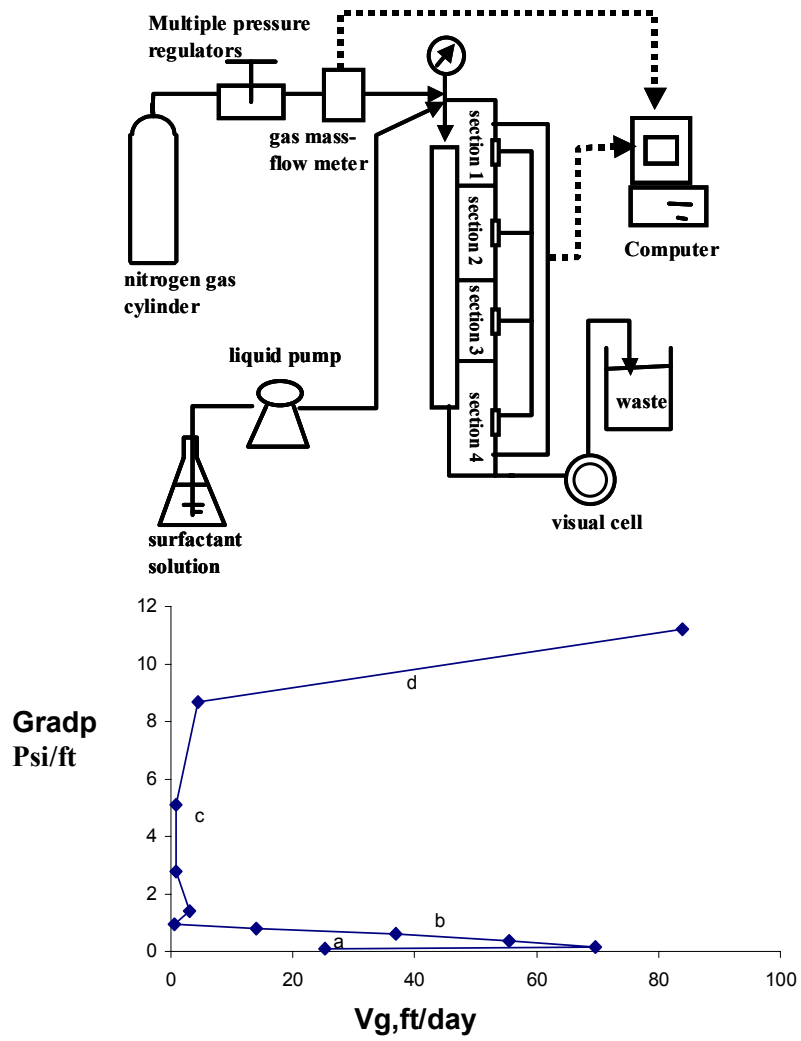


Fig. 3.29. Top: Schematic of sandpack apparatus. Bottom: typical result: pressure gradient as a function of gas interstitial velocity V_g in a 45.5-darcy sandpack; 1 wt% surfactant; liquid interstitial velocity $V_w = 1.745$ ft/day.

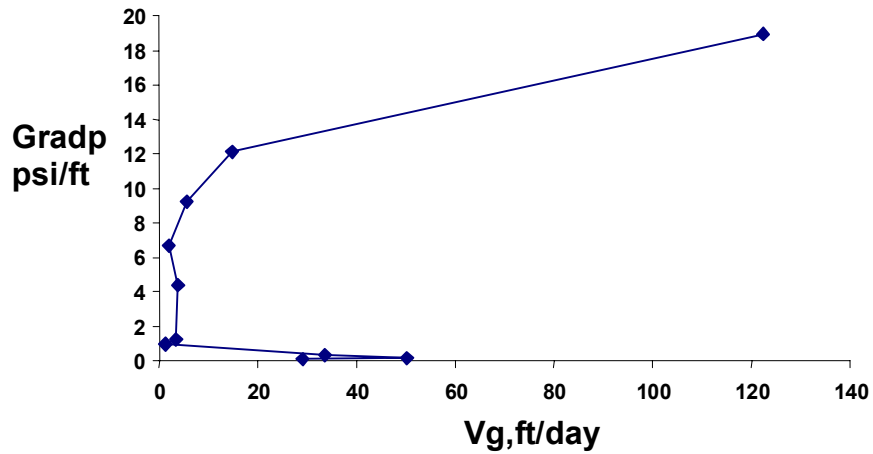


Fig. 3.30. Pressure gradient as a function of gas interstitial velocity V_g in a 45.5-darcy sandpack; 1 wt% surfactant; liquid interstitial velocity $V_w = 6.98$ ft/day.

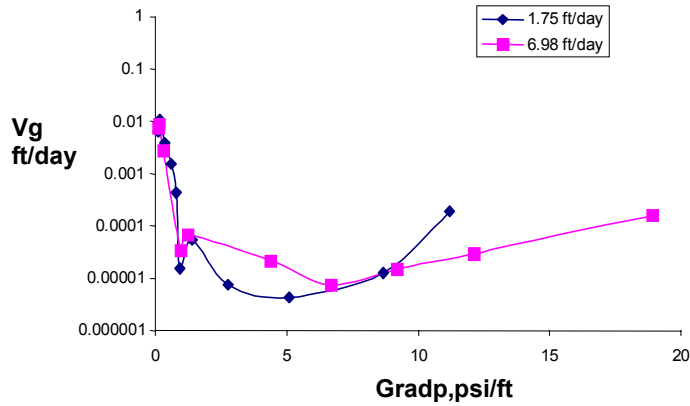


Fig. 3.31. Effective gas relative permeability (incorporating entire effect of foam on gas mobility into gas relative permeability) for experiments in Figs. 3.29 and 3.30.

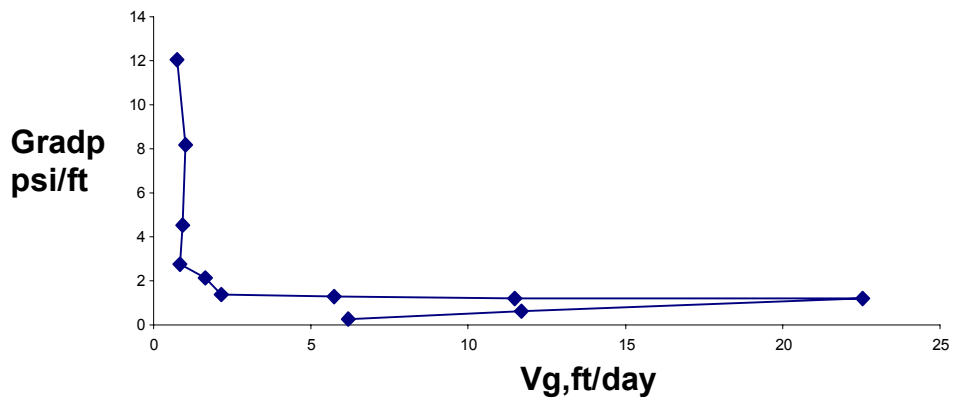


Fig. 3.32. Pressure gradient as a function of gas interstitial velocity V_g in a 7.1-darcy sandpack; 1 wt% surfactant; liquid interstitial velocity $V_w = 13.6$ ft/day.

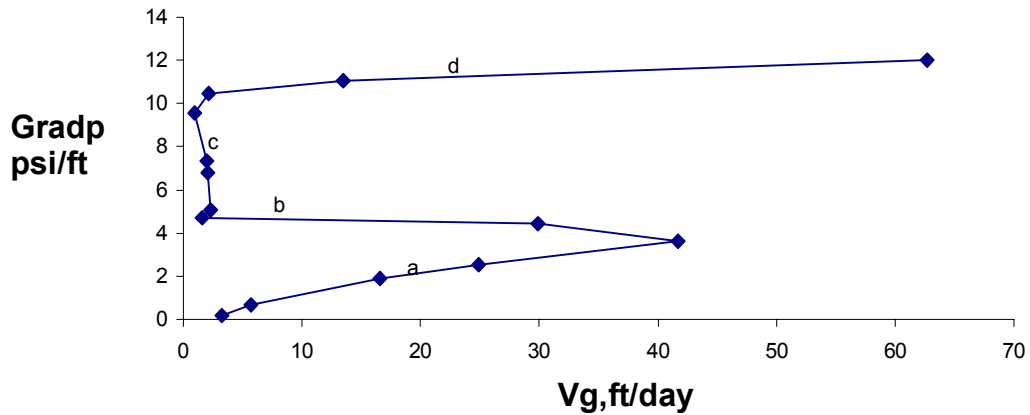


Fig. 3.33. Pressure gradient as a function of gas interstitial velocity V_g in a 7.1-darcy sandpack; 1 wt% surfactant; liquid interstitial velocity $V_w = 6.8$ ft/day.

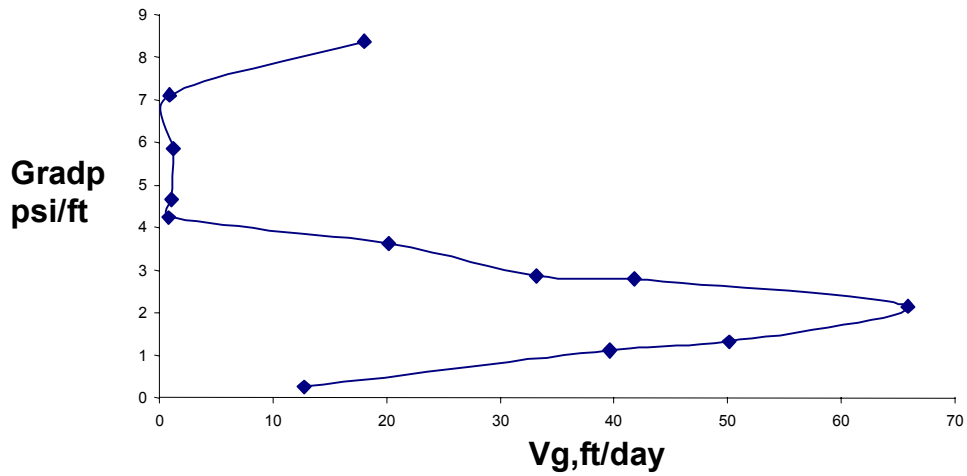


Fig. 3.34. Pressure gradient as a function of gas interstitial velocity V_g in a 7.1-darcy sandpack; 0.1 wt% surfactant; liquid interstitial velocity $V_w = 13.6$ ft/day.

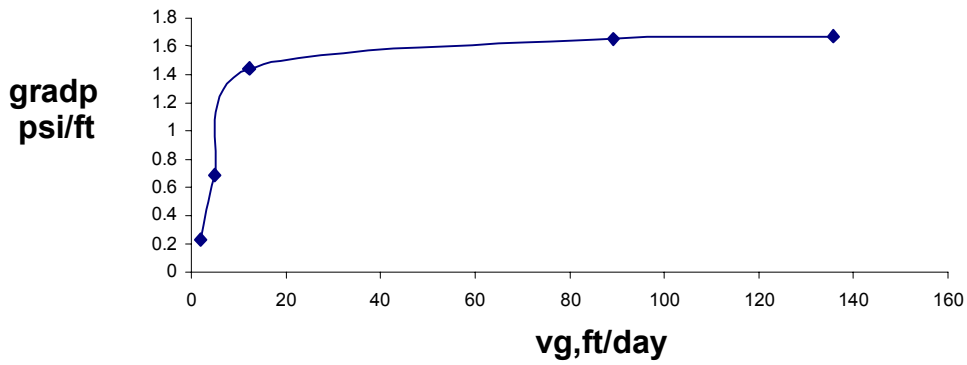


Fig. 3.35. Pressure gradient as a function of gas interstitial velocity V_g in a 7.1-darcy sandpack; 0.01 wt% surfactant; liquid interstitial velocity $V_w = 13.6$ ft/day.

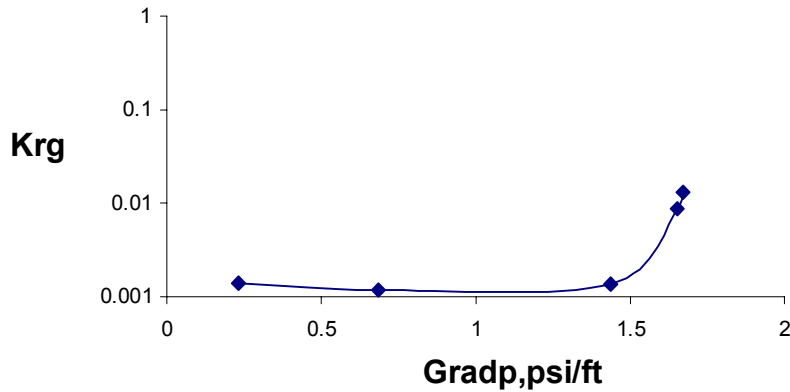


Fig. 3.36. Effective gas relative permeability (incorporating entire effect of foam on gas mobility into gas relative permeability) for experiment in Fig. 3.35.

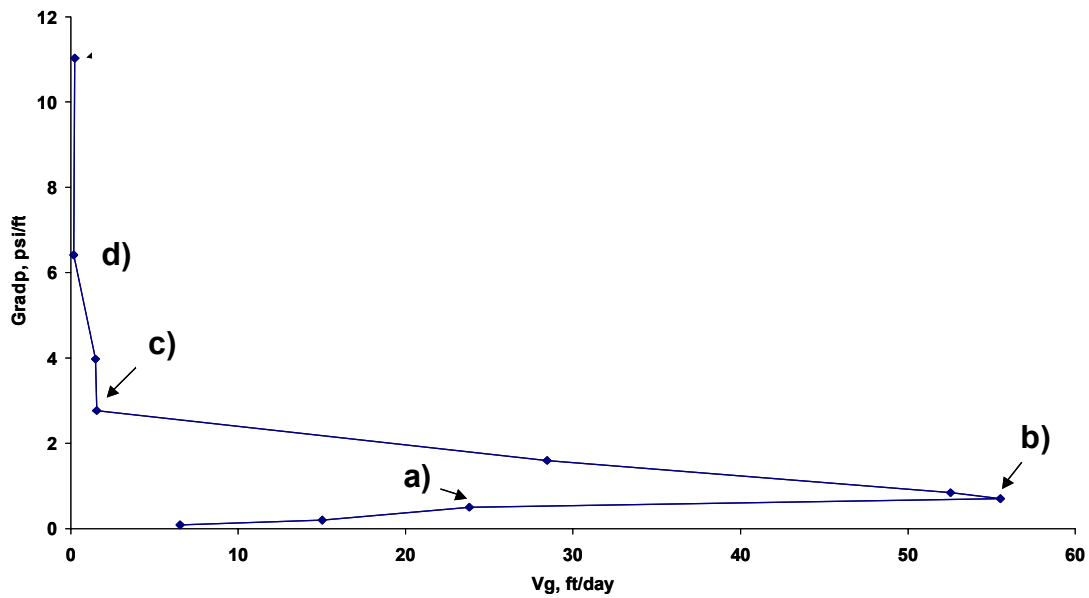


Fig. 3.37. Gas interstitial velocity as a function of applied pressure drop (averaged here across the sandpack to give an average pressure gradient) across a heterogeneous sandpack. Liquid interstitial velocity is held fixed at 5.24 ft/day, and gas flow is regulated at fixed pressure drop by a pressure regulator upstream of the sandpack. Dots represent steady-state points. Letters refer to plots in Fig. 3.38.

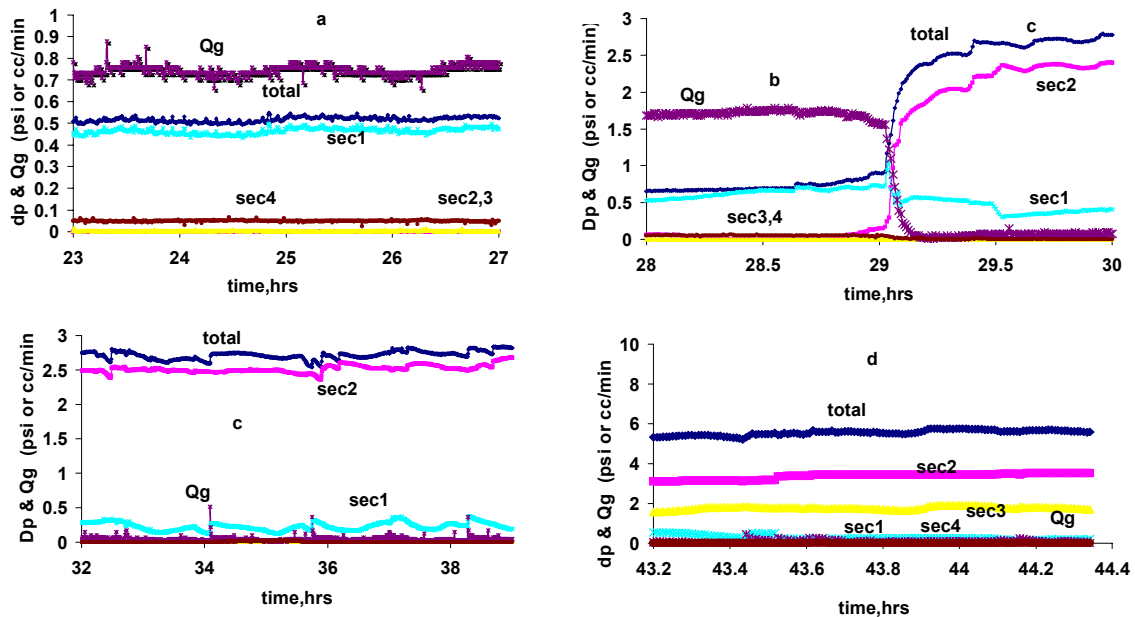


Fig. 3.38. Gas flow rate, and pressure drop in the individual sections in experiment of Fig. 3.37.

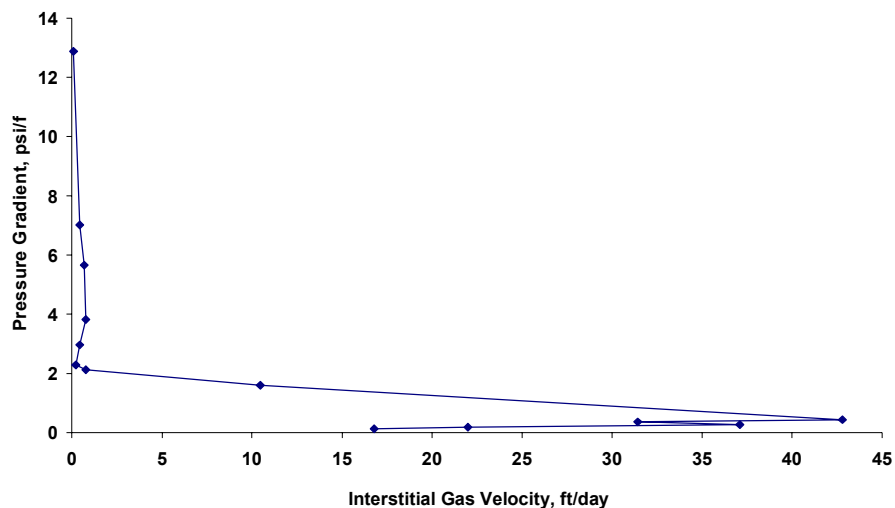


Fig. 3.39. Experiment similar to Fig. 3.37, but with a higher liquid interstitial velocity (3.49 ft/day).

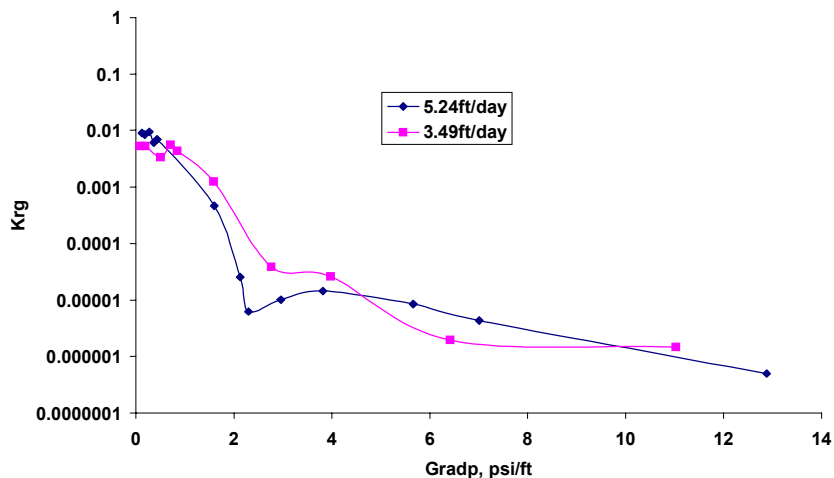


Fig. 3.40. Effective gas relative permeability for experiments in Figs. 3.37 and 3.39.

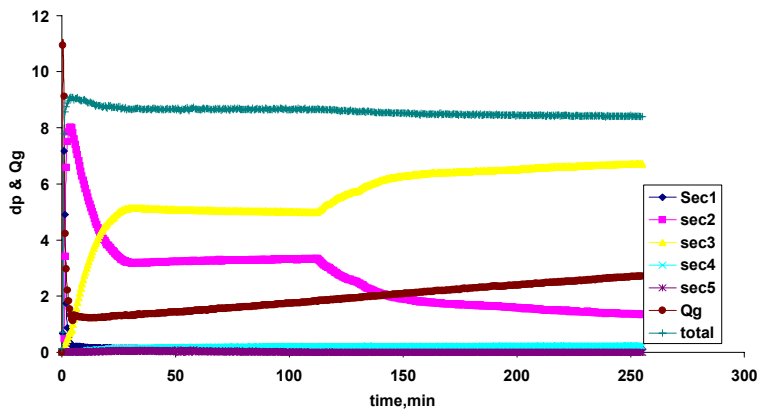


Fig. 3.41. Sectional pressure drop and gas flow rate in fixed-pressure SAG injection into a beadpack with 1.2 darcy permeability upstream (sections 1 to 3) and 97.8 darcy downstream (sections 3 to 5).

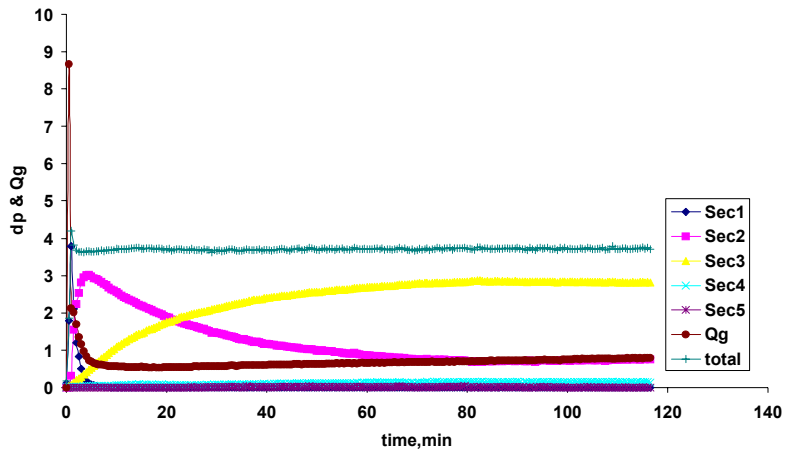


Fig. 3.42. Result of experiment similar to that in Fig. 3.41, but with fixed pressure drop of 4 psi across sandpack.

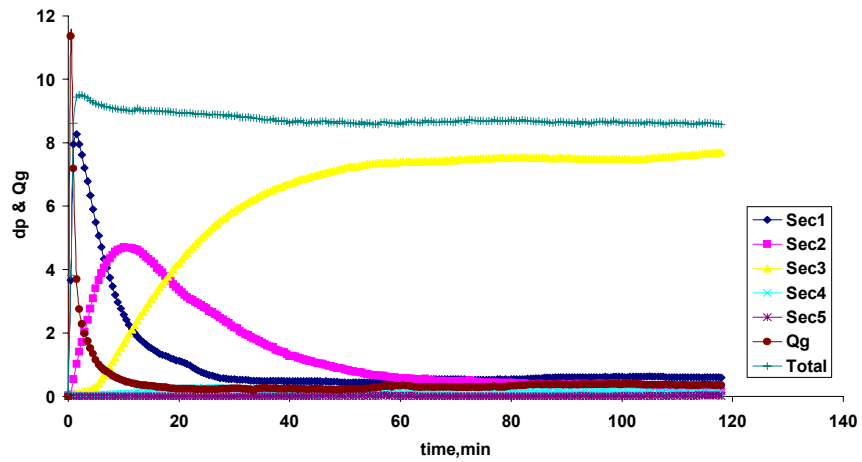


Fig. 3.43. Result of experiment similar to that in Fig. 3.24, but with 1 wt% surfactant in aqueous phase.

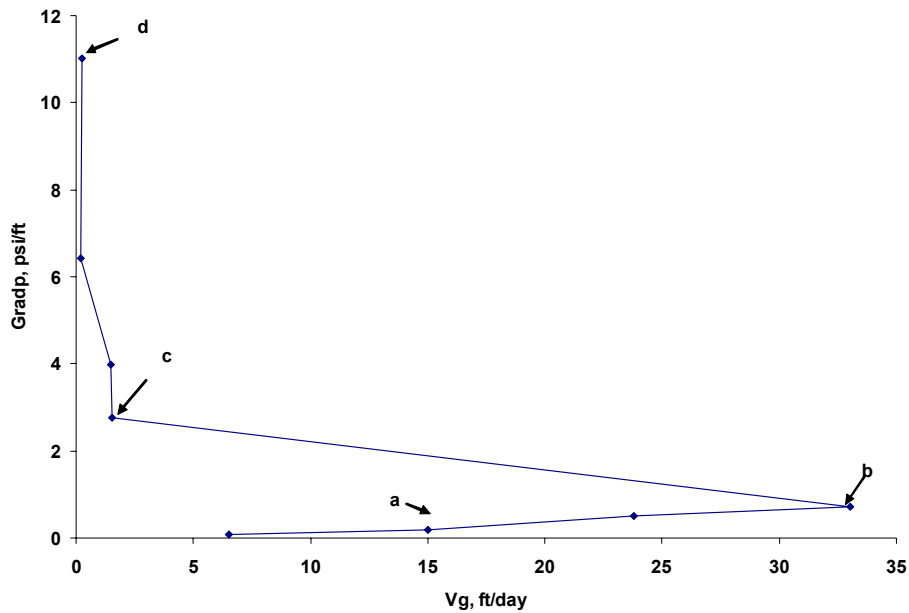


Fig. 3.44. Gas interstitial velocity as a function of applied pressure drop (averaged here across the sandpack to give an average pressure gradient) across a heterogeneous sandpack. Liquid interstitial velocity is held fixed at 5.24 ft/day, and gas flow is regulated at fixed pressure drop by a pressure regulator upstream of the sandpack. Dots represent steady-state points. 1 wt% surfactant concentration. a) coarse-foam regime. b) onset of foam generation. c) onset of plugging. d) gas flow nearly plugged.

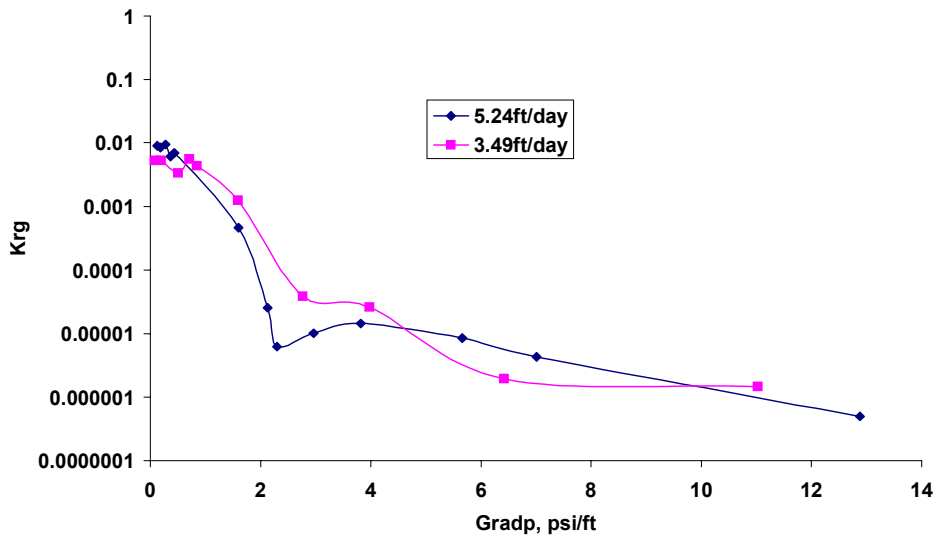


Fig. 3.45. Effective gas relative permeability for the experiment in Fig. 3.444 ($U_w = 5.24$ ft/d) and a similar experiment at lower liquid interstitial velocity ($U_w = 3.49$ ft/d).

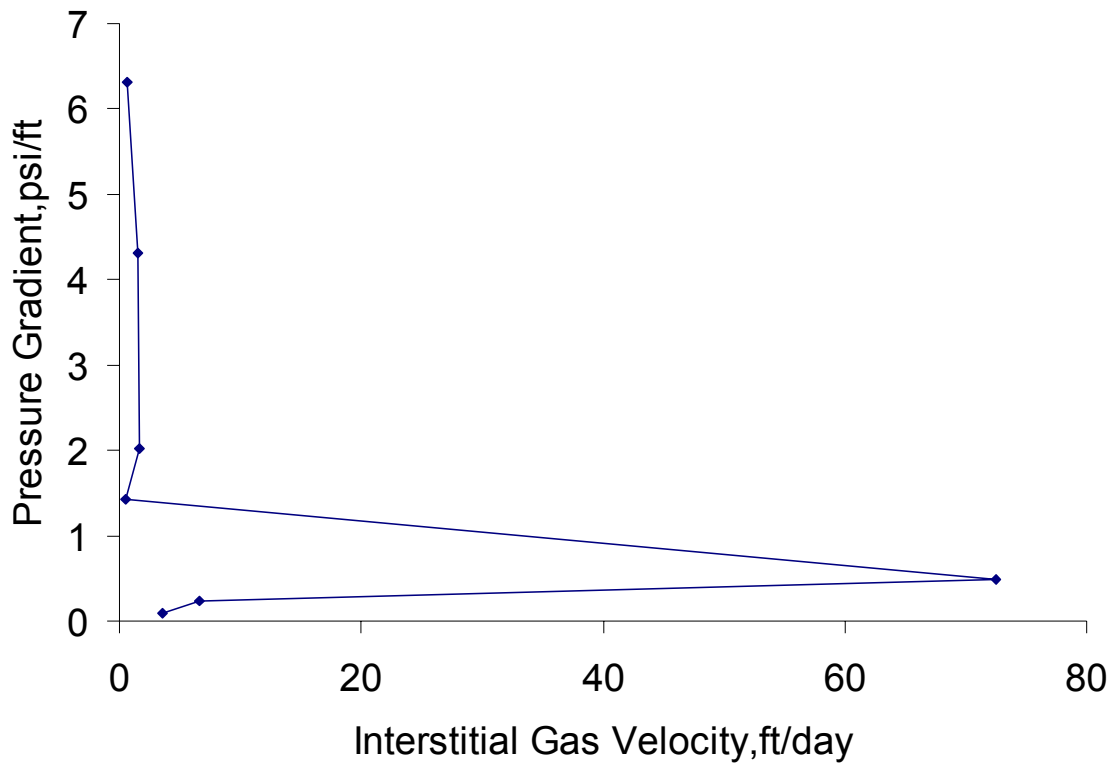


Fig. 3.46. Gas interstitial velocity as a function of average pressure gradient across a heterogeneous sandpack with 10x lower surfactant concentration than in Fig. 3.44, i.e. 0.1 wt% surfactant. Same liquid interstitial velocity, 5.24 ft/d.

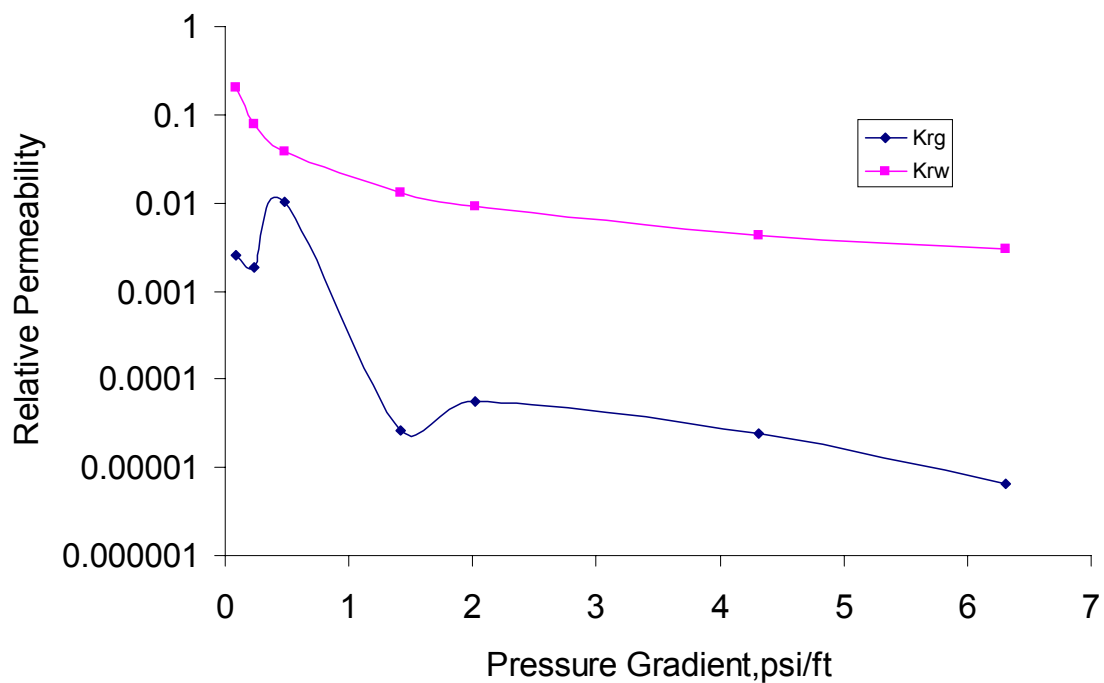


Fig. 3.47. Effective gas relative permeability and liquid relative permeability for the experiment in Fig. 3.46.

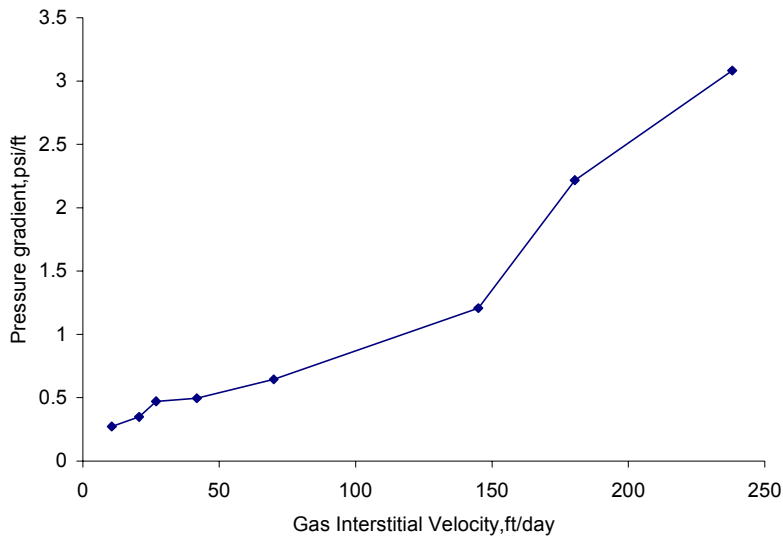


Fig. 3.48. Gas interstitial velocity as a function of average pressure gradient across a heterogeneous sandpack with 100x lower surfactant concentration than in Fig. 3.44, i.e. 0.01 wt% surfactant. Liquid interstitial velocity U_w is much higher here, 13.98 ft/d. Higher U_w promotes foam generation, but even so none is observed here.

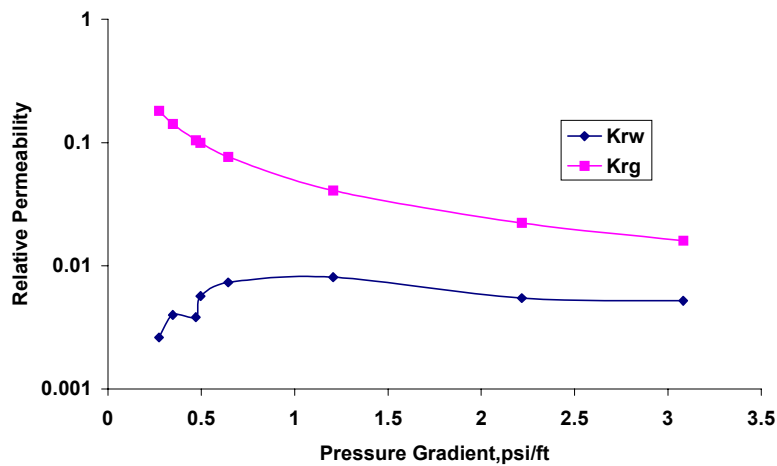


Fig. 3.49. Effective gas relative permeability and liquid relative permeability for the experiment in Fig. 3.48.

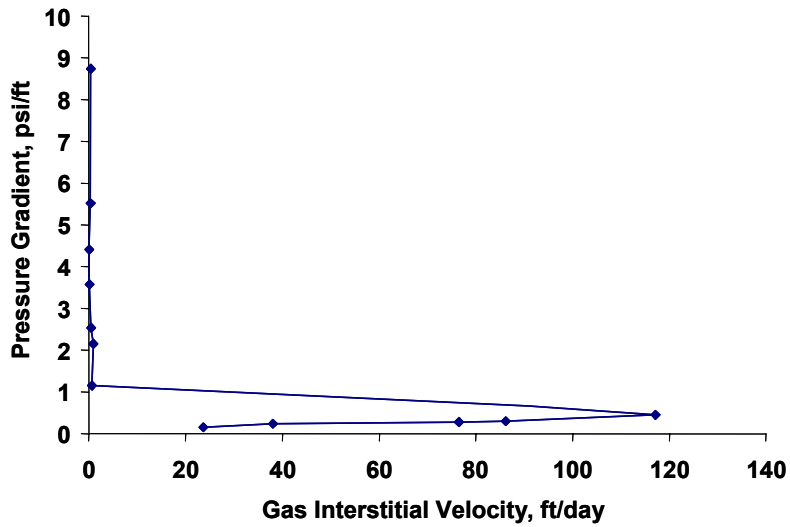


Fig. 3.50. Interstitial gas velocity as a function of steady pressure gradient in a homogeneous 18.6-d sandpack; liquid interstitial velocity = 7.61 ft/d.

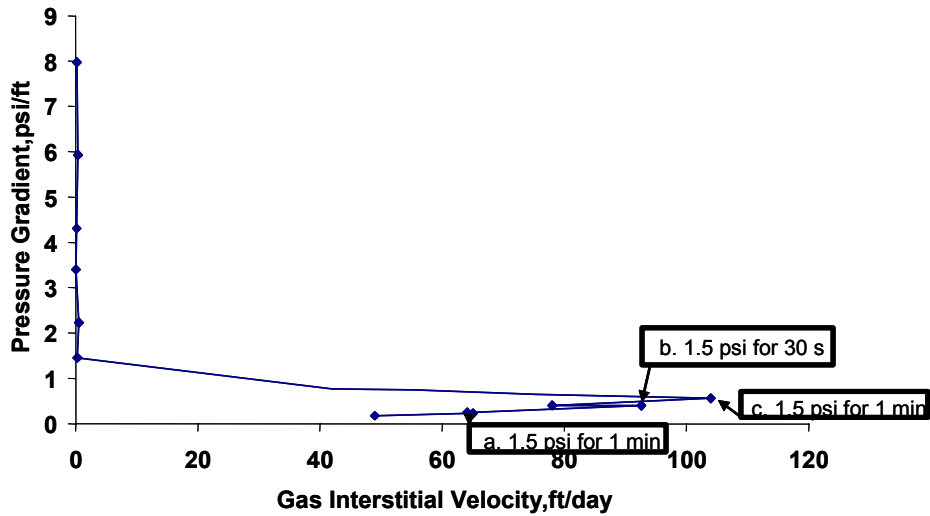


Fig. 3.51. Experiment similar to that in Fig. 3.50, but where pressure gradient is increased to 1.5 psi/ft for brief periods.

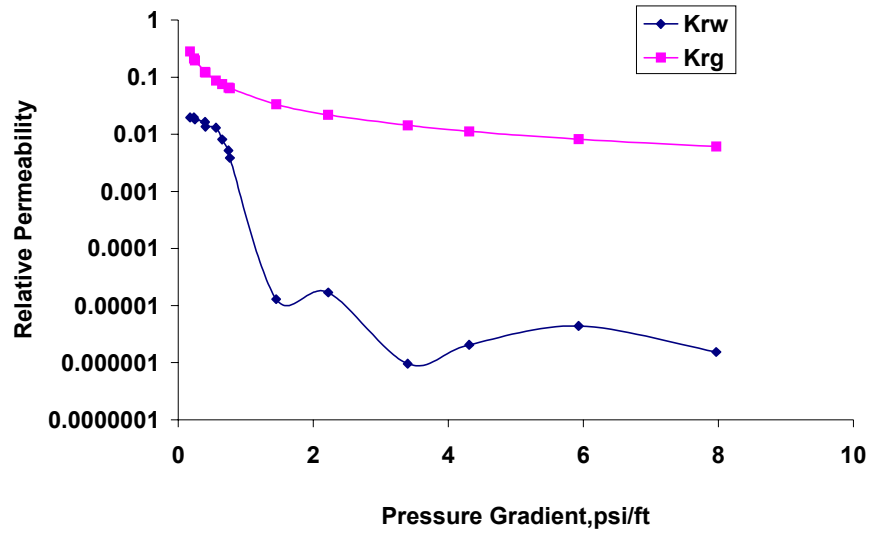


Fig. 3.52. Effective gas relative permeability and liquid relative permeability for the experiment in Fig. 3.51.

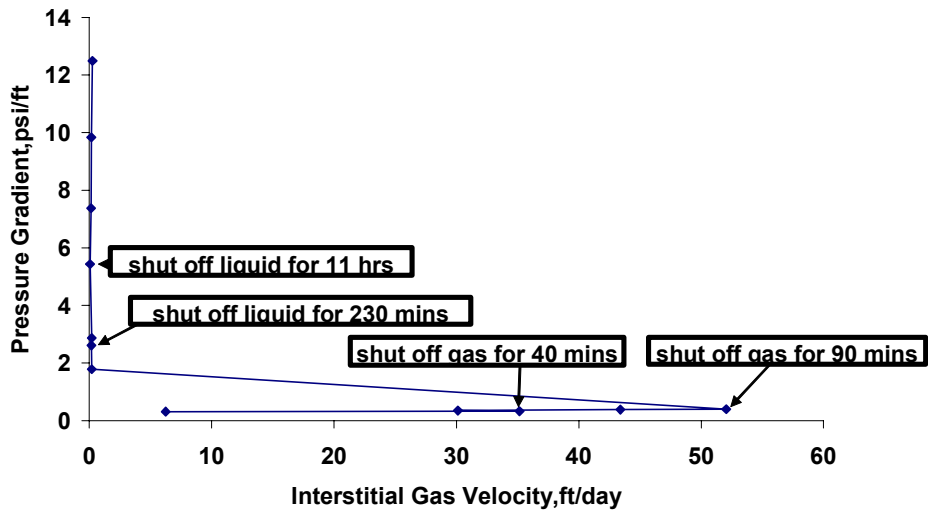


Fig. 3.53. Experiment similar to that in Fig. 3.50, but where liquid or gas injection is interrupted at times.

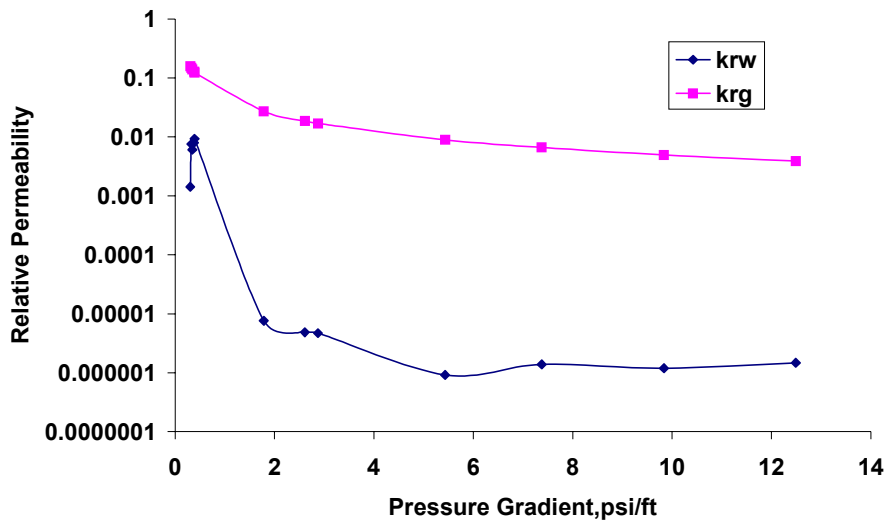


Fig. 3.54. Effective gas relative permeability and liquid relative permeability for the experiment in Fig. 3.53.

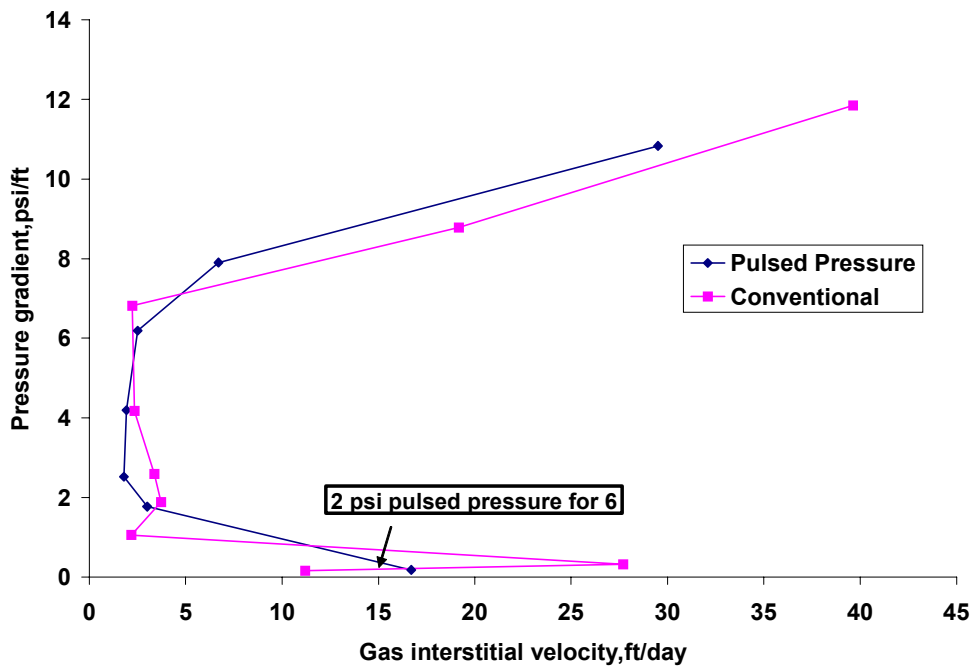


Fig. 3.55. Pressure gradient as a function of gas interstitial velocity with liquid interstitial velocity fixed at 7.57 ft/d, with a permeability ratio of 87.3/17.1 in the sandpack; with 0.1 wt% surfactant. Also shown are the results with pressure drop raised to 2 psi for 6 min after the initial steady state at low pressure drop.

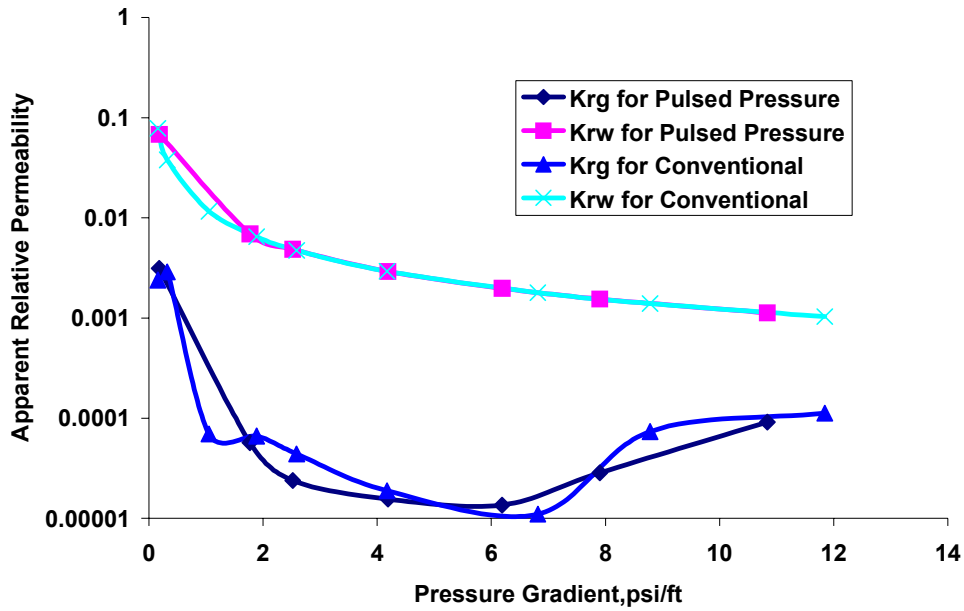


Fig. 3.56. Effective gas relative permeability and liquid relative permeability for the experiments in Fig. 3.55.

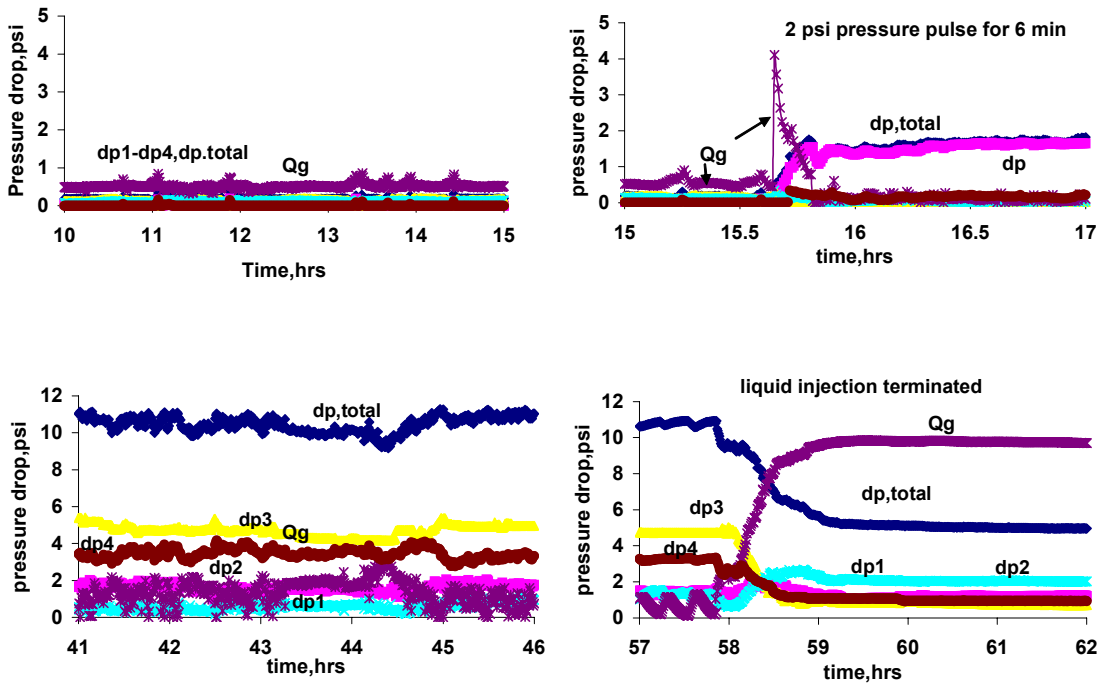


Fig. 3.57. Pressure profiles and gas flow rate for the pulsed-pressure experiment in Fig. 3.55.

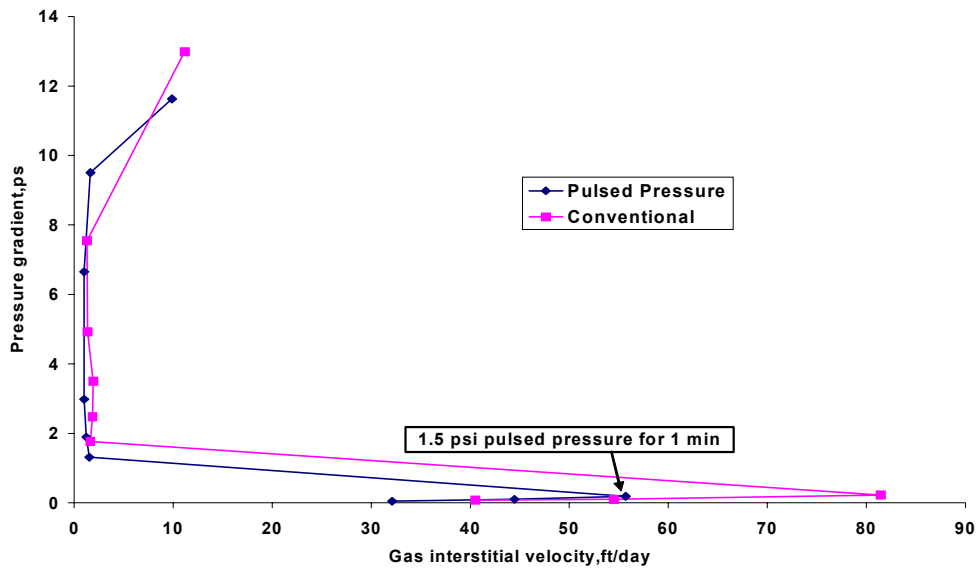


Fig. 3.58. Pressure gradient as a function of gas interstitial velocity with liquid interstitial velocity fixed at 7.57 ft/d, with a permeability ratio of 87.3/17.1 in the sandpack; with 1.0 wt% surfactant. Also shown are the results with pressure drop raised to 1.5 psi for 1 min after the initial steady state at low pressure drop.

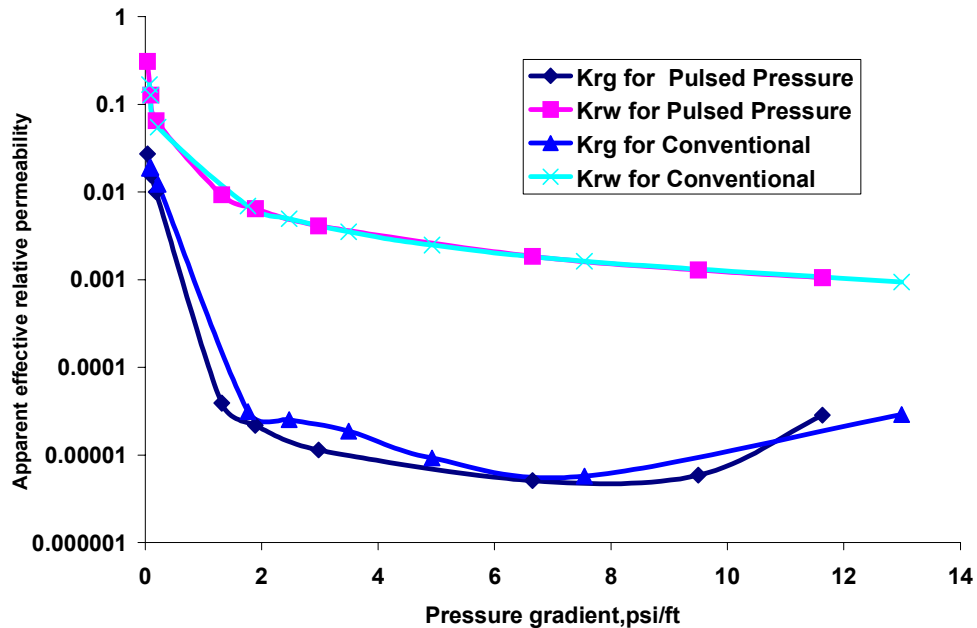


Fig. 3.59. Effective gas relative permeability and liquid relative permeability for the experiments in Fig. 3.48.

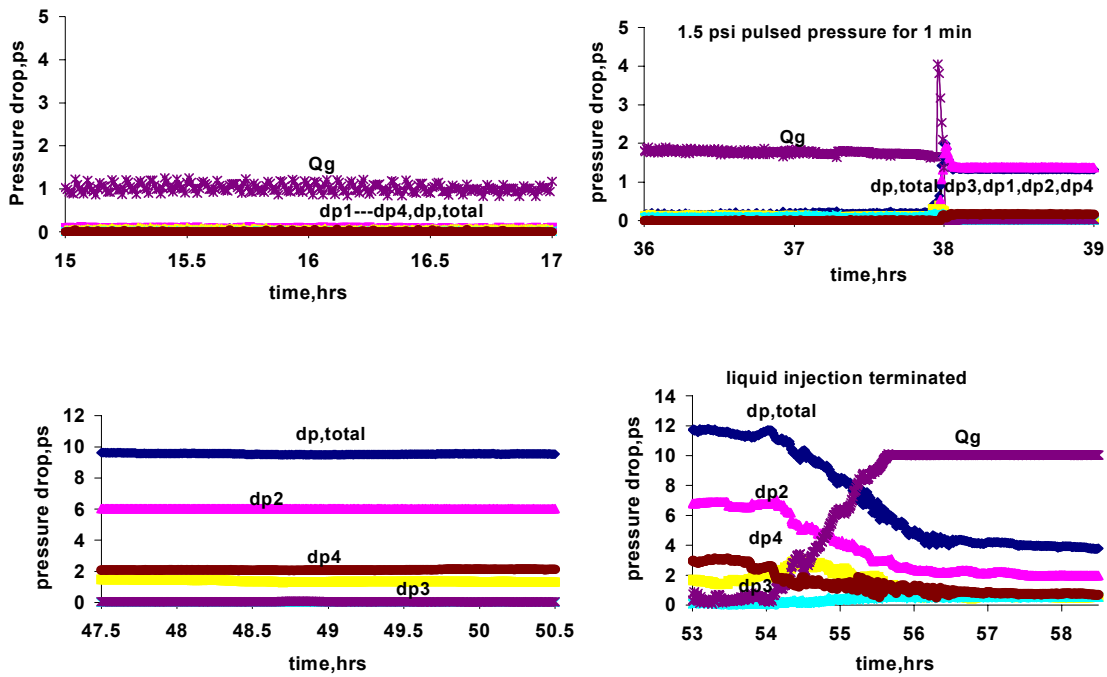


Fig. 3.60. Pressure profiles and gas flow rate for pulsed-pressure experiment in Fig. 3.48.

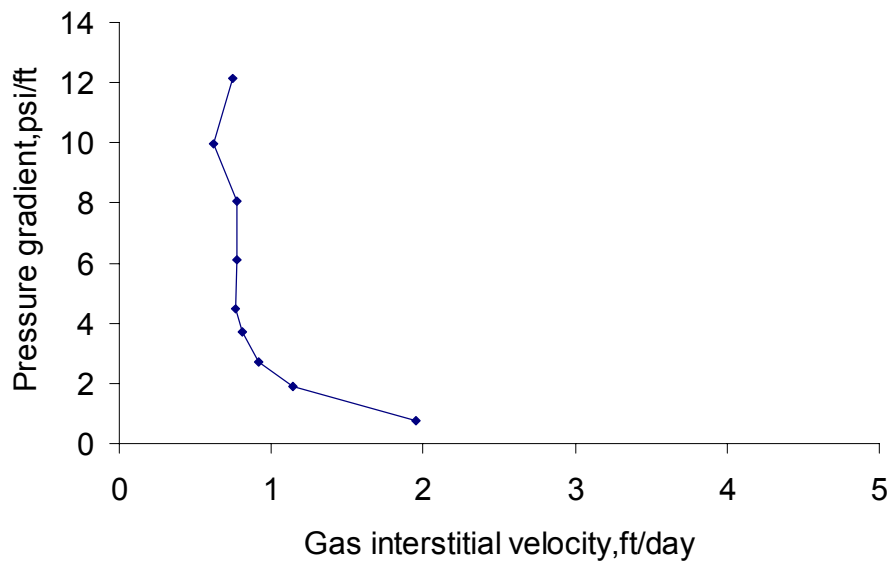


Fig. 3.61. Pressure gradient as a function of gas interstitial velocity in a $k=73.4$ darcy sand pack pre-saturated with 1.0 wt% surfactant; liquid interstitial velocity = 1.256 ft/day once gas injection begins. Note change of scale from previous figures.

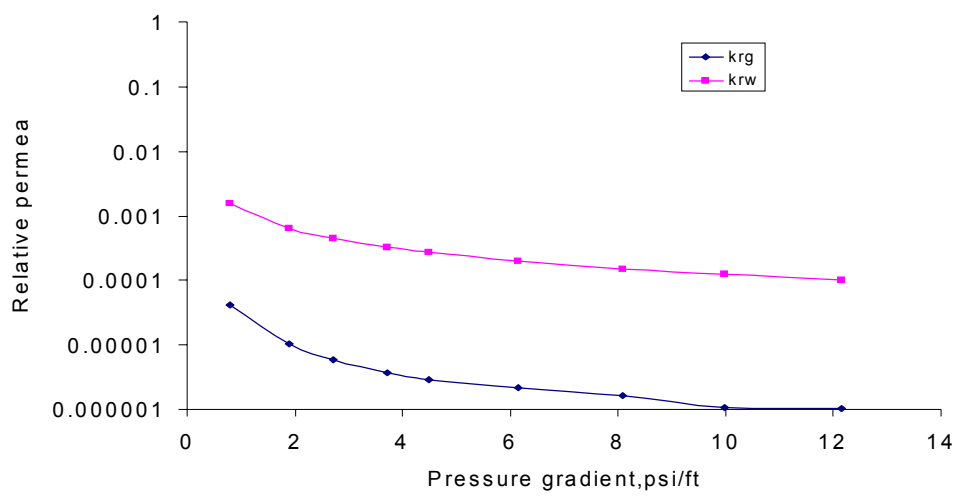


Fig. 3.62. Effective gas and liquid relative permeabilities as a function of pressure gradient for the data in Fig. 3.61.

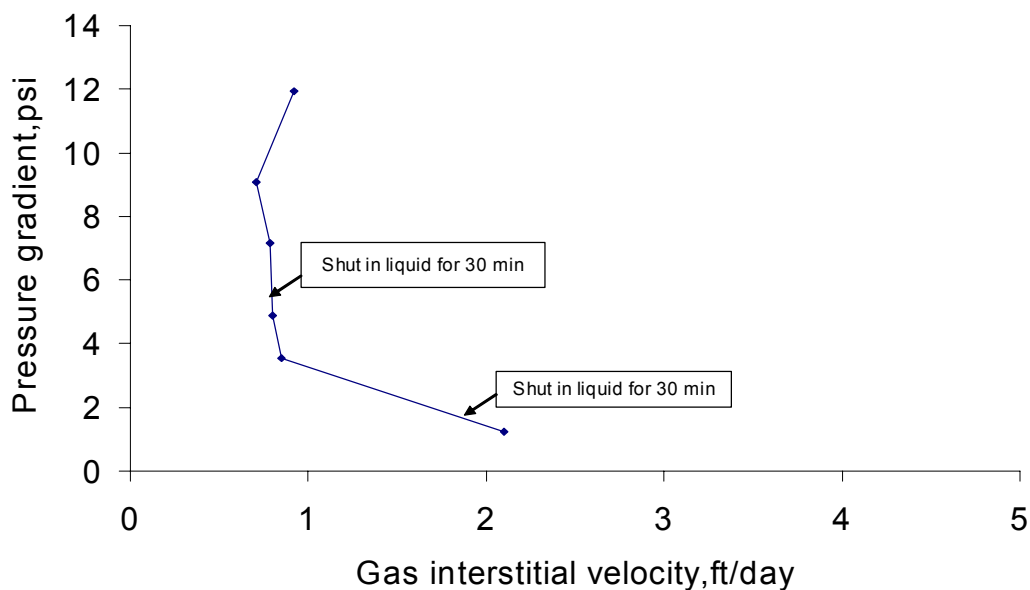


Fig. 3.63. Pressure gradient as a function of gas interstitial velocity in a $k = 73.4$ darcy sand pack pre-saturated with 1.0 wt% surfactant with two episodes of liquid shut-in; at other times, liquid interstitial velocity $V_w = 1.256$ ft/day

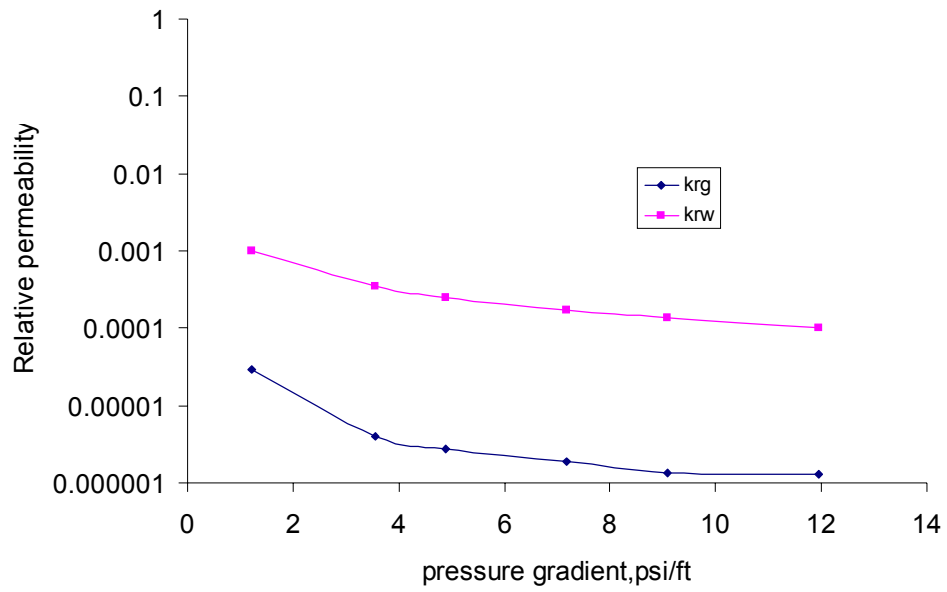


Fig. 3.64. Effective gas and liquid relative permeabilities as a function of pressure gradient for the data in Fig. 3.63.